A STUDY ON
THE FORMATION AND DYNAMICS OF GALAXIES

Thesis by
James Arthur Fillmore

In Partial Fulfillment of the Requirements
for the Degree of
Doctor of Philosophy

California Institute of Technology
Pasadena, California
1985
(Submitted 9 May 1985)

Acknowledgments

Although a Ph.D. represents the accomplishment of the individual, one achieves this mark with the support of many people. I have benefited from friends, colleagues, staff, and faculty.

I hail my fellow graduate students for their friendship, including from earlier years, Alexei Filippenko, Keith Horne, Matt Malkan, Jeff Pier, and Abi Saha.

Special note goes to Todd Boroson, Elliott Brown, Alan Dressler, Rick Edelson, Pawan Kumar, Charles Kowal, Peter Parnicky, Eric Persson, Alain Porter, Ian Thompson, John Tonry, and Ken Young.

Kay Campbell, Lilo Hauck, Jill King, Helen Knudsen, Marilynne Rice, Lorna Thayer, and JoAnn Pearson Wolpert made sure no bureaucracy stood in my way.

The faculty, of course, gave me tasks to do, problems to solve, and knowledge for my keeping. I extend gratitude to Wal Sargent, Maarten Schmidt, Roger Blandford, and Judy Cohen. I am indebted to Peter Goldreich who gave his advice on all aspects of my work and career, and made sure I was always moving forward. Peter also generously gave his time to carefully read and comment on this thesis.

Close friendship with Marc Goroff and Mary, and Don Schneider has been very fulfilling.

And, love from Beverly and my family gives me a sense of purpose.

I must also acknowledge the National Science Foundation for a Graduate Fellowship, the ARCS Foundation for an award, and the Institute in general for financial support.

ABSTRACT

The first half of this thesis is a study on the growth of perturbations in the early universe which might lead to galaxies, clusters of galaxies, or regions void of galaxies.

The growth of self-similar perturbations in an Einstein-deSitter universe with cold, collisionless particles is investigated. Three classes of solutions are obtained; one each with planar, cylindrical, and spherical symmetry. The solutions follow the development of structure in both the linear and nonlinear regimes.

Self-similar spherical voids which develop from initially underdense regions are also investigated. The character of each solution depends upon the initial density deficit. Steep perturbations result in voids bounded by overdense shells with sharp edges.

The second half of this thesis details solutions of steady-state axisymmetric models of elliptical and disk galaxies, and considers which observable properties can be used as diagnostics of the kinematic configuration of the spheroidal component of these systems.

Two component mass models are fitted to surface brightness measurements and used to fit kinematic models to the velocity data. The models with constant mass-to-light ratios and isotropic velocity dispersions adequately fit the inner regions of spiral galaxies with three caveats:

(i) Several galaxies show significant differences between the two sides of the major axis in both their rotation rate and velocity dispersion. While the differences might be caused by non-axisymmetric potentials, variations in the line-of-sight extinction are a more likely cause.

(ii) The inner segment ($R \leq 1$ kpc) of the emission line (gas) rotation curve falls below the predicted circular velocity derived from the stellar velocities. We rule out a variation in the mass-to-light ratio as a cause for this discrepancy because M/L would have to significantly decrease at small radii; this trend is opposite to typical expectations of M/L. Significant emission from gas produced by stellar mass loss, particularly planetary nebulae, which is not yet settled into the disk

might explain this observation.

(iii) Some of the bulges are flatter than one would expect from their rotation rate assuming isotropic random motions, but this additional flattening could be caused by the disk potential.

Self-consistent solutions of the stellar hydrodynamic equations for systems with isodensity surfaces which are concentric oblate spheroids and have constant mass-to-light ratios are presented. Various kinematic configurations are constructed to develop observational diagnostics which can distinguish these configurations. Because the inclination and true flattening of each elliptical is indeterminable, several kinematically distinct configurations are indistinguishable. Observations can uniquely characterize only those galaxies which lie at certain kinematic extremes.

Table of Contents

INTRODUCTORY NOTE

The compilation of two projects is contained within this thesis. The first part is a study on the growth of scale-free perturbations in an Einstein-deSitter Universe. Chapter One considers the gravitational collapse of overdense perturbations, and Chapter Two follows the development of spherical voids. This work was performed in collaboration with Peter Goldreich.

Chapter Three presents detailed fits of two component axisymmetric models to long-slit observations of early-type spirals. Todd Boroson and Alan Dressler supplied the observational data and some questions to be answered.

Chapter Four entails my efforts to find self-consistent models to oblate spheroids, apply them to a sample of bulges and ellipticals, and consider which observations can yield information about the kinematic structure of these systems.

Chapter One

SELF-SIMILAR GRAVITATIONAL COLLAPSE IN AN EXPANDING UNIVERSE

Reprinted from
The Astrophysical Journal (1984, **281**, 1)

THE ASTROPHYSICAL JOURNAL, 281: 1–8, 1984 June 1

SELF-SIMILAR GRAVITATIONAL COLLAPSE IN AN EXPANDING UNIVERSE[1]

JAMES A. FILLMORE AND PETER GOLDREICH
California Institute of Technology
Received 1983 October 10; accepted 1983 December 5

ABSTRACT

We derive similarity solutions which describe the collapse of cold, collisionless matter in a perturbed Einstein–de Sitter universe. We obtain three classes of solutions, one each with planar, cylindrical, and spherical symmetry. Our solutions can be computed to arbitrary accuracy, and they follow the development of structure in both the linear and nonlinear regimes.

Subject headings: cosmology — relativity

I. INTRODUCTION

Understanding the formation of structure in an expanding universe is one of the outstanding problems of modern cosmology. Zel'dovich (1970) was the first to emphasize that anisotropic collapse characterizes the evolution of structure in a universe filled with pressureless matter. High-density regions exhibiting approximate planar, cylindrical, and spherical symmetry commonly form in three-dimensional N-body simulations (Klypin and Shandarin 1983; Frenk, White, and Davis 1983; Centrella and Melott 1983).

We investigate self-similar collapse solutions with planar, cylindrical, and spherical symmetry. Study of these solutions provides considerable insight into the more complicated results obtained from numerical simulations. Of course, the restriction to specialized initial conditions is the price we must pay to obtain similarity solutions. It is convenient to treat the three symmetries in parallel. We use the parameter n to distinguish among them; n equals 1, 2, and 3 for planar, cylindrical, and spherical symmetry, respectively.

The plan of the paper is as follows. In § II we derive the equations which govern the evolution of the similarity solutions. In § III we obtain analytic expressions for the asymptotic properties of the solutions. The results of numerical integrations of the similarity equations are presented in § IV. The relation of our solutions to previous work is discussed in § V. The scale factors used for the three different symmetries are calculated in the Appendix.

II. DERIVATION OF SIMILARITY EQUATIONS

As the scale of the perturbations which we are investigating is always small compared with that of the horizon, Newtonian cosmology is an adequate approximation (Peebles 1980). The equation of motion of a test particle reads

$$\frac{d^2\mathbf{r}(t)}{dt^2} = -\frac{4\pi}{3} G\rho_b(t)\mathbf{r} + \delta\mathbf{g}(\mathbf{r}, t) . \tag{1}$$

The first term on the right-hand side of the equation is the deceleration due to the unperturbed Einstein–de Sitter background density

$$\rho_b(t) = \frac{1}{6\pi G t^2} . \tag{2}$$

The second term is the peculiar acceleration caused by the perturbation density

$$\delta\rho(\mathbf{r}, t) = \rho(\mathbf{r}, t) - \rho_b(t) . \tag{3}$$

The position of a particle is denoted by its distance from the center of symmetry x. For planar, cylindrical, and spherical symmetry, x denotes the distance from the symmetry plane z, the distance from the symmetry axis ϖ, the distance from the symmetry point r.

We define the mass $M(x, t)$ and excess mass $\delta M(x, t)$ within x by

$$M(x, t) = \int_0^x dx' x'^{n-1} \rho(x', t) . \tag{4}$$

For planar symmetry,

$$M(z, t) = \int_0^z dz' \rho(z', t) , \tag{5}$$

the mass per unit area. For cylindrical symmetry,

$$M(\varpi, t) = \int_0^\varpi d\varpi' \varpi' \rho(\varpi', t) , \tag{6}$$

the mass per unit length per unit angle. For spherical symmetry,

$$M(r, t) = \int_0^r dr' r'^2 \rho(r', t) , \tag{7}$$

the mass per unit solid angle.

The peculiar acceleration is related to δM by

$$\delta g(x, t) = -\frac{4\pi G \delta M}{x^{n-1}} . \tag{8}$$

Inserting this expression into the equation of motion yields

$$\frac{d^2x}{dt^2} = -\frac{2}{9}\frac{x}{t^2} - \frac{4\pi G\delta M}{x^{n-1}} = \frac{2}{9}\frac{(3-n)}{n}\frac{x}{t^2} - \frac{4\pi G M}{x^{n-1}} . \tag{9}$$

We choose initial conditions such that at time t_i the unperturbed Hubble law

$$\frac{dr}{dt} = \frac{2}{3}\frac{r}{t} \tag{10}$$

is exactly satisfied. We can imagine that t_i corresponds to the time of decoupling of radiation and matter. The initial position

[1] Contribution No. 3992 of the Division of Geological and Planetary Sciences, California Institute of Technology.

of a test particle is denoted either by its initial distance from the center of symmetry, x_i, or by the initial mass, M_i, between it and the center of symmetry; $M_i \equiv M(x_i, t_i)$.

The initial perturbation is characterized by the profile of δM_i. We express δM_i as a function of M_i. The search for similarity solutions dictates that the initial perturbation be scale free; thus $\delta M_i(M_i)$ must be a power law. We write

$$\delta \equiv \frac{\delta M_i}{M_i} = \left(\frac{M_i}{M_0}\right)^{-\epsilon}, \tag{11}$$

where M_0 is a reference mass; the corresponding reference position is x_0. The parameter ϵ is restricted to values between zero and unity by the requirements that the initial mass perturbation increase and the initial density perturbation decrease away from the center of symmetry.

Our choice of initial conditions is clearly incompatible with exact self-similarity; at t_i there is no collapsed material although the overdensity in the inner regions diverges. It is a plausible assumption that the trajectories of the material with small δ will approach a self-similar solution. This would be satisfactory since for $t \gg t_i$ almost all of the collapsed material has small δ.

Because the initial density exceeds the critical value $\rho_b(t)$, the trajectory of each particle will ultimately oscillate through the center of symmetry. We refer to the events corresponding to the local maxima of $x(t, M_i)$ as apapsis passages. The first apapsis passage is of special significance, and we reserve the name of turnaround for it. The turnaround distance and time are denoted by $x_*(M_i)$ and $t_*(M_i)$. Prior to reaching turnaround, a particle does not cross the orbits of other particles. Thus, for $t < t_*$,

$$\frac{M(x, t)}{M_i} = \left(\frac{t_i}{t}\right)^{2(3-n)/3}, \tag{12}$$

where the $(t_i/t)^{2(3-n)/3}$ factor is a consequence of the unperturbed Hubble expansion along $3 - n$ of the coordinate axes. Using this simple expression for $M(x, t)$, we solve the equation of motion in the interval $t_i < t \leq t_*$ (cf. Appendix), to obtain

$$\frac{x_*}{x_i} = \frac{C_x}{\delta}, \tag{13}$$

$$\frac{t_*}{t_i} = \left(\frac{C_t}{\delta}\right)^{3/2}. \tag{14}$$

Equations (13) and (14) are valid to lowest order in $\delta \ll 1$. The appropriate values of C_x and C_t for the three symmetries are

$$C_x = \tfrac{5}{12}, \quad 0.74, \quad 1;$$

$$C_t = \frac{5}{6}, \quad 1.39, \quad \left(\frac{3\pi}{4}\right)^{2/3}.$$

Inserting equation (11) into equations (13) and (14) yields

$$\frac{x_*}{x_i} = C_x\left(\frac{M_i}{M_0}\right)^{\epsilon}, \tag{15}$$

$$\frac{t_*}{t_i} = C_t^{3/2}\left(\frac{M_i}{M_0}\right)^{3\epsilon/2}. \tag{16}$$

With the aid of equation (4), we find

$$x_* = C_x\left[\frac{nM_0}{\rho_b(t_i)}\right]^{1/n}\left(\frac{M_i}{M_0}\right)^{\epsilon+1/n}. \tag{17}$$

We denote the current turnaround distance by $X(t)$ and the corresponding initial mass by M_t. From equations (16) and (17) it follows that

$$X(t) = \frac{C_x}{C_t^{1+1/n\epsilon}}\left[\frac{nM_0}{\rho_b(t_i)}\right]^{1/n}\left(\frac{t}{t_i}\right)^{2/3+2/(3n\epsilon)}, \tag{18}$$

$$\frac{M(X, t)}{M_0} = \frac{1}{C_t^{1/\epsilon}}\left(\frac{t}{t_i}\right)^{2/(3\epsilon)-2(3-n)/3}. \tag{19}$$

We define dimensionless coordinate and time variables

$$\lambda \equiv \frac{x}{x_*}, \quad \tau \equiv \frac{t}{t_*}. \tag{20}$$

We now prove that, expressed in terms of these scaled variables, the equation of motion is independent of M_i.

Sometime after turnaround a particle crosses the trajectory of other particles, so the simple relation (eq. [12]) for $M(x, t)$ is no longer valid. The major step in the derivation of the similarity equation is to express $M(x, t)$ as a functional of $\lambda(\tau)$. We appeal to self-similarity and write

$$M(x, t) \equiv M(X, t)\mathcal{M}(x/X), \tag{21}$$

where $\mathcal{M}$ is the dimensionless mass profile function given by

$$\mathcal{M}\left(\frac{x}{X}\right) \equiv \int_0^{M_t} \frac{dM_i'}{M_t} H[x(t; M_i) - x(t; M_i')], \tag{22}$$

for $x/X \leq 1$. Here $H[u]$ is the Heaviside function; $H[u] = 0$ for $u < 0$, and $H[u] = 1$ for $u \geq 0$. Changing the variable of integration from M_i to τ with the help of equation (16) yields

$$\mathcal{M}\left(\frac{\lambda}{\Lambda}\right) = \frac{2}{3\epsilon}\int_1^{\infty} \frac{d\xi}{\xi^{1+2/(3\epsilon)}} H\left[\frac{\lambda}{\Lambda} - \frac{\lambda(\xi)}{\Lambda(\xi)}\right], \tag{23}$$

where Λ is defined by

$$\Lambda(\tau) \equiv \tau^{2/3+2/(3n\epsilon)}. \tag{24}$$

Finally, we use equations (17), (18), and (20) to rewrite the equation of motion (9) in terms of the scaled variables:

$$\frac{d^2\lambda}{d\tau^2} = \frac{2(3-n)}{9n}\frac{\lambda}{\tau^2} - \frac{2}{3n}\left(\frac{C_t}{C_x}\right)^n \frac{\tau^{2/(3\epsilon)-2(3-n)/3}}{\lambda^{n-1}}\mathcal{M}\left(\frac{\lambda}{\Lambda}\right). \tag{25}$$

Equation (25) governs the evolution of the similarity solutions for all values of τ. It requires the boundary conditions

$$\lambda(1) = 1, \quad \frac{d\lambda(1)}{d\tau} = 0, \tag{26}$$

which reflect that turnaround occurs at $\tau = 1$, $\lambda = 1$.

Proper application of Newtonian cosmology requires that the linear dimensions of the structures be small compared with the distance to the horizon. This restricts the interval of time over which the similarity solutions are valid in two respects. First, it implies that the planar and cylindrical solutions must be thought of as possessing edges along $3 - n$ symmetry directions. Our analysis neglects edge effects, but they must become important when the turnaround distance approaches the system's dimensions along the symmetry directions. This is inevitable since, for all cases, the turnaround distance grows more rapidly than $t^{2/3}$, the rate of expansion along the symmetry directions. Second, for spherical solutions with $\epsilon < \frac{2}{3}$, the turnaround distance grows faster than t and must eventually approach the horizon scale.

III. ASYMPTOTIC BEHAVIOR OF SIMILARITY SOLUTIONS

The similarity solutions describe a basic type of motion. There is an initial period of expansion which ends at turnaround. After turnaround, the trajectory oscillates through the center of symmetry. With the passage of time, the ratio of the apapsis distance to the current turnaround distance decreases as does the ratio of the oscillation period to the time scale for halo evolution. Thus the trajectory is asymptotically buried ever more deeply in the halo of collapsed material.

The above picture implies that there is an adiabatic invariant associated with buried trajectories. Furthermore, the scale-free nature of the similarity solutions suggests that the mass profile in the halo might be approximated by a power law in the distance from the center of symmetry. These features enable us to deduce the asymptotic properties of the similarity solutions.

We parameterize the halo mass profile by

$$M(x, t) = \kappa(t)x^{\gamma}, \tag{27}$$

and the variation of the apapsis distance x_a by

$$\frac{x_a}{x_*} = \left(\frac{t}{t_*}\right)^q. \tag{28}$$

Our goal is to relate γ and q to ϵ.

The equation of motion of a halo particle may be written as

$$\frac{d^2x}{dt^2} = -4\pi G\kappa(t)x^{\gamma-n+1}. \tag{29}$$

Orbits for which $x_a \ll X$ have periods which are much shorter than t. Thus it is a good approximation to treat κ as constant over one orbit period. For constant κ, equation (29) has the energy integral

$$\left(\frac{dx}{dt}\right)^2 = \frac{8\pi G\kappa(t)}{(\gamma-n+2)}(x_a^{\gamma-n+2} - x^{\gamma-n+2}). \tag{30}$$

The gradual variation of the apapsis distance due to the time dependence of κ is obtained from the action

$$J = 4\int_0^{x_a} dx\left(\frac{dx}{dt}\right) = 8\left[\frac{2\pi G\kappa(t)}{\gamma-n+2}\right]^{1/2} x_a^{(\gamma-n+4)/2}\int_0^1 du(1-u^{\gamma-n+2})^{1/2}, \tag{31}$$

which is an adiabatic invariant. We define the auxiliary parameter s by $\kappa(t) = ct^{-s}$. Thus $q = s/(\gamma-n+4)$. We use equations (18), (19), and (27) to express s in terms of γ and ϵ as

$$s = \frac{2}{3\epsilon}\left[\frac{(\gamma-n)}{n} + (\gamma-n+3)\epsilon\right]. \tag{32}$$

Hence

$$q = \frac{2}{3\epsilon(\gamma-n+4)}\left[\frac{(\gamma-n)}{n} + (\gamma-n+3)\epsilon\right]. \tag{33}$$

We define $P(x/x_a)$ to be the fraction of time a particle with apapsis x_a spends inside x:

$$P(v) = \frac{I(v)}{I(1)} \quad (v \le 1),$$

$$P(v) = 1 \quad (v > 1), \tag{34}$$

where

$$I(v) \equiv \int_0^v \frac{du}{(1-u^{\gamma-n+2})^{1/2}}. \tag{35}$$

Self-consistency demands that

$$\left(\frac{x}{X}\right)^{\gamma} = \frac{M(x, t)}{M(X, t)} = \int_0^{M_t}\frac{dM_i}{M_t}P\left[\frac{x}{x_a(t; M_i)}\right]. \tag{36}$$

Transforming the integration variable from M_i to $u \equiv x/x_a$ using equations (17), (18), and (28), we obtain

$$\left(\frac{x}{X}\right)^{\gamma-p} = \frac{1}{p}\int_{x/X}^{v}\frac{du}{u^{1+p}}P(u), \tag{37}$$

where

$$p = \frac{2n}{2+n(2-3q)\epsilon}. \tag{38}$$

Now we have arrived at the crucial point. For $u \ll 1$, $P(u) \approx u/I(1)$. Thus the integral in equation (37) converges or diverges as x/X approaches 0 according to whether p is less than or greater than 1. In the former case,

$$p \le 1, \quad \gamma = p,$$

whereas, in the latter,

$$p \ge 1, \quad \gamma = 1.$$

The physical distinction between the two cases is clear. For $p < 1$, the mass in the inner halo is dominated by particles with small apapsides, $x_a/X \ll 1$, which passed their turnaround events a long time ago. On the other hand, for $p > 1$, the mass in the inner halo comes from particles whose apapsides are spread throughout the halo.

Completing the allowable solutions with the aid of equations (33) and (38), we find

$n = 1$:

$$\gamma = p = \frac{3}{3+\epsilon} \le 1, \quad q = \frac{4}{9};$$

$n = 2$:

$$\gamma = 1, \quad p = \frac{3}{2+\epsilon} \ge 1, \quad q = \frac{4\epsilon-1}{9\epsilon}; \tag{39}$$

$n = 3$:

$$\gamma = 1, \quad p = \frac{6}{4+3\epsilon} \ge 1, \quad q = \frac{3\epsilon-2}{9\epsilon}, \quad \text{for } \epsilon \le \frac{2}{3};$$

$$\gamma = p = \frac{3}{1+3\epsilon} \le 1, \quad q = 0, \quad \text{for } \epsilon \ge \frac{2}{3}.$$

IV. NUMERICAL INTEGRATION OF SIMILARITY EQUATIONS

The similarity solutions are determined by numerical integration of the second-order differential equation (25) subject to the boundary conditions given by equations (26). Backward integration is straightforward because $\mathcal{M} = \tau^{-2/(3\epsilon)}$ for $\tau \le 1$. For $\tau \ge 1$, $\mathcal{M}$ is a functional of λ, so an iterative method must be employed. Following an initial guess for $\mathcal{M}$, we alternately integrate equation (25) over the selected domain of $\tau \ge 1$ and then compute $\mathcal{M}$ over the same domain of τ from equation (23). This procedure is continued until the desired level of convergence is achieved. The solutions are quite robust, and

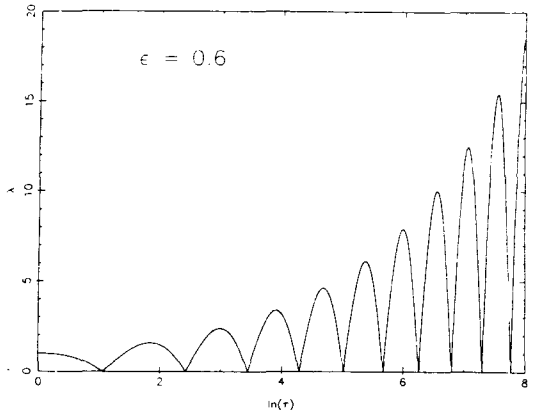

FIG. 1

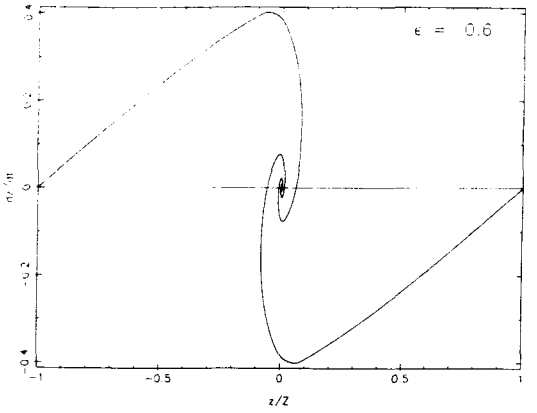

FIG. 2

FIG. 1.—Planar symmetry: particle trajectory for $\epsilon = 0.6$

FIG. 2.—Planar symmetry: instantaneous location of all particles in phase space for $\epsilon = 0.6$.

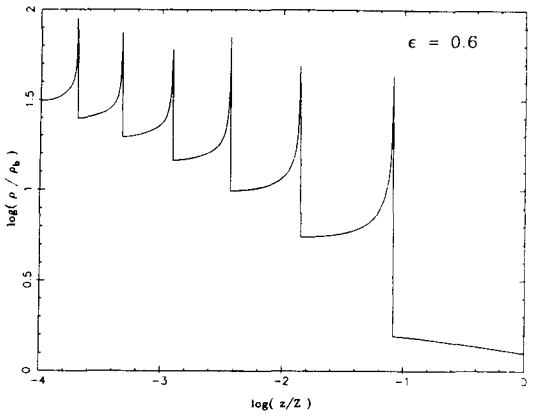

FIG. 3

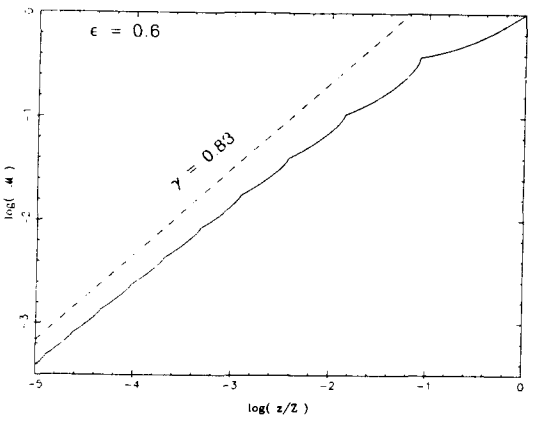

FIG. 4

FIG. 3.—Planar symmetry: ratio of actual to background density for $\epsilon = 0.6$.

FIG. 4.—Planar symmetry: profile of mass per unit area for $\epsilon = 0.6$. Dashed line shows predicted power-law slope.

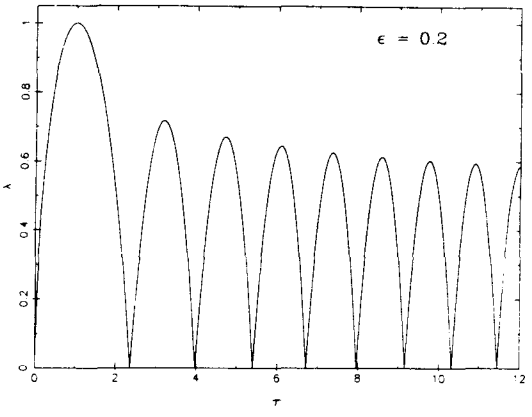

FIG. 5*a*

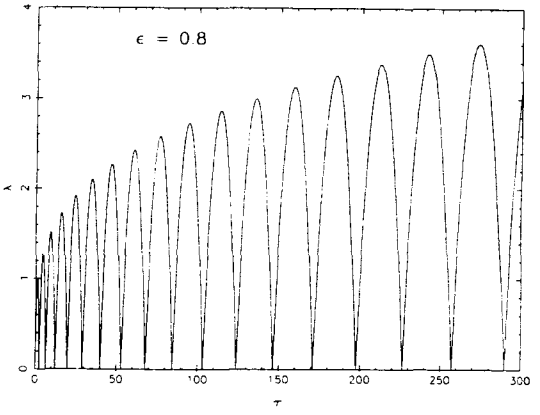

FIG. 5*b*

FIG. 5.—Cylindrical symmetry: particle trajectory for (*a*) $\epsilon = 0.2$, (*b*) $\epsilon = 0.8$

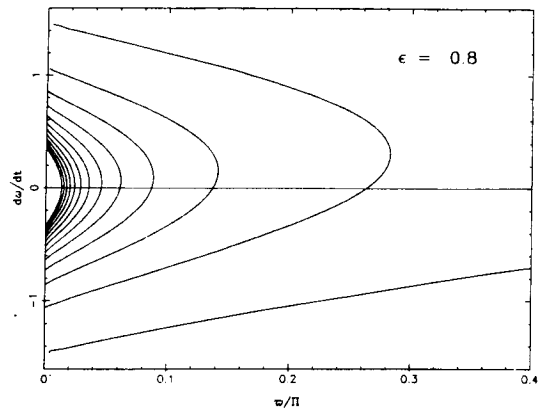

FIG. 6.—Cylindrical symmetry: instantaneous location of all particles in phase space for $\epsilon = 0.8$.

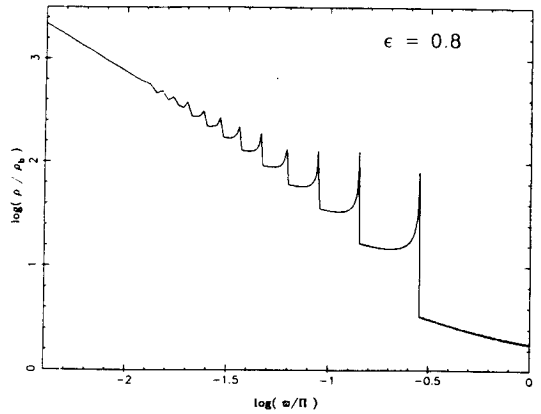

FIG. 7.—Cylindrical symmetry: ratio of actual to background density for $\epsilon = 0.8$.

almost any monotonic function of λ/Λ which satisfies $\mathcal{M}(0) = 0$ and $\mathcal{M}(1) = 1$ provides an adequate input guess.

The integral giving $\mathcal{M}$ is calculated at a discrete grid of points; typically 500 are used. It is evaluated between these points by linear interpolation. A higher order spline interpolation is unsuitable because $\mathcal{M}$ is not a smooth function. The ratio of the particle's apapsis distance to the current turnaround distance, λ_a/Λ, decreases with increasing τ. The similarity solution is generally determined out to the value of τ at which λ_a/Λ falls below the lowest grid point.

At small values of λ the acceleration is proportional to $\lambda^{(\gamma-\alpha+1)}$. Thus, near the origin it vanishes in the planar case, equals unity in the cylindrical case, and diverges in the spherical case. In the last two cases the trajectory is integrated analytically through the origin.

The principal features of each solution are illustrated in a sequence of four figures. There are three such sequences (Figs. 1–12), one for each symmetry. The first figure of each sequence depicts the oscillatory behavior of $\lambda(\tau)$. The second figure of

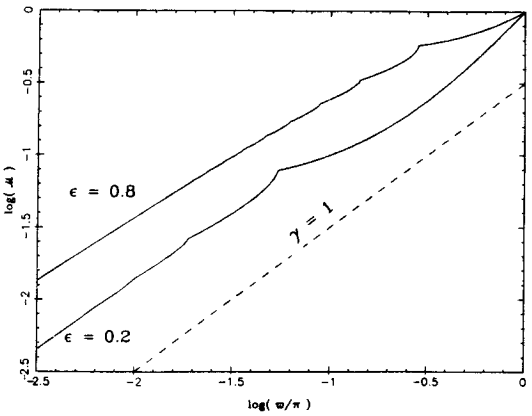

FIG. 8.—Cylindrical symmetry: profiles of mass per unit length per unit angle for $\epsilon = 0.2$ and 0.8. Dashed line shows predicted power-law slope.

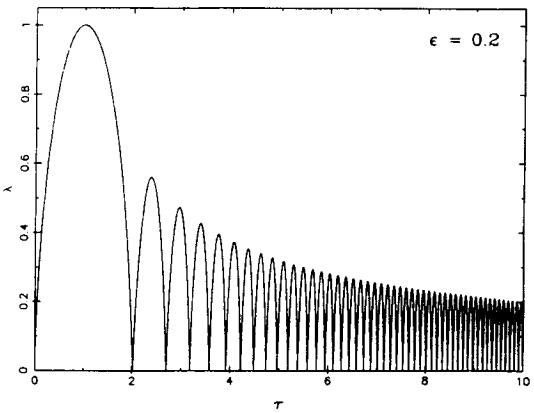

FIG. 9a

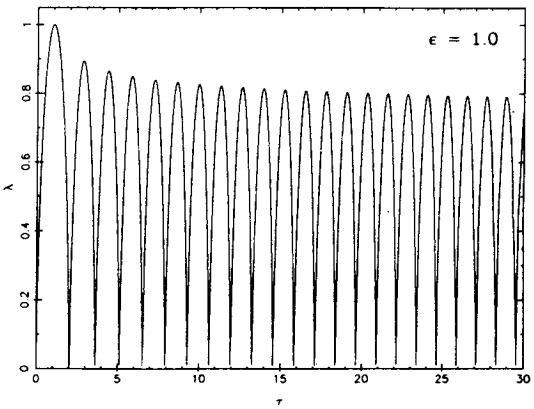

FIG. 9b

FIG. 9.—Spherical symmetry: particle trajectory for (a) $\epsilon = 0.2$, and (b) $\epsilon = 1.0$

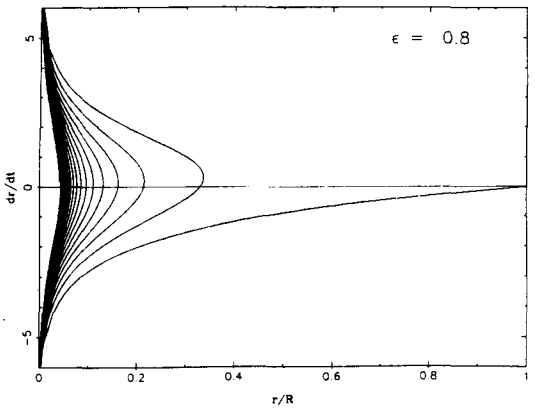

FIG. 10.—Spherical symmetry: instantaneous location of all particles in phase space for $\epsilon = 0.8$.

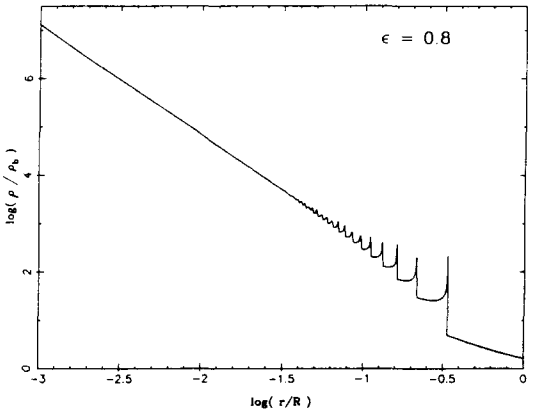

FIG. 11.—Spherical symmetry: ratio of actual to background density for $\epsilon = 0.8$.

each sequence shows the simultaneous location of all particles on the $dx/dt - x$ plane and demonstrates the existence of a denumerably infinite set of points along the phase plane curve at which $\partial x(t, M_i)/\partial M_i = 0$. These points are associated with the density spikes seen in the third figure of each sequence. The spikes are contributed by particles which are approaching apapsis, with the exception that the first apapsis passage, turnaround, is not associated with a spike. The infinite-density spikes are truncated in the figures because the density is averaged over bins. The fourth and final figure in each sequence displays log ($\mathcal{M}$) versus log (x/X) and illustrates the power-law nature of the mass profiles.

By and large, the detailed numerical solutions confirm the predictions of the asymptotic analytic theory which are summarized in equations (39). The largest discrepancy is that the value of γ obtained from the analytic theory does not accurately estimate the rate at which $\mathcal{M}$ increases with x. This may be seen by comparing the slopes of the log ($\mathcal{M}$) versus log (x/X) plots with the theoretically predicted power laws given by the dashed lines.

V. COMPARISON WITH PREVIOUS CALCULATIONS

a) Planar Simulations

Other planar similarity solutions may be compared with numerical calculations done by Melott (1983), who used a one-dimensional cloud-in-cell method to simulate the large-scale clustering of 10,000 collisionless particles. Melott began his calculation at redshift $z = 10{,}000$ and terminated it at $z = 0$. His initial density perturbation was produced by a sinusoidal variation of amplitude 10^{-3} in the spacing of the particles. The entire system extended over one wavelength. Our similarity solutions demand different initial conditions. Nevertheless, they display the same qualitative features found in Melott's simulations. For example, compare the dx/dt versus x plot shown in our Figure 2 with Melott's Figure 8*a*.

b) Spherical Simulations

Interest in galaxy formation stimulated many investigations of spherically symmetric gravitational collapse. Early studies attempted to account for the approximate $\rho \propto r^{-3}$ distribution of the luminous material in elliptical galaxies. It was found that the collapse of an initially static, uniform-density sphere resulted in a final configuration with $\rho \propto r^{-3}$ (Henon 1964; Gott 1973). The secondary infall of bound but initially expanding material onto a collapsed core was discussed by Gunn and Gott (1972). Gott (1975) made the first attempt to determine a final density profile due to secondary infall. He considered a central overdense core embedded in an Einstein–de Sitter universe, essentially our $\epsilon = 1$ case. Gott predicted that the asymptotic density profile would have $\rho \propto r^{-9/4}$. However, his numerical simulations produced $\rho \propto r^{-2.8}$. The extended flat rotation curves of spiral galaxies (Rubin, Ford, and Thonnard 1980; Krumm and Salpeter 1980) imply the presence of halos with $\rho \propto r^{-2}$. This led Gunn (1977) to extend Gott's study to more general initial-mass profiles in an attempt to discover conditions compatible with a final halo with $\rho \propto r^{-2}$. Gunn's analytic treatment is in some respects similar to the asymptotic theory presented in § III of our paper. However, he explicitly assumed that each particle's apapsis reaches a final value which is a fixed fraction of the turnaround radius. We find this

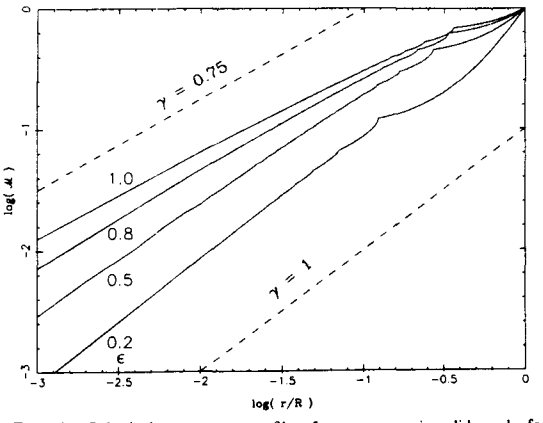

FIG. 12.—Spherical symmetry: profile of mass per unit solid angle for several ϵ-values. Dashed lines show predicted power-law slopes for $\epsilon < \frac{2}{3}$ and for $\epsilon = 1.0$.

assumption to be invalid for $\epsilon < \frac{2}{3}$, precisely the range for ϵ for which the asymptotic theory predicts $\gamma = 1$.

The evolution of an initially uniform-density region of finite radius surrounding a collapsed core was investigated by Dekel, Kowitt, and Shaham (1981) using a three-dimensional N-body code and by Pryor (1982) using a spherically symmetric code. Neither group produced models displaying extended flat rotation curves, although the Dekel *et al.* results provided some support for Gunn's (1977) predictions. However, these investigations were based on initial perturbations whose fractional excess masses δ decrease rather rapidly with increasing M_i; a relatively large fraction of the excess mass is contained in the collapsed cores as a consequence of the small radii at which the surrounding regions of uniform density are truncated. We find similarity solutions compatible with extended flat rotation curves for small ϵ; these correspond to initial configurations for which δ decreases slowly as M_i increases. Of course, our similarity solutions include continuous infall. It remains to be seen how extended the flat rotation curves are in truncated versions of low-ϵ models.

Support for this research was provided by the National Science Foundation through a graduate fellowship awarded to J. A. F. and through grant 80-20005.

APPENDIX

We determine the turnaround time t_* and turnaround distance x_* in terms of t_i, x_i, and δ. The calculations are straightforward since a particle does not cross the orbits of other particles before it reaches turnaround.

a) Planar Symmetry

The equation of motion reads

$$\frac{d^2z}{dt^2} = \frac{4}{9}\frac{z}{t^2} - 4\pi G M(z, t) . \tag{A1}$$

Inserting equations (5) and (12) into equation (9) yields

$$\frac{d^2z}{dt^2} = \frac{4}{9}\frac{z}{t^2} - \frac{2z_i}{3(1-\delta)t_i^2}\left(\frac{t_i}{t}\right)^{4/3} , \tag{A2}$$

for $t < t_*$. Solving the linear equation (A2) subject to the initial condition of unperturbed Hubble expansion, we obtain

$$\frac{z}{z_i} = \frac{1}{(1-\delta)}\left\{\left(\frac{t}{t_i}\right)^{2/3} - \frac{\delta}{5}\left[3\left(\frac{t}{t_i}\right)^{4/3} + 2\left(\frac{t}{t_i}\right)^{-1/3}\right]\right\} . \tag{A3}$$

From equation (A3), we find that to lowest order in $\delta \ll 1$,

$$\frac{z_*}{z_i} = \frac{5}{12\delta} , \qquad \frac{t_*}{t_i} = \left(\frac{5}{6\delta}\right)^{3/2} . \tag{A4}$$

b) Cylindrical Symmetry

The equation of motion is written

$$\frac{d^2\varpi}{dt^2} = \frac{\varpi}{2t^2} - \frac{2G}{\varpi} M(\varpi, t) . \tag{A5}$$

Inserting equations (6) and (12) into equation (9) yields

$$\frac{d^2\varpi}{dt^2} = \frac{\varpi}{9t^2} - \frac{1}{3(1-\delta)}\frac{\varpi_i^2}{t_i^2\varpi}\left(\frac{t_i}{t}\right)^{2/3} , \tag{A6}$$

for $t < t_*$. Equation (A6) is nonlinear, and we have not been able to solve it analytically. However, numerical integrations imply that

$$\frac{\varpi_*}{\varpi_i} \approx \frac{0.74}{\delta} , \qquad \frac{t_*}{t_i} = \left(\frac{1.39}{\delta}\right)^{3/2} . \tag{A7}$$

c) Spherical Symmetry

The equation of motion simplifies to

$$\frac{d^2r}{dt^2} = -\frac{4\pi}{3} G\rho_b(t) r - \frac{G}{r^2}\delta M(r, t) = -\frac{G}{r^2} M(r, t) . \tag{A8}$$

Since $M(r, t)$ is constant for $t < t_*$,

$$\frac{d^2r}{dt^2} = -\frac{2r_i^3}{9(1-\delta)t_i^2}\frac{1}{r^2} . \tag{A9}$$

Although equation (A9) is nonlinear, it has an energy integral. We evaluate the energy constant by requiring that the velocity satisfy the unperturbed Hubble relation at $t = t_i$. This procedure yields

$$\left(\frac{dr}{dt}\right)^2 = \frac{4}{9(1-\delta)}\left(\frac{r_i}{t_i}\right)^2\left(\frac{r_i}{r} - \delta\right). \tag{A10}$$

The turnaround parameters, to lowest order in $\delta \ll 1$, are

$$\frac{r_*}{r_i} = \frac{1}{\delta}, \qquad \frac{t_*}{t_i} = \frac{3\pi}{4\delta^{3/2}}. \tag{A11}$$

REFERENCES

Centrella, J., and Melott, A. L. 1983, *Nature*, **305**, 196.
Dekel, A., Kowitt, M., and Shaham, J. 1981, *Ap. J.*, **250**, 561.
Frenk, C. S., White, S. D. M., and Davis, M. 1983, *Ap. J.*, **271**, 417.
Gott, J. R. 1973, *Ap. J.*, **186**, 481.
———. 1975, *Ap. J.*, **201**, 296.
Gunn, J. E. 1977, *Ap. J.*, **218**, 592.
Gunn, J. E., and Gott, J. R. 1972, *Ap. J.*, **176**, 1.
Henon, M. 1964, *Ann. d'Ap.*, **27**, 83.
Klypin, A. A., and Shandarin, S. F. 1983, *M.N.R.A.S.*, **204**, 891.
Krumm, N., and Salpeter, E. E. 1980, *A.J.*, **84**, 1138.
Melott, A. L. 1983, *Ap. J.*, **264**, 59.
Peebles, J. G. E. 1980, *The Large-Scale Structure of the Universe* (Princeton: Princeton University Press), §§ 6–8.
Pryor, C. P. 1982, Ph.D. thesis, Harvard University.
Rubin, V. C., Ford, W. K., Jr., and Thonnard, N. 1980, *Ap. J.*, **238**, 471.
Zel'dovich, Ya. B. 1970, *Astr. Ap.*, **5**, 84.

J. A. FILLMORE: Robinson 105-24, Caltech, Pasadena, CA 91125

P. GOLDREICH: 170-25 So. Mudd, Caltech, Pasadena, CA 91125

Chapter Two
SELF-SIMILAR SPHERICAL VOIDS IN AN EXPANDING UNIVERSE

Reprinted from
The Astrophysical Journal (1984, **281,** 9)

THE ASTROPHYSICAL JOURNAL, 281: 9–12, 1984 June 1

SELF-SIMILAR SPHERICAL VOIDS IN AN EXPANDING UNIVERSE[1]

JAMES A. FILLMORE AND PETER GOLDREICH
California Institute of Technology
Received 1983 October 24; accepted 1983 December 5

ABSTRACT

We derive similarity solutions which describe the evolution of spherically symmetric voids in a perturbed Einstein–de Sitter universe filled with cold, collisionless matter. The character of a solution depends upon the profile of the initial density deficit. Gradual perturbations give rise to holes within which the density rises smoothly to the background value. Steep perturbations result in voids bounded by overdense shells with sharp edges, i.e., collisionless gravitational shocks.

Subject headings: cosmology — relativity

I. INTRODUCTION

The existence of large voids in the density of galaxies is a major new discovery of observational cosmology (Davis *et al.* 1982; Kirshner *et al.* 1981). Spherically symmetric numerical simulations (Peebles 1982; Hoffman, Salpeter, and Wasserman 1983; Hausman, Olson, and Roth 1983) and analytic fluid dynamical calculations (Sato 1982; Maeda, Sasaki, and Sato 1983; Sato and Maeda 1983) have been applied to demonstrate that empty holes may evolve from initial perturbations of slightly subcritical density. Similar voids commonly appear in three-dimensional N-body simulations (Klypin and Shandarin 1983; Frenk, White, and Davis 1983; Centrella and Melott 1983). Some of these simulations produced voids surrounded by dense shells. This suggests that planar superclusters may have formed from the fragmentation of shells which developed about initial perturbations of subcritical density, as well as from the collapse of initial perturbations of supercritical density. Our contribution is the derivation of similarity solutions for voids which display many of the features seen in the numerical simulations. This work is a sequel to Fillmore and Goldreich (1984, hereafter Paper I), which treated similarity solutions describing gravitational collapse.

The plan of the paper is as follows. In § II we study the early development of subcritical density perturbations. The similarity equation is derived in § III. Results obtained from the integration of this equation are presented in § IV.

II. EARLY DEVELOPMENT

As the scale of the perturbations which we are investigating is small compared with that of the horizon, Newtonian cosmology is an adequate approximation (Peebles 1980). For spherical symmetry, the equation of motion of a test particle reads

$$\frac{d^2r}{dt^2} = -\frac{4\pi G M(r, t)}{r^2}, \tag{1}$$

where $M(r, t)$ is the mass per unit solid angle within radius r at time t. The nonstandard definition of M follows Paper I.

We choose initial conditions such that at time t_i the unperturbed Hubble law

$$\frac{dr}{dt} = \frac{2}{3}\frac{r}{t} \tag{2}$$

is exactly satisfied. The initial position of a test particle is denoted either by its initial distance from the center r_i or by the initial mass between it and the origin, $M_i \equiv M(r_i, t_i)$.

Similarity solutions arise from scale-free initial perturbations. We take the initial perturbation mass $\delta M_i(M_i)$ to have the form

$$\delta \equiv \frac{\delta M_i}{M_i} = -\left(\frac{M_i}{M_0}\right)^{-\epsilon}, \quad \delta < 0, \tag{3}$$

where M_0 is a reference mass; the corresponding reference radius is r_0. The parameter ϵ, which determines the steepness of the initial mass deficit, must lie between zero and unity in order that the initial mass perturbation increase and the initial density perturbation decrease away from the origin.

The initial conditions require some comment; clearly, they are not physically reasonable for $r_i < r_0$, where they imply negative initial mass. We imagine that they pertain only in the region of small $|\delta|$. It is then a plausible but unproven conjecture that they give rise to self-similar solutions at large times, $t \gg t_i$.

So long as a particle does not cross the trajectories of other particles, which we refer to as orbit crossing, its interior mass remains constant, and equation (1) may be integrated to determine $t(r)$. To first order in $|\delta| \ll 1$, we find

$$t = \frac{3t_i}{2|\delta|^{3/2}} \int_0^{r/(r_i|\delta|)} \frac{u^{1/2}du}{(1+u)^{1/2}}. \tag{4}$$

The form of equation (4) suggests that we adopt scaled time and radius variables τ and λ defined by

$$\tau \equiv \frac{t}{t_*} = \frac{4t}{3\pi t_i}|\delta|^{3/2}, \tag{5}$$

$$\lambda \equiv \frac{r}{r_*} = \frac{r|\delta|}{r_i}. \tag{6}$$

Although the powers of δ which appear in the scalings are uniquely determined, the multiplicative constants are arbitrarily chosen to be those taken in Paper I. However, they do not have the special significance that they did in Paper I, where $\tau = \lambda = 1$ corresponded to the unique event of turnaround. The trajectories of particles involved in the evolution of a void are not marked by an event of comparable significance; all choices of multiplicative constants are equally good.

Our choice of scaling defines a fiducial radius $R(t)$ and a

[1] Contribution No. 4004 of the Division of Geological and Planetary Sciences, California Institute of Technology.

corresponding initial mass M_i which are associated with particles whose $t_* = t$. From equations (3) and (5), it follows that

$$R(t) = r_0\,\lambda(1)\left(\frac{4t}{3\pi t_i}\right)^{2/3+2/(9\epsilon)}, \tag{7}$$

$$M_i = M_0\left(\frac{4t}{3\pi t_i}\right)^{2/(3\epsilon)}. \tag{8}$$

The factor

$$\lambda(1) \approx 2.3236 \tag{9}$$

is obtained by evaluating the integral in equation (4) for $\tau = 1$.

The study of equation (4) reveals that orbit crossing occurs only for $\epsilon > \frac{2}{3}$. Thus, equation (4) is valid for all t if $\epsilon < \frac{2}{3}$. The distinction between $\epsilon < \frac{2}{3}$ and $\epsilon > \frac{2}{3}$ may be understood by noticing that the particle terminal velocity, computed neglecting orbit crossing, is an increasing function of M for $\epsilon < \frac{2}{3}$ and a decreasing function of M for $\epsilon > \frac{2}{3}$. A similar argument was given by Sato (1982).

Proper application of Newtonian cosmology requires that the linear dimensions of the structures be small compared with the distance to the horizon. This restricts the interval of time over which the similarity solutions with $\epsilon < \frac{2}{3}$ are valid because their fiducial radii grow faster than t.

III. DERIVATION OF SIMILARITY EQUATION

As the derivation of the similarity equation parallels that given in Paper I, we omit many details. The major step is to express $M(r, t)$ as a functional of λ. We appeal to self-similarity and write

$$M(r, t) = M_i\,\mathcal{M}(r/R), \tag{10}$$

where $\mathcal{M}$ is the dimensionless mass profile function given by

$$\mathcal{M}\left(\frac{r}{R}\right) = \int_0^\infty \frac{dM_i'}{M_i}\,H[r(t; M_i) - r(t; M_i')]. \tag{11}$$

Here $H[u]$ is the Heaviside function; $H[u] = 1$ for $u \geq 0$, and $H[u] = 0$ for $u < 0$. Changing the variable of integration from M_i to τ with the help of equation (8) yields

$$\mathcal{M}\left(\frac{\lambda}{\Lambda}\right) = \frac{2}{3\epsilon}\int_0^\infty \frac{d\xi}{\xi^{1+2/(3\epsilon)}}\,H\left[\frac{\lambda}{\Lambda} - \frac{\lambda(\xi)}{\Lambda(\xi)}\right], \tag{12}$$

where

$$\Lambda \equiv \lambda(1)\tau^{2/3+2/(9\epsilon)} \tag{13}$$

has been defined such that

$$\frac{r}{R(t)} = \frac{\lambda}{\Lambda(\tau)}. \tag{14}$$

The integrals in equations (11) and (12) each differ in one boundary value from their counterparts in Paper I. The upper limit on the former and the lower limit on the latter are ∞ and 0; the corresponding values were M_i and 1 in Paper I. These changes are necessary because orbit crossing occurs before $\tau = 1$ for $\epsilon > 0.92$.

We use equations (5), (6), and (14) to rewrite the equation of motion (1) in terms of the scaled variables:

$$\frac{d^2\lambda}{d\tau^2} = -\frac{\pi^2}{8}\frac{\tau^{2/(3\epsilon)}}{\lambda^2}\,\mathcal{M}\left(\frac{\lambda}{\Lambda}\right). \tag{15}$$

Equation (15) governs the evolution of the similarity solutions for all values of τ. It is identical to the equation we used to compute spherically symmetric collapse solutions in Paper I. However, new boundary conditions are needed to obtain void solutions. These are obtained from equation (4) using the definitions given by equations (5) and (6). In principle, any pair (τ, λ) which satisfies equation (4) and precedes the first orbit crossing event is suitable. In practice, we use

$$\tau = 1, \quad \lambda = 2.3236, \quad \frac{d\lambda}{d\tau} = 1.8786 \tag{16}$$

for all of the examples shown in this paper. There is, however, a minor technical complication. For $\epsilon > 0.92$, orbit crossing takes place before $\tau = 1$; for $\epsilon = 1$, it occurs at $\tau \approx 0.6$. In treating these cases, the boundary conditions must be set at smaller values of τ.

IV. RESULTS

a) $\epsilon < \frac{2}{3}$

Since orbit crossing does not occur for this range of ϵ, the solution is given for all time by equation (4). The density profile is found from

$$\frac{\rho(r/R, t)}{\rho_b(t)} = \frac{3\pi^2}{16\epsilon\tau^{2/(3\epsilon)}}\left[\frac{R}{\lambda(1)r}\right]^3\left[\frac{1+3\epsilon}{3\epsilon} - \frac{3\pi\tau}{4}\frac{(1+\lambda)^{1/2}}{\lambda^{3/2}}\right]^{-1}, \tag{17}$$

with the help of equations (4), (5), (6), (13), and (14), which implicitly determine τ and λ as functions of r/R. Here the background density $\rho_b(t) = (6\pi G t^2)^{-1}$.

Density profiles for two values of ϵ are displayed in Figure 1. The density increases monotonically with radius and gradually approaches the background value. Since $R(t)$ grows faster than t, each particle asymptotically approaches the center of the hole.

b) $\epsilon > \frac{2}{3}$

i) *Numerical Integrations*

The similarity solutions are obtained by numerical integration of the second-order differential equation (15) subject to the boundary conditions given by equation (16). Because the inte-

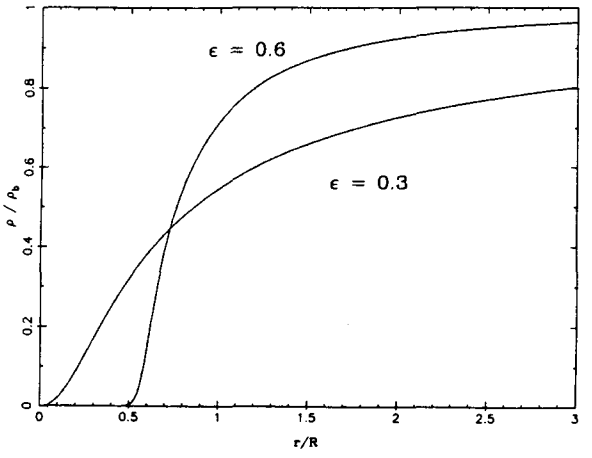

FIG. 1.—Ratio of actual to background density for $\epsilon = 0.3$ and 0.6

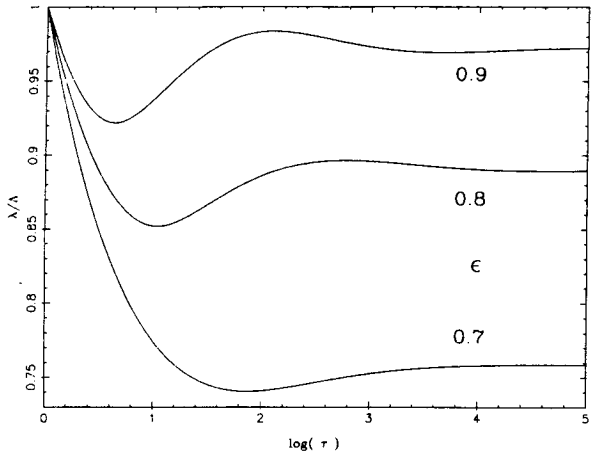

FIG. 2

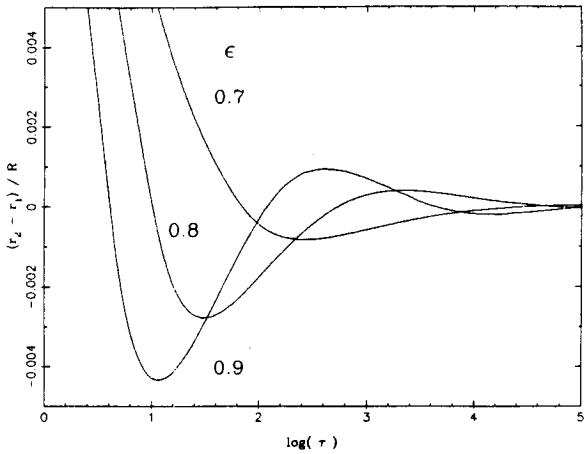

FIG. 3

FIG. 2.—Particle position relative to fiducial distance Λ for $\epsilon = 0.7, 0.8$, and 0.9

FIG. 3.—Difference in position of two nearby particles relative to the fiducial radius for $\epsilon = 0.7, 0.8$, and 0.9

gration must be carried out to very large values of τ, the independent variable is transformed from τ to $v = \ln(\tau)$, and λ is computed on a linear grid in v. Following an initial guess for $\mathcal{M}$, we alternately integrate equation (15) and then update $\mathcal{M}$ by using equation (12). This procedure is continued until the desired level of convergence is obtained.

Plots of λ versus τ are uninteresting, so we do not present any here; particle radii just increase monotonically with time. The variations of λ/Λ drawn in Figure 2 show oscillations of the particle radii scaled to the fiducial radii. Still more revealing are the plots in Figure 3, which illustrate the multiple crossings of neighboring orbits. From a comparison of Figures 2 and 3, it is seen that these crossings coincide with the maxima and minima of λ/Λ.

The orbit crossings have dramatic consequences. The density profiles displayed in Figure 4 all show completely empty holes surrounded by overdense shells. The density is infinite at the inner and outer shell boundaries, but these regions contribute negligibly to the surface density, as can be seen from the mass profiles plotted in Figure 5. The infinite-density spikes are truncated in the figures because the density is averaged over bins.

How does orbit crossing give rise to these structures, especially the sharp edges? Orbit crossing proceeds from the inside out; each particle is passed by all particles of smaller initial radii before passing its immediate outer neighbor. A particle begins orbit crossing when it is overtaken by the outer boundary of the shell. At this time it crosses the orbits of particles with significantly smaller initial radii. The first crossing of orbits of its original neighbors occurs when it reaches the inner

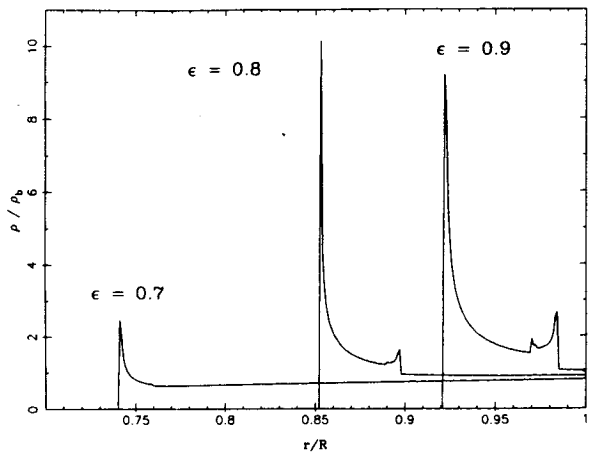

FIG. 4.—Ratio of actual to background density

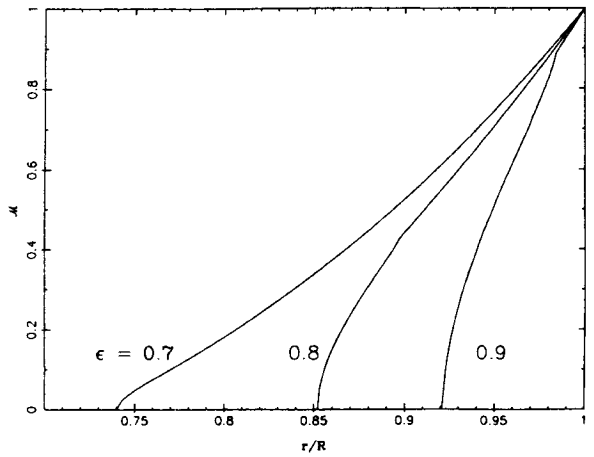

FIG. 5.—Profile of mass per unit solid angle

boundary of the shell. The inner and outer shell edges and other weaker density spikes within the shells are composed of particles which are in the act of crossing their neighbors' orbits.

ii) *Infall Velocity*

Peebles (1982) noted that particles in the shell surrounding a void do not have large streaming velocities. Thus, fragmentation of dense shells surrounding voids might produce planar structures having smaller peculiar velocities than those resulting from planar collapse of regions with supercritical density. This may be quantified by calculating the ratio of the infall velocity to the unperturbed Hubble velocity for both types of planar structures.

The peculiar velocity of a particle crossing the shell around a void for the first time is

$$v_i = \frac{dr}{dt} - f\frac{dR}{dt} = \frac{R(t)}{t}\left[\frac{\tau^{1/3-2/(9\epsilon)}}{\lambda(1)}\frac{d\lambda}{d\tau} - \frac{2f(1+3\epsilon)}{9\epsilon}\right], \quad (18)$$

where f is the ratio of the void's radius to $R(t)$. The Hubble velocity across the void's radius is

$$v_H = HfR = \frac{2f}{3}\frac{R(t)}{t}, \quad (19)$$

where H is the Hubble constant. The ratio of these velocities is

$$\frac{v_i}{v_H} = \frac{3\tau^{1/3-2/(9\epsilon)}}{2f\lambda(1)}\frac{d\lambda}{d\tau} - \left(1 + \frac{1}{3\epsilon}\right). \quad (20)$$

For $0.7 \leq \epsilon \leq 1.0$, we find

$$0.05 \leq \frac{v_i}{v_H} \leq 0.15 .$$

For planar collapse (see Paper I), the infall velocity can be computed approximately by assuming the column density remains constant while a sheet falls toward the symmetry plane. Actually, the column density decreases because a sheet passes through previously collapsed material; however, this effect decreases the infall velocity by less than 15%. The desired velocity ratio is

$$\frac{v_i}{HZ} = 2^{1-1/\epsilon}, \quad (21)$$

where Z is the turnaround distance. The ratio in equation (21) varies from 0 to 1 as ϵ varies from 0 to 1, but it is greater than 0.15 for ϵ above 0.26.

iii) *Particle Motion in the Shell*

The damped oscillations in λ/Λ pictured in Figure 2 are easily modeled analytically. We transform the dependent variable in equation (15) from λ to $\zeta \equiv \lambda/\Lambda$. The equilibrium position, ζ_0, is given by

$$\frac{8\lambda(1)^3}{\pi^2} b\zeta_0^3 = \mathcal{M}(\zeta_0), \quad (22)$$

where

$$b = \left(\frac{2}{3} + \frac{2}{9\epsilon}\right)\left(\frac{1}{3} - \frac{2}{9\epsilon}\right).$$

The mean density interior to the equilibrium point is

$$\frac{\langle\rho(\zeta_0, t)\rangle}{\rho_b(t)} = \frac{9b}{2} \leq \frac{4}{9}. \quad (23)$$

Linearizing the equation of motion in terms of the variable $y = \zeta - \zeta_0$, we arrive at

$$\frac{d^2y}{d\tau^2} = -\frac{2}{\tau}\left(\frac{2}{3} + \frac{2}{9\epsilon}\right)\frac{dy}{d\tau} - \left[\frac{\pi^3}{2\lambda(1)^3}\frac{\rho(\zeta_0)}{\rho_b} - 3b\right]\frac{y}{\tau^2}. \quad (24)$$

Equation (24) is homogeneous in τ and has the solution

$$y = y_0\,\tau^{-\alpha}\cos\left[\beta \ln(\tau)\right], \quad (25)$$

where

$$\alpha = \left(\frac{1}{6} + \frac{2}{9\epsilon}\right), \quad \beta = \left[\frac{\pi^3\rho(\zeta_0)}{2\lambda(1)^3\rho_b} - 3b - \alpha^2\right]^{1/2}. \quad (26)$$

The oscillation period is proportional to τ as a consequence of the τ^{-2} variation of the density. As ϵ increases from 0.7 to 1.0, α decreases from 0.48 to 0.39, and β increases from 0.55 to 0.91.

J. A. F. would like to thank James Binney for a helpful discussion. Support for this research was provided by the National Science Foundation through a graduate fellowship to J. A. F. and through grant 80-20005.

REFERENCES

Centrella, J., and Melott, A. L. 1983, *Nature*, **305**, 196.
Davis, M., Huchra, J., Latham, D. W., and Tonry, J. 1982, *Ap. J.*, **253**, 423.
Fillmore, J. A., and Goldreich, P. 1984, *Ap. J.*, **281**, 1 (Paper I).
Frenk, C. S., White, S. D. M., and Davis, M. 1983, *Ap. J.*, **271**, 417.
Hausman, M. A., Olson, D. W., and Roth, B. D. 1983, *Ap. J.*, **270**, 351.
Hoffman, G. L., Salpeter, E. E., and Wasserman, I. 1983, *Ap. J.*, **268**, 527.
Kirshner, R., Oemler, A., Jr., Schechter, P., and Shectman, S. 1981, *Ap. J. (Letters)*, **248**, L57.
Klypin, A. A., and Shandarin, S. F. 1983, *M.N.R.A.S.*, **204**, 891.
Maeda, K., Sasaki, M., and Sato, H. 1983, *Progr. Theor. Phys.*, **69**, 89.
Peebles, J. E. 1980, *The Large-Scale Structure of the Universe* (Princeton: Princeton University Press), §§ 6–8.
———. 1982, *Ap. J.*, **257**, 438.
Sato, H. 1982, *Progr. Theor. Phys.*, **68**, 236.
Sato, H., and Maeda, K. 1983, *Progr. Theor. Phys.*, **70**, 119.

J. A. FILLMORE: Robinson 105-24, Caltech, Pasadena, CA 91125

P. GOLDREICH: 170-25 So. Mudd, Caltech, Pasadena, CA 91125

Chapter Three

INTERNAL KINEMATICS OF SPIRAL GALAXIES: GAS AND STELLAR ROTATION CURVES AND DISPERSION PROFILES

James A. Fillmore, Todd A. Boroson, and Alan Dressler

Submitted to
The Astrophysical Journal, 14 February 1985

I. INTRODUCTION

While much effort in recent years has been devoted to understanding rotation curves, studies have concentrated primarily on their behavior at large radii. The velocities of material at small radii are important, however, for determining the distribution of mass within galaxies, as well as the dynamical effects of the different galaxian components upon each other. For example, the questions which one might hope to address with high resolution data on the inner regions of disk galaxies include: 1) are bulges flattened by rotation or anisotropic residual velocities? 2) how do the bulge and disk interact? and 3) how does the mass-to-light ratio (M/L) change with radius? This last question involves such aspects as how centrally concentrated a massive halo is, and whether black holes are commonly found in the centers of galaxies.

Recent progress in both observational capabilities and theoretical models suggest that the time is now right to study inner rotation curves in some detail. The same advances in detector technology which allow the measurement of optical rotation curves at very large radii, and hence, very low surface brightnesses, enable the measurement of the inner parts of galaxy rotation curves at unprecedentedly high spatial and spectral resolution. Also, the advances made in modelling elliptical galaxies provide a good framework for studying the velocity and surface brightness distributions of spheroids within disk systems.

In this paper we present observations and analysis of velocity data from six spiral galaxies. These data consist of radial velocities and velocity dispersions of both the gaseous and the stellar components. The measurements extend out to several kiloparsecs and the spatial resolution is limited by the seeing. The analysis utilizes all the velocity data as well as light distributions for the galaxies to model the mass distributions and the motions of the material in a nearly self-consistent way. Section II contains the details of the observations and the data reduction. Section III is an explanation of the modelling procedure. In §IV, this procedure is applied to each of the six galaxies observed. In §V, we discuss the trends and individual peculiarities and their implications for galaxy formation and evolution.

II. OBSERVATIONS AND REDUCTIONS

All the observations were made with the Double Spectrograph at the Cassegrain focus of the Hale 5-m telescope. A 320×512 RCA CCD was the detector

on the blue side of the spectrograph and an 800 × 800 TI CCD was the detector on the red side. All of the emission line measurements were made in the λ6500 - λ6800 region, which includes Hα, the [N II] λλ6548, 6583 lines, and the [S II] λλ6716, 6731 lines. The absorption line measurements were made either in the λ4400 - λ5400 region which contains Hβ and the Mg I b feature, or in the λ8400 - λ8700 region which contains the Ca II infrared triplet. The calcium triplet and Hα regions were often observed simultaneously by replacing the normal dichroic, which splits the light between the two optical paths at λ5200, with one which splits the light at λ6900.

Details of the observations are listed in Table 1. A two arcsecond wide slit was used for most of the exposures. One pixel corresponds to 0.78" on the blue side and 0.58" on the red side. The slit was about 120" long, and for most of the emission line (the Hα region) observations, the nucleus of the galaxy was placed near one end. For the Mg I b exposures, the nucleus was centered along the slit. Comparison lamp exposures were taken after every object integration, and late G or early K giants were observed for templates with the same setup on each night that we obtained absorption line data. All observations were made with gratings having 1200 grooves mm^{-1} used in first order. These gratings give a reciprocal dispersion of about 1Å per pixel, and the resolution was about 2.6Å for both the blue and red cameras with a 2" slit.

The frames were all bias subtracted and flat-field corrected. The two-dimensional spectra were then separated into groups of one-dimensional spectra, composed of individual rows in regions where the signal was strong, and averages of several rows in other regions. For each object spectrum, the same rows of the accompanying comparison frame were averaged and the resulting comparison line positions were used to determine a wavelength polynomial. This procedure removes the effects of distortion in the spectrograph and any slight tilt of the slit with respect to the CCD pixel columns. The wavelength functions were cubic polynomials fitted to between 8 and 15 arc lines. The residuals in the fits were typically 0.05Å or less. This corresponds to about 4 km s^{-1} uncertainty due to the wavelength calibration. Moreover, the residuals of a given comparison line were similar from fit to fit, suggesting that the relative velocities along the slit are measurable to even higher accuracy than this.

The emission line spectra were measured by fitting a Gaussian to each of the five emission lines in the wavelength region observed. The center of the Gaussian was converted to a velocity and a heliocentric correction was applied. The velocities were then averaged with approximate weighting by the strengths of the individual lines.

The resulting rotation curves are presented in Table 2. The position angles listed for each observation give the direction of the positive axis. Note that in some cases, the velocities are determined from the sum of a number of rows. These velocities are listed only for the central row in such a sum. In practice, the shorter exposures were of insufficient quality to yield precise information. Thus, we were unable to use any of the minor axis emission line frames or the major axis emission line frame for NGC 2841. By summing the pixel counts between the major emission lines, a rough continuum intensity (hereafter CI) measurement can be made; these are also listed in Table 2. Because the galaxies in this sample have large angular extent, the slit did not reach sufficiently far for a reliable measurement of the sky brightness. Thus, accurate sky subtraction was not possible, so the CI values may have systematic errors.

In addition to the velocities, the reduction procedure yielded line widths for the emission lines in each spectrum. These values are not presented here but we describe the general trends seen. In all objects, the lines were unresolved ($\sigma < 40$ km s^{-1}) at radii greater than about 5". Within this radius, they broadened, reaching widths (Gaussian standard deviations) of 100 - 150 km s^{-1} at the centers. Some fraction of these widths come from the rotation of the material and are dependent upon slit width and seeing.

The absorption line frames were reduced using the Fourier quotient method developed by Schechter (Sargent *et al.* 1977). The sky was determined either from the edges of each object frame or from separate sky frames and was subtracted from the object frames. Tilts in the slit relative to the detector were removed for galaxy and template star frames. The rows of each frame were co-added such that the signal-to-noise ratio in a one-dimensional spectrum was at least 30. Then each one-dimensional spectrum was wavelength calibrated and run through the Fourier quotient program, which outputs a velocity, a velocity dispersion, and an average line-strength factor.

The center of each galaxy was determined by finding the point around which the rotation curve is most symmetric, and the radial velocity at this point was considered the systemic velocity. This value was then subtracted from each other point, so all the rotation curves are centered on zero. Table 3 gives the absorption line data, the rotation curves and dispersion profiles used for each object in the sample.

III. MODELS

Our galaxy models contain two components, a bulge and a disk, each described below. Here we describe the coordinate systems used in the models. The models are axisymmetric, so we use a cylindrical-polar system (R, z, ϕ) of spatial coordinates in the galaxy. In the bulge, where an oblate spheroid is assumed, ξ is a spheroidal coordinate which is constant along equidensity surfaces:

$$\xi^2 = R^2 + f^2 z^2, \tag{1}$$

where f is the flattening parameter, related to the ellipticity ϵ by $f = (1-\epsilon)^{-1}$. In the plane of the sky, a Cartesian system (p, q) aligned with the projected principle axes is used. The variable s is distance along the line-of-sight, where $s = 0$ is the plane passing through the galaxy center. The inclination of the galaxy is i; for edge-on $i = 0$. The two sets of coordinates are related by:

$$R^2 = p^2 + [s\cos i - q\sin i]^2, \tag{2}$$

$$z = s\sin i + q\cos i, \tag{3}$$

$$\xi^2 = \xi_0 + s\xi_1 + s^2\xi_2, \tag{4}$$

where,

$$\begin{aligned} \xi_0 &= p^2 + q^2\left[\sin^2 i + f^2\cos^2 i\right], \\ \xi_1 &= 2q\sin i\cos i\left[f^2 - 1\right], \\ \xi_2 &= f^2\sin^2 i + \cos^2 i. \end{aligned} \tag{5}$$

For an observation point (p, q), minimum ξ occurs at

$$\xi_m^2 = \xi_0 - \frac{\xi_1^2}{4\xi_2} = p^2 + \frac{q^2}{s^2 + c^2 f^{-2}}. \tag{6}$$

a) Disk

We use the disk model from van der Kruit and Searle (1981*a*, 1982), which is an exponential disk with constant scale height. The density is specified by

$$\rho_D(R,z) = \rho_0 e^{-R/R_D} \mathrm{sech}^2(z/z_0), \tag{7}$$

where ρ_0 is the central density, R_D is the disk scale length, and z_0 is twice the scale height. These authors have shown this model to be a reasonable representation of the disk surface brightness out to a few scale lengths, after which it rapidly drops off (see also Seiden, Schulman, and Elmegreen 1984). We do not impose an outer edge in our models because the range of our observations is interior to the typically observed cut-off radius. This exclusion might cause a slight systemic over-estimate in our disk masses. The surface density is calculated by integrating equation (7) over z:

$$\mu_D(R) = \mu_0 e^{-R/R_D}, \tag{8}$$

where the central surface density $\mu_0 = 2\rho_0 z_0$. The total mass M_D is $2\pi\mu_0 R_D^2$. Note that the disk surface density can be determined by R_D and M_D without specifying the scale height. The light and the acceleration from the disk is calculated assuming the disk is very thin and has a constant mass-to-light ratio M_D/L_D. The scale height is used only to compute the velocity dispersion, which we assume to be isotropic (see Bahcall 1984),

$$\sigma_D^2(R) = \pi G \mu_D(R) z_0. \tag{9}$$

Since the disk is thin, and the galaxies in this sample are not edge-on, line-of-sight projection effects will be ignored for the disk component.

b) Bulge

The bulge component is modelled as an oblate spheroid whose flattening is specified by its true ellipticity $\varepsilon = 1 - b/a$, where b/a is the axial ratio. The bulge ellipticity is assumed to be constant even though observations of other galaxies show an outward increase in the flattening (van der Kruit and Searle 1981*a*, 1981*b*, 1982). This effect is probably caused by the presence of the disk, but to include it is beyond the scope of this paper.

Observations of many disk systems (Kormendy 1977, Burstein 1979, Boroson 1981) have shown that the bulge surface brightness is acceptably represented by a

deVaucouleurs' law (1948), which in magnitudes is

$$\mu^m(p) = \mu_e^m + 8.325[(p/R_e)^{1/4} - 1], \tag{10}$$

where R_e is the effective radius and μ_e^m is the surface brightness at R_e, measured along the major axis. The bulge density profiles are fits to a deprojected $r^{1/4}$ law taken from approximate formulae derived by Young (1976) and Tonry (1984*b*). The density on a spheroidal surface is

$$\rho_B(\xi) = f M_B R_e^{-3} \rho^*(\xi/R_e), \tag{11}$$

where $f\rho^*$ is a dimensionless function whose total volume integral is unity; M_B is the total bulge mass.

Along with the mass model we must know the 3-D velocity structure of the bulge. This information can not be entirely obtained from observations, so we must make some assumptions. We use the mean rotation velocity in the equatorial plane as an independent function to be determined by fitting the observations, but assume the mean rotation out of the plane follows the scaling

$$u(R,z) \simeq \frac{u_0(R)}{[1+(z/R)^2]^{1/2}}, \tag{12}$$

where u_0 is the mean rotation in the equatorial plane. This scaling was derived by using $\rho^* \propto \xi^{-2}$ and computing the circular velocity for an oblate spheroid at low z and to first order in ε; this result is sufficently accurate for $\varepsilon \leq 0.4$. We then assume that the mean rotation rate scales in the same way as the circular velocity. Note that adopting this relation is equivalent to assuming that the angular velocity is constant on spheroidal shells, in which case u_0 is a function of ξ, not R. If the equatorial rotation curve is flat these two forms give the same result.

The relation (12) has been tested on measurements of edge-on disk galaxies; projection effects have been ignored. Kormendy and Illingworth (1982, hereafter KI), measured v and σ along slits both parallel and perpendicular to the major axis. Two of their four galaxies fit the above relation quite well, as shown in Figure 1; these are bulge-dominated systems with dynamically significant rotation. The other two galaxies do not fit the relation; for these there is a large difference in the bulge and disk rotation rates so a fit can not be found.

We must also assume the form of the velocity dispersion structure. We shall use the radial velocity dispersion in the equatorial plane as an independent function $\sigma_R(R)$. We allow for anisotropy in our models, but as will be shown, it is not necessary to invoke it. Since the projected velocity dispersion in KI's galaxies did not change significantly with z, we shall assume that σ_R and σ_ϕ are not a function of z. This assumption is imposed only to simplify the model. If σ_R decreases outward, this predicts that the line-of-sight velocity dispersion, σ_s, observed along the minor axis falls off more slowly than along the major axis, since over-the-pole line-of-sight pulls the mean value up. This is in agreement with our minor axis data.

A pressure-supported, isotropic spheroid whose density distribution follows a deprojected deVaucouleurs' law has central depression in the velocity dispersion (Binney 1980). The projected velocity dispersion peaks near $\sim 0.1R_e$. Two plausible modifications can remove this depression. First, the addition of a central point mass, which causes the surrounding stars to move faster. Only 15% additional mass inside $\sim 0.1R_e$ is sufficient to keep σ_s rising inward. Alternatively, a core radius may be introduced into the density profile, which decreases the number of slow moving stars near the center, so the (mass-weighted) velocity dispersion increases. This deviation from deVaucouleurs' law should be visible in high-resolution surface brightness measurements unless the mass-to-light ratio decreases in the center. Previous surface brightness studies of ellipticals reveal that some show a central core radius while others follow a $r^{1/4}$ law to the seeing limit (Schweizer 1979). However, most bulges are smaller than those ellipticals, so seeing effects severely limit the detectability of cores.

c) Projection and Measurement Effects

External galaxies are, of course, seen only in the plane of the sky, so we must calculate how these models would appear in projection in order to compare them with observations. Here we discuss the projection of the bulge component, subsequently we will detail the procedure for including the disk. The bulge model is specified by ε, R_e, M_B, M_B/L_B, and the 3-D kinematic assumptions. First we will calculate line-of-sight quantities; a subscript s will be used on some variables to denote integration along s.

The surface brightness is

$$\mu_L(p,q) = \int_{-\infty}^{\infty} \rho_L(\xi)\, ds, \tag{13}$$

where ρ_L is the luminosity density $\rho(\xi)L_B/M_B$. For the special case of an oblate spheroid,

$$\mu_L(p,q) = \frac{2\xi_m}{\xi_2^{1/2}} \int_1^{\infty} \frac{\rho_L(\xi_m x)x\, dx}{[x^2-1]^{1/2}}. \tag{14}$$

Because μ_L is a function only of $\xi_m(p,q)$ the isophotes are elliptical (see equation [6]). The projected mean rotation is

$$v_s(p,q) = \mu_L^{-1} \int_{-\infty}^{\infty} \rho_L\, u(R,z)\frac{p\cos i}{R}\, ds. \tag{15}$$

The observed velocity dispersion has several components; first the true velocity dispersion must be projected:

$$\sigma_s^2(p,q) = \mu_L^{-1} \int_{-\infty}^{\infty} \rho_L \sigma_R^2 \left[1 - \beta\frac{p^2\cos^2 i}{R^2} - \beta_z \sin^2 i\right] ds, \tag{16}$$

where β and β_z are anisotropy parameters, $\beta = 1 - \sigma_\phi^2/\sigma_R^2$, and $\beta_z = 1 - \sigma_z^2/\sigma_R^2$. Second, the contribution from the projection of the rotation curve is

$$\sigma_{vr}^2(p,q) = < u^2 >_{los} - v_s^2(p,q), \tag{17}$$

where the mean squared line-of-sight velocity is

$$< u^2 >_{los} = \mu_L^{-1} \int_{-\infty}^{\infty} \rho_L\, u^2 \frac{p^2\cos^2 i}{R^2}\, ds. \tag{18}$$

These integrals can be performed analytically if idealizations such as a power law luminosity density and flat rotation curves are assumed. In typical cases one finds $v_s/u \sim 60 - 80\%$ and $\sigma_{vr}/u \sim 20 - 30\%$. (See also Tonry 1984*a* and Young *et al.* 1978.)

The observed quantities are modified by atmospheric seeing and instrumental resolution. We denote the broadening function as S; its integral is unity. Convolution will be denoted by an asterisk. The model "observed" surface brightness is

$$\mu_{obs} = S * \mu_L. \tag{19}$$

Rotation curve and velocity dispersion profiles are modified by a luminosity-weighted convolution, defined as

$$P * f \equiv \frac{S * (\mu_L f)}{S * \mu_L}. \tag{20}$$

Thus,

$$v_{obs}(p,q) = P * v_s. \tag{21}$$

The observed line-width is increased because the mean velocity (line-center) is simultaneously observed at many different projected spots on the galaxy by a finite-sized aperture (plus atmospheric agitation). The additional contribution to the observed velocity dispersion from an aperture is

$$\sigma^2_{ap} = P * v_s^2 \; - \; v^2_{obs}, \tag{22}$$

which is significant only near the center, if at all. The predicted total velocity dispersion is

$$\sigma^2_{obs} = P * \left[\sigma_s^2 + < u^2 >_{los}\right] \; - \; v^2_{obs}. \tag{23}$$

Since we have a two component model, the true first and second moments of the line-of-sight velocity should be the sum of the two components weighted by their relative surface brightness. However, the measured moments do not directly represent the true moments because the observations were reduced using a Fourier quotient method (abbreviated FQ hereafter, see §II). This technique fits a Gaussian to the line-broadening profile, but the superposition of two components can be a distinctly non-Gaussian profile; this fitting error biases the measured values (Illingworth and Schechter 1982; Whitmore 1980; McElroy 1983; Whitmore, Rubin, and Ford 1984, hereafter WRF). In our situation the biases are competing; the method emphasizes the narrower component (disk) but is more sensitive to the stronger line component (bulge).

First we must consider the bias effect on the measured mean velocity. If the fraction of bulge light contributed at a particular projected location is $b = \mu_b/\mu_{tot}$, and the velocity difference between the two components is Δv, then the expected measured velocity $v_{exp} = \Delta v\,(1-b)$. However, the measured value v_m is frequently different from v_{exp}, so we define an effective fraction from $v_m = \Delta v\,(1-b_{eff})$, so

$$1 - b_{eff} \equiv \frac{v_m}{v_{exp}}\,(1-b). \tag{24}$$

Thus, b_{eff} indicates what fraction of light the bulge would have to contribute to achieve the same measured value if the FQ method properly returned the mean velocity. Figure 2 shows the difference between mixing two components of equal line-strength and mixing one component with half the line-strength of the other. The result is that the absorption line data mostly reflects the bulge rotation even in regions where the disk light contributes a significant fraction of the light (WRF).

The velocity dispersion expected from the combination of two components is not a simple linear interpolation between the two values. Fitting a Gaussian to two components with a non-zero seperation in the mean values can result in a much larger width than either component. The expected value is

$$\sigma^2_{exp} = b\sigma^2_B + (1-b)\sigma^2_D + b(1-b)(\Delta v)^2, \tag{25}$$

where Δv is the mean separation between the components. The measured values from the FQ method will not follow this relation because it is biased towards the narrower component; in worst cases σ_{meas} will be 30% below σ_{exp}.

Different authors have used different schemes to compute the goodness of fit of a Gaussian to the Fourier quotient (e.g., Sargent *et al.* 1977, and Dressler 1979). The goal is to choose the best fit despite noise in the data, particularly at high wave-numbers. Our tests show that biases introduced by typical goodness-of-fit tests are smaller than those inherent in the method when two components are present.

d) Fitting Procedure

In this section we detail the procedure used to fit a kinematic model to velocity data while satisfying physicial constraints.

Two of the constraints used are Poisson's equation

$$\nabla^2\Phi = 4\pi G(\rho_B + \rho_D), \tag{26}$$

and a velocity moment of the collisionless Boltzmann equation

$$u^2 - \sigma_R^2\left[\frac{\partial \ln \rho\sigma_R^2}{\partial \ln R} + \beta\right] = R\frac{\partial\Phi}{\partial R}, \tag{27}$$

which is solved for the bulge and disk separately. These two relations are necessary but not sufficient restrictions on the kinematic model. Note that we still have no criteria as to the value or variation of the anisotropy parameters β and β_z. Higher moment equations could supply additional constraints, but these introduce more unknown functions, so we are unable to close the moment equations. Recall that when only two integrals of motion are present Jean's Theorem requires that $\beta_z = 0$. However, numerical studies show that a third integral is frequently present. Nonetheless, we fit $\beta = \beta_z = 0$ models to our sample of galaxies.

By specifying the form of the off-equatorial plane kinematics (in §III*b*), we have reduced the unknown dynamical structure of the bulge to two functions; $u(R)$, the mean stellar equatorial rotation rate, and $\sigma_R(R)$, the radial dispersion profile. These reductions allow predicted projected profiles to be compared with observed ones. Note that an ambiguity exists because we have constructed a two-component model to be constrained by measurements which combine information from the real both bulge and disk components.

The fitting procedure is as follows. The luminosity density is fitted to the observed photometry; this determines the scale lengths R_e and R_D, and the relative surface brightness contributions of the bulge and disk. The bulge R_e measured along the major axis is independent of i and ε. Since i is determined by the apparent axial ratio of the disk, ε can in principle be determined by the apparent axial ratio of the bulge. The two scale lengths must be determined by an iterative process; the solution for R_e is particularly sensitive to the disk solution since small changes in the disk fit at the exterior can extrapolate inward to large changes in the residuals attributed to the bulge. Accurate sky subtraction is necessary for a proper disk solution. Errors up to 25% in R_e exist for those galaxies for which we have only continuum intensity (CI) data. The initial guess for the disk mass is set by fitting

the emission line rotation curve at the outermost measured points; then a rough fit to the bulge mass is approximated by fitting the interior absorption line data. The potential is computed from ρ_B and ρ_D.

There are two approaches to solving equation (27): (i) An intrinsic mean stellar rotation curve is estimated, initially by scaling up a fit to the observed rotation rate, and σ_R is computed from it by an iterative procedure; (ii) a fit is made to the intrinsic velocity dispersion, and the rotation curve computed from it. Either approach will arrive at the same result; the choice is simply a matter of which intrinsic profile is easier to model. Once u and σ_R are derived, they are projected, seeing corrected, and compared to the observed profiles. The seeing profile is chosen to be a single Gaussian, since no better information is available, and these corrections are not critical (except for the photometry). A few iterations are required to fine-tune the fits. Note that one of the two profiles, v_{obs} or σ_{obs}, can be made to fit the observations arbitrarily well, perhaps at a sacrifice to the other; the goodness-of-fit must be made by comparing both profiles.

If a satisfactory fit is still not achieved, there are other options to exercise depending on how the fit needs to be improved; these will be discussed below. We note here that asymmetry observed in the velocity data hints that axisymmetry is an idealization which might improperly restrict the results.

IV. RESULTS

Graphs of the observations and kinematic fits are presented in Figures 3-8. The parameters used in the models are contained in Table 4. Our notation is as follows. The stellar motions are described by their equatorial mean rotation u, and velocity dispersion σ_R. The model circular velocity is U_c, the bulge line-of-sight mean rotation is v_s, and the velocity dispersion is σ_s. The predicted observed values, including disk light and seeing effects are v_{obs} and σ_{obs}. We refer to the model projected peak rotation velocity as v_{peak}, σ_0 is the central velocity dispersion, and $\bar{v}$ and $\bar{\sigma}$ are the mass-weighted rms values from our models. To compute the means we have assumed that each spheroidal shell rotates at constant angular velocity, and that σ_R is constant along z.

a) NGC 2841

Using the bulge and disk decomposition from Boroson (1981), fits for this galaxy were straightforward since i, ε, R_E and R_D were already available. The

emission line data were not usable in the observed region; there appears to be an HI hole inside 6 kpc (Bosma 1978). The disk mass was initially set by from a gas rotation measurement of 260 km s^{-1} at 3.9 kpc by Rubin and Thonnard (1984).

The absorption line data mostly reflect the bulge; however, a contribution from the disk is expected at the outer observed points. The major axis data are shown in Figure 3*a*, the minor in Figure 3*b*; v_{peak}/σ_0 is 0.64. The inner peak in the stellar rotation curve is also seen by WRF; although their two sides of the major axis are not symmetric in the location of the peak, this region is affected by beam-bending. Our measured values of the velocity dispersion do not decrease with radius as fast as the WRF values.

The dip in v_{obs} around 0.7 kpc is consistent with equation (27) and the large velocity dispersion. Two different effects could cause the upturn in the rotation curve. If we assume that the observed profiles completely reflect the bulge component, then only a slight decrease in σ_R is necessary to raise the rotation curve; in this case $\bar{v}/\bar{\sigma}$ is 0.70. On the other hand, if the observed rise is due to disk light, then the bulge rotation curve must remain flat to 1 kpc, in which case $\bar{v}/\bar{\sigma}$ is 0.40. This latter interpretation was used for the final model construction, because a contribution from the disk is expected, even including the bias of the Fourier quotient method. The model profiles are displayed in Figure 3*c*.

b) NGC 3898

The photometry from Boroson (1981) is again used. The observed emission line rotation data are shown as points in Figure 4*a*; the solid line is the model circular velocity. The major axis absorption line data are presented in Figure 4*b*. Since the distance where the surface brightness of the bulge equals the disk, which we call the crossover point, is measured to be 3.5 kpc, while the absorption line data extend only to 0.6 kpc, we will assume the absorption line data purely represent the bulge component.

The asymmetry in both the stellar velocity disperion and rotation rate, which is also seen to a similar degree by WRF. The southeast side of the major axis has a rotation rate 30 km s^{-1} lower than the NW wide inside of 8". The NW side shows a large decrease in velocity dispersion, whereas the SE side displays only a slight decrease in our data and a slow rise in the data of WRF.

The model was fit to the observations by specifying an intrinsic dispersion

profile which produced an acceptable σ_{obs}, and the bulge mass was adjusted until v_{obs} was in the proper range. Note that σ_{obs} and v_{obs} fit well on one side of the galaxy, but fit poorly on the other side. The steep decline in σ_{obs} on the poorly fitting side cannot be reproduced without adding a large central mass concentration. However, this addition is tightly constrained by the restriction that the mass of the bulge must not be lowered to compensate for the central mass to the point where $M_B/L_B < M_D/L_D$.

The model profiles are illustrated in Figure 4*c*. The observed v_{peak}/σ_0 is 0.50; however, $\bar{v}/\bar{\sigma}$ is higher (0.60) since σ_R decreases outward. The model's premature drop to zero rotation velocity inside 0.1 kpc can be corrected by adding $1.6 \times 10^8 M_\odot$ to the central region, a 14% increase to the mass within 0.1 kpc.

c) NGC 4450

Photometry from Whitmore and Kirshner (1982) was applied in conjunction with our CI data. We compared the apparent scale lengths of the major and minor axis to determine a bulge flattening of $\varepsilon = 0.2 \pm 0.2$. The inclination was measured by visual esimates from the Hubble Atlas (Sandage 1961). The bulge scale length is uncertain ($R_e \simeq 1.7 \rightarrow 2.4$) due to irregularities in the disk surface brightness, but the best fit to the early turnover in the absorption line rotation data occurs for a small value of R_e.

The emission line data are quite irregular, as shown in Figure 5*a*, and the model rotation curve is much higher than the observed one. The high circular velocity of the model is required to fit the absorption line data, discussed below. This galaxy is unusual in its strong inner peak and the decline of the gas rotation curve inside 5 kpc to below 50 km s^{-1}.

In NGC 4450 the absorption line data extend to 1 kpc (see Figure 5*b*). The rotation measurements from the two sides agree quite well until 0.5 kpc, then sharply diverge. The two outermost measurements on one side are 50 km s^{-1} higher than the other side, but still well below the circular velocity, which is over 200 km s^{-1}. By removing the FQ measurement bias, v_{obs} would be high enough to fit the outer observed points, but would now be too far above the inner points. This remarkable asymmetry, if real, can not be attributed to a FQ bias or a model with a smoothly varying stellar rotation rate. Thus, line-of-sight variations, perhaps due to obscuration by dust, are a likely cause; the surface brightness crossover point is

at 1.5 kpc, so the disk contribution is becoming significant. Except for this caveat, a simple model provides a satisfactory fit to the observations. The observed velocity dispersion has a near constant value of 140 km s^{-1} within 1 kpc. The bulge mass was adjusted until the projected bulge rotation profile fit the lower rotation curve (dashed line). The disk contribution and seeing effects are included to calculate v_{obs} (solid line).

The bulge model profiles are illustrated in Figure 5*c*. Even though $v_{peak}/\sigma_0 \sim 0.45$, $\bar{v}/\bar{\sigma}$ is only 0.30 because u significantly decreases outside 0.4 kpc.

d) NGC 4569

The inclination and bulge ellipticity of NGC 4569 were measured from a CCD picture supplied by G. Bothun. Scale lengths were obtained from fitting major axis CI data. Figure 6*a* shows the circular velocity fit to the emission line data. The gas rotation data lie below the model rotation curve out to 2 kpc.

The absorption line data and fits are presented in Figure 6*b* and 6*c*. The model bulge rotation curve was fit to the observations, and σ_R derived from it. Projected velocities for the bulge component are shown by dashed lines. The solid lines are computed by combining the line-of-sight bulge and disk velocities weighted by luminosity and corrected for the line strength bias of the FQ method.

Unlike the observed profile, the predicted v_{obs} does not contain a strong inner peak; because the model bulge rotation curve fits the observed profile, any inclusion of disk light raises the predicted rotation profile above the observed one. To reduce the model bulge rotation rate below the observed profile seems even less likely. Evidence for strong absorption is given by asymmetry in the rotation curve and the CI, which differs by 25% from 0.2 to 0.5 kpc. Visual inspection of the galaxy shows abundant dust lanes throughout the inner disk. The observed velocity dispersion profiles are slightly asymmetric, but the predicted profile is roughly consistent with the measured values. The central rise in velocity dispersion is due to the high concentration of the bulge; the contribution from rotational broadening is small.

Model profiles for the bulge kinematics are displayed in Figure 6*d*.

e) NGC 5055

The scale length fits are from the continuum intensity. The surface brightness crossover point is at 0.29 kpc, however the absorption line data extend to 0.8 kpc, so we can expect disk light to have a significant effect. First note in Figure 7*a*

that the circular velocity fits the emission line data on one side of the galaxy quite well. The other side indicates that the gas partakes in non-circular motions since it extends above the model circular rotation curve. Another possibility is that the model should be much higher and something is anomalous with the low velocity side.

The major axis absorption line data are shown in Figures 7*b* and 7*c*. The dashed lines show the projected rotation curve and velocity dispersion for just the bulge component; the solid lines include both bulge and disk contribution. The fact that the bulge rotation curve fits one side of the observations so well, and the bulge-disk combination fits the other, suggests significant absorption on the former side (the CI shows an asymmetry of 25% to 50% from 0.5 to 1 kpc). The irregularity in the emission line data supports this hypothesis. Fish (1961) has commented that the "observed isophotes are far from elliptical." If absorption is prevalent, the flat side of the observed rotation curve could be an underestimate of the bulge rotation rate. The ratio v_{peak}/σ_0 (0.53) underestimates $\bar{v}/\bar{\sigma}$ (0.67) because σ_R decreases from 110 km s^{-1} to under 70 km s^{-1} by 1 kpc ($0.66M_B$). Using a single component model, Burbidge, Burbidge, and Prendergast (1960) arrived at a mass 20% below our determination of 51×10^9 $M_\odot$.

The rise in the velocity dispersion on one side of the galaxy is difficult to model. Since the bulge is very concentrated, it is difficult to create a model with an outward rising velocity dispersion. The average line-strengths are lower on the low rotation side, yet they are expected to be higher if we see more of the bulge on this side. This feature is unexplained at this point.

f) NGC 5879

The continuum intensity for NGC 5879 is too irregular to decompose it into the two components, so the kinematic modelling performed on the other galaxies could not be done for it. Visual inspection indicates a very small bulge; this galaxy is classified as an Sb or Sbc type. The emission line data are presented in Table 2 and Figure 8*a*; the absorption line data, in Table 3 and Figure 8*b*. The stellar mean rotation velocity is everywhere the same as the gas. Because the stellar velocity dispersion is small, the observations probably represent solely disk stars. We estimate the disk mass to be $20 \pm 10 \times 10^9 M_\odot$.

V. DISCUSSION

a) Asymmetries

Several general results of the fitting of the models to the data are interesting. First, we note that the discrepancies between the models and data are often dominated by differences between the two sides of the galaxies. NGC 5055 is a good example of this. Figure *7a* clearly indicates the ambiguity in deriving the circular velocity from the emission line rotation curve. Which side (if either) represents the true circular velocity? A similar problem is encountered in the absorption line data. The same side of the galaxy with higher emission line velocities has an absorption line rotation curve which continues to rise to about 120 km s^{-1} outside of 0.1 kpc, while the rotation curve on other side levels off at 50 km s^{-1} at this radius. Furthermore, the higher rotational velocity seems to be allied with a lower stellar dispersion.

Several effects might produce such an apparent difference in the kinematic behavior between the two sides of a galaxy. A real difference in the gravitational potential between the two sides seems unlikely because that would require a mass distribution which is not even bilaterally symmetric. Moreover, one might argue that a local disturbance in the potential is not likely to manifest itself as a simultaneous change in opposite directions of the rotation and dispersion. A more plausible explanation involves variable extinction, which could result in our observing different blends of the kinematic components on the two sides. For example, if dust were distributed throughout a disk whose thickness is small compared to the bulge height, it would principally occult the disk light. If such dust were then asymmetrically distributed in azimuth or existed only on one side of the nucleus, it could account for the apparent asymmetric kinematics we see. Absorbing material is thought to play a role in the observed stellar kinematics near the center of M31 (McElroy 1983; Teuben, Turner, and Schwarzschild 1984). If dust accounts for the observed asymmetry, there is an inherent limitation to our approach, until we can measure stellar velocities far enough in the infrared to eliminate extinction uncertainties.

b) What supports the gas?

A second interesting feature of virtually all the galaxies is the extent to which the inner part of the emission line rotation curve falls below the predicted

circular velocity. This trend has also been noted by Schechter, Whitmore, and Rubin (private communication). Some of this discrepancy is undoubtedly due to seeing effects; where the velocity gradient is largest, the seeing and the finite slit width will convert some of the change in velocity into an apparent increase in the width of the lines. This effect is confirmed by the emission line widths, which increase dramatically to widths of 100 - 150 km s^{-1} at the centers of the galaxies. Outside of 2 – 3 arcseconds, however, the difference between observed gas velocity and predicted circular velocity persists although seeing effects are negligible. This is particularly apparent in NGC 3898 and NGC 4569.

The most straightforward interpretation of this discrepancy is that we are seeing a change in the M/L at small radii. The variations require that M/L drop by a factor of 2-10 inside of 1 kpc. This is in the opposite sense to what would be expected from stellar population changes; an older or more metal-rich population, as might be found closer to the center, would have a higher M/L. One is then left with the possibility that this drop represents a change in the contribution of unseen material. A dark halo, with a larger core radius than the spheroidal stellar population, might indeed produce a drop near the center, but this would imply that outside of 1 kpc, most of the mass is in this dark halo. Such as model is quite unlike the two models presented by Bahcall and Schmidt (1982), for instance, in which the halo does not dominate until a radius of 12 or 13 kpc is reached.

Alternatively, WRF point out that if the velocity ellipsoid in the bulges is radially elongated, rather than isotropic, then the bulge masses are overestimated. If this were the case, observed velocity dispersion profiles would be much more centrally peaked. Only the very interior of NGC 3898 displays a sufficient gradient to warrant consideration of largely radial orbits (and it does have the largest discrepancy in the rotation rates). The inner dispersion profile of NGC 4569 would be steeper than is observed if it contained more radial orbits, but seeing effects have reduced the observed gradient so this possibility cannot be ruled out.

We believe that mass overestimates are not the source of the discrepancy, and we consider below several reasons why the gas rotation curve might not represent the true circular velocity. Note that in NGC 4569 the gas mean velocities are below the stellar inside 0.5 kpc.

One possible explanation is that these galaxies have bars oriented in the

plane of the sky. As the gas streams along such a bar, its apparent rotational velocity will be less than the circular velocity predicted for an axisymmetric mass distribution. An argument against this is the apparent lack of objects with bars oriented along the line of sight. With the possible exception of NGC 4450, none of the galaxies shows a similar peak rotation velocity at small radii.

A second possibility is that the gas is supported by dispersion rather than by rotation near the center. Again, the line widths support this, although uncertain seeing corrections make a quantitative calculation of the true emission line widths impossible. If dispersions of 100 - 150 km s^{-1} do exist in the gas out to one kpc, such widths must represent bulk motion rather than thermal velocities.

The similarity between the stellar and gas dispersions suggests a scenario in which the two are related. The idea that the ionized gas in the nuclei of early type galaxies could result from stellar mass loss, particularly in the form of planetary nebulae, and could be heated by the hot star contribution to the ambient radiation field was first explored by Minkowski and Osterbrock (1959). A modernization of their arguments suggests that such an explanation might indeed be correct. For the amount of gas being returned to the interstellar medium (ISM) by stars we adopt Tinsley's (1980) estimate of $0.02M_{\odot}$ per solar blue luminosity per 10^9 years at the present epoch. The relevant time to consider is 10^7 years since that is the time required for a star to travel one kpc at 100 km s^{-1}. That is, we assume that the gas around a star is absorbed by the disk each time that star passes through the disk plane. Thus, there are $2 \times 10^{-4} M_{\odot}$ of gas for each solar blue luminosity of stars. This quantity of gas, if ionized, will produce Hα emission amounting to $(4.75 \times 10^{-12})/N_e$ ergs s^{-1} cm^{-2}, where N_e is the electron density in cm^{-3}.

For the electron density we adopt 0.1 cm^{-3}. This is somewhat higher than what might be expected if this amount of gas were uniformly spread throughout the bulge, but is probably more realistic as we assumed that the large velocity dispersion indicates that the material is still clumpy. Also, this is somewhat lower than the density that a planetary nebula will reach in a few times 10^4 years, the lifetime of its central star in its hot, luminous phase. The Hα luminosity produced is then 4.75×10^{-11} ergs s^{-1} cm^{-2}. Each solar blue luminosity, emitted by K0 III stars, is accompanied by 6.3×10^{-11} ergs s^{-1} cm^{-2} $Å^{-1}$ at λ6500, so the equivalent width produced in Hα is a little less than one angstrom. The observed equivalent

widths range from one to three angstroms, so we conclude that there is sufficient gas to produce the observed emission.

The second part of the calculation involves the ionizing flux. For this, we use the IUE measurements of Oke *et al.* (1981) and Bertola *et al.* (1982) of several bright elliptical galaxies. All of these galaxies show spectral upturns below λ2000, which are presumed to be due to either young OB stars or blue horizontal branch stars. Typically, the flux seen in the IUE aperture, which corresponds to a region quite similar to the one which we are considering, is equivalent to about 3000 OB stars having a temperature of 30,000 K. For an emission volume V, this ionizing flux corresponds to $N_e^2 V = 3.52 \times 10^7$ pc^3 cm^{-6}, which for our assumed density of 0.1 cm^{-3} is more than sufficient to produce the observed Hα emission.

Although we have shown that what is known about mass loss and the UV contribution to the ambient radiation field is consistent with our explanation for both the origin of the gas and its kinematics, there are two side issues which complicate the argument. First, the time scale for the gas to fall into the disk is 10^7 years. Thus, one might expect there to be $\sim 10^3$ times as much mass in the gas disk as there is currently falling into it. We assume that this gas cools quickly to a high enough density that the surrounding UV flux can no longer excite it. The gas may be involved in star formation after it has cooled. This process moves material to the center of the galaxy and transports angular momentum outwards.

The other issue to consider is why such emission is not seen in elliptical galaxies. After all, they have all the prerequisite properties we have assumed to produce the Hα emission: gas from stellar mass loss and ionizing radiation from the few hot stars. A search of the literature reveals the fact that very few ellipticals have been observed to the accuracy required to detect such emission. A recent survey is described by Caldwell (1984) who has searched for [O II] λ3727 emission in the nuclei of elliptical galaxies. This line is expected to be about a factor of two weaker than Hα in H II regions (Hawley 1978), and the stellar continuum is somewhat weaker than at λ6500, so the equivalent width of [O II] λ3727 should be about the same as Hα. Caldwell finds that at the few angstrom level, almost half of the ellipticals he has observed show emission. Thus, it might be expected that observations such as ours of the centers of most ellipticals would discover emission line gas.

c) v/σ and Bulge Flattening

There has been some discussion (see WRF and references therein) of which observed v/σ values best reflect the virial $\bar{v}/\bar{\sigma}$. We have calculated both the model $\bar{v}/\bar{\sigma}$ and the projected v_{peak}/σ_0. Although v_{peak}/σ_0 indicates the rough value of $\bar{v}/\bar{\sigma}$, we find that it varies less than $\bar{v}/\bar{\sigma}$ does. The peak values do not sufficiently account for the large variations in either u or σ_R. Thus, if the rotation curve has an inner peak, or the velocity dispersion shows a large gradient, modelling the observations to compute $\bar{v}$ and $\bar{\sigma}$ is necessary.

We compare the $\bar{v}/\bar{\sigma}$ value for each galaxy against the virial value assuming isotropic random velocities (Binney 1978, 1980), as presented in Figure 9. We find four of five bulges below the theoretical curve, in general agreement with WRF who also studied disk galaxies. These results, if significant, suggest that bulges either (i) do not have isotropic velocity dispersions, a result already established for large ellipticals (Davies, *et al.* 1983, and references therein), or (ii) are additionally flattened by the disk potential. Both effects may be present.

To examine the effect of a disk on each bulge in our sample, we compare our results with some simple theories of bulge flattening by a disk. Monet, Richstone, and Schechter (1981, hereafter MRS) computed the flattening of an isotropic, non-rotating spheroid by a thin disk. Both of their components had scale-free density distributions, so the ratio of bulge-to-disk mass within any isophote is constant, which is unlike our models. The isophotal flattening as a function of M_B/M_{tot} is plotted in Figure 10 as a dashed line. Model fits for our sample are shown as filled circles; three of the galaxies fall near the MRS curve.

An evolutionary approach for estimating disk flattening of bulges has been taken by Barnes and White (1984). They started with nearly isotropic bulges and calculated the effect of the slow accumulation of an exponential disk in the equatorial plane. Since the disk mass growth rate was slow compared to the bulge dynamical time, the stellar orbits changed adiabatically. Their Fig. 5 demonstrates that as the disk mass is increased, $\bar{v}/\bar{\sigma}$ increases only slightly whereas the ellipticity increases significantly. Their result for an initially slowly rotating bulge ($\epsilon = 0.25$) is shown as a dotted line in Figure 10. The flattening of the same three bulges which are flatter than expected based on $\bar{v}/\bar{\sigma}$ are consistent with flattening caused by the disk. The remaining bulges are very concentrated, so flattening by a disk is

expected to be small. To what extent a bulge would remain isotropic while a disk forms within it needs further study.

Thus, we do not refute the conclusion that bulges are isotropic oblate rotators (Kormendy and Illingworth 1982; Dressler and Sandage 1983), but in some cases the disk potential has increased the flattening of the bulge, a conclusion also reached by Jarvis and Freeman (1985). The study by WRF noted that most bulges are below the isotropic $\bar{v}/\bar{\sigma}$ versus ϵ curve but ignored the effect of the disk potential on the bulge shape.

Because our models are not completely self-consistent, we can not rule out the presence of velocity anisotropies in the bulge. In particular, since the model profiles show significant variation among themselves, it seems unlikely that they all can be isotropic (since the mass-models are quite similar). For example, NGC 3898 and 4569 show a large observed velocity dispersion gradient, while NGC 4450 shows no gradient. The addition of our data to the WRF sample weakens their correlation of the dispersion gradient with type (see their Fig. 7).

d) General Implications of the Models

The main conclusion to be drawn from the model fitting is that it is possible to simultaneously fit the surface photometry, rotation curve, and dispersion profile of the inner regions of spiral galaxies without recourse to unseen material, central mass concentrations, or even necessarily anisotropic velocity dispersions. We believe that we have identified limitations in both the observational and theoretical aspects of this kind of study. The observations must be more accurate and extend to fainter regions in order to better constrain the models. The presence of unknown amounts of patchy absorption may produce an inherent limitation in studying the kinematics of galaxies, since we may be looking to different line-of-sight depths in different regions.

Another problem is the measurement of the radial velocity and dispersion from a spectrum which consists of a mixture of two populations with different properties. Simulations indicate that the single Gaussian Fourier quotient method is not adequate for this task. Because the region in which the disk and bulge contribute equally to the light is a crucial one for the models, a better technique must be developed for analyzing such data. More general and self-consistent models should be developed; but then more 'unknowns' are required, putting additional

burdens on the observations.

To overcome these difficulties, '3-D' measurements will have to be made: full coverage of a galaxy on the plane of the sky to recognize local obscuration, plus more complete line profile analysis correlated with intensity variations. This approach will both increase the reliability of the data, and supply additional constraints on the models. Only a large observational effort of this sort is ever likely to solve the problem of how galaxies are put together.

Paul Schechter kindly supplied a version of his FQ program for our tests. We thank Alain Porter and Greg Bothun for providing data, Don Schneider for assistance in fitting isophotes, and an anonymous referee for a careful reading of the manuscript and many constructive comments. We appreciate useful discussions with Peter Goldreich, Douglas Richstone, Don Schneider, and John Tonry. This work was supported in part by NSF grant AST 83-13725.

TABLE 1

The Observational Material

Galaxy	Axis	Date	Slit (arcsecs)	Wavelength Region	Camera	Exposure (secs)
NGC 2841	Major	3/09/81	1	Mg I b	Blue	1800
	Minor	3/09/81	1	Mg I b	Blue	1800
	Major	3/10/81	2	H-alpha	Blue	5400
NGC 3898	Minor	3/09/81	1	Mg I b	Blue	1800
	Major	3/09/81	1	Mg I b	Blue	1800
	Major	3/10/81	2	H-alpha	Blue	9000
NGC 4450	Major	4/27/81	2	H-alpha	Blue	4000
	Major	4/27/81	2	H-alpha	Blue	7200
	Major	4/27/81	1	Mg I b	Blue	3300
NGC 4569	Minor	3/09/81	1	Mg I b	Blue	1800
	Major	3/09/81	1	Mg I b	Blue	1800
	Major	3/10/81	2	H-alpha	Blue	10000
	Minor	4/28/82	2	H-alpha	Blue	2500
	Major	4/28/82	2	H-alpha	Blue	9000
	Minor	4/28/82	2	Ca Triplet	Red	2500
	Major	4/28/82	2	Ca Triplet	Red	9000
	Major	4/05/83	1	H-alpha	Red	1500
	Minor	4/05/83	1	H-alpha	Red	1500
NGC 5055	Minor	4/29/82	2	H-alpha	Blue	2500
	Major	4/29/82	2	H-alpha	Blue	9000
	Minor	4/29/82	2	Ca Triplet	Red	2500
	Major	4/29/82	2	Ca Triplet	Red	9000
NGC 5879	Major	4/28/82	2	H-alpha	Blue	8000
	Minor	4/28/82	2	H-alpha	Blue	2400
	Major	4/28/82	2	Ca Triplet	Red	8000
	Minor	4/28/82	2	Ca Triplet	Red	2400

Notes to Table 1:
Observations of H-alpha region are emission line measurements. Observations of Mg I b or Ca triplet region are absorption line measurements. Blue camera has 0.78 arcseconds per pixel. Red camera has 0.58 arcseconds per pixel.

TABLE 2

The Emission Line Rotation Curves

Galactocentric Distance (arcsecs)	Continuum Intensity	Radial Velocity (km/sec)	Galactocentric Distance (arcsecs)	Continuum Intensity	Radial Velocity (km/sec)
		NGC 3898 Major Axis - PA = 287			
-75.66	-15		-30.42	74	
-74.88	-6		-29.64	74	
-74.10	1		-28.86	98	
-73.32	2		-28.08	91	
-72.54	6		-27.30	89	
-71.76	4	1380	-26.52	91	
-70.98	7		-25.74	91	
-70.20	10		-24.96	95	
-69.42	18		-24.18	104	
-68.64	14		-23.40	116	
-67.86	14		-22.62	125	
-67.08	13		-21.84	125	
-66.30	15		-21.06	132	
-65.52	16		-20.28	146	
-64.74	-3		-19.50	154	
-63.96	41		-18.72	161	1372
-63.18	19		-17.94	176	
-62.40	14		-17.16	197	
-61.62	16		-16.38	207	
-60.84	21		-15.60	223	
-60.06	17		-14.82	249	1430
-59.28	15		-14.04	274	
-58.50	16		-13.26	300	
-57.72	17		-12.48	328	
-56.94	20		-11.70	356	
-56.16	22		-10.92	388	1401
-55.38	28		-10.14	423	
-54.60	33		-9.36	458	
-53.82	32		-8.58	509	
-53.04	23	1342	-7.80	563	
-52.26	53		-7.02	634	1357
-51.48	38		-6.24	748	
-50.70	37		-5.46	901	
-49.92	37		-4.68	1069	1325
-49.14	42		-3.90	1355	1308
-48.36	40		-3.12	1810	1287
-47.58	39		-2.34	2579	1238
-46.80	44		-1.56	3885	1215
-46.02	40		-0.78	5588	1193
-45.24	45		0.00	6582	1185
-44.46	41		0.78	5781	1174
-43.68	39		1.56	4267	1169
-42.90	41		2.34	2925	1157
-42.12	47		3.12	2078	1135
-41.34	40		3.90	1571	1108

-40.56	60	4.68	1240	1082
-39.78	51	5.46	1025	1042
-39.00	46	6.24	870	1039
-38.22	47	7.02	754	1028
-37.44	45	7.80	671	1034
-36.66	54	8.58	610	1042
-35.88	55	9.36	558	1014
-35.10	54	10.14	499	1022
-34.32	57	10.92	453	
-33.54	56	11.70	424	
-32.76	60	12.48	382	
-31.98	66	13.26	347	
-31.20	66	14.04	327	

Galactocentric Distance (arcsecs)	Continuum Intensity	Radial Velocity (km/sec)	Galactocentric Distance (arcsecs)	Continuum Intensity	Radial Velocity (km/sec)
		NGC 4450 Major Axis - PA = 183			
-78.78	42		-27.30	114	2043
-78.00	24		-26.52	113	
-77.22	35		-25.74	115	
-76.44	39		-24.96	117	2049
-75.66	16		-24.18	121	
-74.88	18		-23.40	122	
-74.10	16		-22.62	123	2047
-73.32	16		-21.84	133	
-72.54	19		-21.06	141	
-71.76	13		-20.28	153	
-70.98	7		-19.50	156	
-70.20	13		-18.72	159	
-69.42	17		-17.94	170	2048
-68.64	19		-17.16	177	
-67.86	18		-16.38	174	
-67.08	18		-15.60	183	
-66.30	18		-14.82	202	2054
-65.52	20		-14.04	220	
-64.74	16		-13.26	234	
-63.96	12		-12.48	251	2064
-63.18	25		-11.70	272	
-62.40	17		-10.92	287	
-61.62	22		-10.14	314	2082
-60.84	20		-9.36	336	
-60.06	20		-8.58	367	2101
-59.28	23		-7.80	398	2109
-58.50	23	2068	-7.02	452	2102
-57.72	21		-6.24	510	2108
-56.94	18		-5.46	576	2112
-56.16	23		-4.68	668	2100
-55.38	25		-3.90	800	2086
-54.60	26		-3.12	995	2076
-53.82	30	2024	-2.34	1282	2028
-53.04	32		-1.56	1768	2005
-52.26	43		-0.78	2593	2024
-51.48	48		0.00	3449	1972
-50.70	44		0.78	3423	1975
-49.92	50		1.56	2621	1980
-49.14	50		2.34	1884	1974
-48.36	53	2024	3.12	1436	1970
-47.58	55		3.90	1141	1935
-46.80	62		4.68	928	1928
-46.02	63		5.46	765	1937
-45.24	68		6.24	635	1936
-44.46	72		7.02	543	1935
-43.68	76		7.80	480	1932
-42.90	77	2028	8.58	427	1924
-42.12	81		9.36	388	1922
-41.34	80		10.14	357	1940

-40.56	92		10.92	333	1939
-39.78	93		11.70	310	
-39.00	91		12.48	279	1940
-38.22	93		13.26	254	
-37.44	100	2041	14.04	241	
-36.66	103		14.82	217	1963
-35.88	99		15.60	188	
-35.10	99		16.38	165	
-34.32	105		17.16	141	
-33.54	109	2040	17.94	123	
-32.76	111		18.72	108	
-31.98	110	2047	19.50	105	
-31.20	109		20.28	98	
-30.42	109		21.06	101	
-29.64	110	2042	21.84	98	
-28.86	115		22.62	103	
-28.08	117		23.40	102	

Galactocentric Distance (arcsecs)	Continuum Intensity	Radial Velocity (km/sec)	Galactocentric Distance (arcsecs)	Continuum Intensity	Radial Velocity (km/sec)
		NGC 4569 Major Axis 3/10/81 - PA = 203			
-79.56	54		-28.08	226	
-78.78	54		-27.30	232	
-78.00	68		-26.52	237	
-77.22	55		-25.74	243	-102
-76.44	44		-24.96	245	
-75.66	40		-24.18	260	
-74.88	40		-23.40	261	
-74.10	37		-22.62	273	
-73.32	57		-21.84	271	-125
-72.54	53		-21.06	280	
-71.76	57		-20.28	297	
-70.98	54		-19.50	308	
-70.20	48		-18.72	315	
-69.42	47		-17.94	325	-117
-68.64	66	-58	-17.16	334	
-67.86	69	-59	-16.38	354	
-67.08	78	-63	-15.60	374	
-66.30	82	-69	-14.82	381	
-65.52	88	-70	-14.04	399	-148
-64.74	92	-71	-13.26	411	
-63.96	95	-71	-12.48	428	
-63.18	101	-69	-11.70	445	
-62.40	111	-71	-10.92	462	
-61.62	118	-70	-10.14	499	-156
-60.84	125	-67	-9.36	540	
-60.06	129		-8.58	577	
-59.28	117		-7.80	606	
-58.50	110	-74	-7.02	667	-165
-57.72	124	-65	-6.24	787	-170
-56.94	137	-61	-5.46	993	-174
-56.16	134	-54	-4.68	1350	-193
-55.38	138	-54	-3.90	1904	-208
-54.60	141	-53	-3.12	2820	-225
-53.82	142	-42	-2.34	4386	-250
-53.04	149	-55	-1.56	7260	-249
-52.26	155	-78	-0.78	1493	-247
-51.48	149	-78	0.00	5586	-247
-50.70	155	-79	0.78	3199	-245
-49.92	142	-71	1.56	7039	-232
-49.14	141	-74	2.34	3760	-238
-48.36	138	-74	3.12	2249	-246
-47.58	146	-80	3.90	1420	-249
-46.80	142	-82	4.68	972	-249
-46.02	143	-80	5.46	747	-253
-45.24	144	-81	6.24	643	-252
-44.46	148	-86	7.02	574	
-43.68	166	-81	7.80	526	
-42.90	190	-76	8.58	495	
-42.12	223	-71	9.36	468	

-41.34	254	-69	10.14	454
-40.56	250	-67	10.92	437
-39.78	244	-67	11.70	417
-39.00	227	-74	12.48	408
-38.22	209	-79	13.26	395
-37.44	193	-82	14.04	389
-36.66	192	-81	14.82	402
-35.88	204	-75	15.60	433
-35.10	212	-64	16.38	400
-34.32	211	-59	17.16	347
-33.54	209	-50	17.94	312
-32.76	217	-75	18.72	298
-31.98	215	-88	19.50	288
-31.20	215	-83	20.28	282
-30.42	212		21.06	274
-29.64	215		21.84	276
-28.86	217		22.62	283

Galactocentric Distance (arcsecs)	Continuum Intensity	Radial Velocity (km/sec)	Galactocentric Distance (arcsecs)	Continuum Intensity	Radial Velocity (km/sec)
		NGC 4569 Major Axis 4/05/83 - PA = 203			
-57.42	65	-67	0.00	1763	-252
-56.84	69	-58	0.58	1437	-265
-56.26	66	-58	1.16	920	-256
-55.68	44	-65	1.74	575	-245
-55.10	32	-66	2.32	375	-261
-54.52	26	-63	2.90	257	-259
-53.94	22	-63	3.48	177	-267
-53.36	13		4.06	122	-274
-52.78	16	-70	4.64	92	-281
-52.20	3		5.22	-9	-287
-51.62	18		5.80	81	
-51.04	12	-74	6.38	62	-282
-50.46	10		6.96	65	
-49.88	14		7.54	56	
-49.30	8	-78	8.12	54	-285
-48.72	7		8.70	53	
-48.14	2		9.28	53	
-47.56	4	-81	9.86	48	-302
-46.98	3		10.44	49	
-46.40	1		11.02	45	
-45.82	2	-94	11.60	40	-297
-45.24	5		12.18	44	
-44.66	6		12.76	48	
-44.08	11	-91	13.34	44	-299
-43.50	9		13.92	41	
-42.92	10		14.50	49	
-42.34	6	-94	15.08	53	
-41.76	13		15.66	51	
-41.18	12		16.24	41	
-40.60	16	-96	16.82	36	
-40.02	16		17.40	38	
-39.44	19		17.98	32	
-38.86	18	-97	18.56	36	
-38.28	16		19.14	29	
-37.70	18		19.72	31	
-37.12	19	-93	20.30	32	
-36.54	22		20.88	32	
-35.96	17		21.46	26	
-35.38	14	-95	22.04	30	
-34.80	17		22.62	29	
-34.22	24		23.20	29	
-33.64	18	-98	23.78	25	
-33.06	22		24.36	22	
-32.48	12		24.94	29	
-31.90	18		25.52	26	
-31.32	20		26.10	23	
-30.74	22	-102	26.68	26	
-30.16	26		27.26	24	
-29.58	22		27.84	25	

-29.00	24		28.42	24
-28.42	2		29.00	24
-27.84	32		29.58	25
-27.26	31		30.16	24
-26.68	29	-102	30.74	28
-26.10	27		31.32	21
-25.52	29		31.90	7
-24.94	32		32.48	29
-24.36	25		33.06	25
-23.78	28		33.64	32
-23.20	29		34.22	25
-22.62	29	-113	34.80	29
-22.04	24		35.38	19
-21.46	35		35.96	30
-20.88	36		36.54	29
-20.30	30		37.12	25
-19.72	36		37.70	20
-19.14	32		38.28	23
-18.56	31	-107	38.86	24
-17.98	38		39.44	15
-17.40	32		40.02	15
-16.82	40		40.60	17
-16.24	39		41.18	23
-15.66	43		41.76	15
-15.08	42		42.34	15
-14.50	45	-195	42.92	10
-13.92	42		43.50	11
-13.34	43		44.08	-33
-12.76	42		44.66	7
-12.18	47		45.24	11
-11.60	43		45.82	5
-11.02	47		46.40	8
-10.44	53		46.98	8
-9.86	52		47.56	0
-9.28	60		48.14	14
-8.70	56		48.72	7
-8.12	62		49.30	11
-7.54	68		49.88	8
-6.96	75		50.46	4
-6.38	85		51.04	-8
-5.80	100		51.62	14
-5.22	123		52.20	13
-4.64	159		52.78	9
-4.06	209		53.36	11
-3.48	267		53.94	2
-2.90	342		54.52	5
-2.32	92		55.10	6
-1.74	626	-246	55.68	-4
-1.16	1055	-248	56.26	5
-0.58	1548	-248		

Galactocentric Distance (arcsecs)	Continuum Intensity	Radial Velocity (km/sec)	Galactocentric Distance (arcsecs)	Continuum Intensity	Radial Velocity (km/sec)
		NGC 5055 Major Axis - PA = 105			
-30.42	-49		24.18	119	646
-29.64	176	347	24.96	117	
-28.86	118	340	25.74	113	
-28.08	118	345	26.52	106	652
-27.30	126	343	27.30	106	
-26.52	135	356	28.08	101	
-25.74	143		28.86	106	658
-24.96	146	336	29.64	107	
-24.18	156		30.42	107	
-23.40	158		31.20	92	657
-22.62	161	338	31.98	95	
-21.84	161	341	32.76	101	
-21.06	155	345	33.54	108	662
-20.28	158	343	34.32	112	
-19.50	171	346	35.10	116	
-18.72	173	355	35.88	118	656
-17.94	180	351	36.66	118	
-17.16	173	354	37.44	106	
-16.38	182	360	38.22	96	640
-15.60	190	371	39.00	94	
-14.82	191	371	39.78	87	
-14.04	197		40.56	84	656
-13.26	208		41.34	86	
-12.48	220	389	42.12	87	
-11.70	231		42.90	87	654
-10.92	238		43.68	82	
-10.14	251	393	44.46	87	
-9.36	255		45.24	83	650
-8.58	264		46.02	86	
-7.80	259	403	46.80	76	
-7.02	287		47.58	77	666
-6.24	327		48.36	84	
-5.46	387	403	49.14	84	
-4.68	457		49.92	82	658
-3.90	567	419	50.70	73	
-3.12	782	414	51.48	66	
-2.34	1219	455	52.26	63	651
-1.56	1929	478	53.04	62	
-0.78	2449	499	53.82	56	
0.00	2589	519	54.60	53	663
0.78	2307	546	55.38	54	
1.56	1461	576	56.16	53	
2.34	930	584	56.94	52	664
3.12	695	597	57.72	51	
3.90	542	609	58.50	51	
4.68	459	604	59.28	53	667
5.46	397	623	60.06	52	
6.24	351	630	60.84	53	
7.02	325	630	61.62	51	684

7.80	289	636	62.40	51	
8.58	273	627	63.18	51	
9.36	247	654	63.96	47	671
10.14	225		64.74	48	
10.92	210		65.52	47	
11.70	197		66.30	47	665
12.48	143	647	67.08	50	
13.26	146		67.86	50	
14.04	142		68.64	48	663
14.82	124	624	69.42	47	
15.60	126		70.20	49	
16.38	113		70.98	49	
17.16	114	653	71.76	49	
17.94	120		72.54	57	660
18.72	123		73.32	72	
19.50	125	630	74.10	83	
20.28	128		74.88	106	
21.06	130		75.66	125	
21.84	126	640	76.44	138	
22.62	129		77.22	147	666
23.40	123				

Galactocentric Distance (arcsecs)	Continuum Intensity	Radial Velocity (km/sec)	Galactocentric Distance (arcsecs)	Continuum Intensity	Radial Velocity (km/sec)
		NGC 5879 Major Axis = PA 174			
-26.52	3		24.96	35	638
-25.74	4	932	25.74	31	620
-24.96	1		26.52	32	636
-24.18	4		27.30	31	656
-23.40	5	933	28.08	30	659
-22.62	14		28.86	31	668
-21.84	20	905	29.64	27	
-21.06	25	893	30.42	25	672
-20.28	33	892	31.20	22	
-19.50	37	892	31.98	22	
-18.72	43	886	32.76	21	669
-17.94	48	892	33.54	21	
-17.16	49	893	34.32	20	
-16.38	53	895	35.10	16	673
-15.60	54	885	35.88	16	
-14.82	58	881	36.66	16	
-14.04	58	883	37.44	17	678
-13.26	59	887	38.22	17	
-12.48	67	884	39.00	19	
-11.70	70	881	39.78	17	660
-10.92	77	885	40.56	16	
-10.14	85	873	41.34	19	
-9.36	88	869	42.12	15	662
-8.58	89	874	42.90	14	
-7.80	94	865	43.68	14	
-7.02	97	858	44.46	12	659
-6.24	100	837	45.24	15	
-5.46	108	831	46.02	13	
-4.68	111	828	46.80	13	650
-3.90	121	829	47.58	14	
-3.12	136	827	48.36	13	
-2.34	171	806	49.14	16	
-1.56	212	791	49.92	13	
-0.78	251	772	50.70	13	
0.00	274	764	51.48	10	
0.78	248	758	52.26	11	
1.56	225	729	53.04	10	
2.34	195	739	53.82	8	
3.12	172	726	54.60	11	
3.90	146	717	55.38	9	
4.68	122	706	56.16	9	
5.46	108	698	56.94	7	
6.24	96	698	57.72	8	
7.02	88	704	58.50	7	
7.80	80	708	59.28	7	
8.58	80	699	60.06	7	
9.36	75	693	60.84	8	
10.14	73	691	61.62	10	
10.92	69	680	62.40	10	

11.70	65	672	63.18	13
12.48	53	665	63.96	11
13.26	35	656	64.74	11
14.04	29	658	65.52	12
14.82	29	654	66.30	12
15.60	32	660	67.08	10
16.38	32	657	67.86	10
17.16	32	656	68.64	11
17.94	34	651	69.42	10
18.72	37	638	70.20	11
19.50	36	658	70.98	12
20.28	39	652	71.76	12
21.06	36	652	72.54	12
21.84	37	658	73.32	13
22.62	36	649	74.10	15
23.40	34	646	74.88	17
24.18	33	655	75.66	22

TABLE 3

The Absorption Line Velocity Data

Galactocentric Distance (arcsecs)	Mean Velocity (km/sec)	Velocity Dispersion (km/sec)	Galactocentric Distance (arcsecs)	Mean Velocity (km/sec)	Velocity Dispersion (km/sec)
		NGC 2841 Major Axis			
12.15	101	194	-0.72	-28	244
7.86	81	218	-1.50	-59	223
5.96	103	221	-2.28	-74	236
4.74	103	204	-3.06	-91	211
3.96	115	237	-3.84	-99	224
3.18	89	229	-4.62	-116	221
2.40	84	221	-5.40	-89	232
1.62	69	245	-6.57	-97	235
0.84	32	248	-8.52	-92	197
0.06	2	240	-12.03	-127	213
Galactocentric Distance (arcsecs)	Mean Velocity (km/sec)	Velocity Dispersion (km/sec)	Galactocentric Distance (arcsecs)	Mean Velocity (km/sec)	Velocity Dispersion (km/sec)
		NGC 2841 Minor Axis			
7.41	-18	226	-0.78	43	247
5.07	15	300	-1.56	45	252
3.90	16	270	-2.34	37	246
3.12	25	272	-3.12	-12	209
2.34	3	220	-3.90	97	230
1.56	12	230	-4.68	10	264
0.78	16	257	-5.85	15	230
0.00	29	241	-7.80	33	249
Galactocentric Distance (arcsecs)	Mean Velocity (km/sec)	Velocity Dispersion (km/sec)	Galactocentric Distance (arcsecs)	Mean Velocity (km/sec)	Velocity Dispersion (km/sec)
		NGC 3898 Major Axis			
6.68	64	104	-1.12	-36	202
3.95	49	146	-1.90	-53	211
2.78	56	163	-2.68	-48	186
2.00	66	192	-3.46	-58	162
1.22	34	207	-4.24	-95	228
0.44	14	220	-5.41	-87	182
-0.34	-7	215	-7.75	-86	155

Galactocentric Distance (arcsecs)	Mean Velocity (km/sec)	Velocity Dispersion (km/sec)	Galactocentric Distance (arcsecs)	Mean Velocity (km/sec)	Velocity Dispersion (km/sec)
		NGC 3898 Minor Axis			
3.51	-106	185	-1.56	-48	217
2.34	-70	208	-2.34	-50	217
1.56	-61	243	-3.12	-65	226
0.78	-64	239	-3.90	-15	319
0.00	-62	248	-5.07	-64	173
-0.78	-55	247			

Galactocentric Distance (arcsecs)	Mean Velocity (km/sec)	Velocity Dispersion (km/sec)	Galactocentric Distance (arcsecs)	Mean Velocity (km/sec)	Velocity Dispersion (km/sec)
		NGC 4450 Major Axis			
11.47	11	14/	-0.62	-12	142
7.96	24	123	-1.40	-17	147
6.01	31	152	-2.18	-42	148
4.84	45	138	-2.96	-54	147
4.06	43	136	-3.74	-51	157
3.28	53	125	-4.52	-49	150
2.50	45	132	-5.69	-36	142
1.72	33	140	-7.64	-71	74
0.94	16	139	-10.76	-79	177
0.16	-3	139			

Galactocentric Distance (arcsecs)	Mean Velocity (km/sec)	Velocity Dispersion (km/sec)	Galactocentric Distance (arcsecs)	Mean Velocity (km/sec)	Velocity Dispersion (km/sec)
		NGC 4569 Major Axis 3/09/81			
3.12	70	110	-0.78	-38	155
2.34	56	148	-1.56	-59	138
1.56	59	145	-2.34	-88	108
0.78	35	154	-3.12	-86	102
0.00	0	157	-4.29	-107	109
		NGC 4569 Major Axis 4/28/82			
-10.15	-31	93	0.58	26	135
-8.12	-42	114	1.16	46	135
-6.67	-48	125	1.74	68	121
-5.51	-54	125	2.32	84	110
-4.64	-84	116	2.90	92	100
-4.06	-88	114	3.48	99	98
-3.48	-101	109	4.06	99	95

-2.90	-105	100	4.64	86	103
-2.32	-92	111	5.22	84	103
-1.74	-78	115	6.09	76	97
-1.16	-51	126	7.25	72	99
-0.58	-23	136	8.70	54	87
0.00	0	136	10.73	52	82

Galactocentric Distance (arcsecs)	Mean Velocity (km/sec)	Velocity Dispersion (km/sec)	Galactocentric Distance (arcsecs)	Mean Velocity (km/sec)	Velocity Dispersion (km/sec)
		NGC 5055 Major Axis			
20.59	49	134	-0.58	-6	116
18.27	59	102	-1.16	-16	113
15.95	26	122	-1.74	-27	114
12.47	41	115	-2.32	-43	106
11.31	50	112	-2.90	-68	104
10.15	53	111	-3.48	-57	100
8.99	50	116	-4.06	-64	103
8.12	56	97	-4.64	-65	102
7.54	50	108	-5.22	-64	99
6.96	50	100	-5.80	-67	94
6.38	45	109	-6.38	-69	88
5.80	50	98	-6.96	-77	98
5.22	53	98	-7.83	-72	90
4.64	49	102	-8.99	-88	94
4.06	50	101	-10.15	-85	87
3.48	45	104	-11.31	-96	97
2.90	43	95	-12.47	-98	90
2.32	36	106	-13.63	-103	92
1.74	23	110	-14.79	-99	82
1.16	17	116	-15.95	-104	66
0.58	7	111	-17.11	-104	65
0.00	0	118	-18.56	-119	87

Galactocentric Distance (arcsecs)	Mean Velocity (km/sec)	Velocity Dispersion (km/sec)	Galactocentric Distance (arcsecs)	Mean Velocity (km/sec)	Velocity Dispersion (km/sec)
		NGC 5055 Minor Axis			
5.51	-7	119	-0.58	-4	120
3.19	3	117	-1.16	6	113
2.32	4	117	-1.74	-8	110
1.74	3	114	-2.61	3	119
1.16	2	120	-4.06	2	120
0.58	4	117	-6.38	-11	114
0.00	3	120	-10.73	-3	111

Galactocentric Distance (arcsecs)	Mean Velocity (km/sec)	Velocity Dispersion (km/sec)	Galactocentric Distance (arcsecs)	Mean Velocity (km/sec)	Velocity Dispersion (km/sec)
		NGC 5879 Major Axis			
-15.66	-111	38	0.58	11	72
-12.47	-106	40	1.16	20	73
-10.44	-98	51	1.74	9	83
-8.70	-84	48	2.32	26	78
-6.96	-75	54	2.90	37	72
-5.51	-56	57	3.77	38	74
-4.35	-42	61	4.93	49	62
-3.19	-36	65	6.09	74	33
-2.32	-29	68	7.25	68	63
-1.74	-20	78	8.70	83	53
-1.16	-19	79	10.44	95	60
-0.58	-9	73	12.18	99	63
0.00	0	71	14.21	105	59

TABLE 4
MODEL PARAMETERS

NGC	type	D (Mpc)	i (°)	ϵ	R_e (kpc)	M_B ($10^9 M_\odot$)	M_D ($10^9 M_\odot$)	R_D (kpc)	$\mu_B = \mu_D$ (kpc)	v_p/σ_0	$\bar{v}/\bar{\sigma}$
2841	Sb	15.7	25	.37	0.94	63.0	146	5.4	1.5	0.64	0.40
3898	Sab	15.8	23	.33	1.06	44.0	58	4.8	3.5	0.50	0.60
4450	Sab	17.2	30	.20	1.70	35.0	13	4.5	1.4	0.45	0.30
4569	Sb	17.2	25	.17	0.35	6.8	81	3.6	0.4	0.71	0.70
5055	Sbc	8.2	35	.28	0.40	5.5	45	2.7	0.3	0.47	0.67

REFERENCES

Bahcall, J. N. 1984, *Ap. J.*, **276**, 156.

Bahcall, J. N. and Schmidt, M. 1982, *Ap. J. (Letters)*, **258**, L23.

Barnes, J., and White, S. D. M. 1984, *M.N.R.A.S.*, **211**, 753.

Bertola, F., Capaccioli, M., and Oke, J. B. 1982, *Ap. J.*, **254**, 494.

Binney, J. 1978, *M.N.R.A.S.*, **183**, 501.

———. 1980, *M.N.R.A.S.*, **190**, 421.

Boroson, T. 1981, *Ap. J. Suppl.*, **46**, 177.

Bosma, A. 1978, *Ph.D. Thesis, University of Gronigen.*

Burbidge, E. M., Burbidge, G. R., and Prendergast, K. H. 1960, *Ap. J.*, **131**, 282.

Burstein, D. 1979, *Ap. J. Suppl.*, **41**, 435.

Caldwell, N. 1984, *Pub. A. S. P.*, **96**, 287.

Davies, R. L., Efstathiou, G., Fall, S. M., Illingworth, G., and Schechter, P. L. 1983, *Ap. J.*, **266**, 41.

deVaucouleurs, G. 1948, *Ann. d'Ap.*, **11**, 247.

Dressler, A. 1979, *Ap. J.*, **231**, 659.

Dressler, A. and Sandage, A. 1983, *Ap. J.*, **265**, 664.

Fish, R. A. 1961, *Ap. J.*, **134**, 880.

Hawley, S. A. 1978, *Ap. J.*, **224**, 417.

Illingworth, G. and Schechter, P. L. 1982, *Ap. J.*, **256**, 481.

Jarvis, B. and Freeman, K. C. 1985, *Ap. J.*, **295**, 000.

Kormendy, J. 1977, *Ap. J.*, **214**, 359.

Kormendy, J. and Illingworth, G. 1982, *Ap. J.*, **256**, 460.

McElroy, D. B. 1983, *Ap. J.*, **270**, 485.

Minkowski, R., and Osterbrock, D. 1959, *Ap. J.*, **129**, 583.

Monet, D. G., Richstone, D. O., and Schechter, P. L. 1981, *Ap. J.*, **245**, 454.

Oke, J. B., Bertola, F. and Capaccioli, M. 1981, *Ap. J.*, **243**, 453.

Rubin, V. C., and Thonnard, N. 1984, private communication.

Sandage, A. 1961, *The Hubble Atlas of Galaxies* (Washington: Carnegie Institution).

Sargent, W. L. W., Schechter, P. L., Boksenberg, A., and Shortridge, K. 1977, *Ap. J.*, **212**, 326.

Schweizer, F. 1979, *Ap. J.*, **233**, 23.

Seiden, P. E., Schulman, L. S., and Elmegreen, B. G. 1984, *Ap. J.*, **282**, 45.

Teuben, P. J., Turner, E., and Schwarzschild, M. 1984, preprint.

Tinsley, B. M. 1980, *Fund. Cosmic Phys.*, **5**, 287.

Tonry, J. 1984*a*, *Ap. J. (Letters)*, **283**, L27.

———. 1984*b*, personal communication.

van der Kruit, P. C. and Searle, L. 1981*a*, *Astr. Ap.*, **95**, 105.

———. 1981*b*, *Astr. Ap.*, **95**, 116.

———. 1982, *Astr. Ap.*, **110**, 79.

Whitmore, B. C. 1980, *Ap. J.*, **242**, 53.

Whitmore, B. C. and Kirshner, R. P. 1982, *A.J.*, **87**, 500.

Whitmore, B. C., Rubin, V. C., and Ford, W. K., Jr. 1984, *Ap. J.*, **287**, 66.

Young, P. J. 1976, *A.J.*, **81**, 807.

Young, P. J., Sargent, W. L. W., Boksenberg, A., Lynds, C. R., and Hartwick, F. D. A. 1978, *Ap. J.*, **222**, 450.

FIGURE CAPTIONS

FIG. 1.— (*a*) Comparison of KI data for NGC 4565 to spheroidal rotation. Symbols are the rotation rate measured with the slit perpendicular to major axis at a distance R from the center. Dashed lines are model values from equation (11). (*b*) same as (*a*) for NGC 7814. Error bars are not included for $R = 40$" points to avoid confusion.

FIG. 2.— Effect of line strength and velocity dispersion on measurements via Fourier quotient method. The effective fraction of bulge light indicates what fraction of light the bulge would have to contribute to achieve the same measured velocity if the FQ method introduced no bias. The line strength γ of the bulge is 1, and the disk either 0.5 or 1, as labeled. The solid lines are for $\sigma_B/\sigma_D = 4./0.7$, and the dashed line for $\sigma_B/\sigma_D = 0.7/2.5$.

FIG. 3*ab*.— Results for NGC 2841, (*a*) Symbols represent the absorption line mean rotation and velocity dispersion along the major axis. Plus signs and open circles for one side, asterisks and filled circles for the other side. Dashed lines are model projected values for just the bulge, solid lines include disk light and seeing. (*b*) same as (*a*) for the minor axis.

FIG. 3*c*.— Model equatorial velocity profiles for NGC 2841. The total (bulge+disk) circular velocity is U_c, the bulge mean rotation is u, and its velocity dispersion is σ_R.

FIG. 4*ab*.— Results for NGC 3898. (*a*) Different symbols distinguish the two sides of the major axis emission line rotation curve; solid line is the inclined circular rotation rate. (*b*) Symbols show major axis absorption line data; both lines represent model values for bulge light only.

FIG. 4*c*.— Model equatorial velocity profiles for NGC 3898; notation is the same as Fig. 3*c*.

FIG. 5*ab*.— Results for NGC 4450. (*a*) Emission line data; notation same as Fig. 4*a*. (*b*) Symbols show absorption line data for two sides of the major axis. The dashed line represents the projected rotation curve for only the bulge; the solid line includes both bulge and disk plus seeing.

FIG. 5*c*.— Model velocity profile for NGC 4450, see Fig. 3*c*.

FIG. 6*a*.— Symbols represent major axis emission line rotation curve measured in two different years. Solid line is model circular rotation curve.

FIG. 6*bc*.— Major axis absorption line data, different symbols represent the two sides of the galaxy; plus signs and open circles from one side, asterisks and filled circles the other. Dashed lines show bulge only; solid lines include disk and seeing. (*b*) mean rotation, (*c*) velocity dispersion.

FIG. 6*d*.— Model velocity profiles for NGC 4569; see Fig. 3*c*.

FIG. 7*a*.— Major axis emission line rotation curve for NGC 5055, notation same as Fig. 6*a*.

FIG. 7*bc*.— Absorption line data, notation is the same as Fig. 6*bc*.

FIG. 7*d*.— Model profiles, see Fig. 3*c*.

FIG. 8*a*.— NGC 5879 emission line rotation curve, different symbols distinguish the two sides of the galaxy.

FIG. 8*b*.— NGC 5879 absorption line data; (+,*) show mean rotation and (o,•) velocity dispersion for each side of the galaxy, respectively.

FIG. 9.— The ratio $\bar{v}/\bar{\sigma}$ is calculated from the models for each of the galaxies, and measures the relative dynamical importance of rotation. The ellipticity ϵ is based on observations. The dashed line is from Binney (1980), and represents an oblate-spheroidal rotator with isotropic velocity dispersion.

FIG. 10.— Spheroidal bulge flattening caused by a disk as a function of the bulge-to-total mass ratio. The dashed line is taken from Monet, Richstone, and Schechter (1981); the dotted line is the result of adding a disk to an initially slowing rotation bulge (Barnes and White 1984).

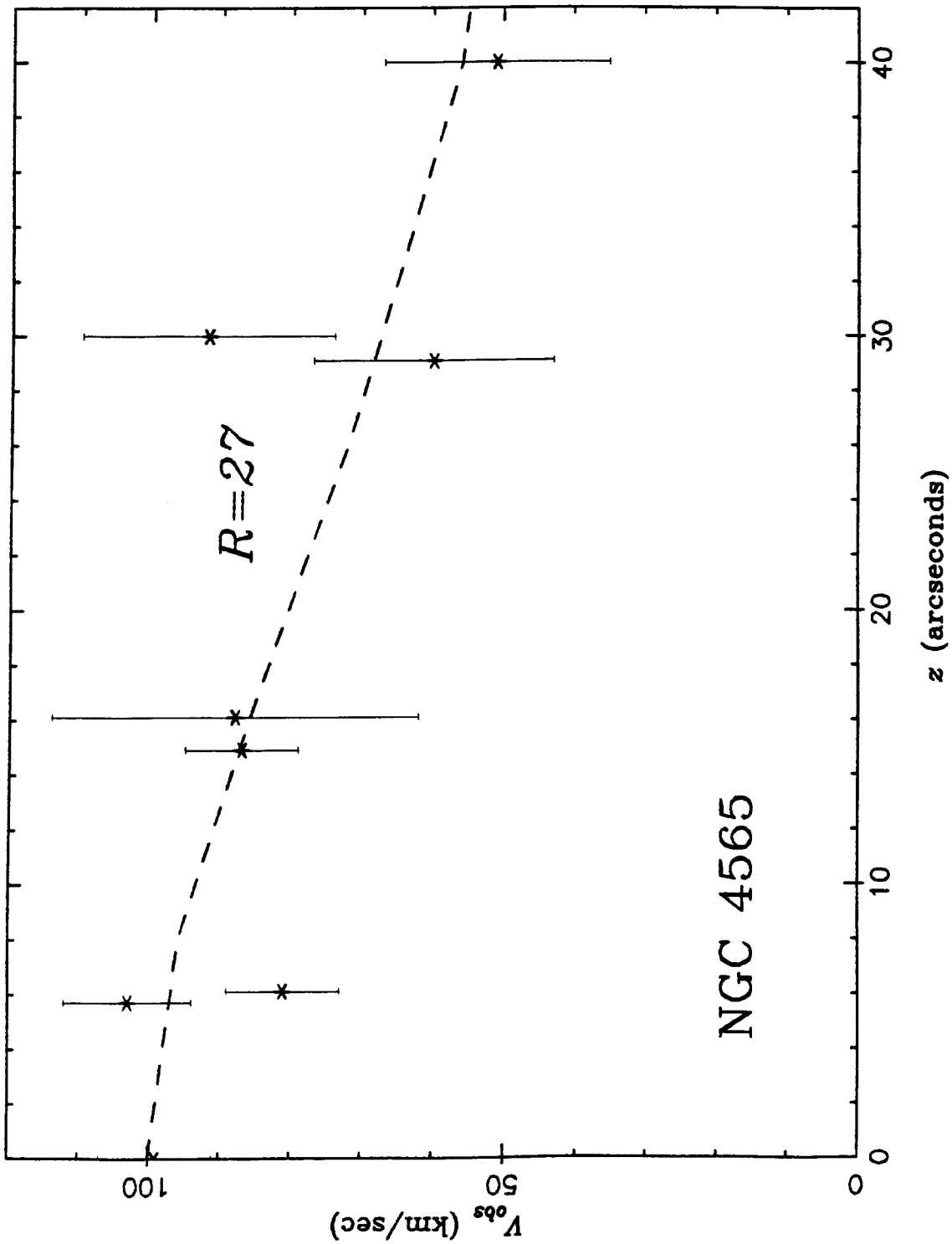

Fig. 1a

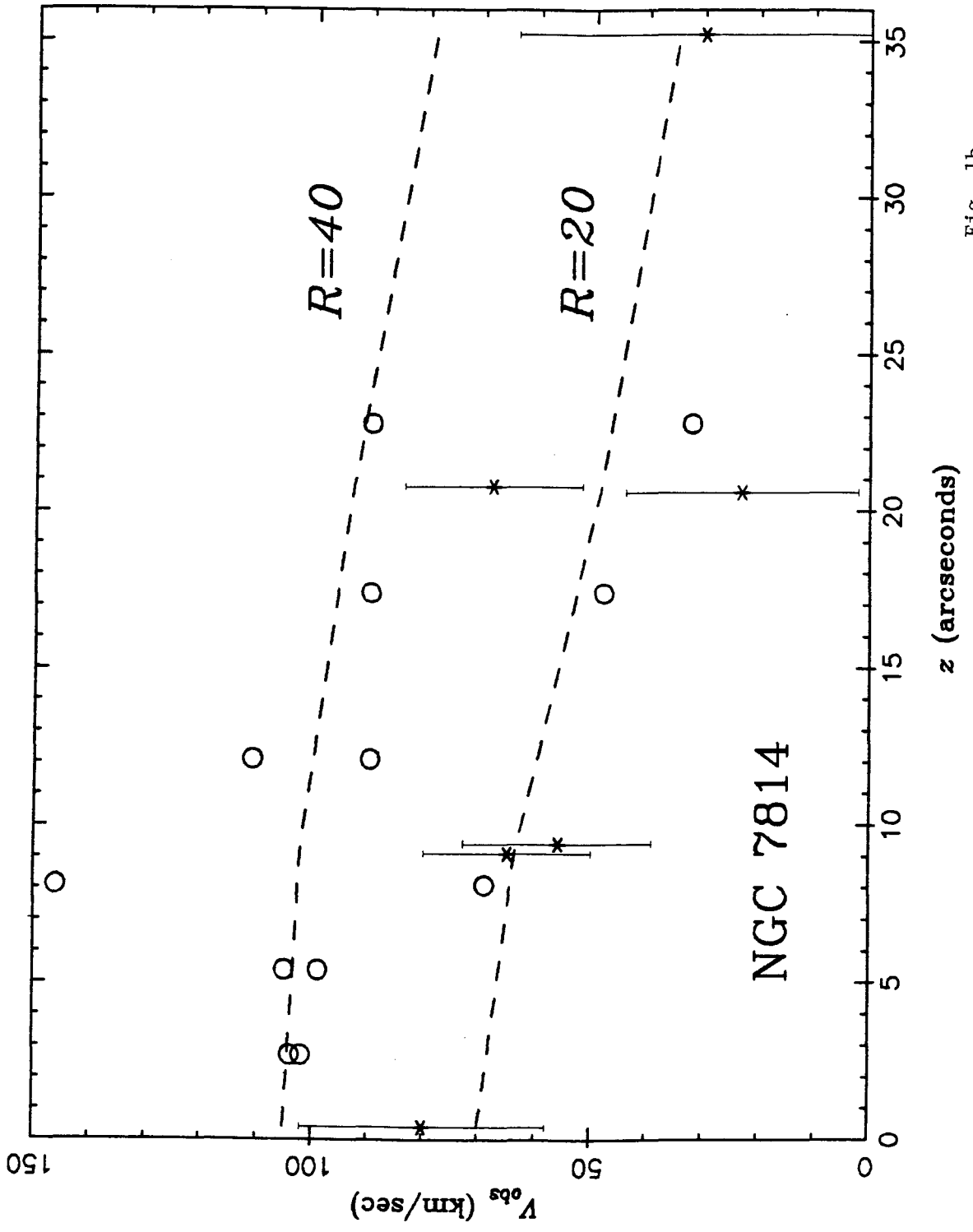
R=40
R=20
NGC 7814
V_{obs} (km/sec)
z (arcseconds)
150
100
50
0
0
5
10
15
20
25
30
35

Fig. 1b

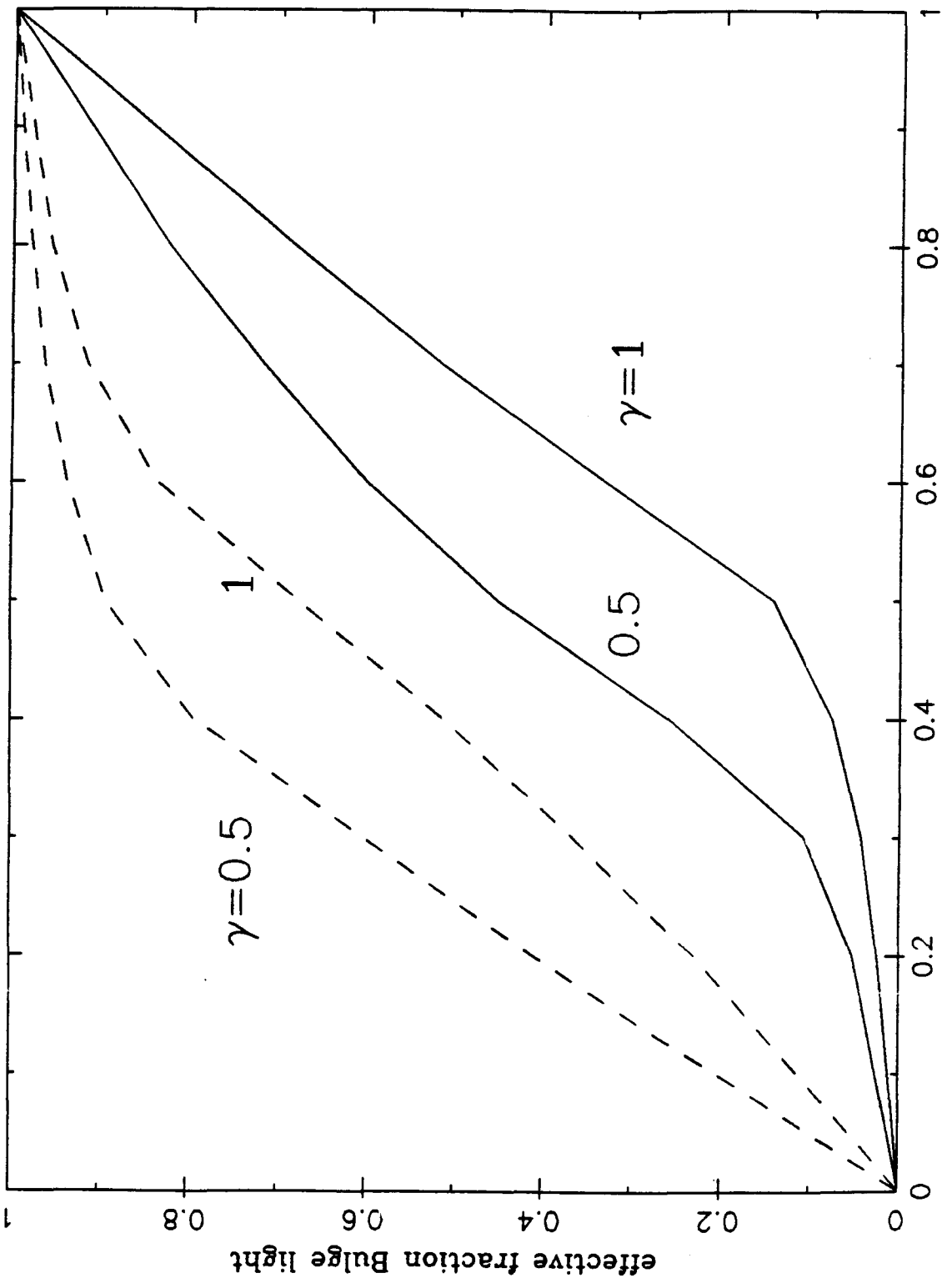
effective fraction Bulge light
fraction Bulge light
0
0.2
0.4
0.6
0.8
1
γ=0.5
1
0.5
γ=1

Fig. 2

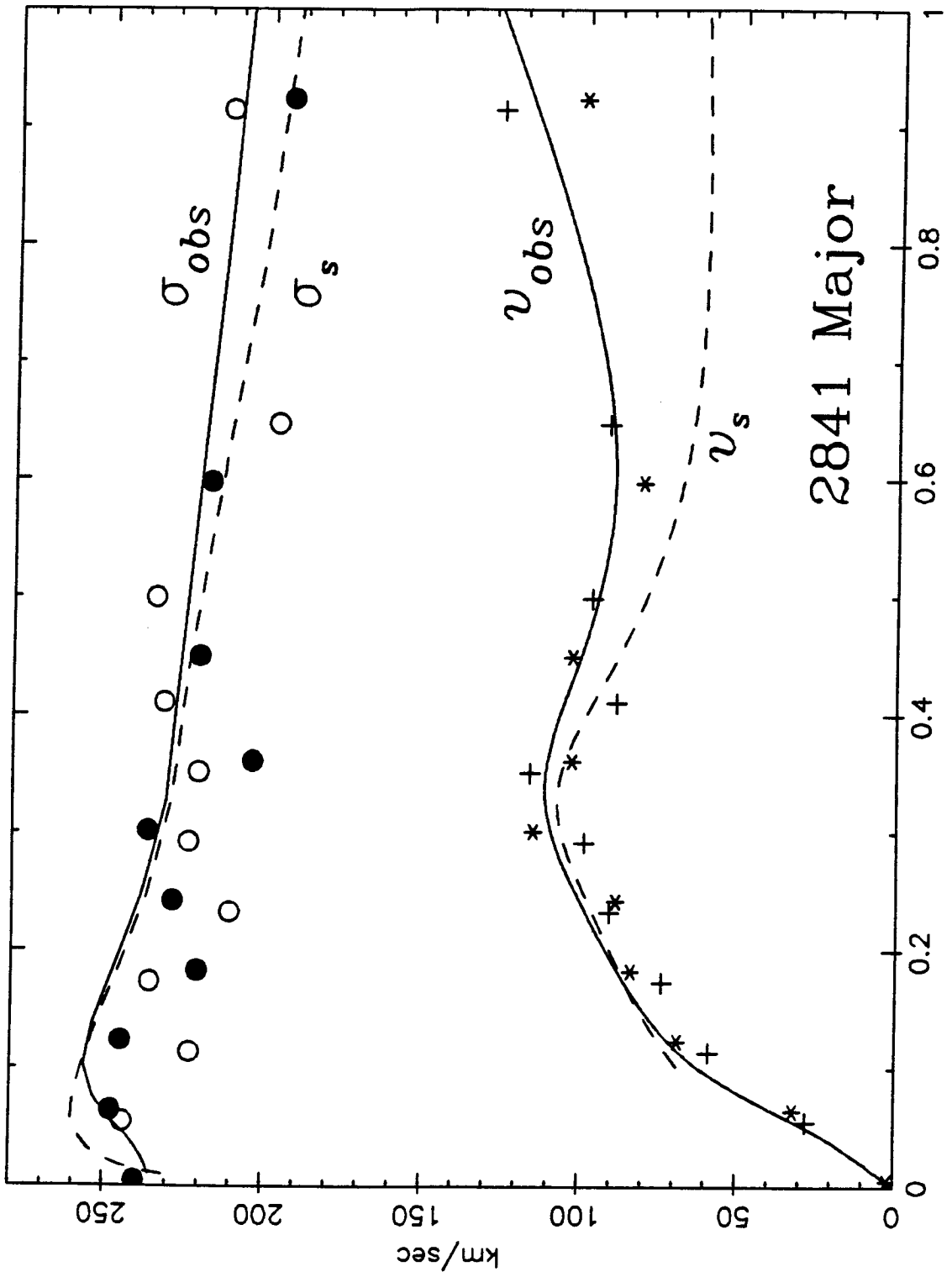
2841 Major
σ_{obs}
σ_s
v_{obs}
v_s
km/sec
radius (kpc)
0
50
100
150
200
250
0.2
0.4
0.6
0.8
1

Fig. 3a

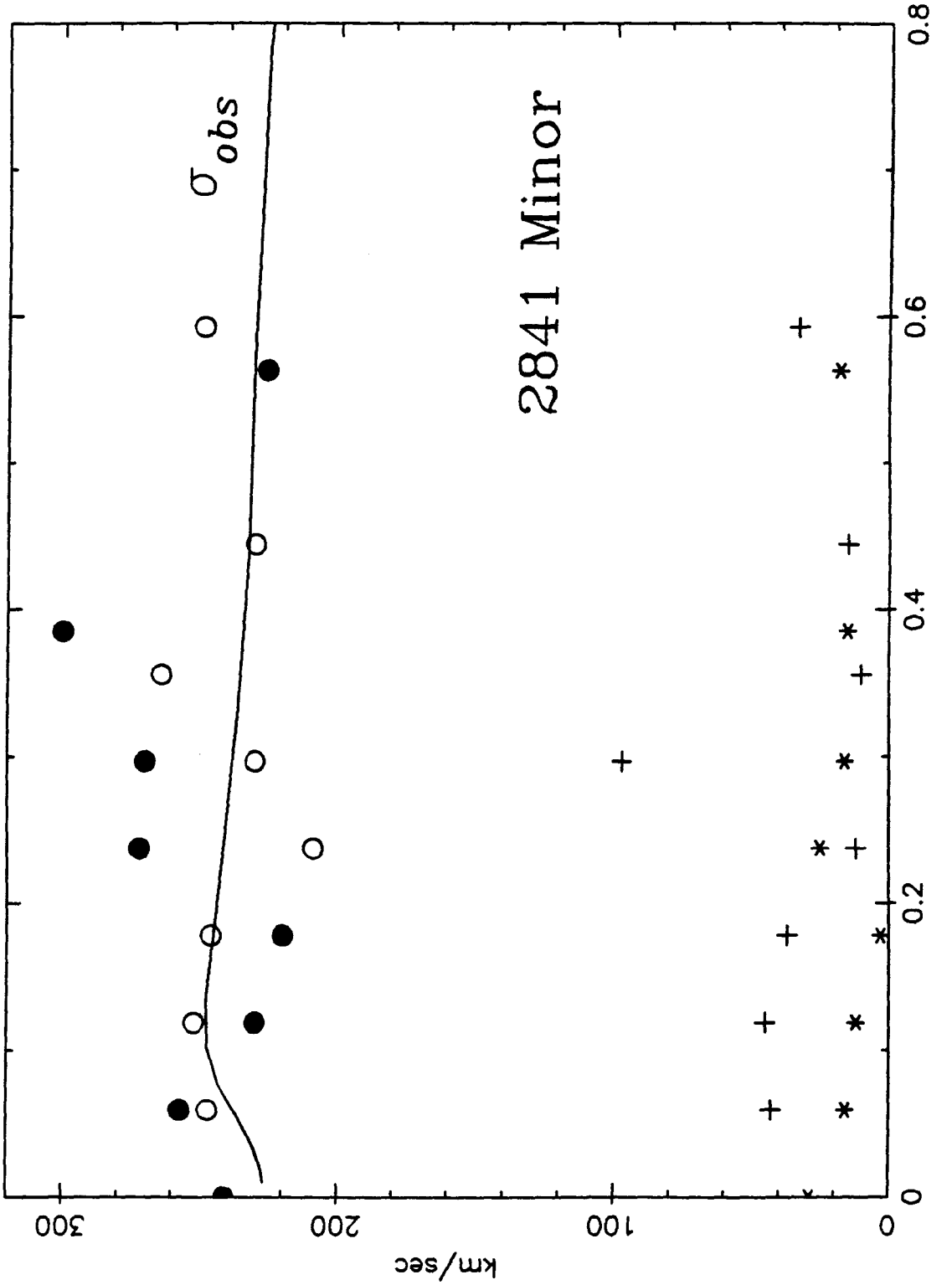
2841 Minor
σ_{obs}
km/sec
300
200
100
0
0
0.2
0.4
0.6
0.8
projected radius (kpc)

Fig. 3b

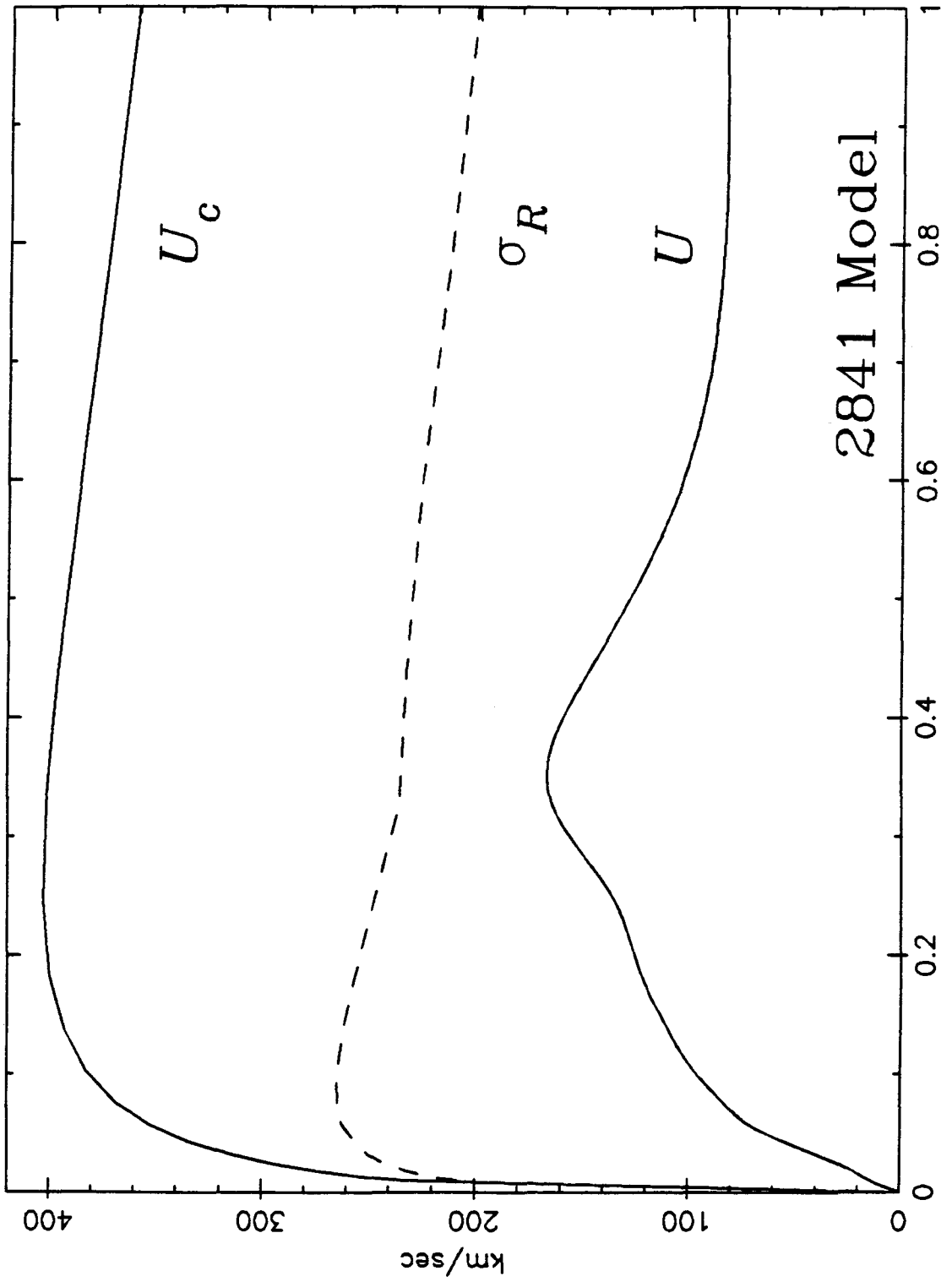
2841 Model
U_c
σ_R
U
km/sec
radius (kpc)
0
100
200
300
400
0.2
0.4
0.6
0.8
1

Fig. 3c

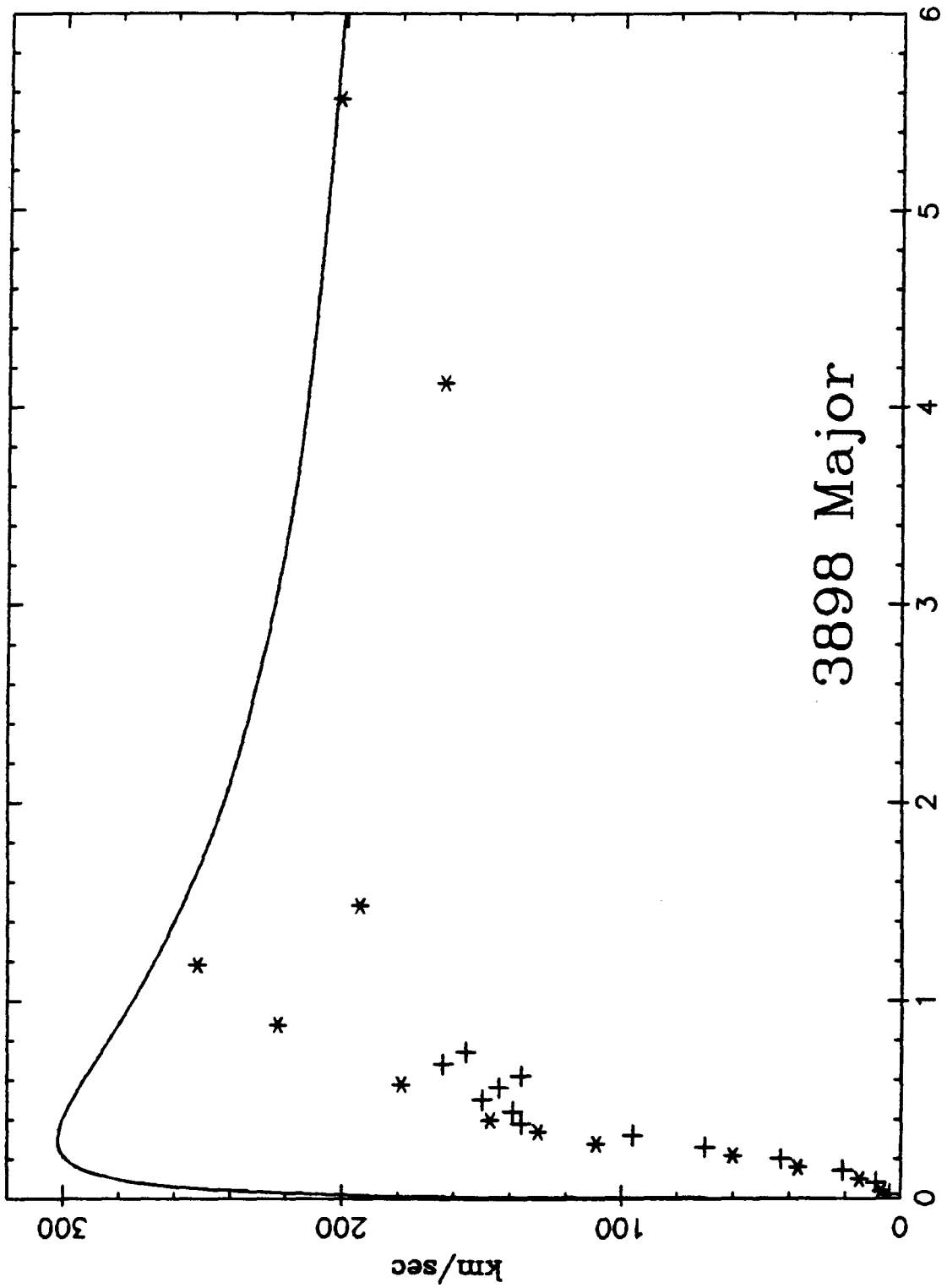

Fig. 4a

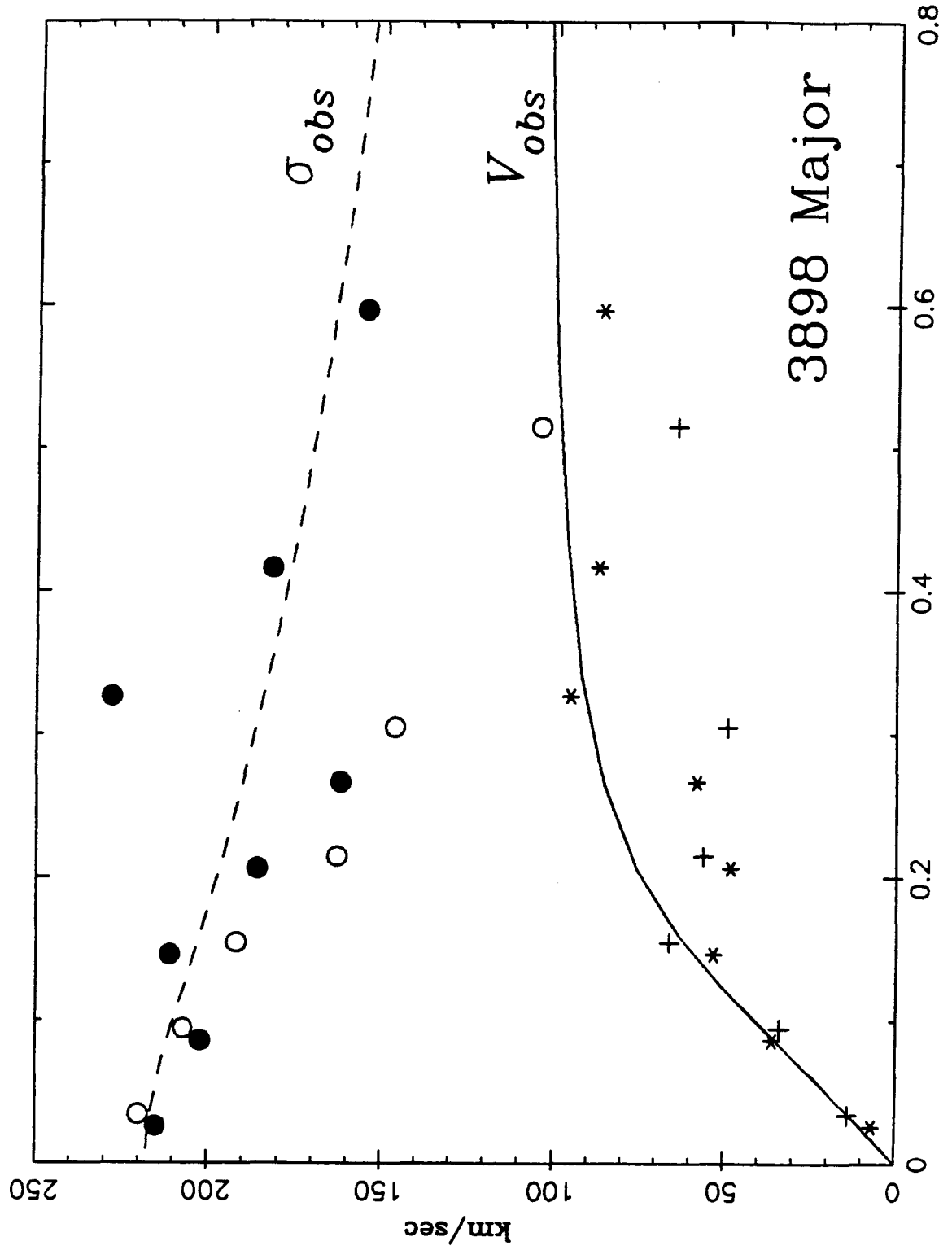
3898 Major
V_{obs}
σ_{obs}
km/sec
radius (kpc)
0
50
100
150
200
250
0.2
0.4
0.6
0.8

Fig. 4b

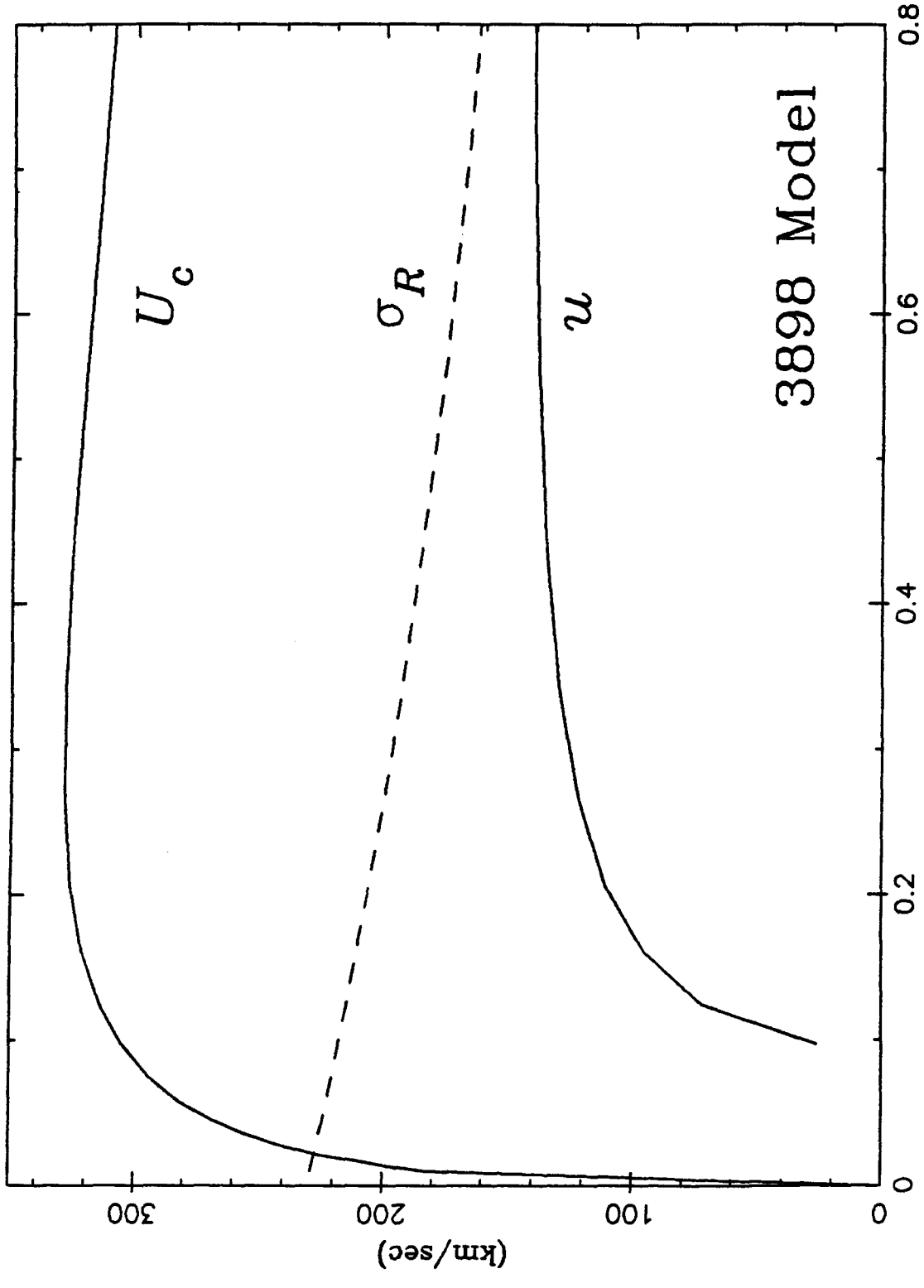
3898 Model
U_c
σ_R
$\mathcal{U}$
(km/sec)
0
100
200
300
R (kpc)
0
0.2
0.4
0.6
0.8

Fig. 4c

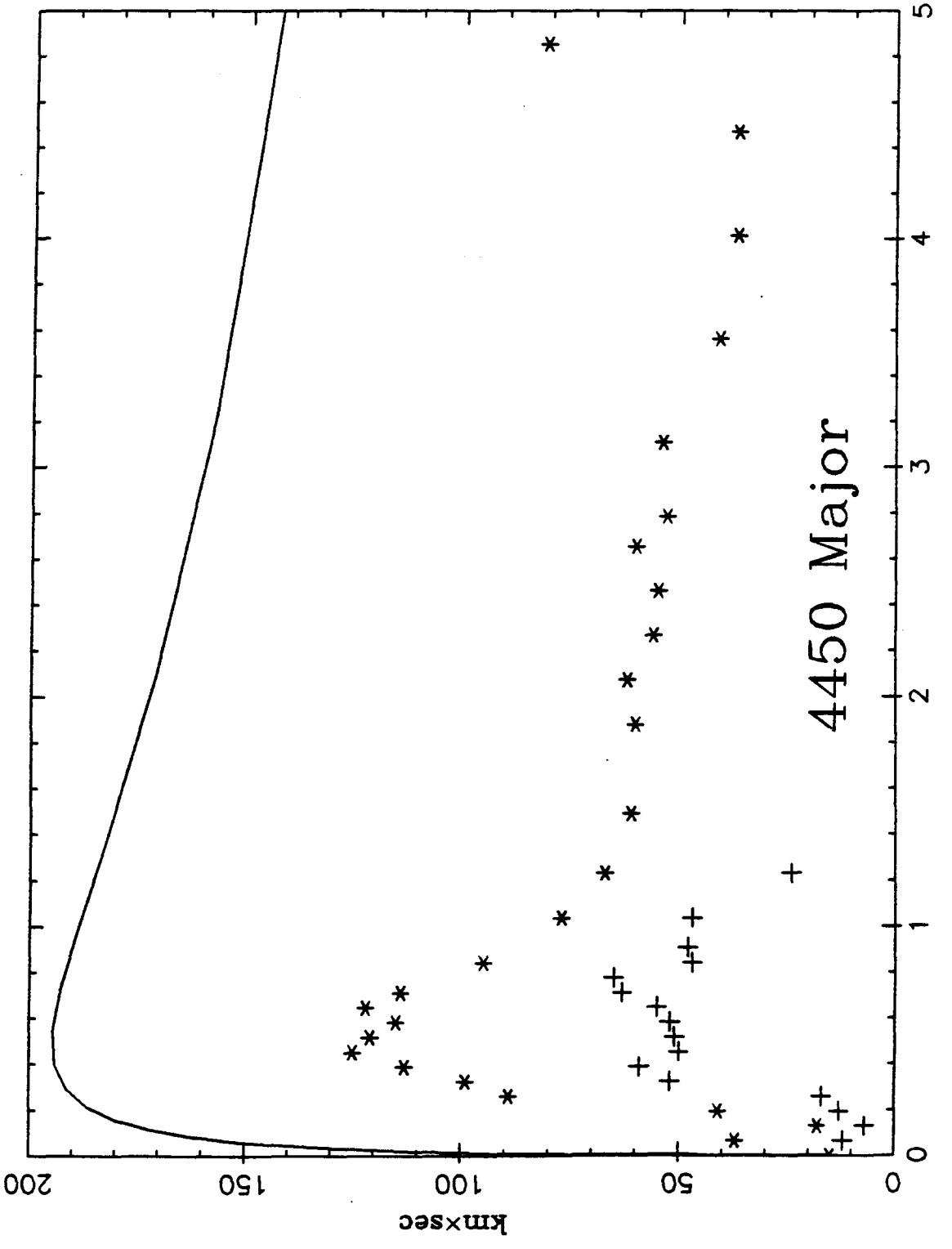

Fig. 5a

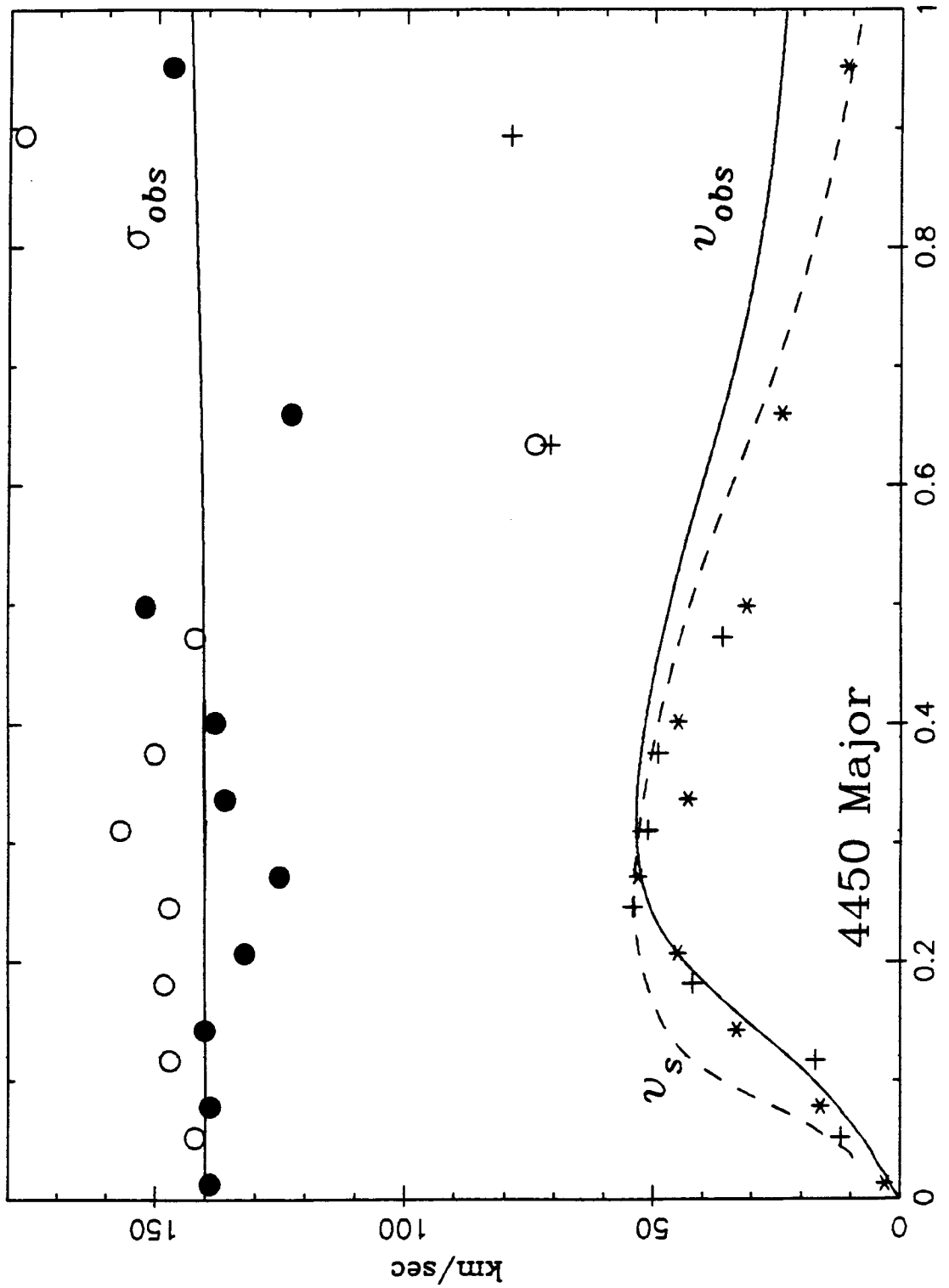
4450 Major
σ_{obs}
v_{obs}
v_s
km/sec
radius (kpc)
0
50
100
150
0.2
0.4
0.6
0.8
1

Fig. 5b

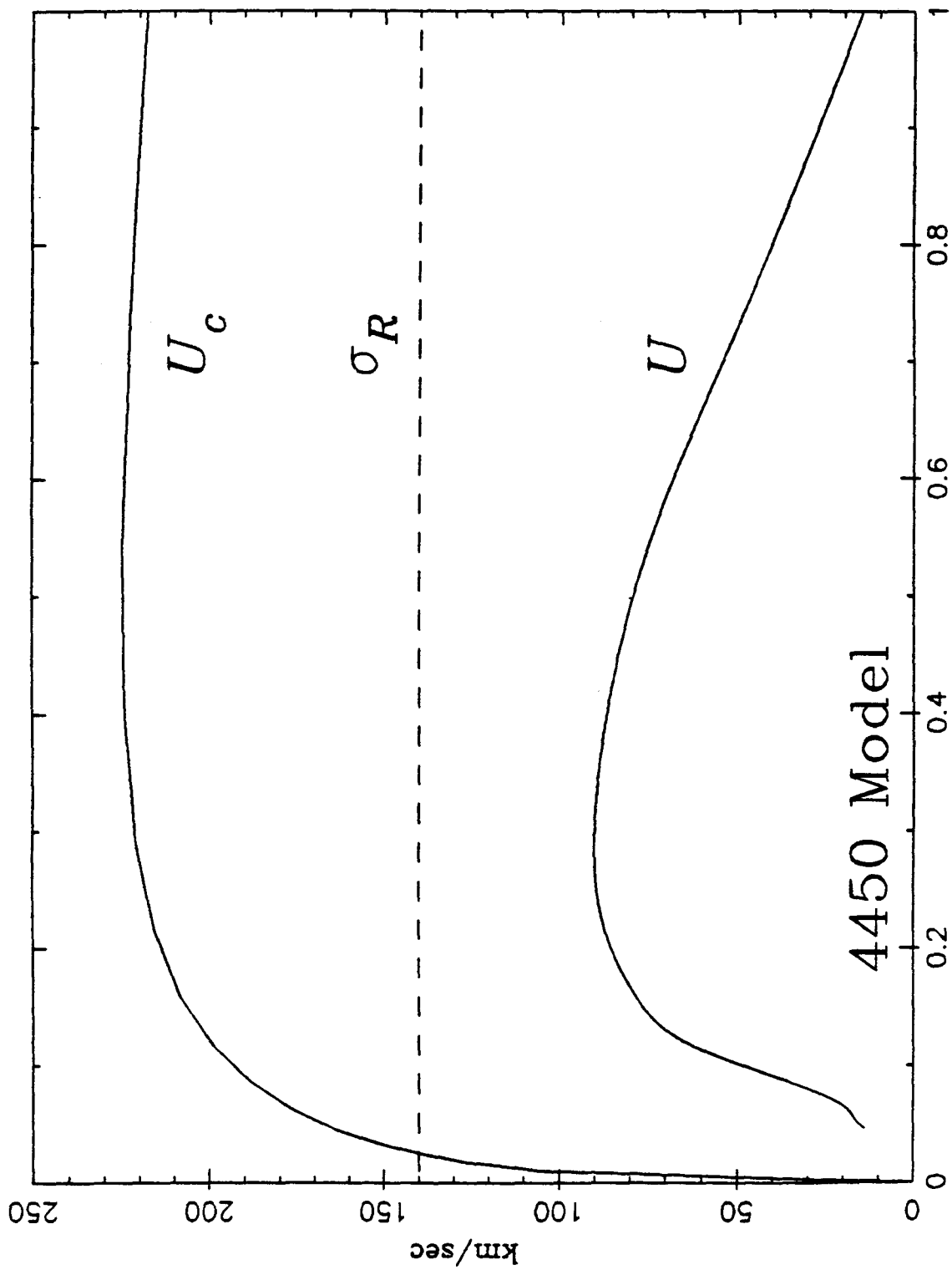
4450 Model
U_c
σ_R
U
km/sec
radius (kpc)
0
50
100
150
200
250
0.2
0.4
0.6
0.8
1

Fig. 5c

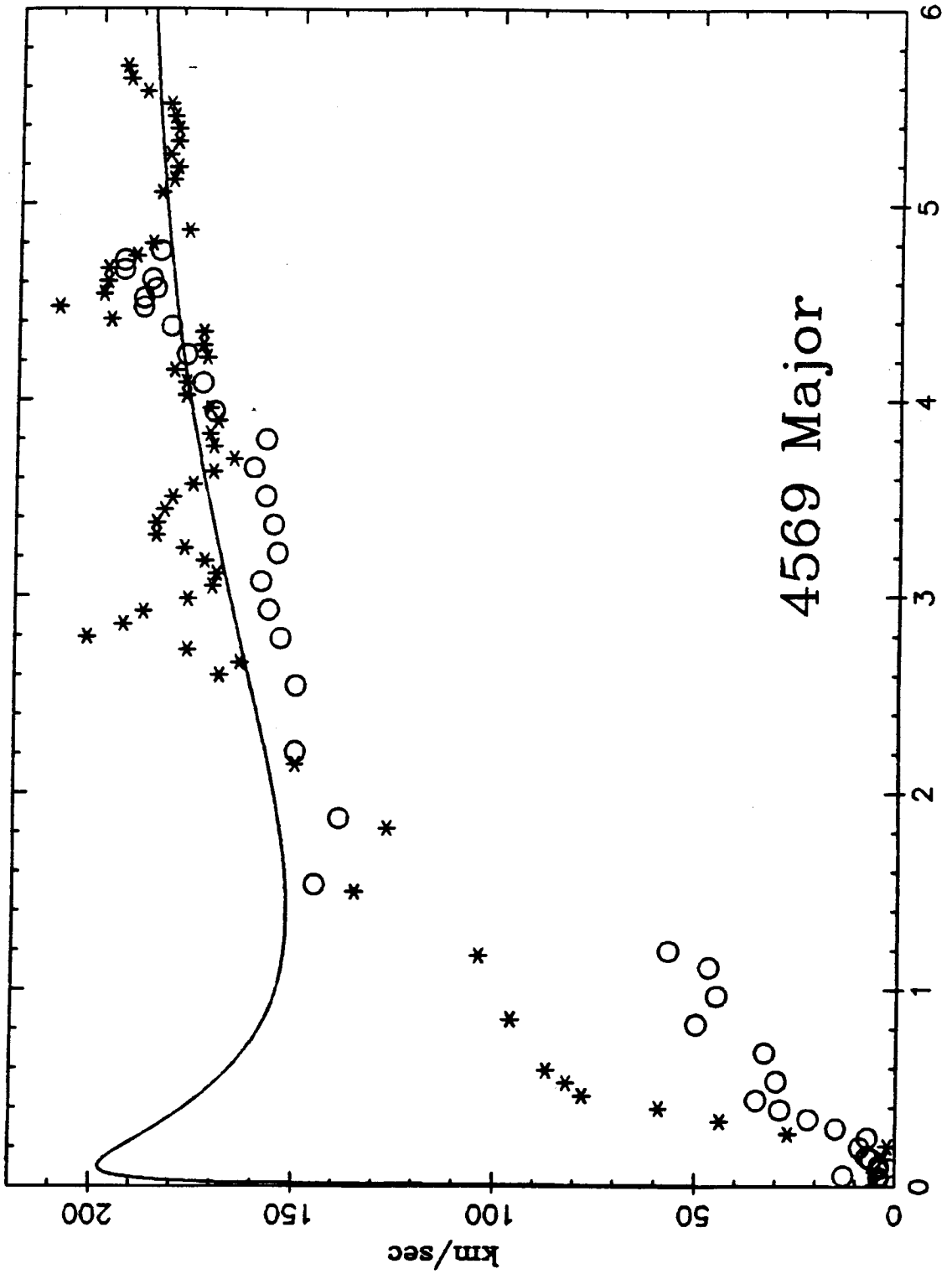

Fig. 6a

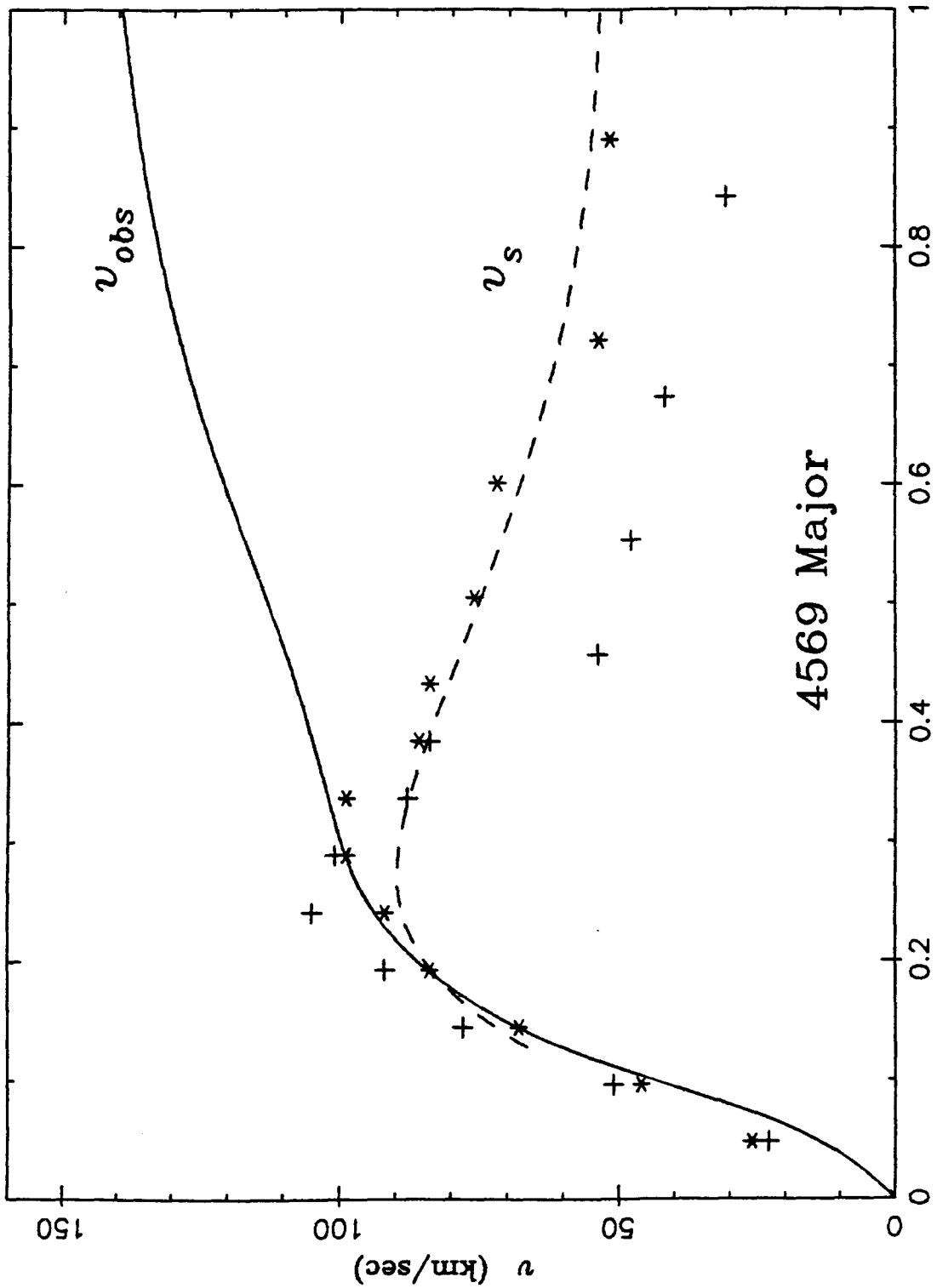

Fig. 6b

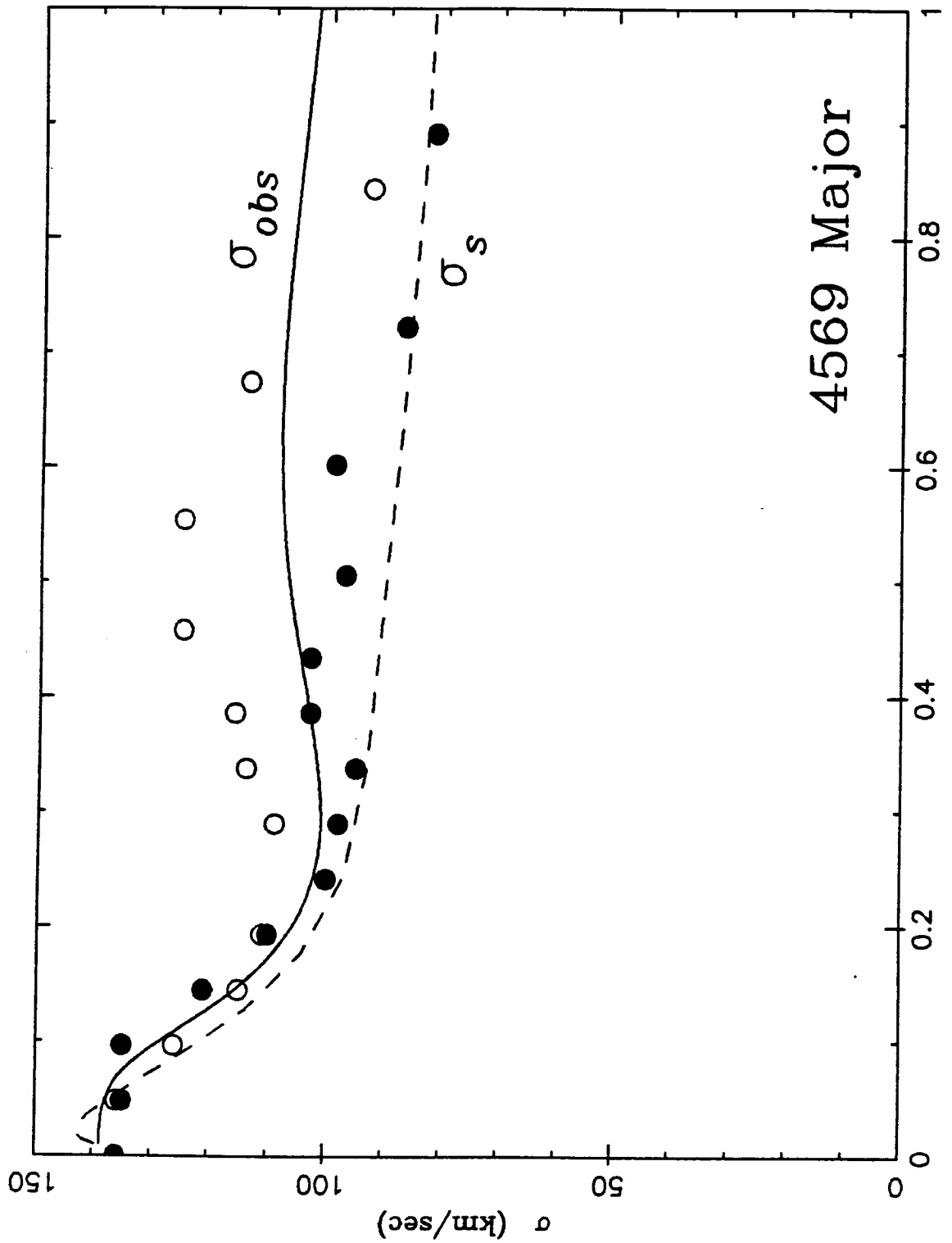
4569 Major
σ_{obs}
σ_s
σ (km/sec)
R (kpc)
0
50
100
150
0.2
0.4
0.6
0.8
1

Fig. 6c

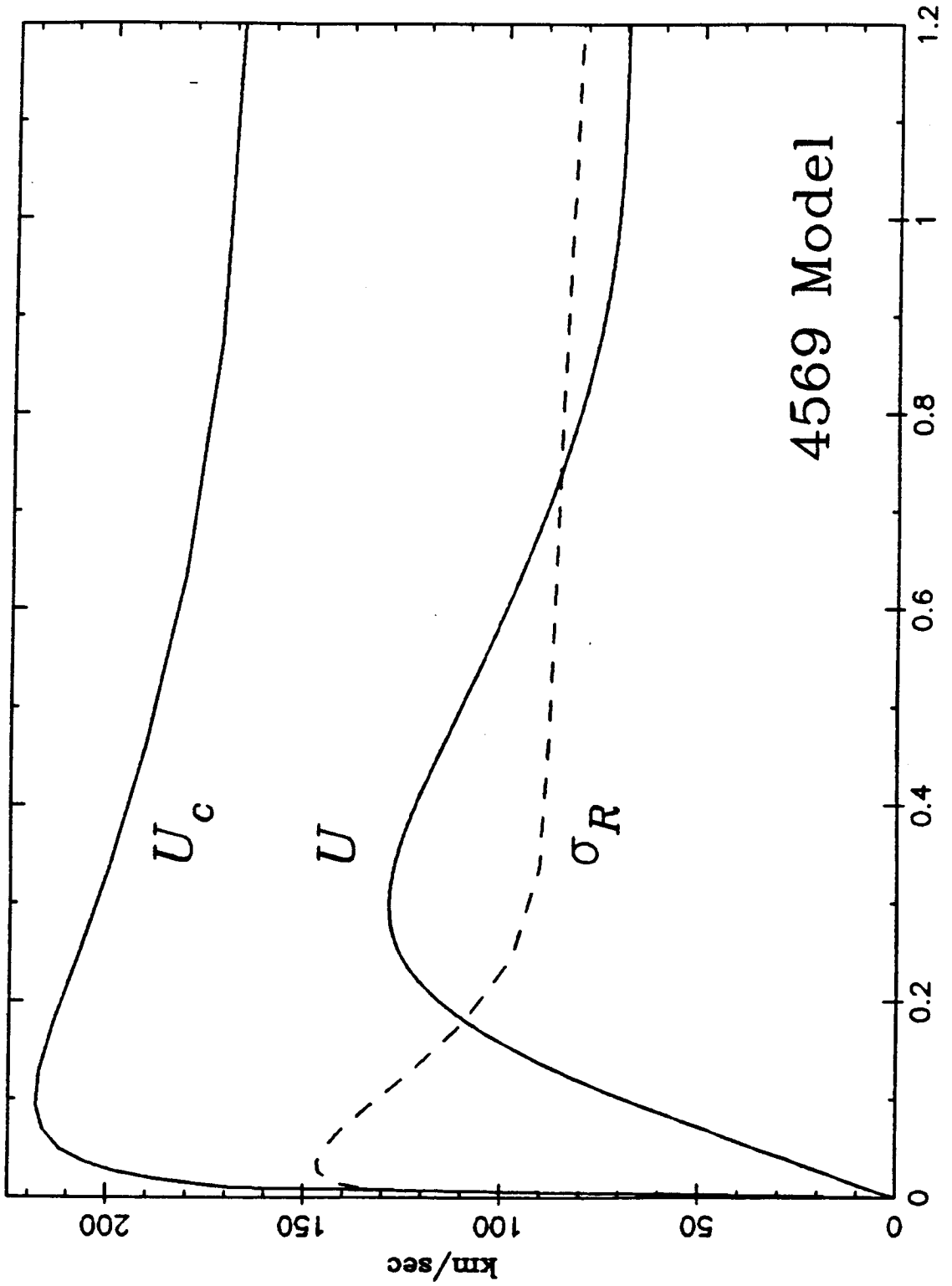
4569 Model
U_c
U
σ_R
km/sec
radius (kpc)
0
50
100
150
200
0.2
0.4
0.6
0.8
1
1.2

Fig. 6d

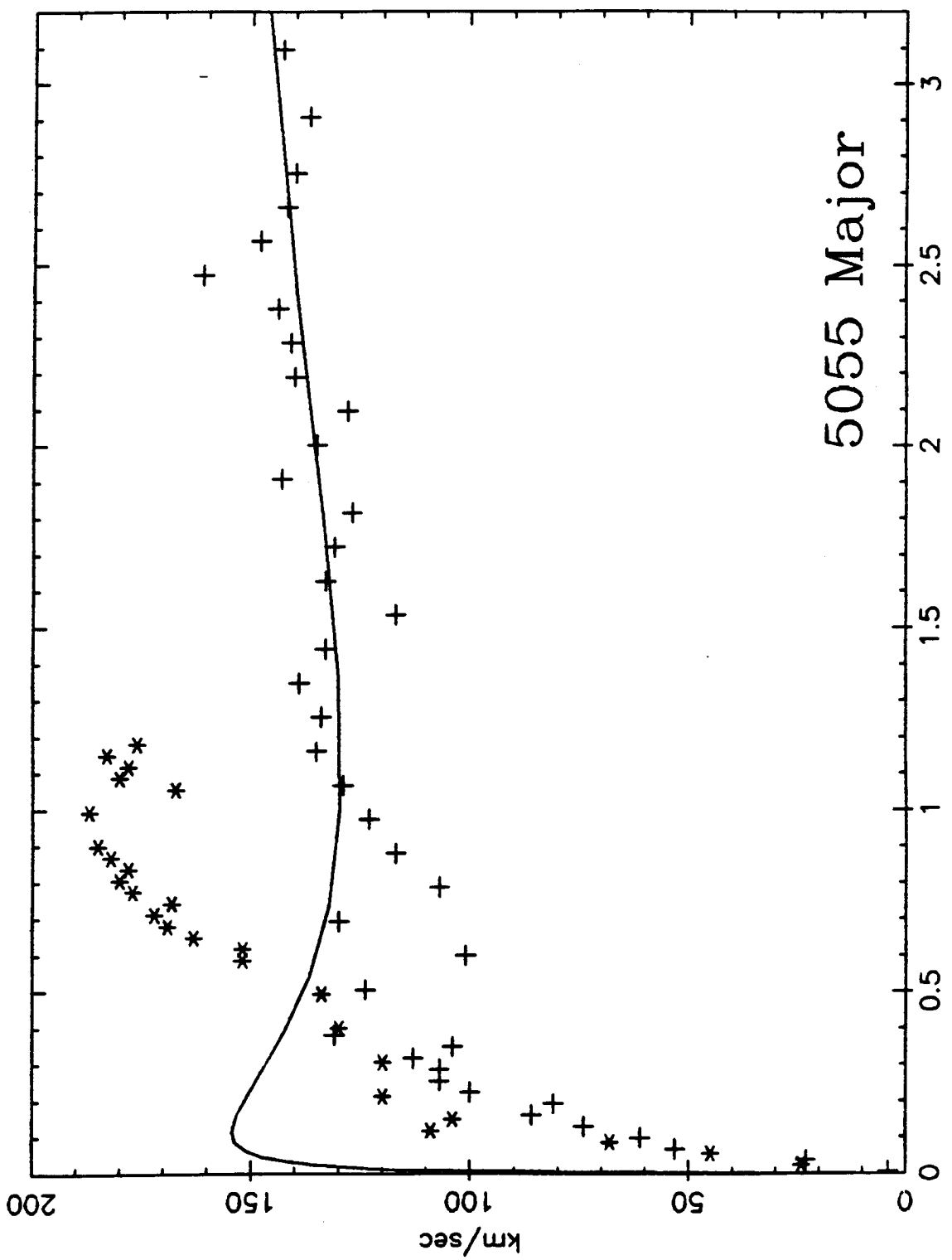

Fig. 7a

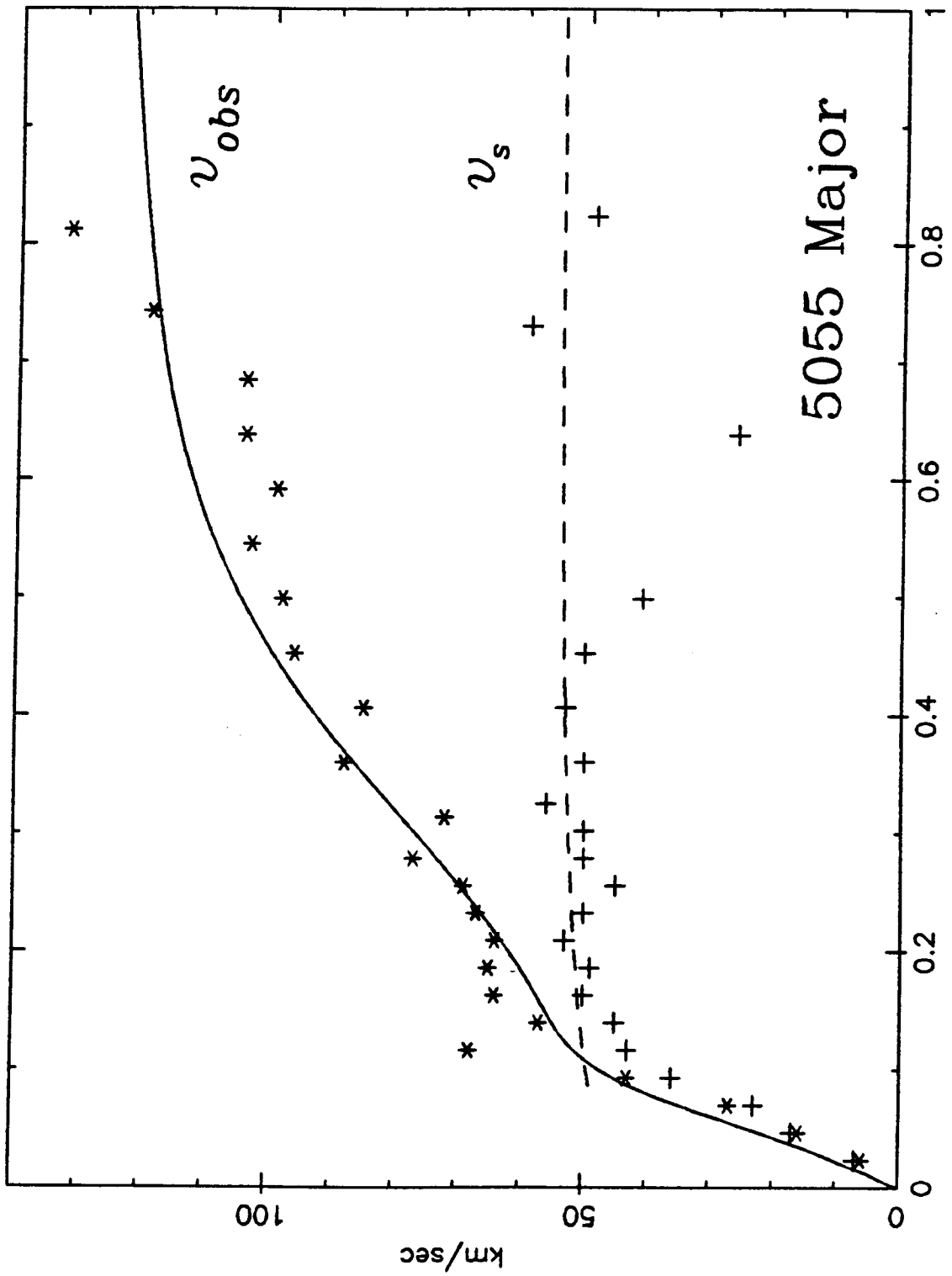

Fig. 7b

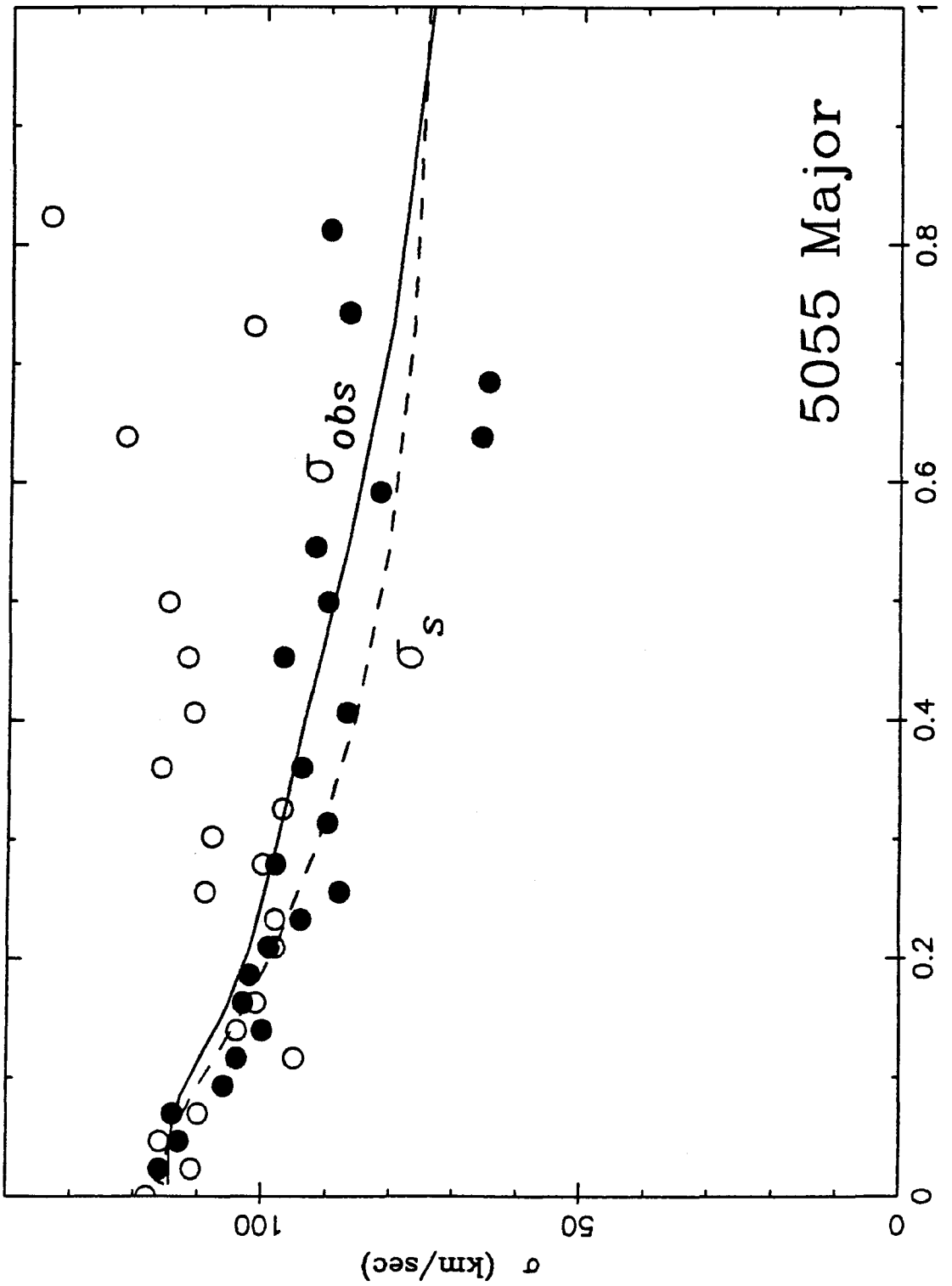

Fig. 7c

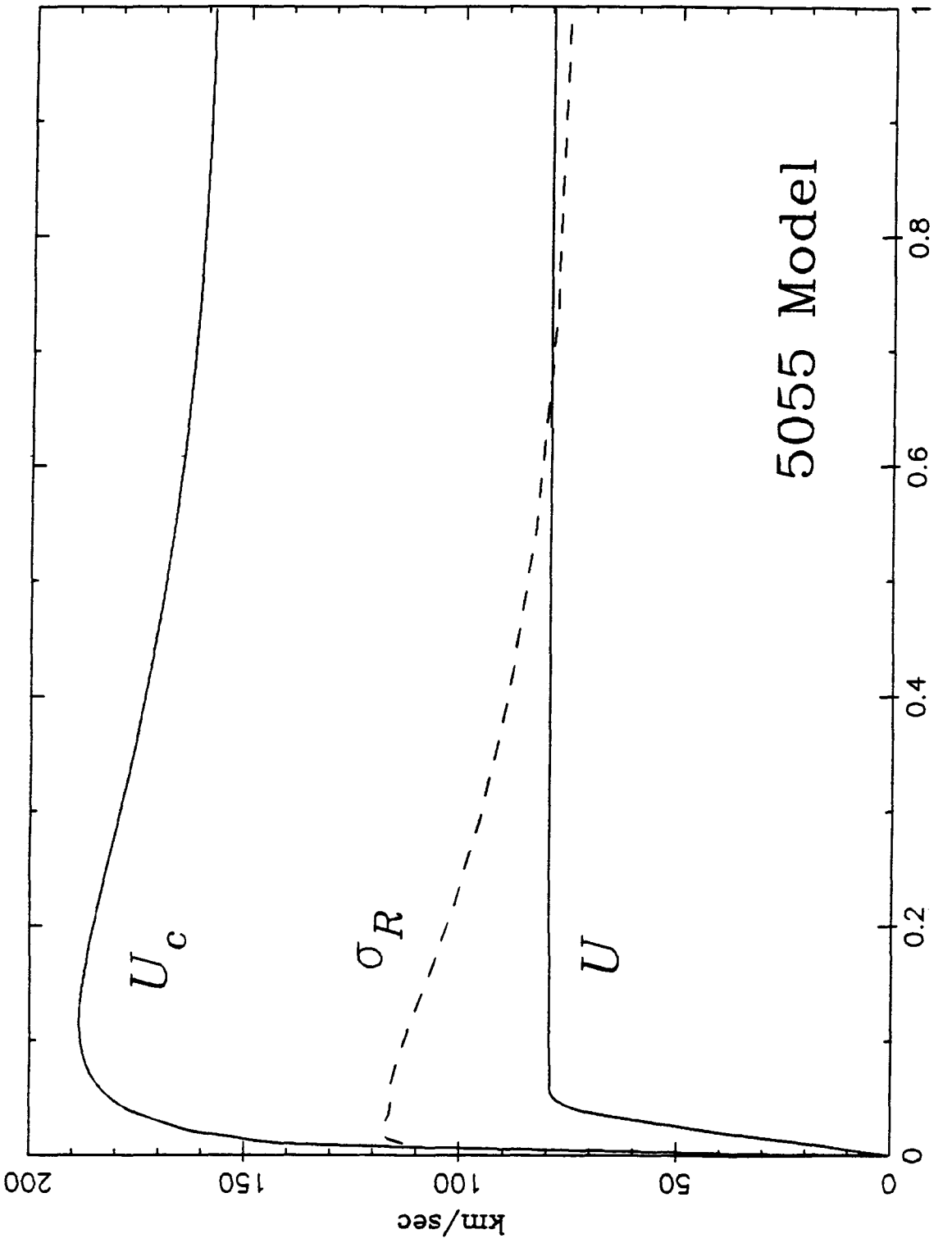
5055 Model
U_c
σ_R
U
km/sec
radius (kpc)
0
50
100
150
200
0.2
0.4
0.6
0.8
1

Fig. 7d

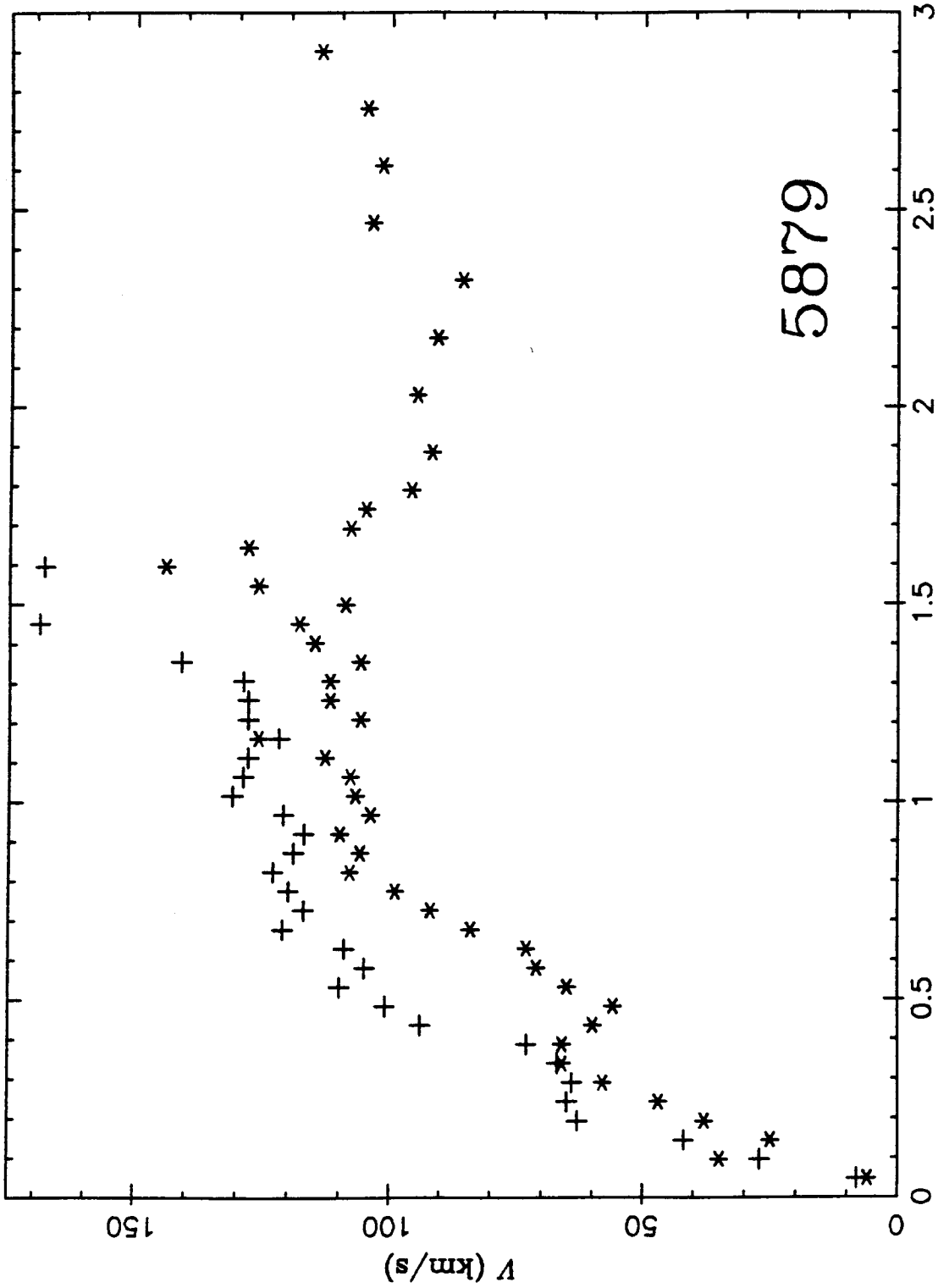

Fig. 8a

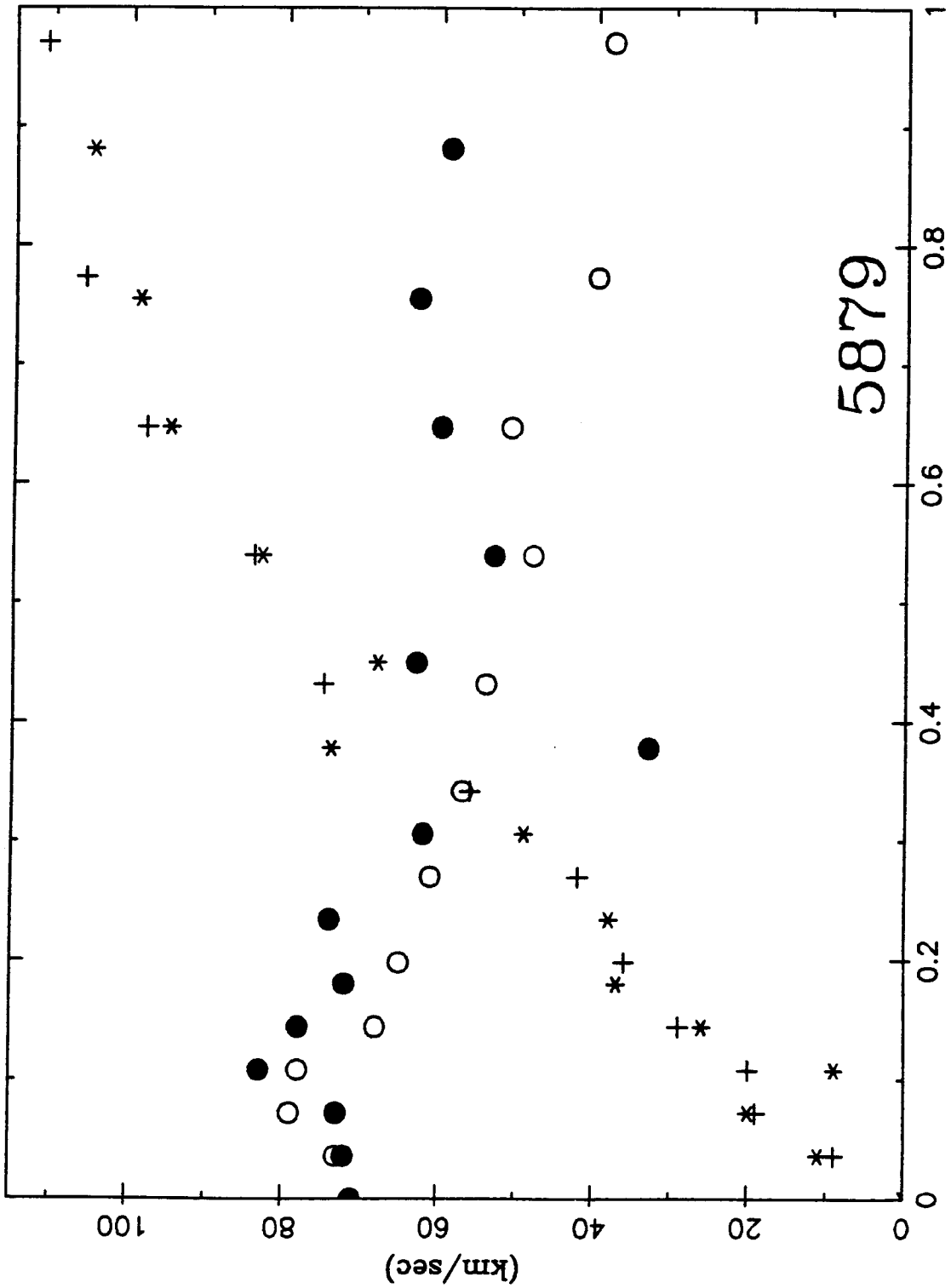

Fig. 8b

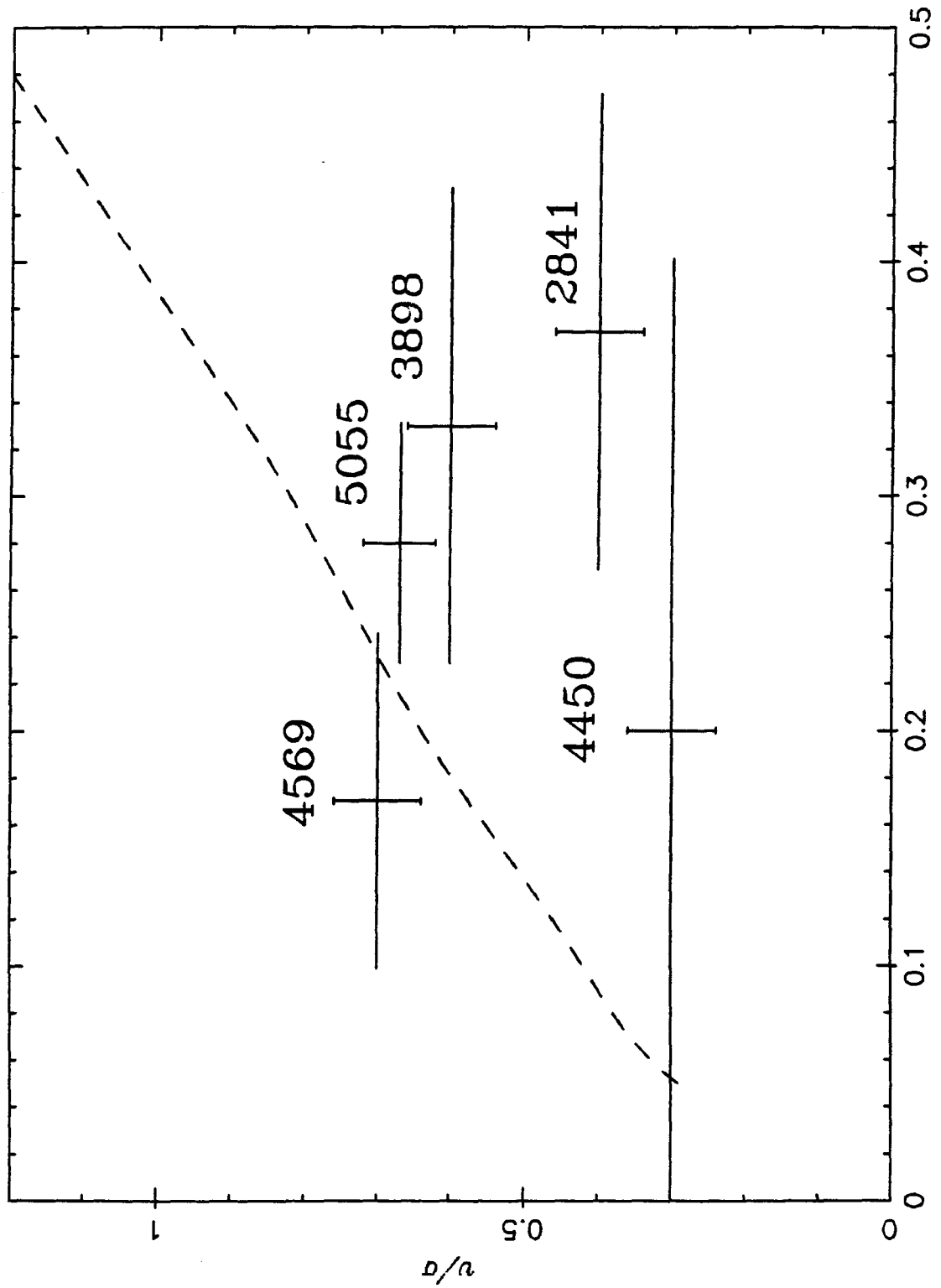

Fig. 9

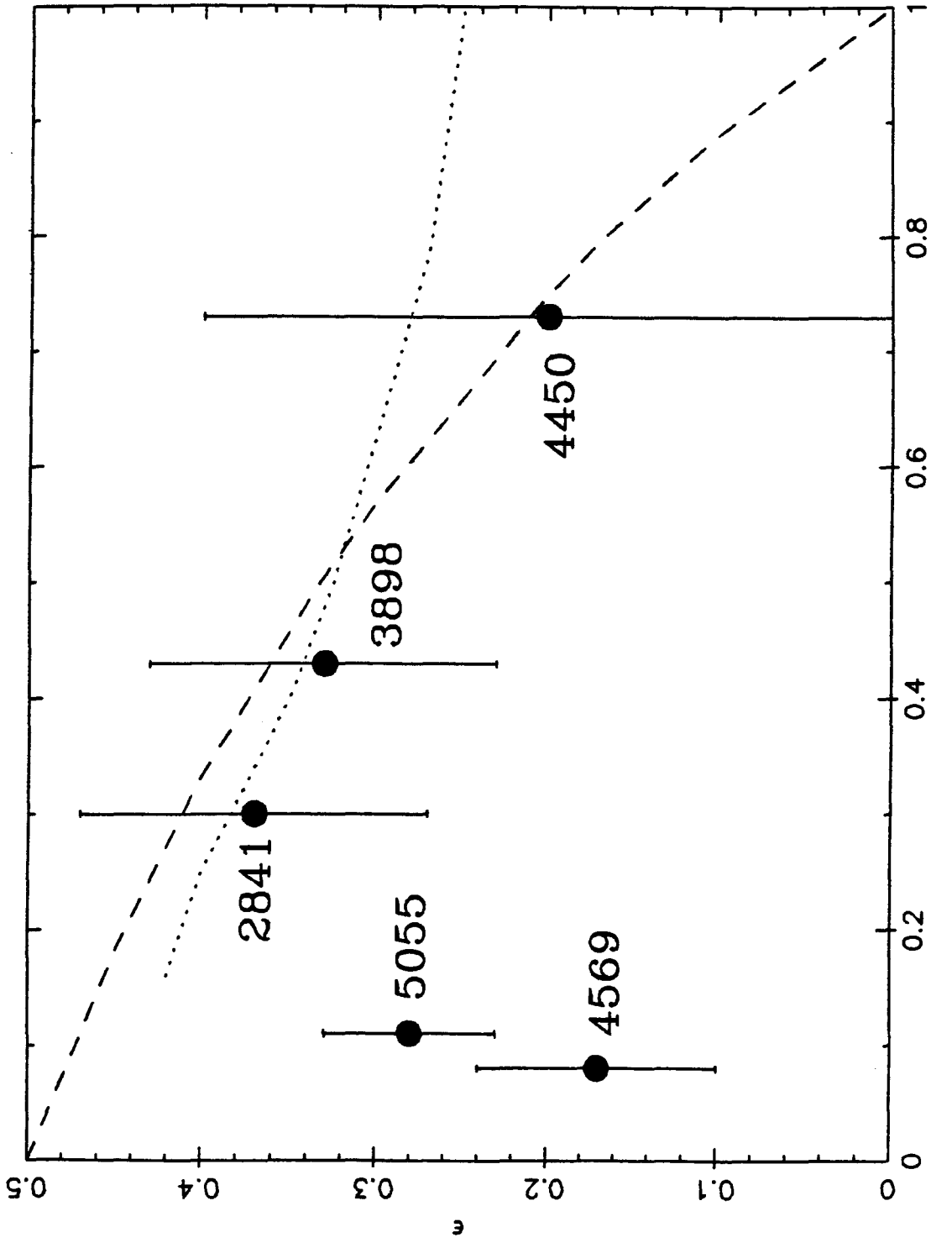

Fig. 10

Chapter Four
OBSERVABLE PROPERTIES OF OBLATE SPHEROIDS

I. INTRODUCTION

Most recent papers on galaxy dynamics have concentrated on simple parameter analyses such as $\bar{v}/\bar{\sigma}$ versus ellipticity or luminosity versus σ^n. Although these studies are important, no one claims that one or two parameters give a definitive kinematic description of a galaxy or yield sufficient information about its formation. Details which are not resolved are the form of anisotropies and variations in mass-to-light ratios. A better understanding of these issues will place additional kinematic restrictions on formation theories.

For example, most formation scenerios predict that galaxian exteriors are dominated by radial orbits. Numerical simulations by van Albada (1982) and McGlynn (1984) yield roughly isotropic residual motions inside one (deVaucouleurs') effective radius, but outside this point the velocity ellipsoid becomes radial and decreases in amplitude. Despite limited spatial coverage ($\leq 1R_e$), existing velocity data for ellipticals suggest that either tangential velocity dispersions or M/L ratios increase with radius (Illingworth 1981).

Naturally, extra work is required to gain more information. First, much more observational data are required. Second, more complete models that distinguish among various configurations or formation paths must be constructed. Third, enlarged statistical techniques must be used to test whether the data are consistent with one or another model. Extensive observations seem slow in coming; perhaps they have not been properly urged on by theoretical work.

At this time, a definitive method of analysis of observational data has been enumerated only for spherically symmetric systems. Assuming a constant but unknown M/L, Binney and Mamon (1982) and Tonry (1983) have shown that surface brightness and line-of-sight velocity dispersion measurements can formally be inverted to yield a unique anisotropy parameter $\beta(r) = 1 - \sigma_t^2/2\sigma_r^2$ (although it is not guaranteed to be physical). Newton and Binney (1984) developed an iterative procedure to construct a distribution function consistent with these kinematic functions. Richstone and Tremaine (1984, 1985) presented a method to incorporate observational constraints in constructing models via linear programming techniques. So far these techniques have been applied only to M87.

Non-spherical axisymmetric systems have an additional free function which is the orientation of the velocity ellipsoid in the $R-z$ plane. Another complication is that the velocities are functions of two variables rather than one. Since formal inversion of the observations is not possible without assuming additional constraints, the goal of this paper is to develop diagnostics which will yield at least a qualitative understanding of the kinematic configurations of oblate systems. As a working hypothesis, I assume that ellipticals and bulges are oblate spheroids; it is not known if or how many of these systems are triaxial.

The construction of self-consistent oblate models and their projection onto the plane of the sky are described in §II. Various kinematic configurations are explored in §III, and their observable properties are discussed in §III*c*. Comparison of the models with observational data is presented in §IV. The results are summarized in §V. The asymptotic power law density profile for systems composed purely of radial orbits is included in the Appendix.

II. MODELS

The models are single component oblate spheroids with constant eccentricity and mass-to-light ratio M/L. Because the models are axisymmetric, I adopt a cylindrical-polar system (R, z, ϕ) of spatial coordinates in the galaxy. The spheroidal coordinate ξ is constant along equidensity surfaces, and specified by

$$\xi^2 = R^2 + f^2 z^2, \tag{1}$$

where f is the flattening parameter, related to the ellipticity ε by $f = (1-\varepsilon)^{-1}$. The Cartesian system aligned with the projected principle axes of the galaxy in the plane of the sky is denoted (p, q). The variable s is distance along the line-of-sight, where $s = 0$ is the plane passing through the galaxy center. The inclination of the galaxy is i; for edge-on $i = 0$. These two sets of coordinates are related by:

$$R^2 = p^2 + [s\cos i - q\sin i]^2, \tag{2}$$

$$z = s\sin i + q\cos i, \tag{3}$$

and,

$$\xi^2 = \xi_0 + s\xi_1 + s^2\xi_2, \tag{4}$$

where,

$$\xi_0 = p^2 + q^2\left[\sin^2 i + f^2\cos^2 i\right],$$
$$\xi_1 = 2q\sin i\cos i\left[f^2 - 1\right], \tag{5}$$
$$\xi_2 = f^2\sin^2 i + \cos^2 i.$$

For an observation point (p, q), minimum ξ occurs at

$$\xi_m^2 = \xi_0 - \frac{\xi_1^2}{4\xi_2} = p^2 + \frac{q^2}{\sin^2 i + f^{-2}\cos^2 i}. \tag{6}$$

Observations of ellipticals (Kormendy 1977) and bulges of disk systems (Burstein 1979; Boroson 1981) have shown that their surface brightness profiles are acceptably represented by a deVaucouleurs' law (1948), which in magnitudes is

$$\mu^m(p) = \mu_e^m + 8.325[(p/R_e)^{1/4} - 1], \tag{7}$$

where R_e is the effective radius and μ_e^m is the surface brightness at R_e, measured along the major axis. The density distribution is specified by a deprojected $r^{1/4}$ law taken from approximate formulae derived by Young (1976) and Tonry (1984*b*). Young presented a dimensionless density function ρ^* which was calculated for a spherically symmetric distribution; this function is adopted as the density distribution applied to an oblate configuration. The density on a spheroidal surface ξ is

$$\rho(\xi) = fM_T R_e^{-3}\rho^*(\xi/R_e), \tag{8}$$

where M_T is the total mass. The form of ρ^* is illustrated in Figure 1.

External galaxies are, of course, only seen in the plane of the sky, so we must calculate how these models appear in projection in order to compare them with observations. A subscript s will be used on some variables to denote integration along s.

The surface brightness is

$$\mu_L(p,q) = \int_{-\infty}^{\infty} \rho_L(\xi)\, ds, \tag{9}$$

where ρ_L is the luminosity density $\rho(\xi)L_T/M_T$, and L_T is the total luminosity. For the case of an oblate spheroid, equation (9) becomes

$$\mu_L(p,q) = \frac{2}{\xi_2^{1/2}} \int_{\xi_m}^{\infty} \frac{\rho_L(\xi)\xi\, d\xi}{[\xi^2 - \xi_m^2]^{1/2}}. \tag{10}$$

Because μ_L is a function only of $\xi_m(p,q)$, the isophotes are elliptical (see equation [6]).

The projected mean rotation is computed from the intrinsic mean rotation u by

$$v_s(p,q) = \mu_L^{-1} \int_{-\infty}^{\infty} \rho_L\, u(R,z) \frac{p\cos i}{R}\, ds. \tag{11}$$

I define an apparent angular velocity by the quantity

$$\Omega_s(p,q) = \frac{v_s(p,q)}{p}. \tag{12}$$

The expression on the right-hand side can be put into a more revealing form by the following steps. From equation (4) and (6), we find that

$$s = \frac{-\xi_1}{2\xi_2} \pm \frac{[\xi^2 - \xi_m^2]^{1/2}}{\xi_2^{1/2}}. \tag{13}$$

The value of s at ξ_m is $s_m = -\xi_1/2\xi_2$. For a given (p,q), each $\xi > \xi_m$ corresponds to two points within the galaxy which I denote by $\mathbf{r}_+$ and $\mathbf{r}_-$ for $s \geq s_m$ and $s < s_m$, respectively. Thus,

$$\Omega_s(p,q) = \frac{\cos i}{\xi_2^{1/2}\mu_L} \int_{\xi_m}^{\infty} \rho_L[\Omega(\mathbf{r}_+) + \Omega(\mathbf{r}_-)] \frac{\xi\, d\xi}{[\xi^2 - \xi_m^2]^{1/2}}, \tag{14}$$

where Ω is the intrinsic mean angular velocity u/R. If Ω is constant along spheroidal surfaces (a function of ξ only), then Ω_s is constant along isophotes (a function only of ξ_m).

The projected velocity dispersion is

$$\sigma_s^2(p,q) = \mu_L^{-1} \int_{-\infty}^{\infty} \rho_L \sigma_R^2 \left[1 - \beta \frac{p^2 \cos^2 i}{R^2} - \beta_z \sin^2 i\right] ds, \tag{15}$$

where β and β_z are anisotropy parameters, $\beta = 1 - \sigma_\phi^2/\sigma_R^2$, and $\beta_z = 1 - \sigma_z^2/\sigma_R^2$.

III. KINEMATIC CONFIGURATIONS

The gravitational potential Φ of the system is computed from the density distribution through Poisson's equation. The kinematic structure is determined by simultaneous solution of the hydrostatic equations:

$$\frac{\partial \rho \sigma_z^2}{\partial z} + \frac{\partial(\rho \overline{v_R v_z} R)}{R\,\partial R} = -\rho \frac{\partial \Phi}{\partial z}, \tag{16}$$

and

$$u^2 + \sigma_\phi^2 = R \frac{\partial \Phi}{\partial R} + \sigma_R^2 + \frac{R}{\rho}\left[\frac{\partial(\rho \overline{v_R v_z})}{\partial z} + \frac{\partial \rho \sigma_R^2}{\partial R}\right], \tag{17}$$

where u is the mean rotation rate. Because the models are axisymmetric, one of the principal axes of the velocity dispersion tensor points in the ϕ-direction. The remaining two axes lie in the $R - z$ plane; the orientation of the the larger moment relative to the positive R-axis is termed the tilt of the velocity ellipsoid (a radial vector in the positive $R - z$ quadrant has positive tilt). Equations (17) and (16) are coupled by the off-diagonal term in the dispersion tensor. Because of symmetry requirements, $\overline{v_R v_z}$ is zero along the coordinate axes.

The results of the calculations will be discussed in three stages. First, solutions in which the velocity ellipsoid is restricted to be aligned with the coordinate axes (termed *axially aligned*) are presented. Next, solutions with radially aligned ellipsoids will be discussed. In §IIIc, distinguishing observable properties of the various configurations are illustrated.

a) Axially Aligned Velocity Ellipsoids

Assuming that the principal axes of the velocity dispersion tensor are aligned with the coordinate axes, equations (16) and (17) decouple and may be solved

independently. In particular, σ_z is uniquely constrained by the mass model, leaving σ_R, σ_ϕ, and u as inter-related functions to satisfy equation (17). Besides their computational convenience, systems with axially aligned ellipsoids are investigated because there is evidence that some systems have may this form (Ratnatunga and Freeman 1985; Richstone 1984). As a starting point for each mass model, isotropic configurations ($\sigma_R = \sigma_\phi = \sigma_z$) are calculated; the magnitude of the dispersion is computed from equation (16), and the rotation curve via equation (17). The isotropic configurations are labeled model 1, and illustrated in Figures 2-4 for (*a*) $\epsilon = 0.1$ and (*b*) $\epsilon = 0.5$. For isotropic distributions, contours of constant velocity dispersion are prolate (see Figure 2) and the constant angular velocity contours are oblate but rounder than the equidensity surfaces (see Figure 4).

Three configurations with no mean rotation are computed; this series is called model 2. These configurations result from the following restrictions: (2A) leaving $\sigma_R = \sigma_z$, and removing all rotational streaming from model 1 by increasing σ_ϕ; (2B) maintaining $\sigma_R = \sigma_\phi$ and raising their value until $u = 0$; (2C) minimizing σ_ϕ and attaining as much support as possible from the radial dispersion. The motivation for each of these choices will be discussed presently.

The model 2 series, which all have $u = 0$, are investigated because some bulges and, in general, large ellipticals have dynamically insignificant rotation. Since σ_z is determined by equation (16), only σ_R and σ_ϕ may be varied in constructing different configurations. One obvious choice is to remove all net rotation from model 1 by reflecting half of the orbits. This change leaves σ_R=σ_z but increases σ_ϕ; the results for σ_ϕ are shown in Figure 5.

Another simple configuration maintains σ_ϕ=σ_R, but increases their value at each point relative to model 1 until $u = 0$. Because of the pressure gradient term, the effective coefficient for ${\sigma_R}^2$ in equation (17) is typically 2-4, while the ${\sigma_\phi}^2$-term has a coefficient of unity; thus the radial dispersion is much more "effective" than the tangential dispersion in generating support. Complete removal of all net rotation from model 1 increases σ_R (and σ_ϕ) by only 65% in model 2B compared to an increase of 277% for σ_ϕ in model 2A. Figure 6 displays contours of constant σ_R for model 2B.

Finally, I consider the case where σ_R is maximized. Because symmetry requires σ_ϕ=σ_R along the minor axis (except at $z = 0$), σ_ϕ cannot be set to zero. Instead, σ_ϕ is reduced smoothly and rapidly as R increases. Figures 7 and 8 illustrate σ_R and σ_ϕ for model 2C. Anisotropy between σ_R and σ_z is not greater than 2:1 for $\varepsilon = 0.5$ and is less for smaller ε.

b) Radially Aligned Velocity Ellipsoids

Before the recent evidence sighted above, the common expectation was that velocity ellipsoids were radially aligned. In a spherically symmetric system this is clearly the case. In general, the ellipsoid tilt is a free function, but the largest contrast with the previous section should be obtained for radially aligned ellipsoids, so some configurations of this type have been computed.

Models 4 and 5 have the major axis of the velocity ellipsoid pointed towards the center of the system, and a maximum axial ratio of 2:1. In model 4 the axial ratio is unity in the interior and smoothly approaches 2:1 at large radius, whereas model 5 has a 2:1 ratio everywhere. Since the elongation and tilt of the ellipsoid are specified, the amplitude is determined by iteratively solving equation (16) until a self-consistent solution is found. The tangential second moment $(u^2 + \sigma_\phi{}^2)$ is determined from equation (17); there is no relation between u and σ_ϕ. Models 4A and 5A set σ_ϕ equal to the smaller of σ_R and σ_z and contain some net rotation; Models 4B and 5B set $u = 0$ and maximize σ_ϕ. Results from model 5A are displayed in Figures 9 and 10. More elongated ellipsoids have not been calculated for two reasons. First, deVaucouleurs' law can not be reproduced by a system of entirely radial orbits (Richstone and Tremaine 1984; Appendix). Second, systems composed of purely radial orbits are subject to both radial and transverse instabilities which produce triaxial systems (Barnes, Goodman, and Hut 1985).

Since the vertical velocity dispersion is not uniquely determined, σ_R and σ_z compete to support the specified shape. In particular, increased support at $R > z$ can come from σ_R rather than σ_z. However, I don't expect the total velocity dispersion to vary greatly because the virial theorem requires that the total kinetic energy in the system depend only on the total gravitational potential energy. Thus, in a case where the rotation is energetically insignificant, the total kinetic energy

of random motions is the same no matter which component is maximized.

c) Observable Properties

Although the profiles shown in the subsequent graphs do not include effects from atmospheric seeing and instrument aperture, these effects must be kept in mind when considering the observable differences between various configurations. Observationally studied bulges typically have R_e in the range 10-20 arcseconds, whereas R_e for ellipticals is 20-70 arcseconds; regions inside $\sim 0.1R_e$ are typically blurred by seeing.

Figures 11-15 display one quadrant of each model projected edge-on ($i = 0$) onto the plane of the sky for $(a)\,\varepsilon = 0.1$ and $(b)\,\varepsilon = 0.5$. Dotted lines represent isophotes, and solid lines show contours of constant projected velocity dispersion. In face-on projections these contours would be circular since the models are rotationally symmetric.

The isotropic configuration is shown in Figure 11. Velocity dispersion contours are slightly prolate; in the $\varepsilon = 0.5$ case the contours are elongated in the z-direction by 17%.

In some cases the different anisotropic configurations have quite distinct observable properties. Because σ_ϕ contributes much more strongly to the projected dispersion along the major axis than σ_R does, the models with σ_ϕ maximized will show much larger dispersions than those with σ_R maximized (when $i \sim 0$). Models with maximum σ_ϕ tend to display constant σ_s contours that are more flattened than the isophotes, whereas radially maximized models show rounder or even prolate σ_s contours.

Rather than requiring data from the entire plane of the sky around a galaxy, a more observationally feasible program is to acquire data along the major and minor axis. Figure 16 presents various projected velocity dispersion profiles along the major axis for $\varepsilon = 0.5$ models of the same mass. Although the differences between model 2A and 2C relative to the isotropic configuration are quite apparent, model 5 is not easily distinguished from model 2C if the mass of either model is adjusted to move one profile on top of the other. At high inclinations the different configurations appear very similar to each other, as illustrated in Figure 16*b*. Because σ_z is the

same in models 1 and 2, their face-on views are the same. Model 5 is distinguished only by its strong central rise in σ_s.

High spatial resolution velocity measurements may be able to determine the presence of anisotropy in the central regions. An isotropic system which follows a deVaucouleurs' density law has a central depression in its velocity dispersion which should be observable (Binney 1980). Systems with radially oriented velocity ellipsoids (e.g., model 5) do not have a central depression in the dispersion. Figure 17 compares the projected velocity dispersion for the isotropic case and models 4A and 5A. Even configurations with an isotropic core but radially biased exteriors (e.g., model 4) may not have an observable central depression. An increase in M/L at small radii also increases the velocity dispersion, so the cause of an observed rise would be ambiguous.

Measurements along different lines-of-sight through a galaxy permit the relative strengths of the velocity dispersion components to be measured. Comparing the projected velocity dispersions measured at some fiducial distance along the major and minor axes relative to the center (or peak) value relates the strengths of the different components. In other words, comparing the large-scale gradient along the minor axis relative to that along the major axis roughly compares σ_R to σ_z (minor axis) and σ_R to σ_ϕ (major axis); The locations of the various $\varepsilon = 0.5$ configurations projected edge-on in this plane using fiducial radii of $1.2R_e$ and $2.1R_e$ are marked in Figures 18*a* and 18*b*. The isotropic configuration is located in the upper center of each diagram. For configurations in which more energy is put into the tangential component, higher σ_s values are observed along the major axis, and the representative point moves to the right. For larger σ_R (cylindrical R) configurations (relative to model 1) the representative point moves leftward and up. If more energy is put into (spherical) radial motions, the ratios decrease.

Since few galaxies are viewed edge-on, the appearance of the kinematic profiles at different inclinations must be considered. In particular, only the apparent axial ratio is known for ellipticals; it supplies a lower limit to the true flattening. Figures 18*c* and 18*d* display the locations in the $\sigma_m - \sigma_M$ plane of many different configurations and true axial ratios ($\varepsilon = 0.1$, 0.3, and 0.5), each viewed at an

inclination such that it appears as an E1. Galaxies observed at high inclination display less differentiation among the various configurations. ***Thus I conclude that many kinematically distinct configurations are observationally indistinguishable.*** Observations can uniquely characterize only those galaxies which lie at certain kinematic extremes.

IV. COMPARISON WITH OBSERVATIONS

Projected profiles for various configurations can be compared with the observed profiles from Chapter 3. Note that I am not presenting fits to the observations; rather, the different model extremes are compared to a sub-sample of the observations to aid qualitative understanding.

Because the spirals discussed here are nearly edge-on, the projected profiles are computed from an edge-on point of view. The rotation velocities have been corrected for the galaxies' inclinations. In the discussion which follows, I denote the square root of the ratio of the total rotational kinetic energy to the total random kinetic energy by $\bar{v}/\bar{\sigma}$.

a) NGC 2841

An $\epsilon = 0.4$ model is displayed with observed profiles from NGC2841 (an Sb with $\epsilon = 0.37$) in Figure 19. First note that for the isotropic model the rotation curve lies well above the observed curve, and the projected velocity dispersion lies below the observed points. This disparity is expected since $\bar{v}/\bar{\sigma}$ for NGC2841 is below that of an isotropic rotator of the observed ellipticity. As an extreme comparison, the dispersion profiles for configurations with no rotation are also presented. The profiles are labeled σ_A and σ_C for maximized σ_ϕ and maximized σ_R, respectively. A radially biased model does not fit the observed points; σ_C decreases too fast. Configurations with more tangential dispersion fit the slow decrease in the observed dispersion better.

b) NGC 3898

An $\epsilon = 0.3$ model compared with NGC3898 data (an Sb with $\epsilon = 0.33$) is shown in Figure 20. As shown in Chapter 3, the isotropic model rotates faster than the galaxy does. The observed velocity dispersion cannot distinguish between

the different anisotropic configurations because of its limited radial coverage and the lack of symmetry in the outer few points. However, if the steep decline in the observed dispersion profile is real, a radially biased configuration is needed; if not, the tangentially optimized configuration fits the outer points better.

c) NGC 4569

NGC4569 is the only bulge from Chapter 3 for which the observed $\bar{v}/\bar{\sigma}$ falls above the isotropic $\bar{v}/\bar{\sigma}$ versus ϵ curve. Although its observed ellipticity is only $\epsilon \simeq 0.17 \pm 0.07$, an $\epsilon = 0.3$ model is displayed with the observed profiles in Figure 21 because the observed rotation curve has a large inner peak which is consistent with an $\epsilon = 0.3$ isotropic configuration, but then drops off more steeply. The projected rotation curve and velocity dispersion for the isotropic configuration are illustrated by solid lines. Likewise, the observed velocity dispersion falls off more slowly (outside of a strong inner peak), and is consistent with the maximized tangential model at the outer points. Thus, even though the $\bar{v}/\bar{\sigma}$ value for this bulge is appropriate for its flattening, detailed comparision shows that it is not an ideal isotropic rotator.

d) Two Ellipticals

For illustration, two ellipticals with major axis data to $\sim 1R_e$ (Davies and Illingworth 1983) have been compared with these models. NGC3379 has an apparent ellipticity of 0.13 and half the rotation rate expected for its shape. If we assume that NGC3379 is an edge-on E1, then models with enhanced radial dispersion fit the observed velocity dispersion slightly better than the isotropic model, as demonstrated in Figure 22*a*. However, with only major axis data we cannot distinguish between the edge-on $\epsilon = 0.1$ model or an $\epsilon = 0.5$ model inclined 60°; see Figure 22*b*.

NGC6909's velocity dispersion is essentially constant along the major axis out to $1.1R_e$. In this case, constant mass-to-light models with radially oriented velocity ellipsoids can be ruled out in favor of tangential orbits (see Figure 22*c*). However, the possibility of an increasing mass-to-light ratio must also be considered (assuming that the luminosity density follows a deprojected deVaucouleurs' law). Systems with isotropic or radially biased orbits but an increasing M/L could also

display a constant projected velocity dispersion.

e) Apparent Angular Velocity

If a spheroid rotates with constant angular velocity on spheroidal surfaces which have the same axial ratio as the equidensity surfaces, then the apparent angular velocity as defined by equation (12) will be constant along isophotes. Figures 23*a* and 23*b* show that for isotropic configurations the contours of constant apparent angular velocity (Ω_s) are rounder than the isophotes; the ellipticity of the Ω_s-contours are typically half that of the isophotes. This is expected because the constant-Ω surfaces are rounder than the equidensity surfaces (see Figure 4). The apparent angular velocity of a body which has cylindrical rotation (u constant with z) has an strikingly different appearance. A cylindrically rotating spheroid with Keplerian rotation along the equator is shown in Figure 23*c*. The near-vertical appearance of the Ω_s-contours is not strongly dependent on the rotation law.

The contours of apparent angular velocity have been computed for NGC7814, using data from Kormendy and Illingworth (1982, hereafter KI), and for M32, using data supplied by J. Tonry. The results are displayed in Figure 24. The ellipticity (defined as the axial ratio subtracted from one) of the Ω_s-contours for M32 varies from 0.15 at 10" to 0.3 at 20"; the isophotal ellipticity is $\simeq 0.3$ at 10" but decreases further outward (Tonry 1984*a*). The ellipticity of the Ω_s-contours inside 20" for NGC7814 is ~ 0.26, and the isophotes have $\epsilon \simeq 0.47$.

The rotation data for these two galaxies are consistent with spheroidal-like rotation. Two other SA spirals, NGC 7814 and NGC 4595, have been studied by Jarvis and Freeman (1985) who found the mean rotation to be consistent with spheroidal type rotation. Little more information can be extracted from these contour maps, but it would be useful to know how many galaxies show cylindrical-like rotation such as NGC 128 (Bertola and Capaccioli 1977; Jarvis 1982) and perhaps NGC4565 (KI) do.

f) Internal Views

Line-of-sight velocity dispersions from inside the model spheroids could be compared to measurements in the spheroid of our galaxy (high-velocity stars), but the model potentials used here include only a spheroidal component with no disk,

so they are of limited applicability to the observable part of our galaxy. Also, it is not known whether our bulge follows a deVaucouleurs' law. Nonetheless, as an example, Figure 25*a* graphs the line-of-sight velocity dispersions for different configurations of the $\varepsilon = 0.5$ model at a low galactic latitude. At small distances from the observation point (on the equator at a distance of $5R_e$), the separation between tangentially and radially enhanced velocity dispersion models is quite large, whereas at greater distances only the radial component is sampled, so the difference becomes small. The view toward the model galactic pole is illustrated in Figure 25*b*; the separation between models 2 and 5 is small.

A qualitative difference between the models considered here and the observations of our galaxy convey important information. Because the models are self-gravitating and decrease in density quite steeply at large r, the velocity dispersion amplitude also decreases significantly at large r; this trend is not in agreement with the observations of halo stars (Ratnatunga and Freeman 1985, and references therein). The best-fitting models are those with a dark, massive halo which produces a flat rotation curve (White 1985; Richstone 1985).

A few models that included a thin disk component to the potential were computed, but were not explored further because these configurations were highly contrived. The ellipticity was externally specified (either constant or varying with radius) and did not respond to the disk potential. Growing a disk inside a pre-existing spheroid using N-body techniques is a more fruitful approach for this problem (cf. Barnes and White 1984).

V. SUMMARY

A series of model configurations of oblate spheroids with surface brightness profiles which follow deVaucouleurs' law have been constructed. Various forms of velocity anisotropy were introduced to test their observability. By comparing the velocity dispersion along the minor axis relative to that along the major axis the relative strengths of the velocity dispersion components are determined. However, because the true inclination and flattening of ellipticals are not known, different kinematic configurations may be observationally indistinguishable.

Diagrams of the contours of constant apparent angular velocity can reveal

the form of the rotation structure, but this method requires extensive data. Fitting measurements made parallel to the minor axis but offset from the nucleus can distinguish between spheroidal or cylindrical type rotation.

Application of these models to velocity measurements of bulges and ellipticals is reasonably successful. The predicted range of velocity dispersion profiles adequately, but not perfectly, covers the sample of observations selected here. Some spheroids are better fit by more radially oriented velocity ellipsoids, whereas some are closer fit by tangentially biased configurations.

Although the fluid approximation permits quick solutions to be obtained for specific configurations, this approach is not suited for extensive modelling or for studying formation processes because too many of the parameters are specified *a priori* rather than obtained as part of a solution. Another disadvantage is that model configurations may not be constructible from a particle distribution function. A major deficiency with the fluid approach is that it attempts to specifiy all the physics locally when in fact the details at each point depend on the global distribution because many particles have elongated or inclined orbits. This extra information is lost since only the lowest moment equations of the collisionless Boltzmann equation are solved.

I thank Peter Goldreich and Douglas Richstone for discussions which helped guide this work. John Tonry kindly supplied his wealth of data on M32. This work was supported in part by NSF grant AST 83-13725.

APPENDIX: RADIAL DISTRIBUTIONS

This appendix demonstrates that a spheroid which follows a deVaucouleurs' surface brightness law cannot be composed of purely radial orbits, assuming that the luminosity density represents mass density. For spherically symmetric configurations with radial orbits, the distribution function depends only on the energy,

$$f(E, L^2) = g(E)\,\delta(L^2), \tag{18}$$

where $g(E)$ is non-negative. I denote the gravitational potential as $U(r)$ and the

density as $\rho(r)$. Then, following Richstone and Tremaine (1985, hereafter RT),

$$r^2\rho(r) = \int_{U(r)}^{E_\infty} \frac{g(E)\,dE}{[E - U(r)]^{1/2}}, \tag{19}$$

where E_∞ is the particle energy cutoff for a finite distribution, with a cutoff radius R_∞ defined by $U(R_\infty) \equiv E_\infty$. The asymptotic behaviour of $\rho(r)$ is the topic of this appendix.

Consider a distribution which has a core radius R_c, such that no particle has an apapsides inside R_c. Every particle's energy is greater than $E_c = U(R_c)$, so for $E < E_c$, $g(E) = 0$.

At $r < R_c$, $U(r) < E_c$, the right-hand side of equation (19), which I shall denote as ψ, becomes

$$\psi(r) = \int_{E_c}^{E_\infty} \frac{g(E)\,dE}{[E - U(r)]^{1/2}}. \tag{20}$$

And for $r < R_c$,

$$\frac{d\psi}{dr} = \int_{E_c}^{E_\infty} \frac{g(E)}{2[E - U(r)]^{3/2}} \frac{dU}{dr}\,dE = \frac{dU}{dr}\,\psi_s(r), \tag{21}$$

where ψ_s is the new integral over E and is positive.

Finally, the slope of the density distribution is

$$\gamma(r) \equiv \frac{d\ln\rho}{d\ln r} = -2 + \frac{d\ln\psi}{d\ln r} = -2 + r\frac{\psi_s}{\psi}\frac{dU}{dr}. \tag{22}$$

Since gravity is an attractive force, $dU/dr > 0$, so equation (22) requires $\gamma \geq -2$. RT showed that if the central force remains finite as $r \to 0$, then $\gamma \leq -2$. Thus, by combining these limits, γ must asymptotically approach -2.

If the system contains a dominant central point mass, then the central force does not remain finite and the constraint that $\gamma \leq -2$ is not applicable. Consider a configuration with a central mass surrounded by a system of particles which all

have the same apapsides, r_{max}, but make negligible contribution to the potential. The mass contribution from the particle cloud is

$$m(s) = \frac{2}{\pi}\left[\sin^{-1}(s^{1/2}) - s^{1/2}[1-s]^{1/2}\right], \tag{23}$$

where $s = r/r_{max}$. The density law is

$$\rho(s) = \frac{1}{2\pi^2}\frac{s^{-3/2}}{(1-s)^{1/2}}. \tag{24}$$

The power-law slope γ is

$$\gamma(s) = -2 + \frac{1}{2(1-s)} = \frac{-3}{2} + \frac{s}{2(1-s)}. \tag{25}$$

Although dU/dr is infinite at $r = 0$, γ is well behaved if one excludes the central point mass. The flatter slope at $\gamma(0)$ in this case is caused by the unbounded velocity as a particle approaches the center. As it speeds up, its effective density contribution is smaller, so the geometric concentration is reduced.

Inside the core of a system the density profile from purely radial orbits must asymptotically approach either r^{-2} or $r^{-3/2}$. Since at small r the deprojected deVaucouleurs' law asymptotes to $\rho_L \propto r^{-3/4}$, such a system cannot be constructed from radial orbits.

REFERENCES

Barnes, J., and White, S. D. M. 1984, *M.N.R.A.S.*, **211**, 753.

Barnes, J., Goodman, J., and Hut, P. 1985, *M.N.R.A.S.*, **000**, 000.

Bertola, F. and Capaccioli, M. 1977, *Ap. J.*, **211**, 697.

Binney, J. 1978, *M.N.R.A.S.*, **183**, 501.

———. 1980, *M.N.R.A.S.*, **190**, 873.

Binney, J. and Mamon, G. A. 1982, *M.N.R.A.S.*, **200**, 361.

Boroson, T. 1981, *Ap. J. Suppl.*, **46**, 177.

Burstein, D. 1979, *Ap. J. Suppl.*, **41**, 435.

Davies, R. L. and Illingworth, G. 1983, *Ap. J.*, **266**, 516.

deVaucouleurs, G. 1948, *Ann. d'Ap.*, **11**, 247.

Illingworth, G. 1981, in *The Structure and Evolution of Normal Galaxies*, ed. S. M. Fall and D. Lynden-Bell (Cambridge: Cambridge University Press).

Jarvis, B. J. 1982. Ph.D. thesis, Mount Stromlo Observatory, Australian National University, Canberra.

Jarvis, B. and Freeman, K. C. 1985, *Ap. J.*, **295**, 000.

Kormendy, J. 1977, *Ap. J.*, **218**, 337.

Kormendy, J. and Illingworth, G. 1982, *Ap. J.*, **256**, 460.

McGlynn, T. A. 1984, preprint.

Newton, A. J. and Binney, J. 1984, *M.N.R.A.S.*, **210**, 711.

Ratnatunga, K. U. and Freeman, K. C. 1985, preprint.

Richstone, D. O. 1984, *Ap. J.*, **281**, 100.

———. 1985, private communication.

Richstone, D. O. and Tremaine, S. 1984, *Ap. J.*, **286**, 27.

———. 1985, preprint.

Tonry, J. 1983, *Ap. J.*, **266**, 58.

———. 1984*a*, *Ap. J. (Letters)*, **283**, L27.

———. 1984*b*, personal communication.

van Albada, T. S. 1982, *M.N.R.A.S.*, **201**, 939.

White, S. D. M. 1985, preprint.

Young, P. J. 1976, *A.J.*, **81**, 807.

FIGURE CAPTIONS

Fig. 1 — Density profile for deprojected deVaucouleurs' law. Points represent values computed by Young (1976), and the solid line shows the fit by Tonry (1984*b*).

Fig. 2 — Meridian slice through a spheroid: dotted lines show equidensity surfaces and are spaced logarithmically in radius. Solid lines are contours of constant σ_z for the isotropic configuration; contours are linearly spaced in velocity. (*a*) $\varepsilon = 0.1$, and (*b*) $\varepsilon = 0.5$.

Fig. 3 — Solid lines are contours of constant rotation velocity for the isotropic configuration and are linearly spaced. (*a*) $\varepsilon = 0.1$, and (*b*) $\varepsilon = 0.5$.

Fig. 4 — Dashed and solid lines show contours of constant angular velocity, and are spaced uniformly on logarithmic intervals of angular velocity. Dotted lines represent isodensity contours. (*a*) $\varepsilon = 0.1$, and (*b*) $\varepsilon = 0.5$.

Fig. 5 — Meridian slice for model 2A. Solid lines show contours of constant σ_ϕ, linearly spaced in velocity. (*a*) $\varepsilon = 0.1$, and (*b*) $\varepsilon = 0.5$.

Fig. 6 — Meridian slice for model 2B. Solid lines are contours of constant σ_R. (*a*) $\varepsilon = 0.1$, and (*b*) $\varepsilon = 0.5$.

Fig. 7 — Meridian slice for model 2C. Solid lines are contours of constant σ_R. Dotted lines represent isodensity contours. (*a*) $\varepsilon = 0.1$, and (*b*) $\varepsilon = 0.5$.

Fig. 8 — Contours of constant σ_ϕ in model 2C. (*a*) $\varepsilon = 0.1$, and (*b*) $\varepsilon = 0.5$.

Fig. 9 — Model 5A: dotted lines are equidensity surfaces, solid lines show contours of constant σ_z. (*a*) $\varepsilon = 0.1$, and (*b*) $\varepsilon = 0.5$.

Fig. 10 — Solid lines are contours of constant σ_R for model 5A. (*a*) $\varepsilon = 0.1$, and (*b*) $\varepsilon = 0.5$.

Fig. 11 — Isotropic configuration: Solid lines are contours of constant projected velocity dispersion in the plane of the sky linearly spaced in velocity. Dotted lines represent isophotes spaced

logarithmically in radius. $(a)\,\varepsilon = 0.1$, and $(b)\,\varepsilon = 0.5$.

Fig. 12 — Model 2A: solid lines are contours of constant projected velocity dispersion in the plane of the sky. $(a)\,\varepsilon = 0.1$, and $(b)\,\varepsilon = 0.5$.

Fig. 13 — Contours of σ_s for model 2B. $(a)\,\varepsilon = 0.1$, and $(b)\,\varepsilon = 0.5$.

Fig. 14 — Contours of constant projected velocity dispersion for model 2C. Dotted lines represent isophotes. $(a)\,\varepsilon = 0.1$, and $(b)\,\varepsilon = 0.5$.

Fig. 15 — Model 5A: dotted lines are isophotes, solid lines denote contours of constant σ_s. $(a)\,\varepsilon = 0.1$, and $(b)\,\varepsilon = 0.5$.

Fig. 16 — (a) Line-of-sight velocity dispersion profiles for $\varepsilon = 0.5$ model at zero inclination: solid line—model 1, dashed—2A, dash-dotted—2C, and dotted—5B. (b) same as (a) only with 60° inclination.

Fig. 17 — Projected velocity dispersion for an edge-on $\varepsilon = 0.5$ plotted in log-log coordinates. Solid line represents the isotropic case, dashed line—model 4A, and dotted line—model 5A.

Fig. 18*ab* — Values of edge-on projected velocity dispersion ratios at $1.2R_e$ from the center for $\varepsilon = 0.5$ model. *Abscissa*—σ_s(major axis)/σ_s(peak), *ordinate*—σ_s(minor axis)/σ_s(peak). The positions of the different configurations are denoted by: filled circle—isotropic, open circle—2A, asterisk—2B, plus sign—2C, triangle—4A and 4B, square—5A and 5B. (b) Same as (a) with ratios measured at a distance of $2.1R_e$.

Fig. 18*cd* — Values of projected velocity dispersion ratios for models with different intrinsic flattenings but viewed at inclinations such that they appear as E1 spheroids. Circles represent $\varepsilon = 0.1$ model points, triangles—$\varepsilon = 0.3$, and squares—$\varepsilon = 0.5$ model points. Filled symbols mark the isotropic cases. Fiducial radii are (c) $1.2R_e$, and (d) $2.1R_e$.

Fig. 19 — Comparision of NGC 2841 data to $\epsilon = 0.4$ model. (*a*) Circles represent the observed velocity dispersion. Open and filled symbols represent the two sides of the major axis. Lines are model profiles: solid—isotropic, dotted—2A, dash-dotted—2C. (*b*) Symbols represent the observed rotation curve, and the solid line is the model projected rotation curve for the isotropic configuration.

Fig. 20 — Observations of NGC 3898 compared with an $\epsilon = 0.3$ model. Symbols are the same as in Fig. 19.

Fig. 21 — Observations of NGC 4569 compared with an $\epsilon = 0.3$ model. Symbol descriptions are given in Fig. 19.

Fig. 22*a* — Comparison of model profiles to major axis measurements of ellipticals. Open circles and squares denote observed velocity dispersion for NGC 3379, filled symbols show the rotation curve. Dashed line is σ_s for $\epsilon = 0.1$ isotropic configuration, solid line is its associated rotation curve. Dash-dotted line displays σ_s for model 2C.

Fig. 22*b* — Open symbols mark observed dispersion data. Lines are projected velocity dispersion for model 2C with the solid line representing an $\epsilon = 0.1$ model inclined edge-on, and the dash-dotted line an $\epsilon = 0.5$ model with $i = 60°$.

Fig. 22*c* — Open circles show the velocity dispersion profile of NGC 6909, and asterisks denote its rotation curve. Dotted line is σ_s profile for $\epsilon = 0.5$ model 2A, dash-dotted line is for model 2C.

Fig. 23*ab* — Apparent angular velocity for (*a*) $\epsilon = 0.1$ and (*b*) $\epsilon = 0.5$. Dotted lines represent isophotes on the plane of the sky. Dashed and solid lines are contours of constant apparent angular velocity spaced on logarithmic intervals of Ω_s.

Fig. 23*c* — Contours of constant apparent angular velocity for a spheroid rotating on cylinders. A Keplerian rotation curve is specified along the equator. Isophotes are shown by dotted lines.

Fig. 24 — (*a*) Apparent angular velocity diagram for M32. Plus signs mark locations of measured mean velocity on the plane of the sky. Solid lines display contours of constant apparent angular velocity, contours are spaced logarithmically in Ω_s. The two circled points are hand-averaged points included to smooth the contour interpolation. Smoothed isophotes reproduced from ellipse fitting are shown by dotted lines. (*b*) Apparent angular velocity contours for NGC 7814.

Fig. 25 — Line-of-sight velocity dispersions for internal views. *Abscissa* is distance from the observation point. Symbols which illustrate σ_{los} for Models 2A, 2B, 2C, and 5B are open circles, asterisks, plus signs, and triangles, respectively. (*a*) tangential view: longitude=270°, latitude=10°; (*b*) pole view, latitude=90°.

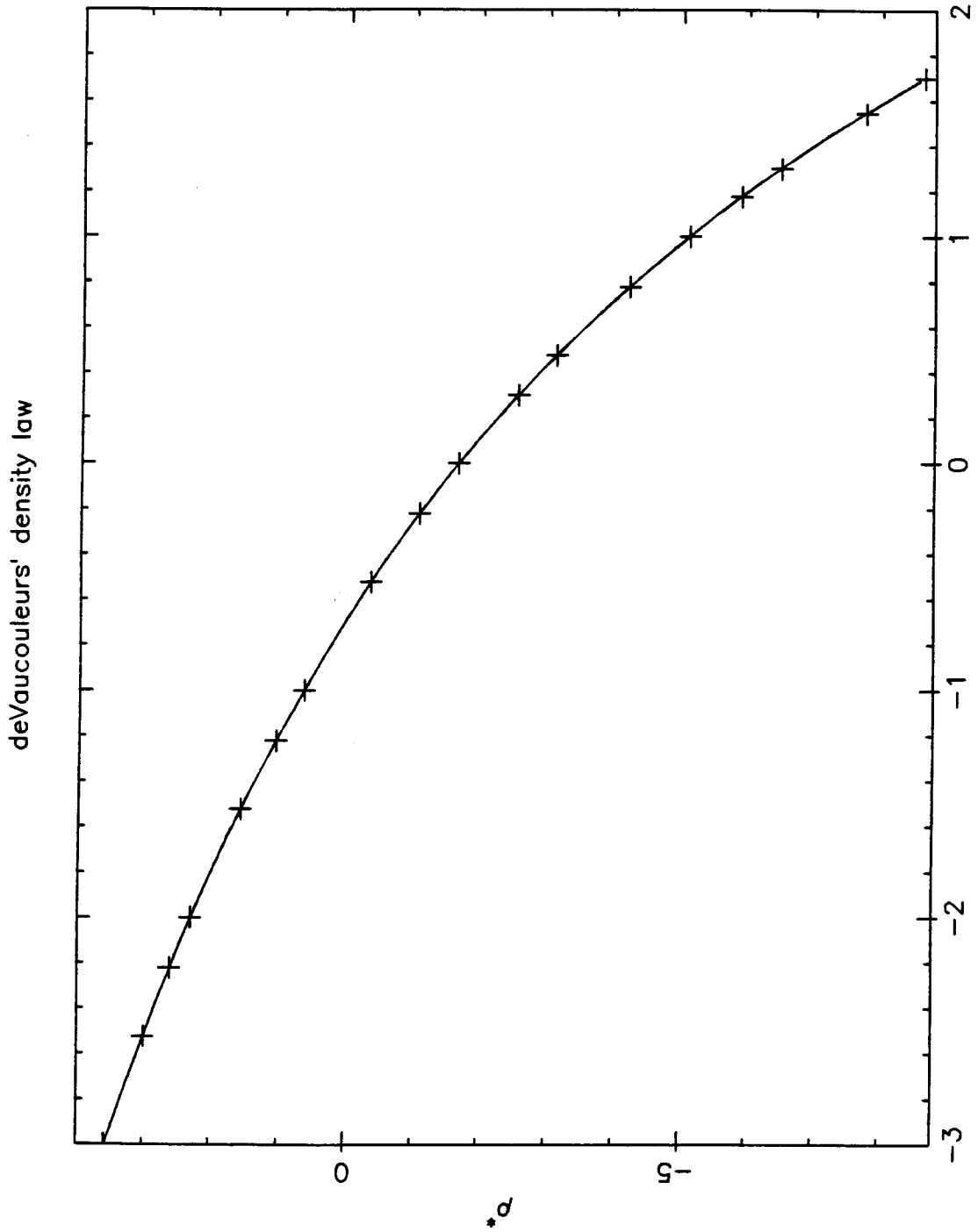

Fig. 1

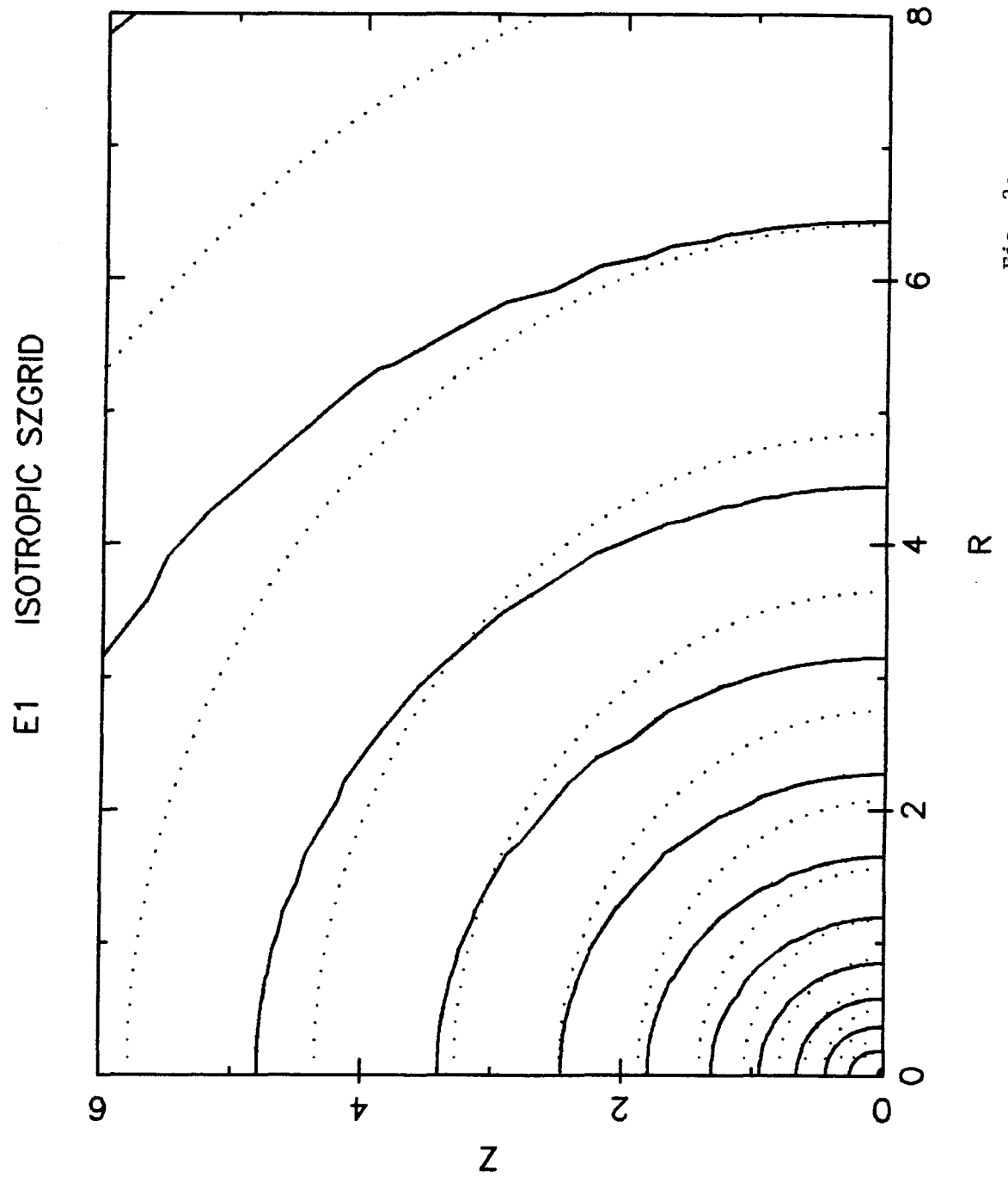

Fig. 2a

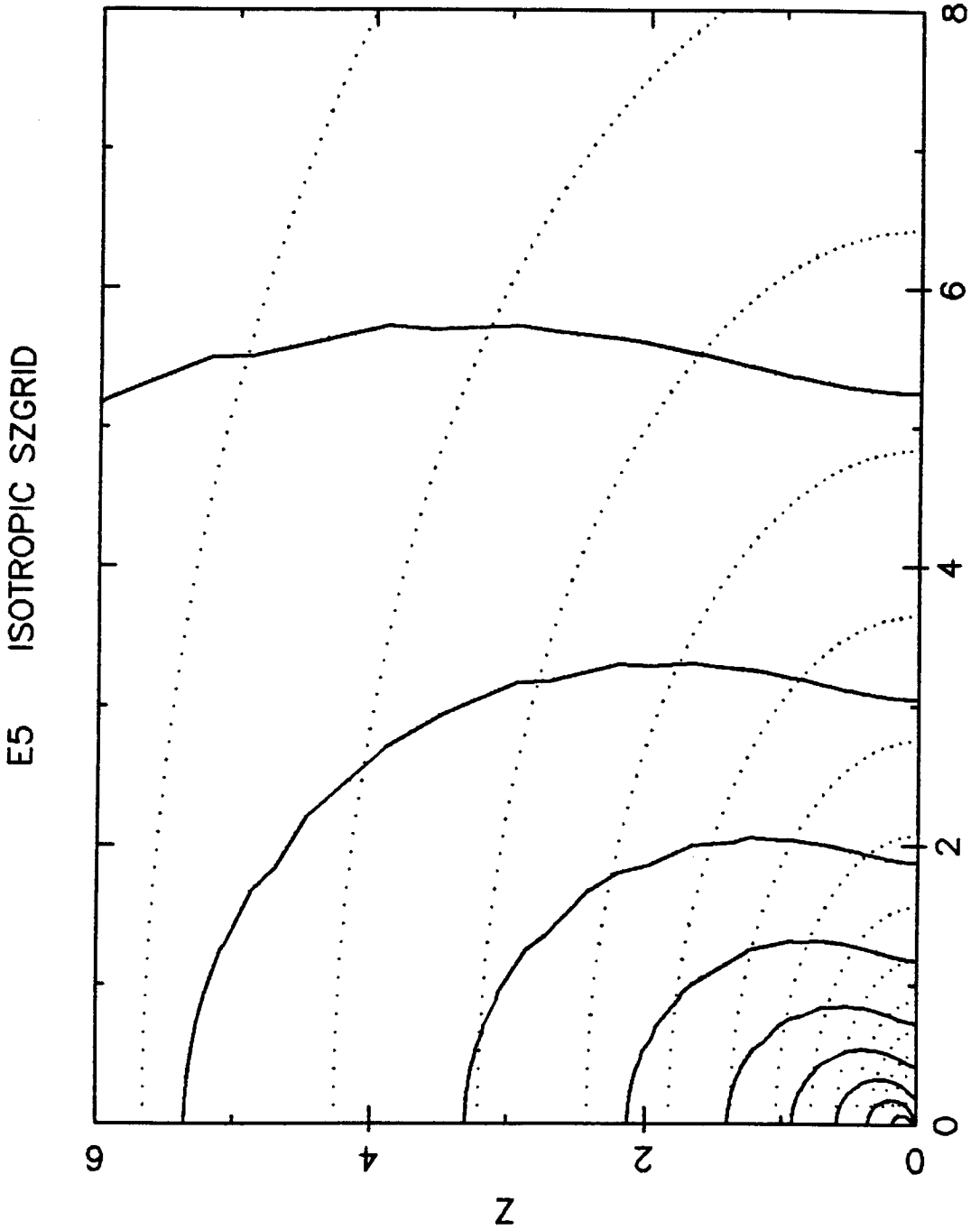

Fig. 2b

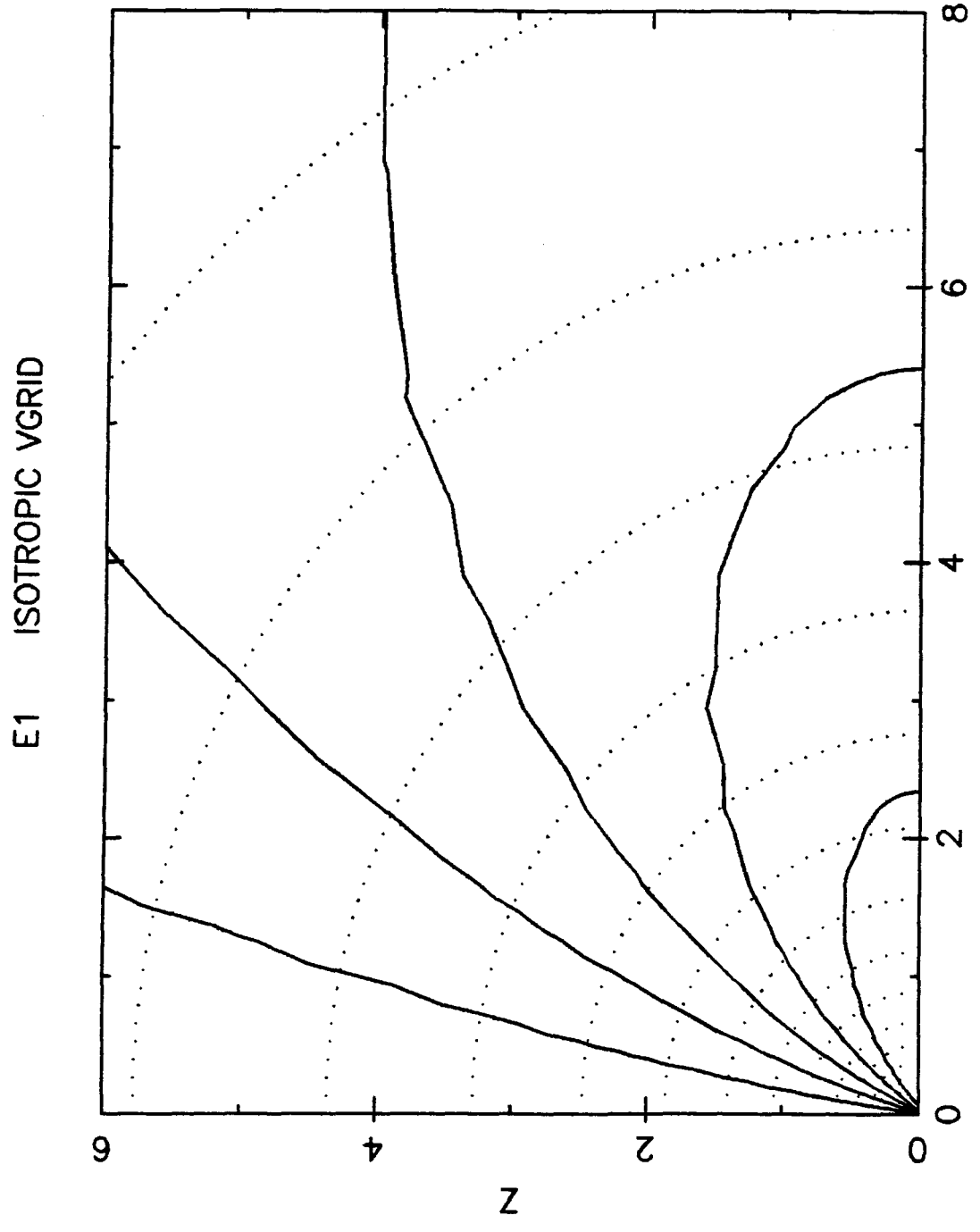

Fig. 3a

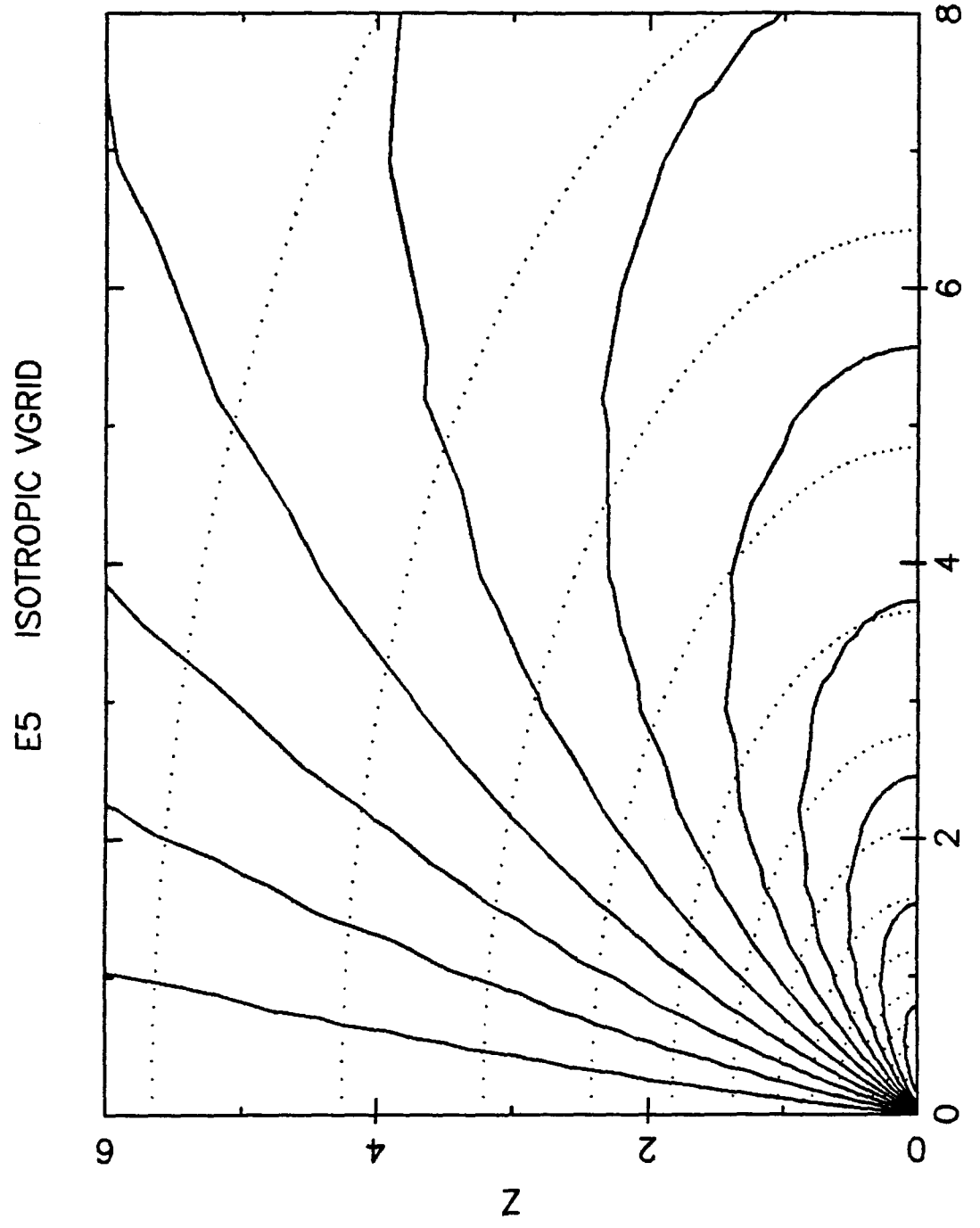

Fig. 3b

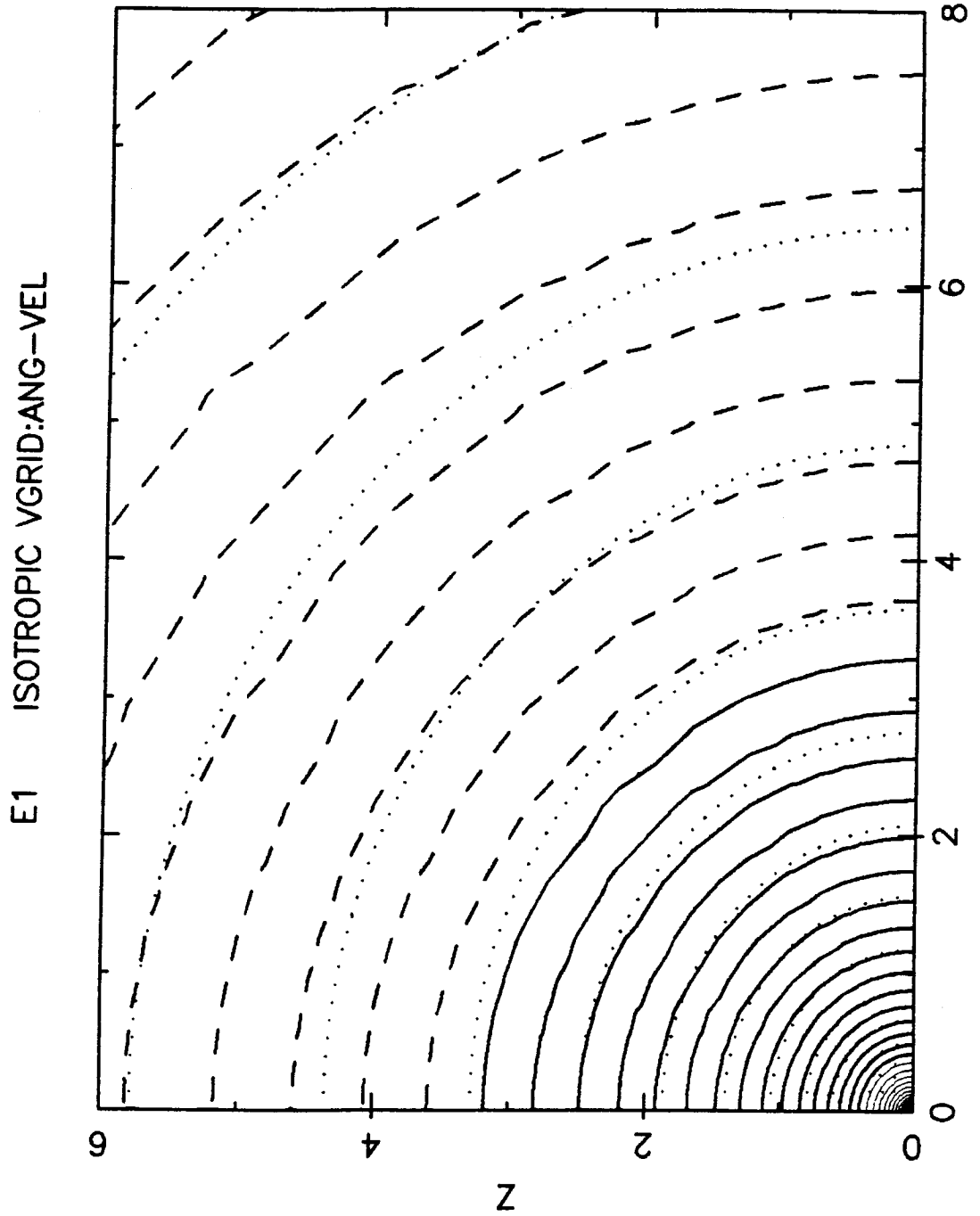

Fig. 4a

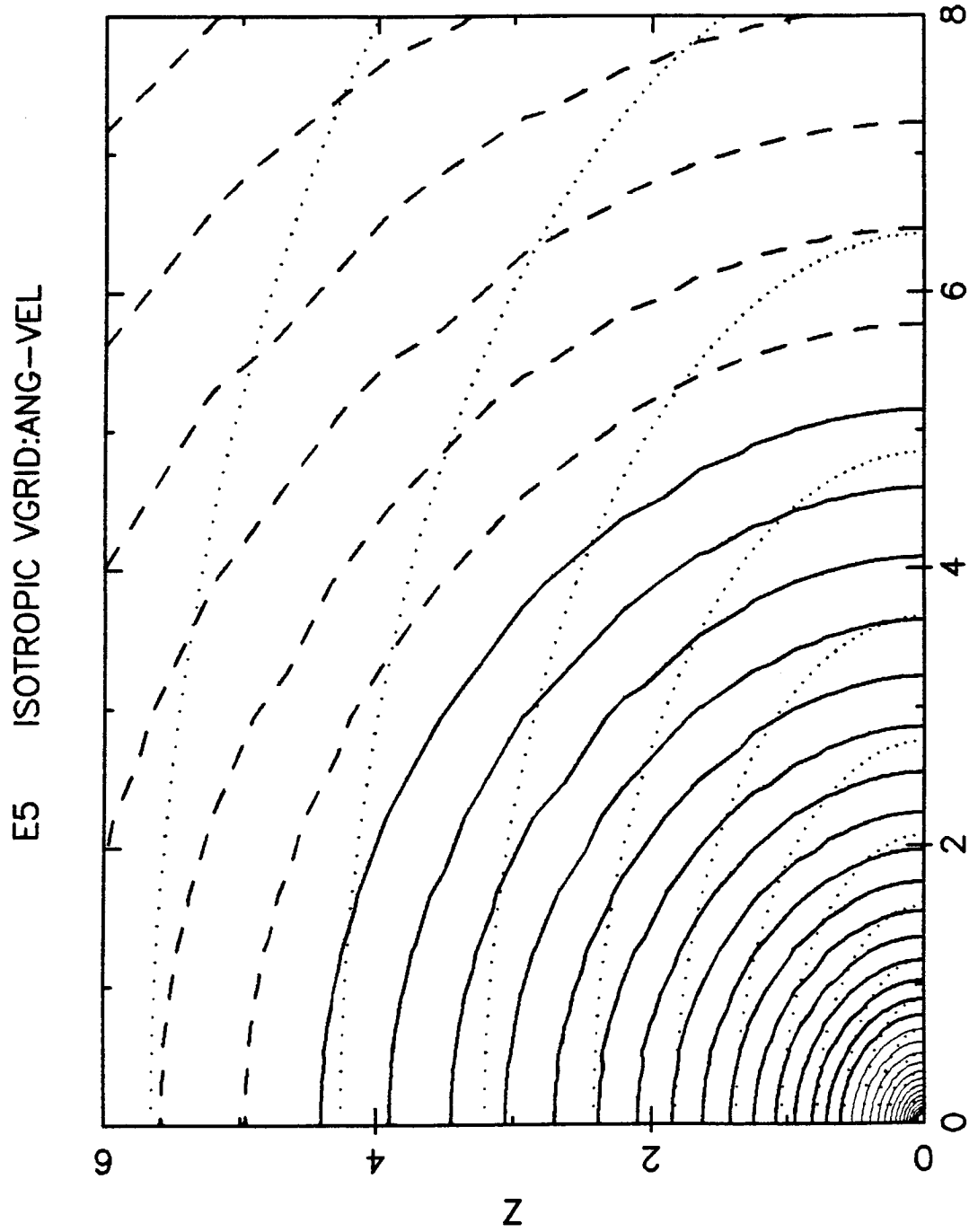

Fig. 4b

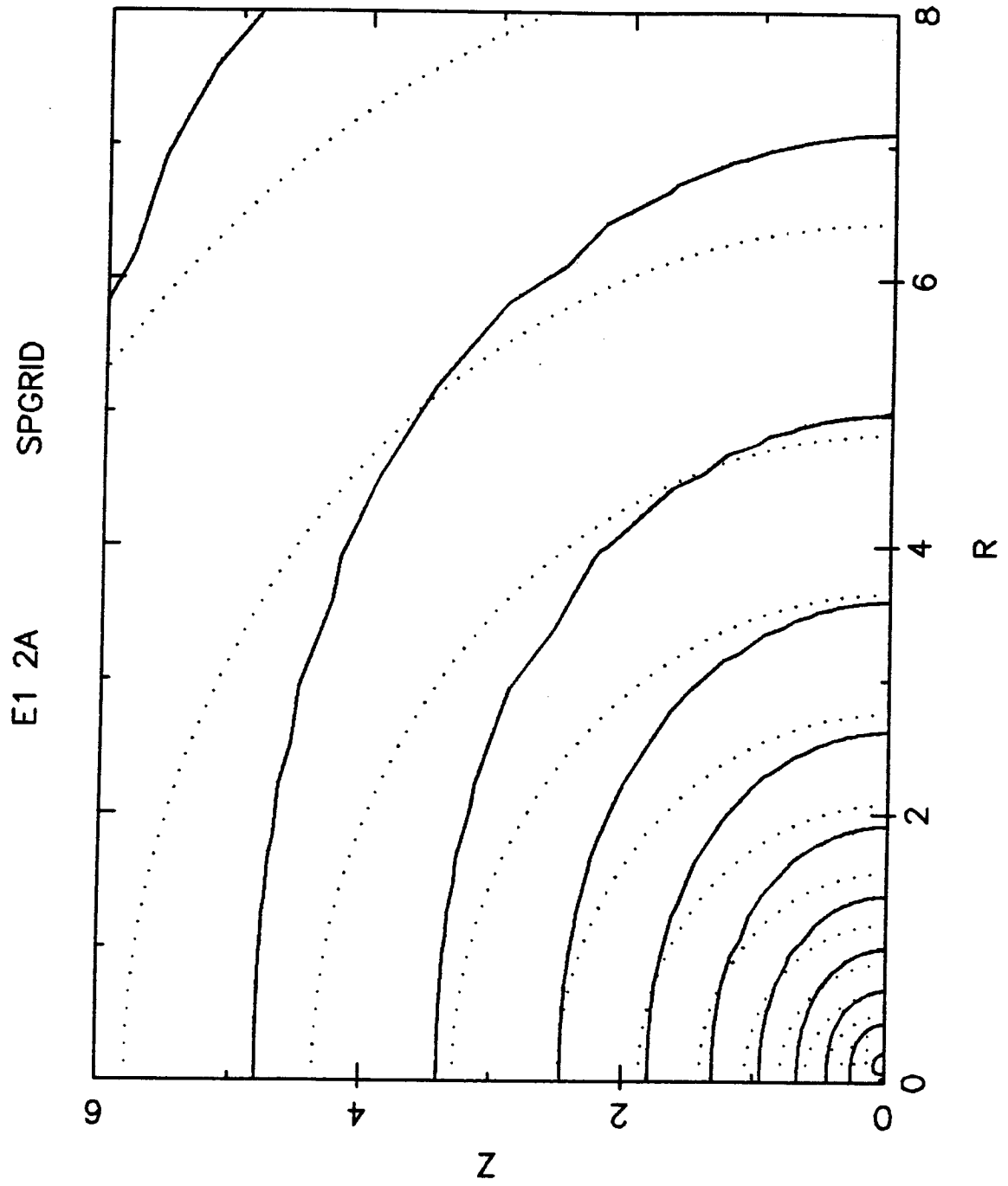

Fig. 5a

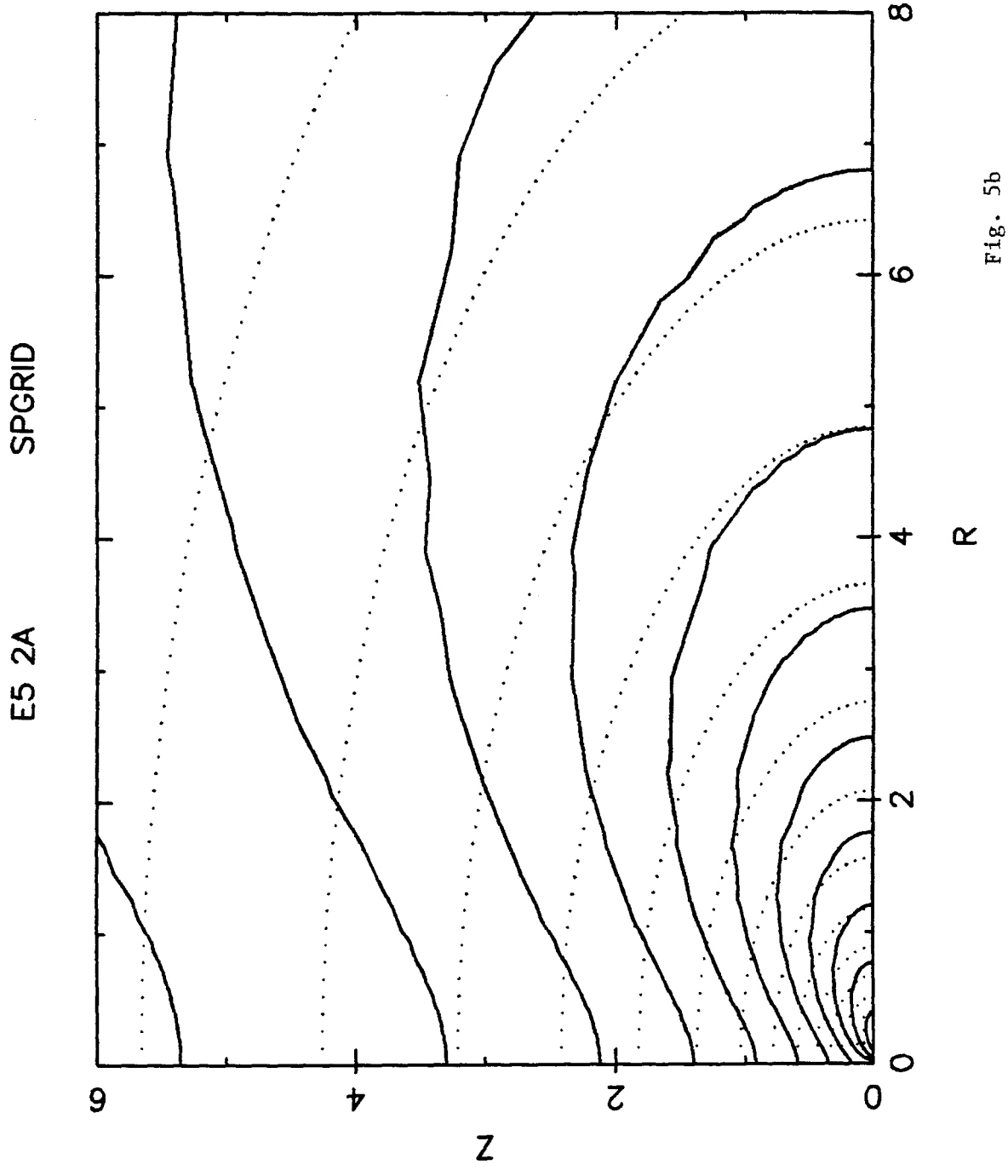

Fig. 5b

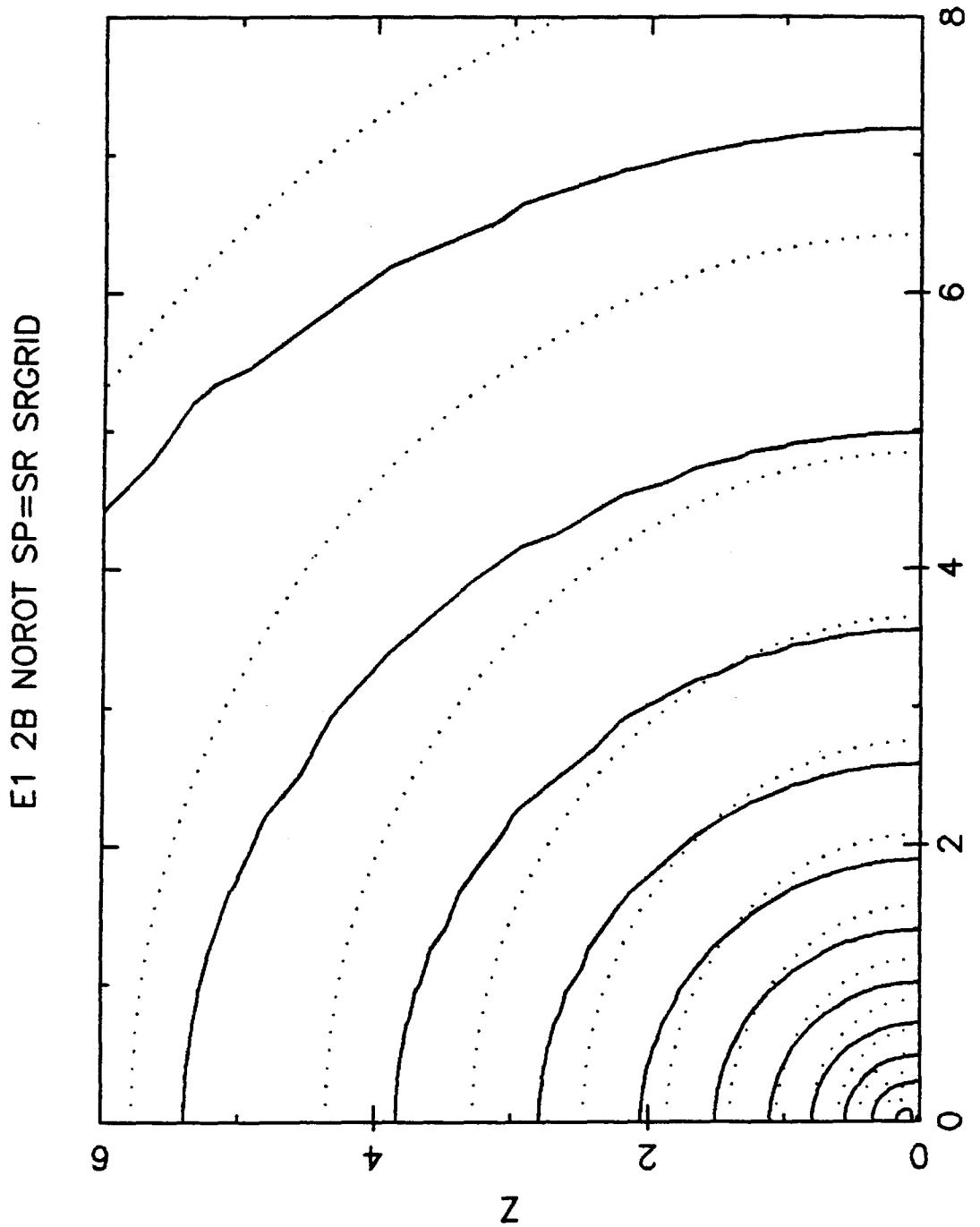

Fig. 6a

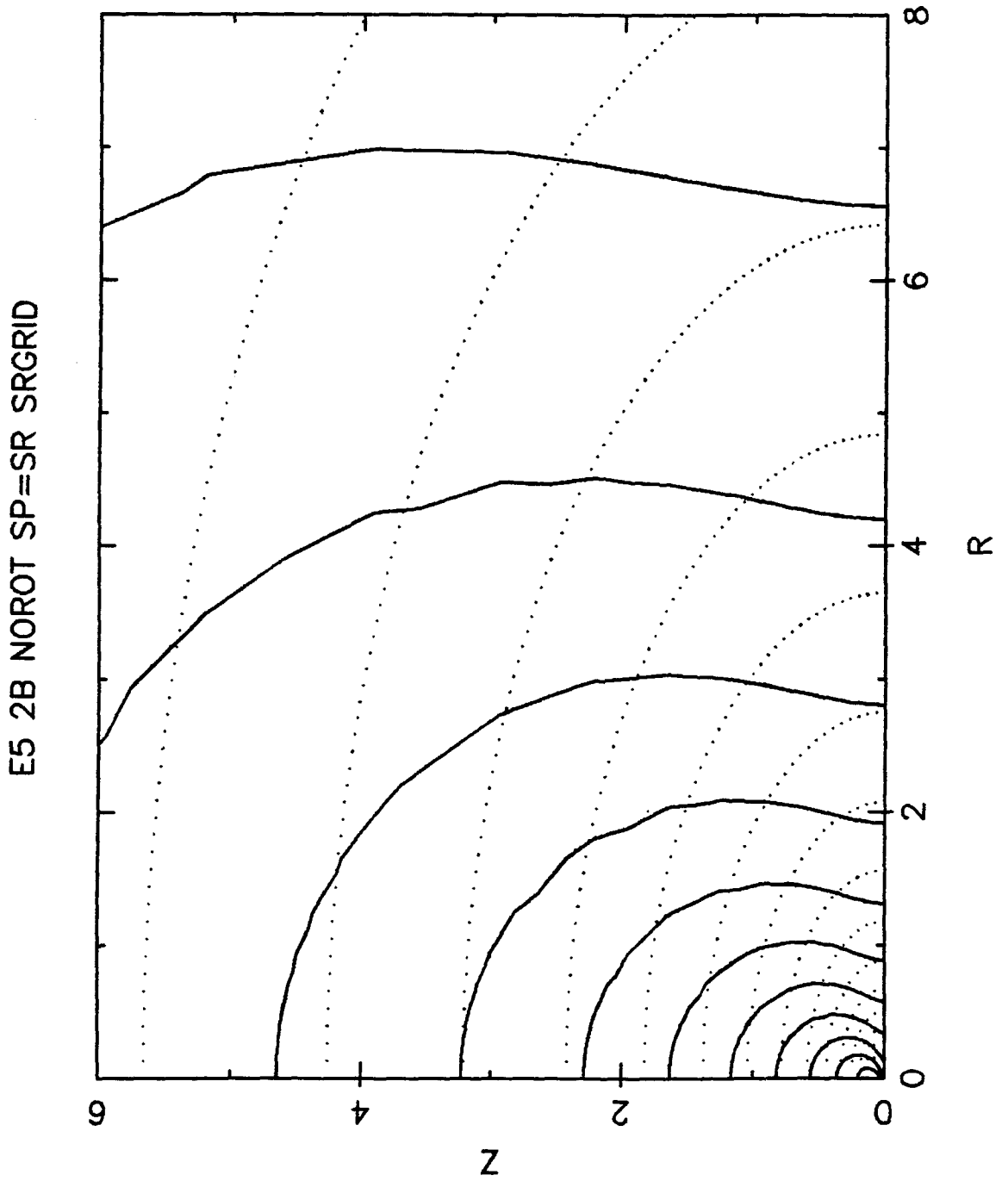

Fig. 6b

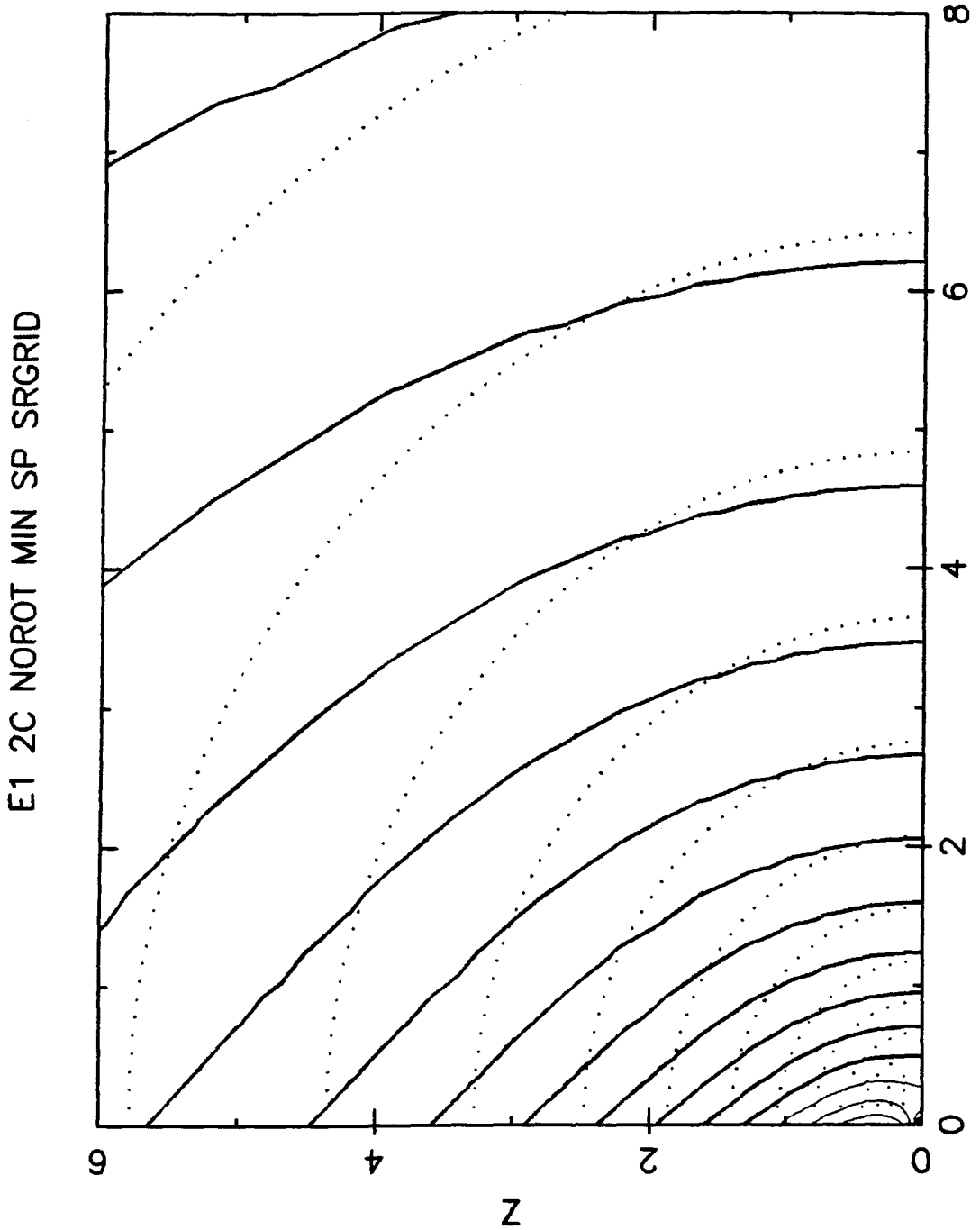

Fig. 7a

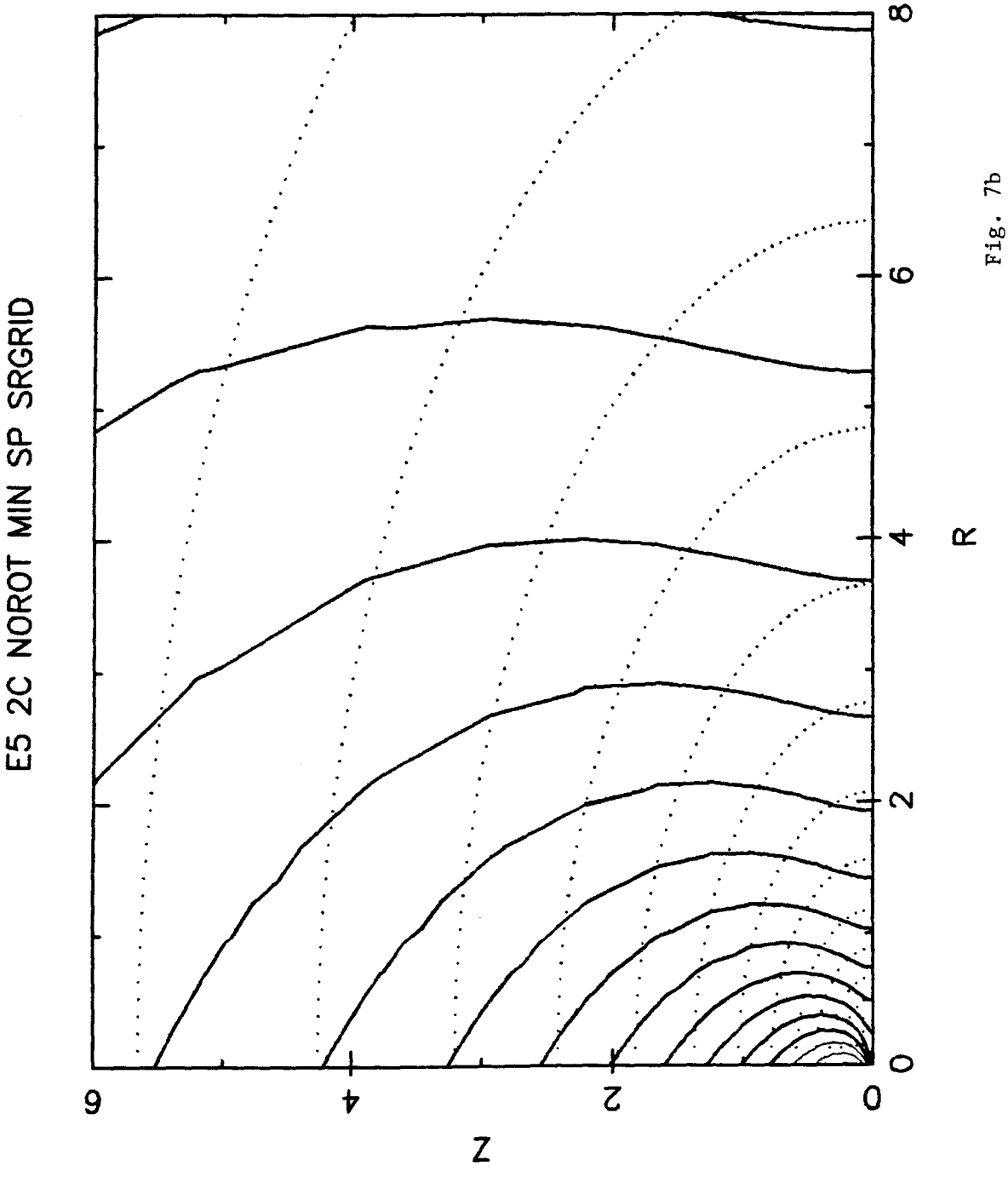

Fig. 7b

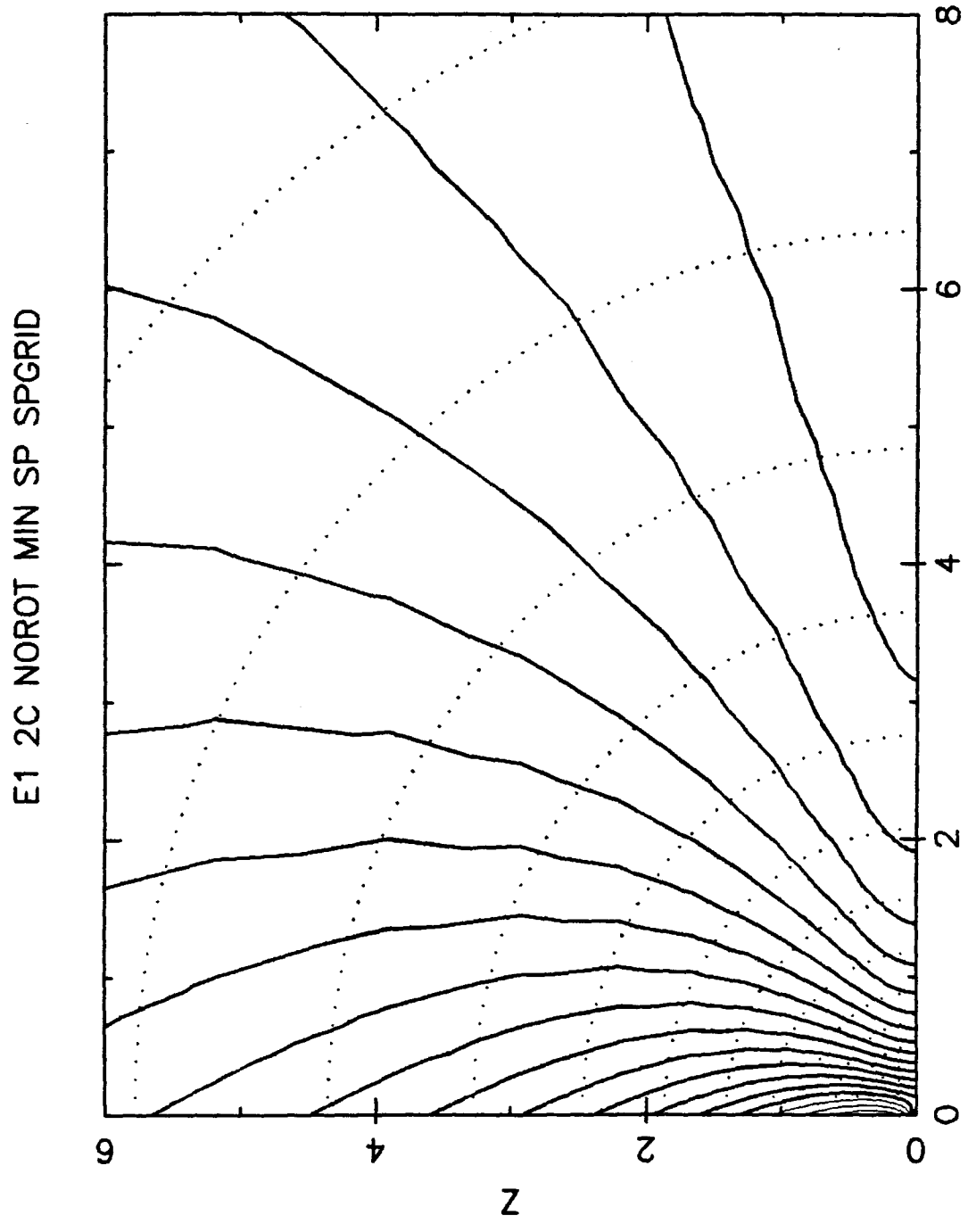

Fig. 8a

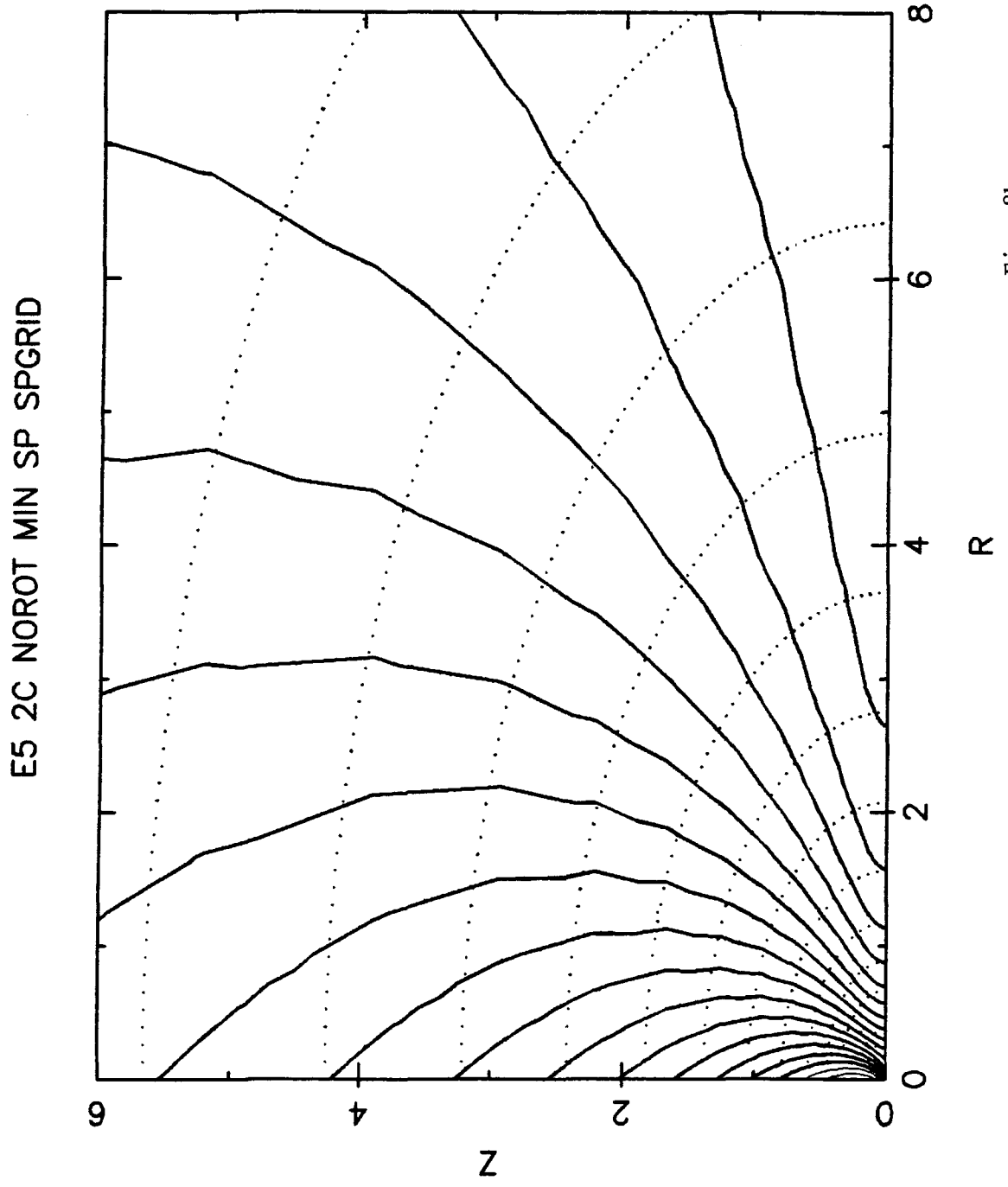

Fig. 8b

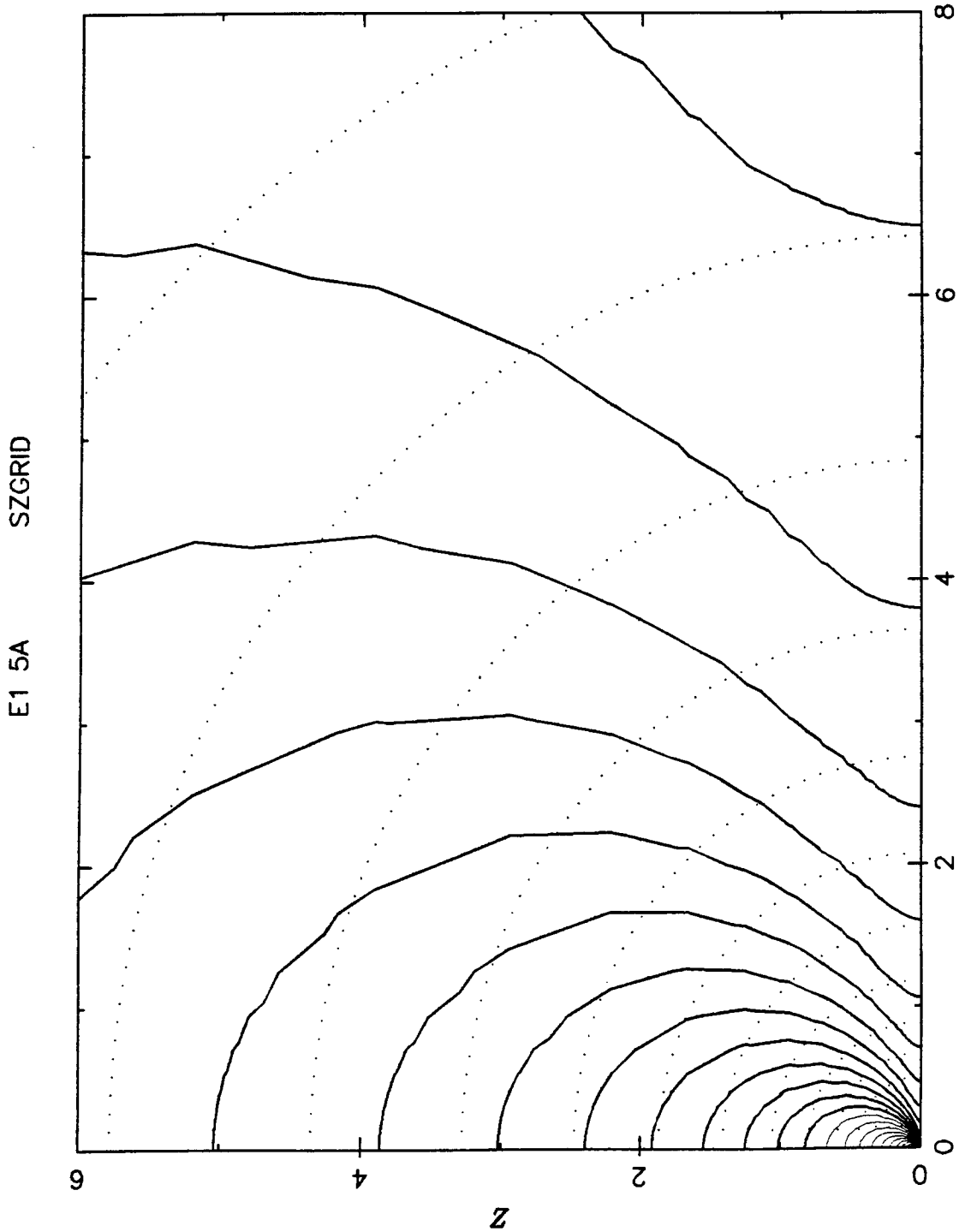

Fig. 9a

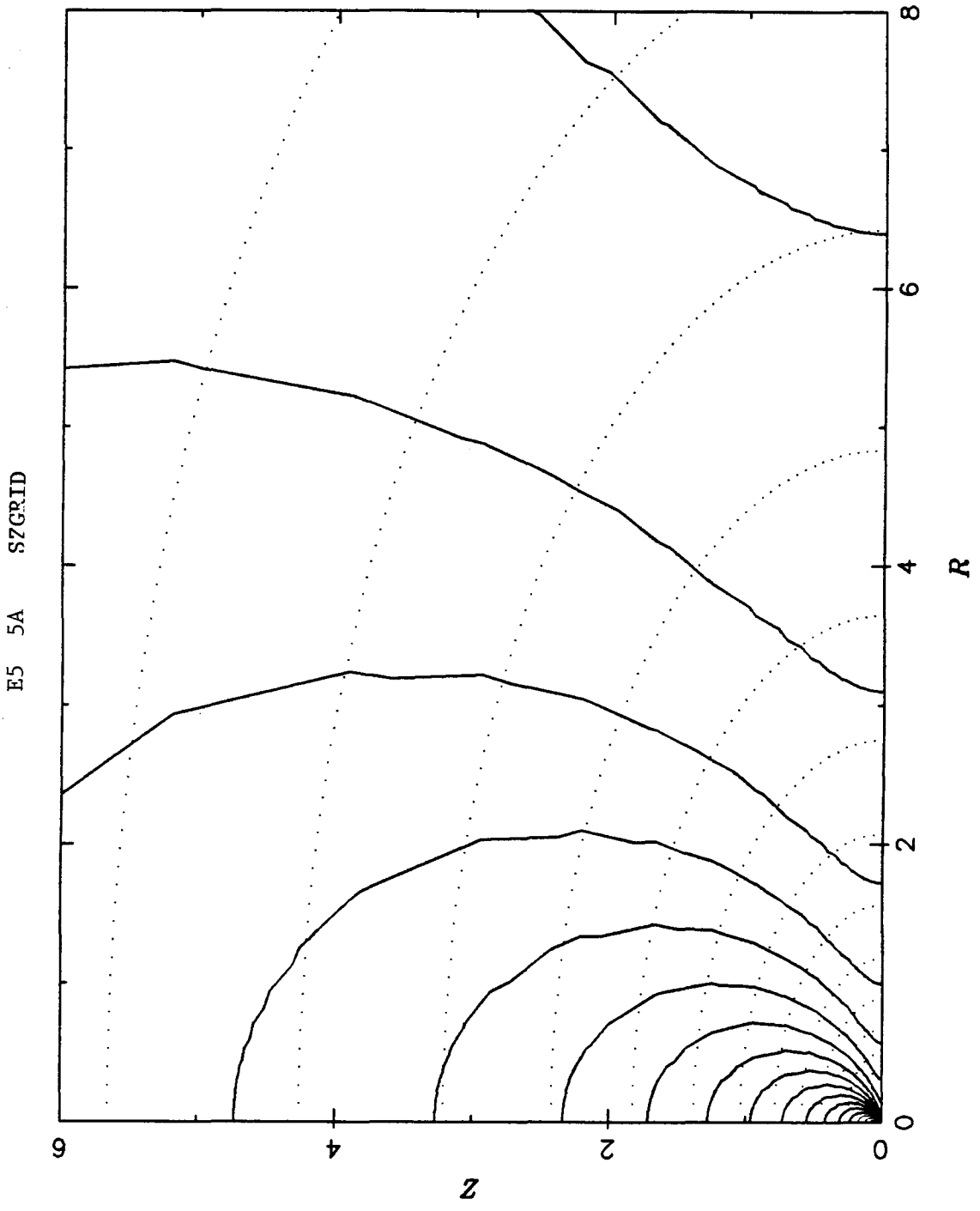

Fig. 9b

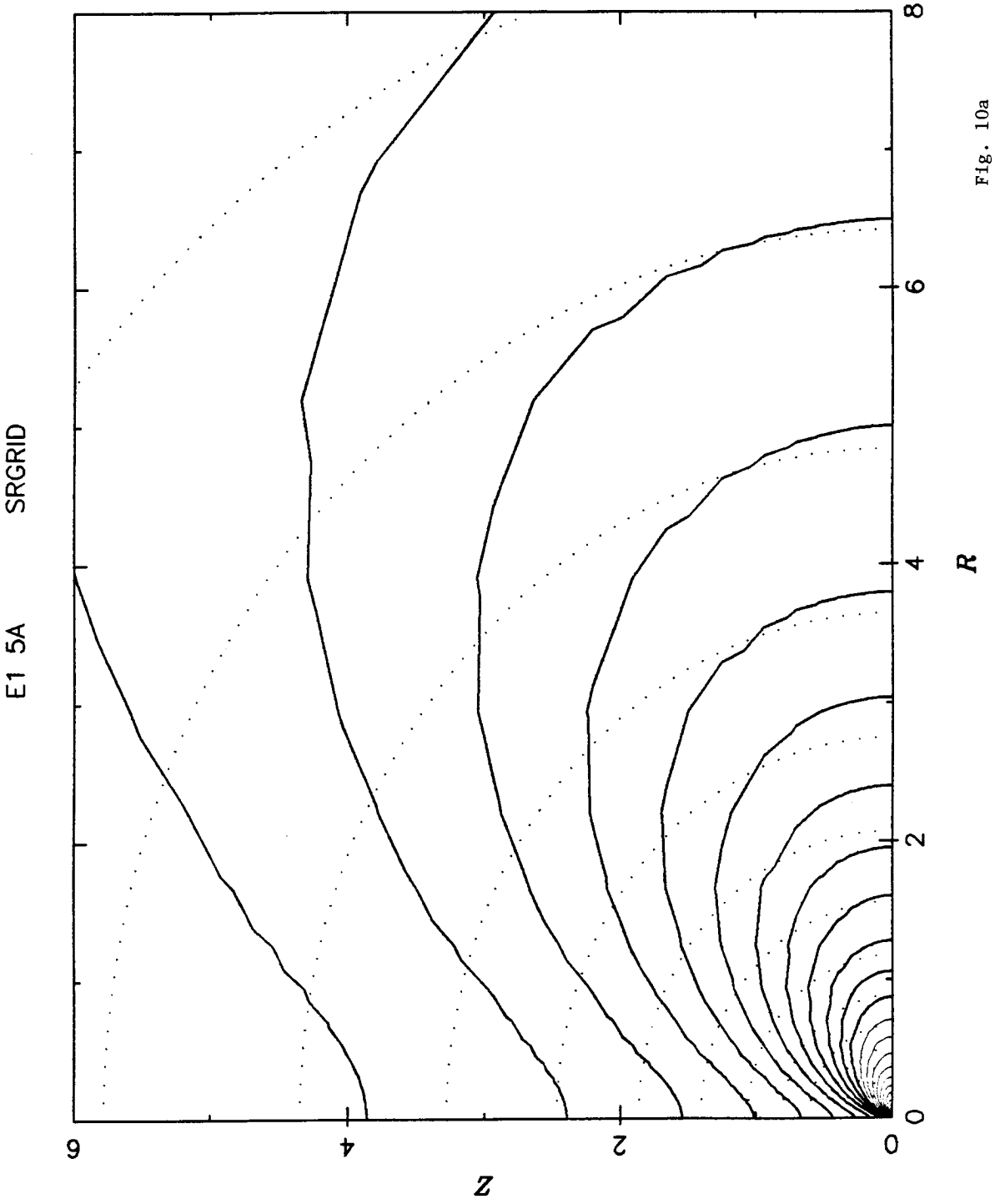

Fig. 10a

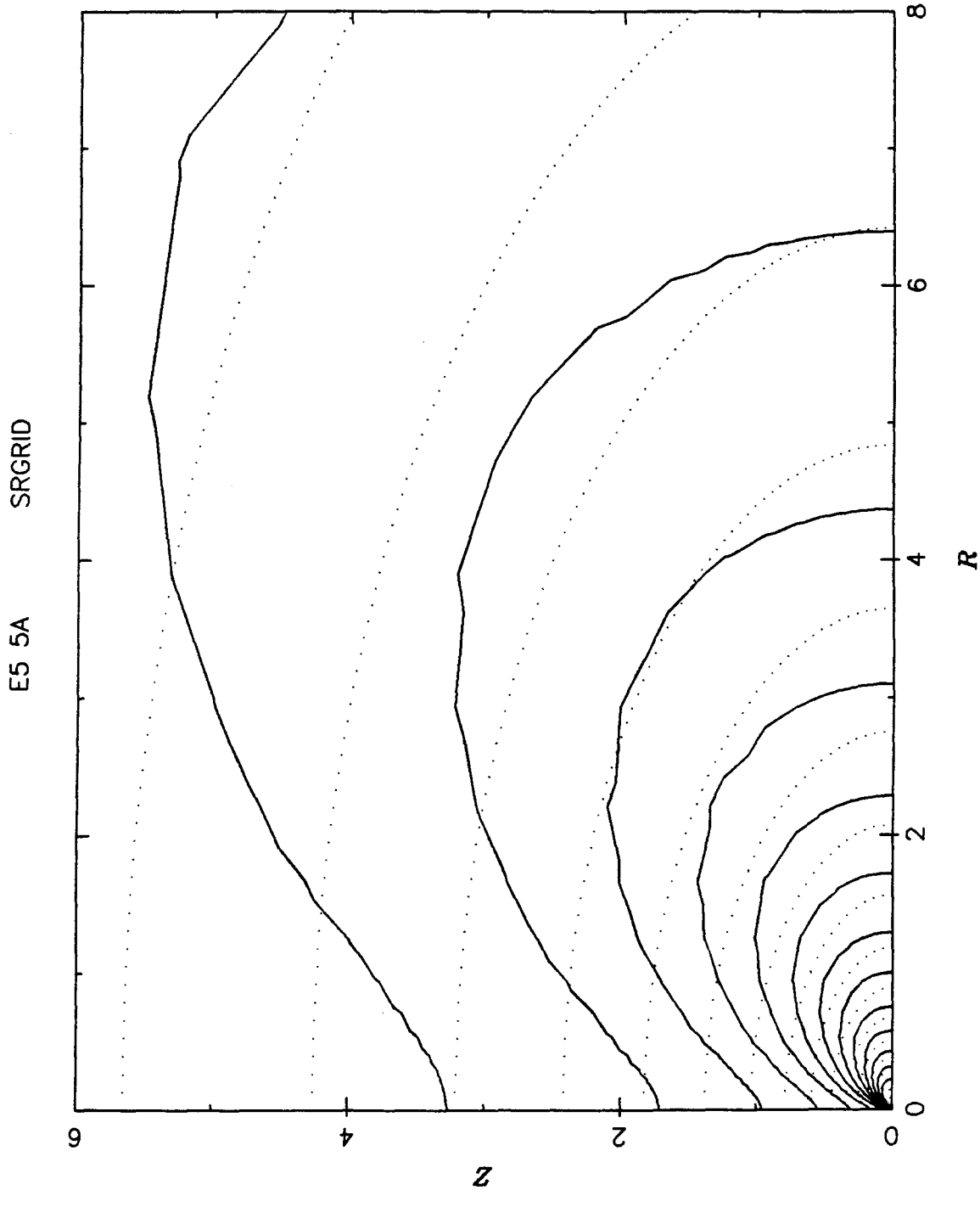

Fig. 10b

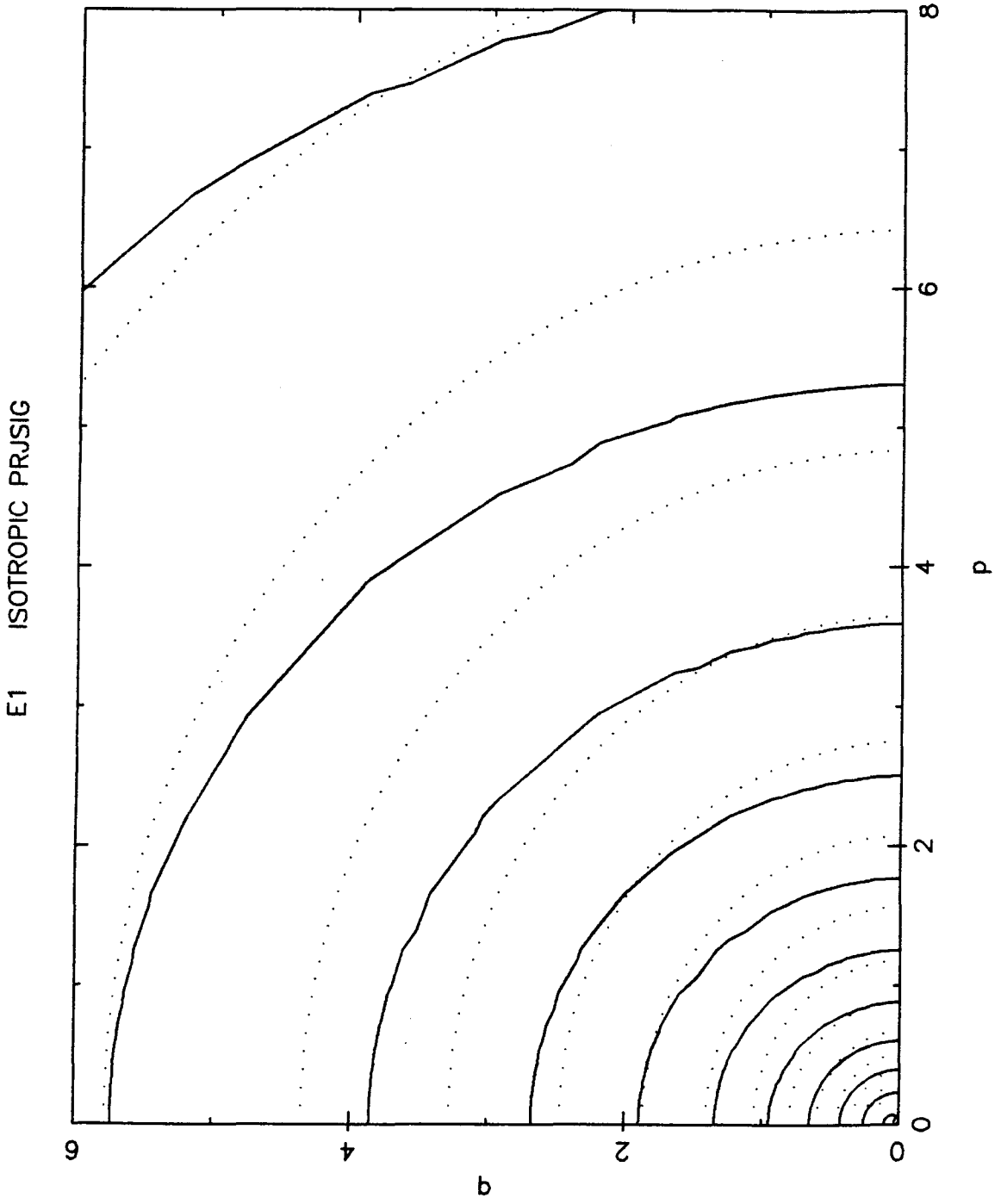

Fig. 11a

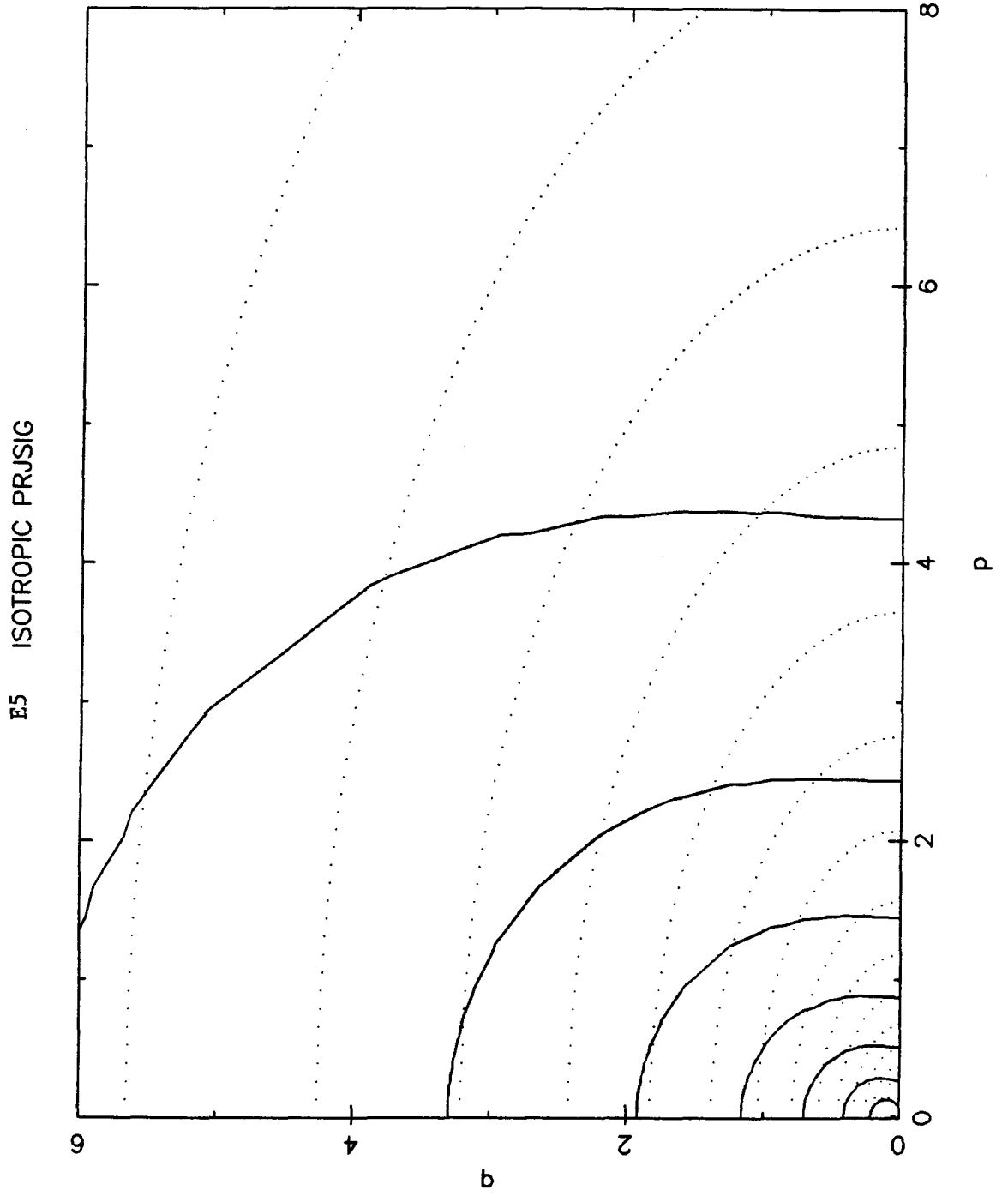

Fig. 11b

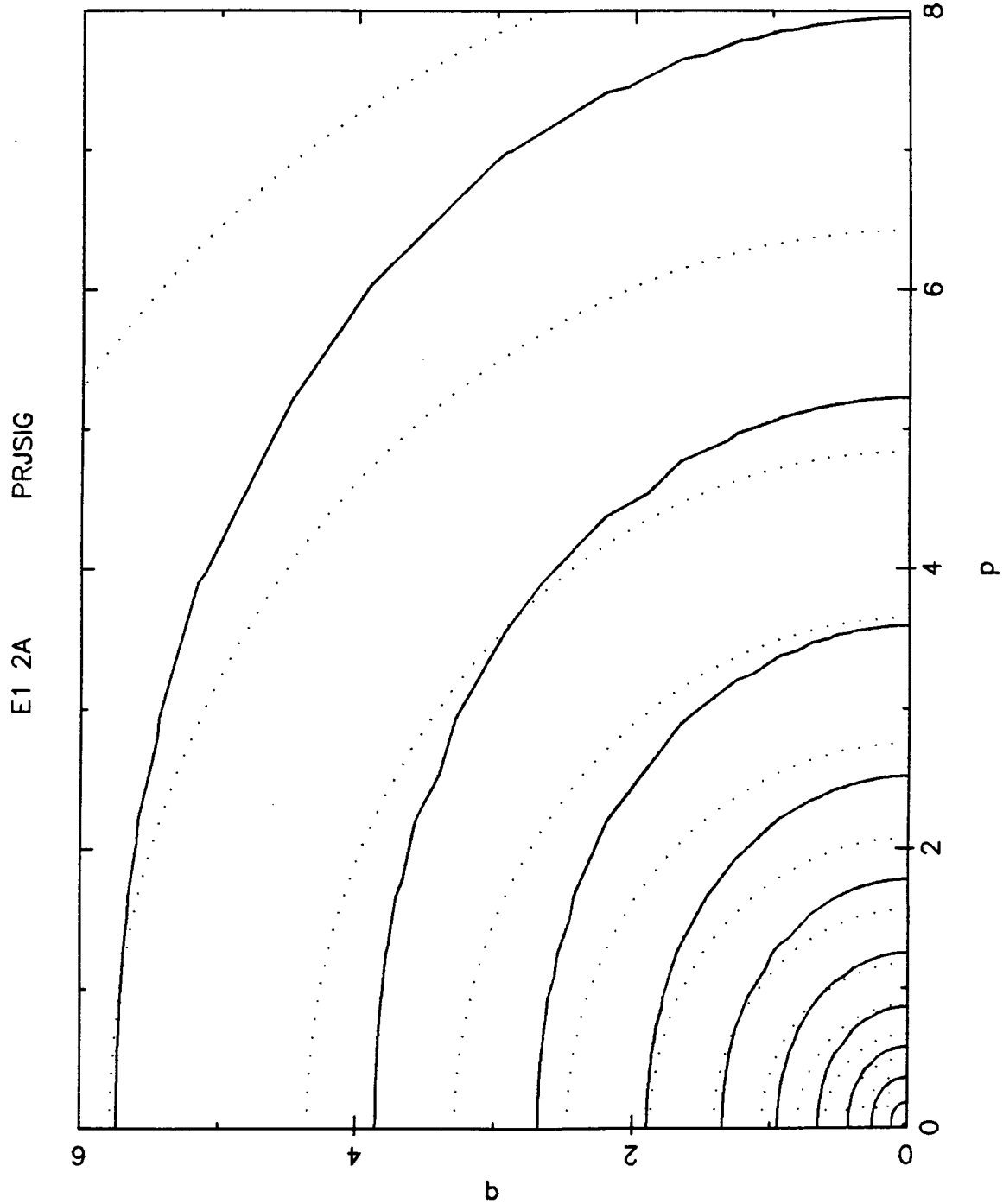

Fig. 12a

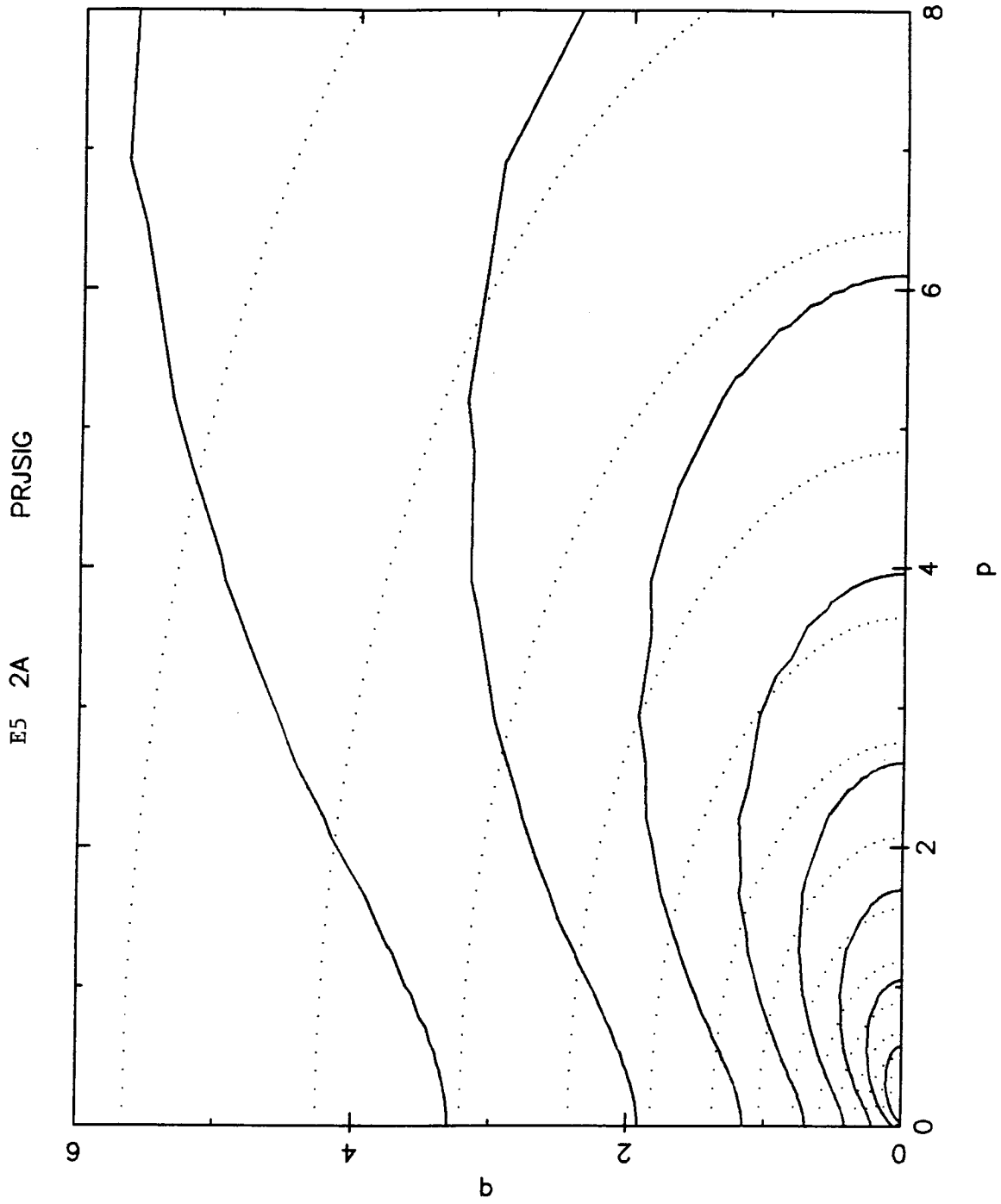

Fig. 12b

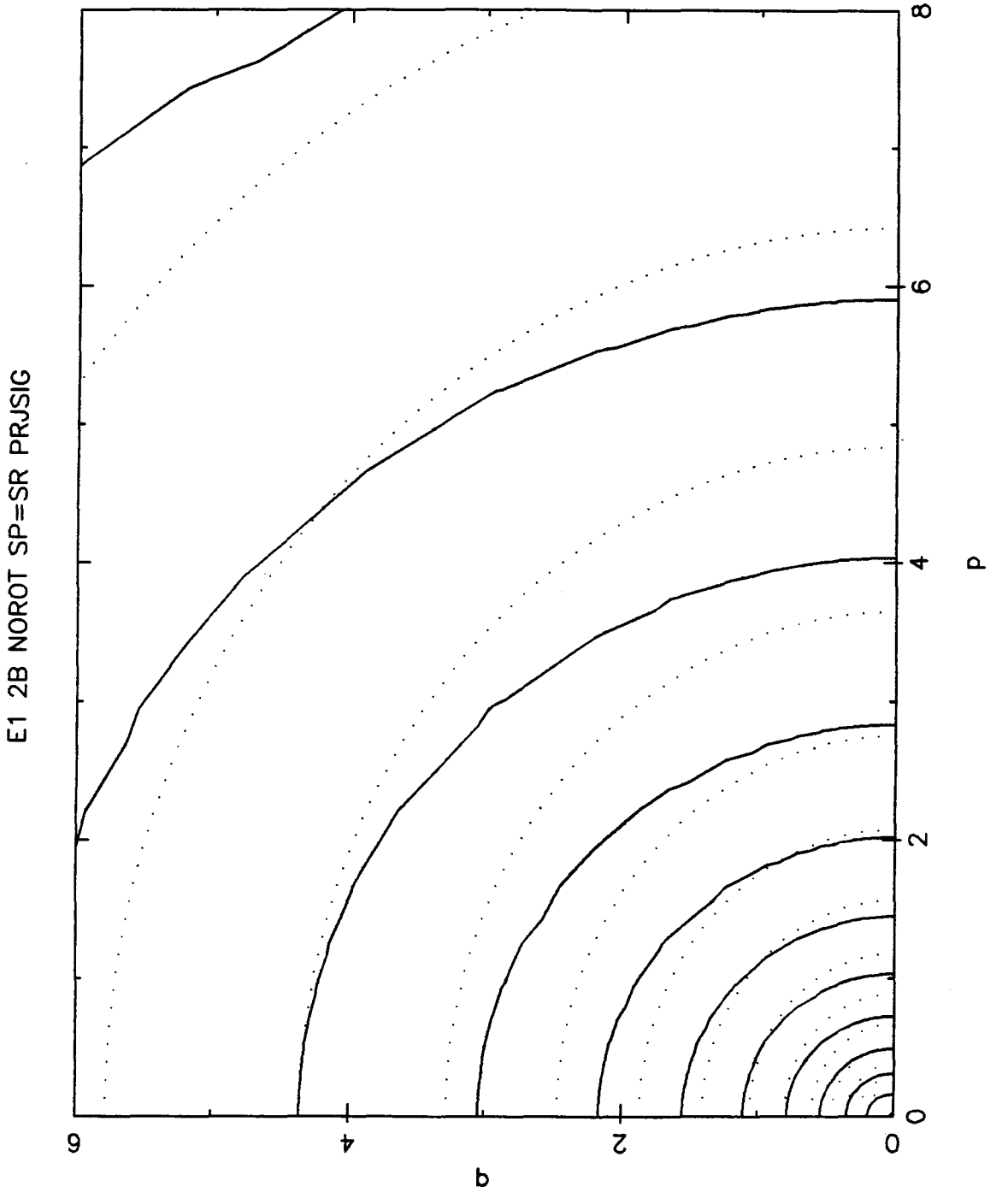

Fig. 13a

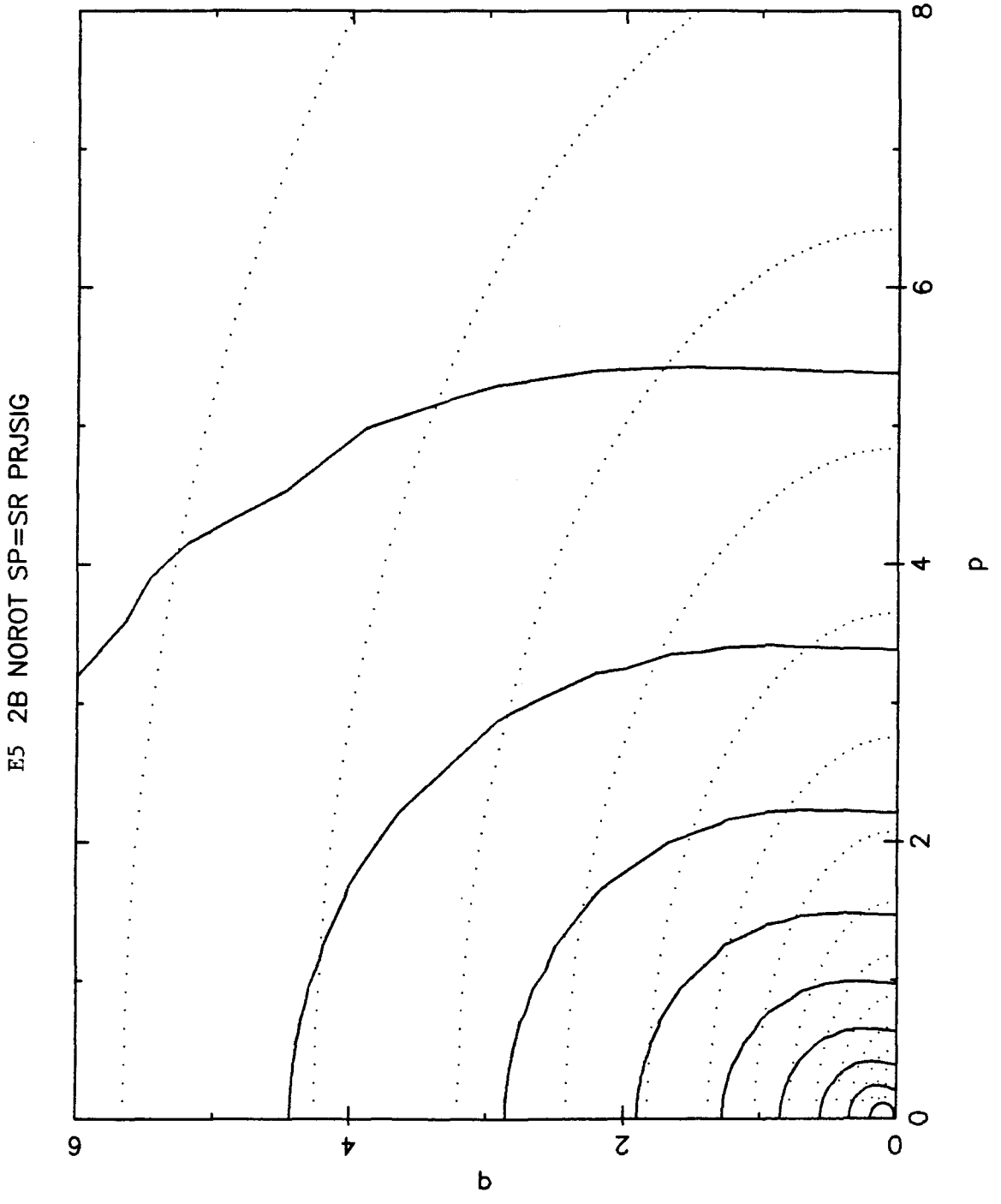

Fig. 13b

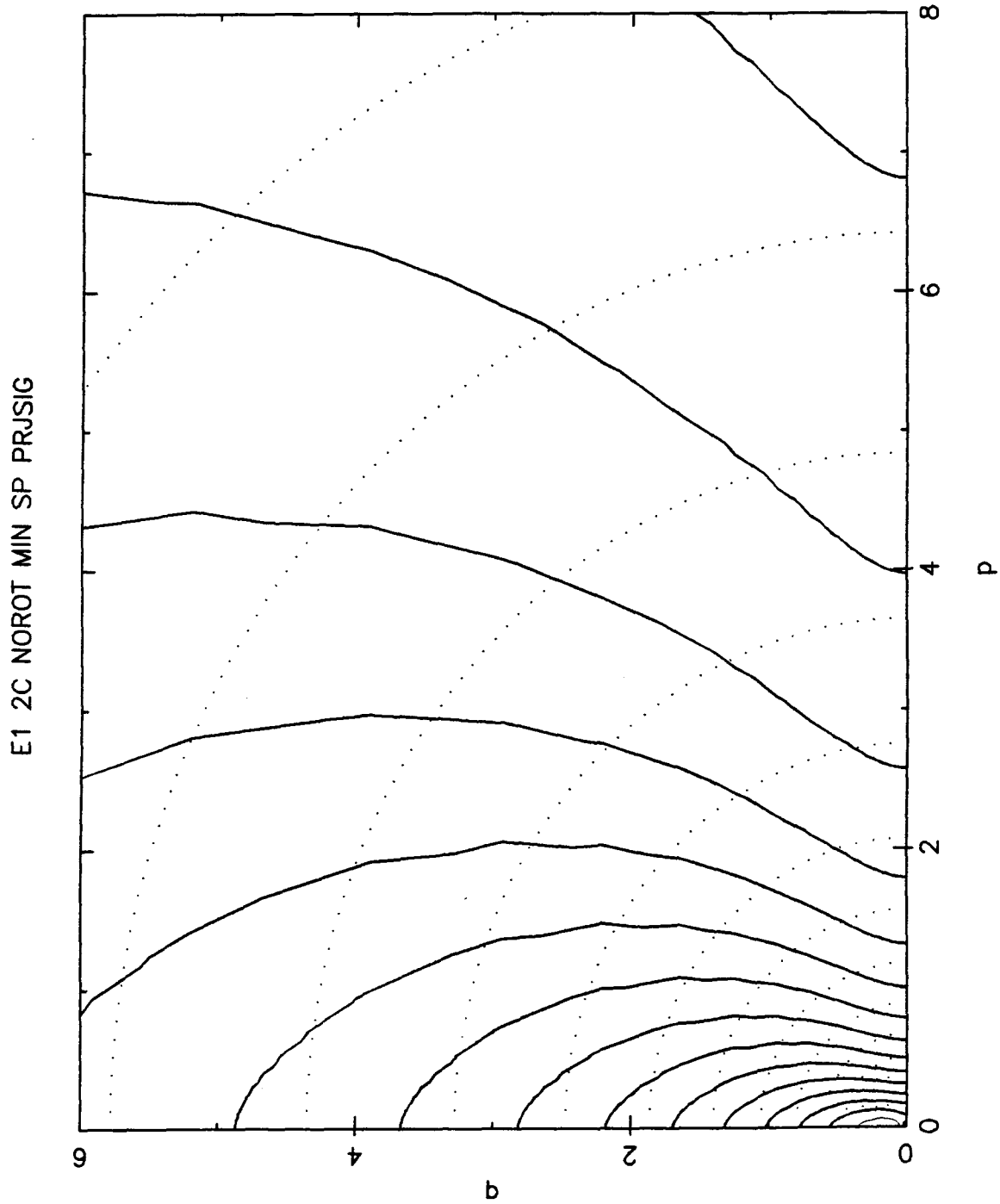

Fig. 14a

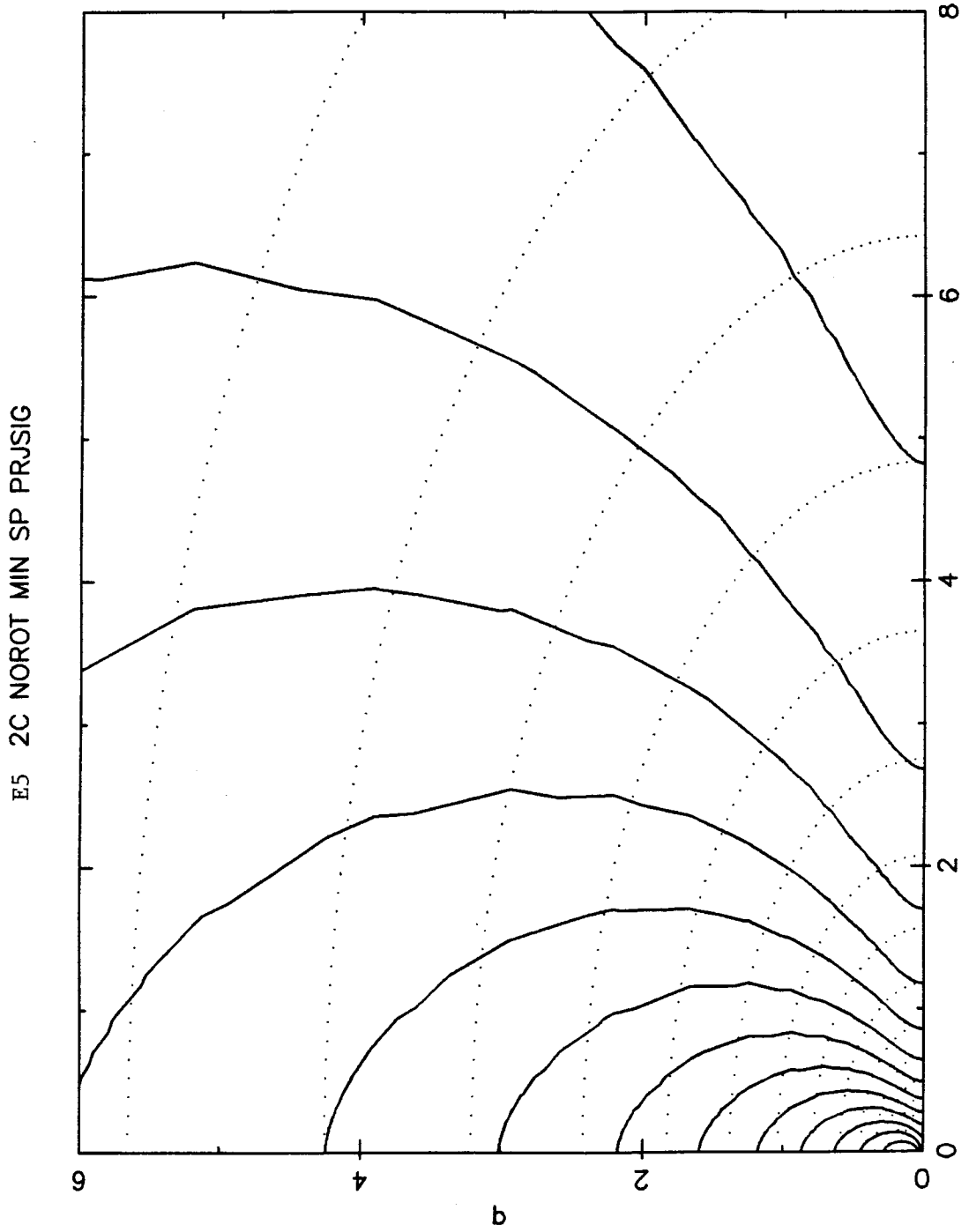

Fig. 14b

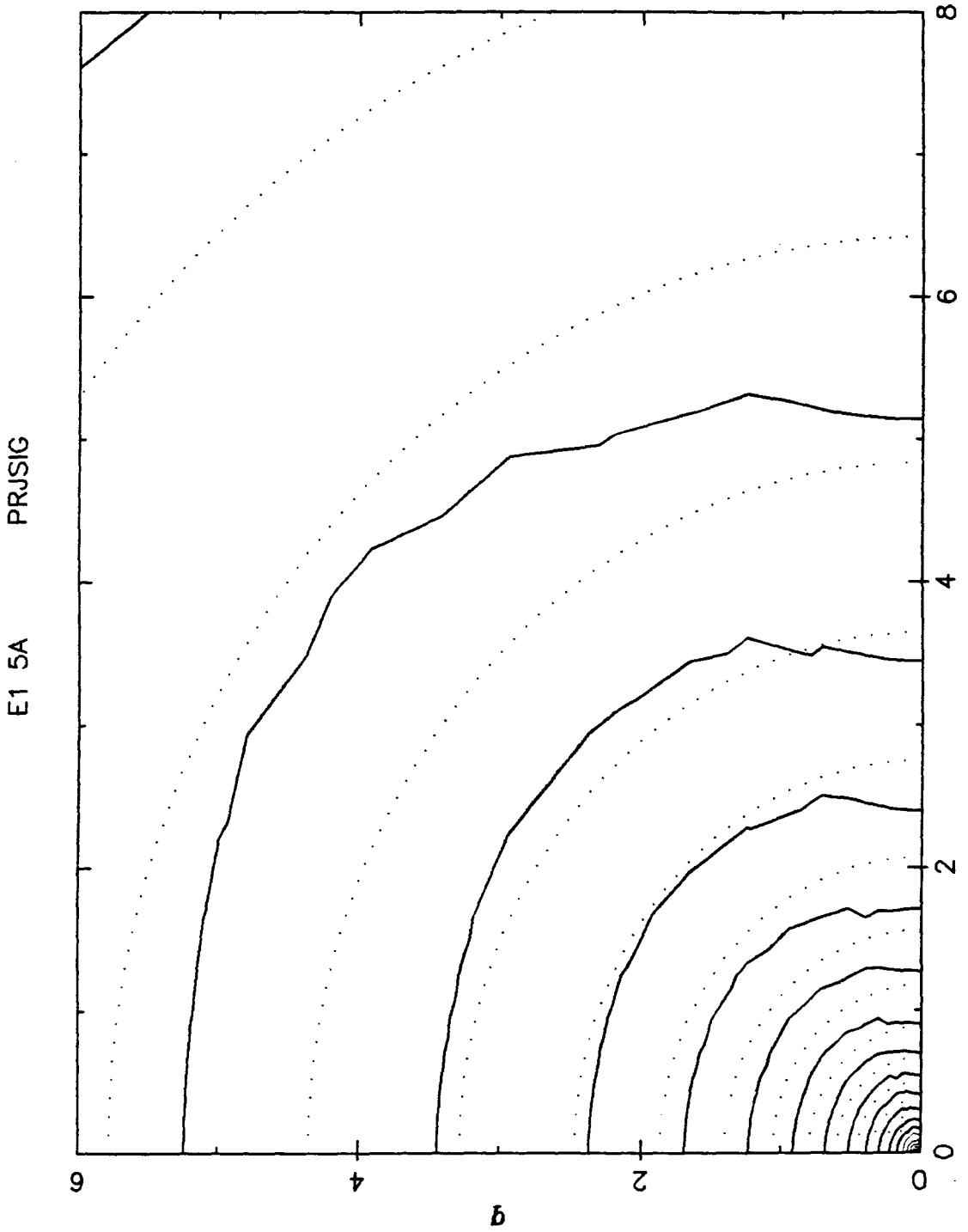

Fig. 15a

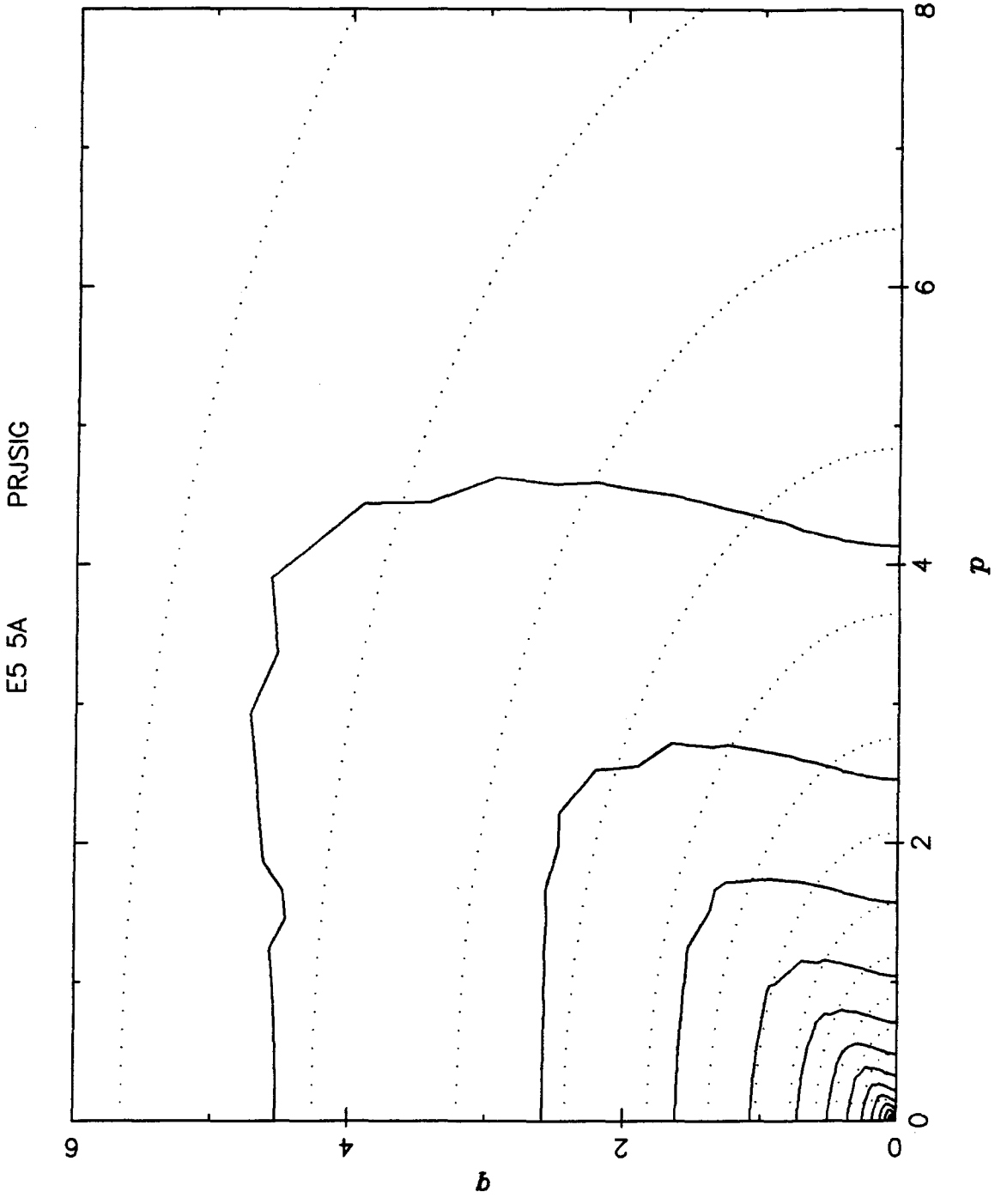

Fig. 15b

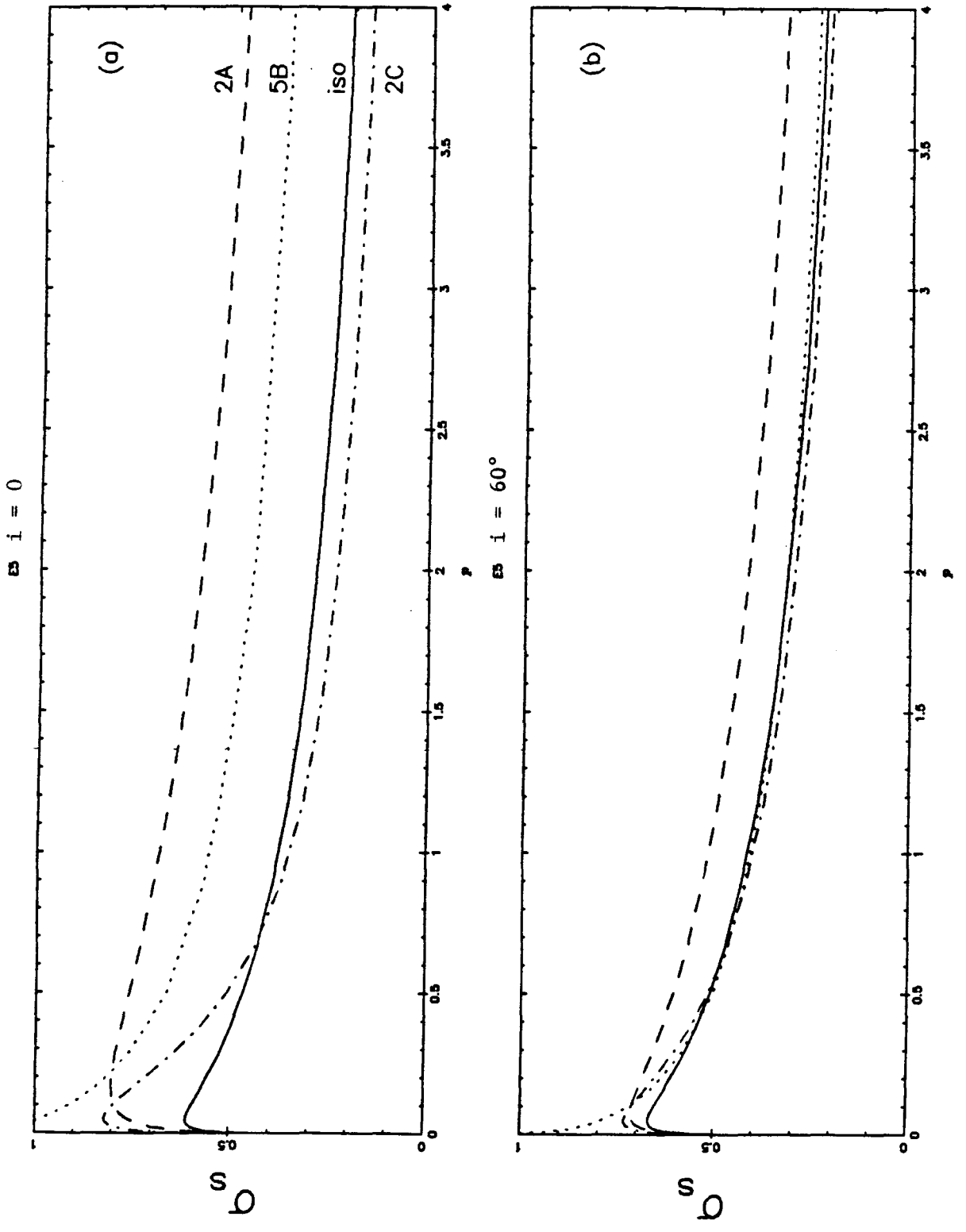

Fig. 16

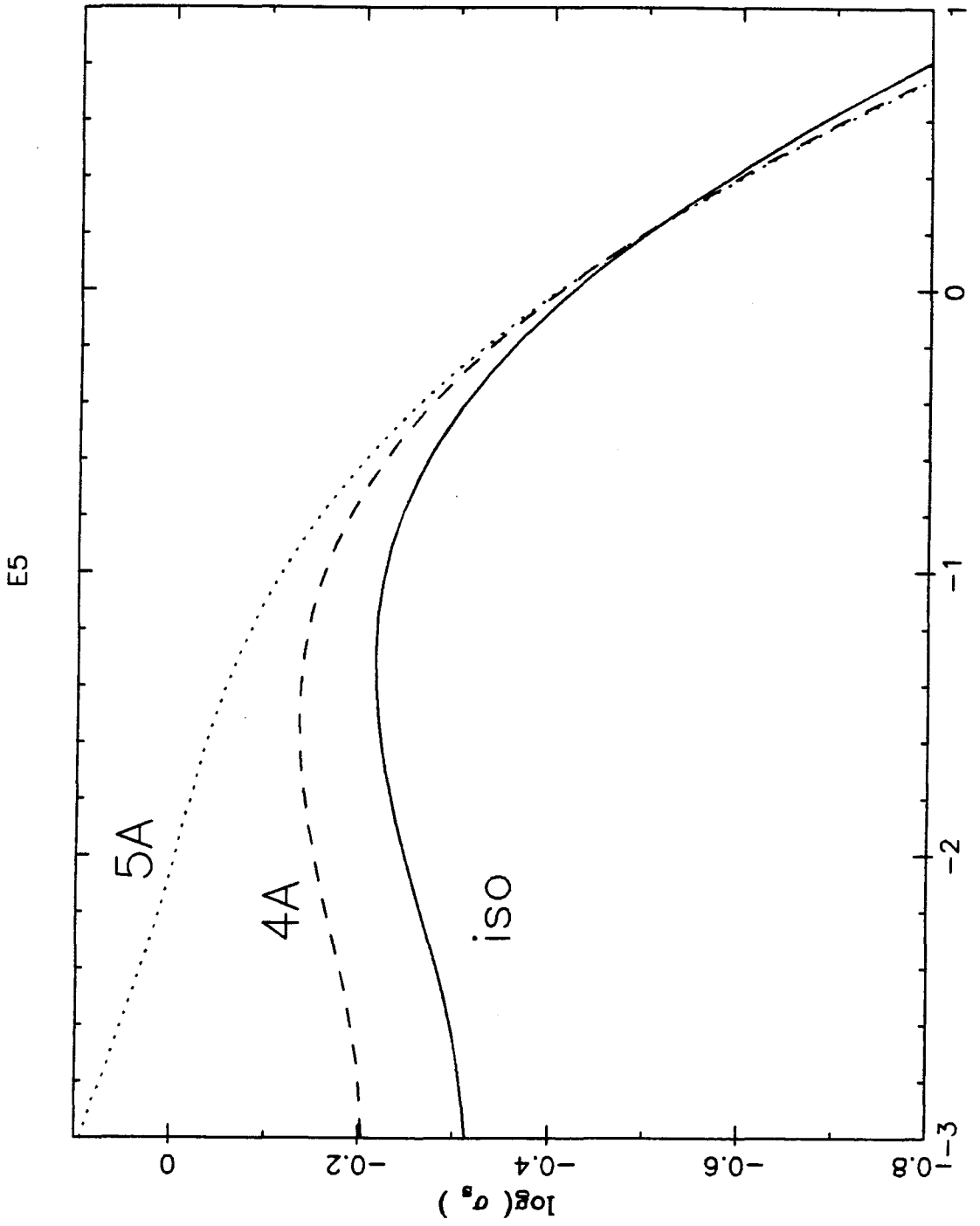

Fig. 17

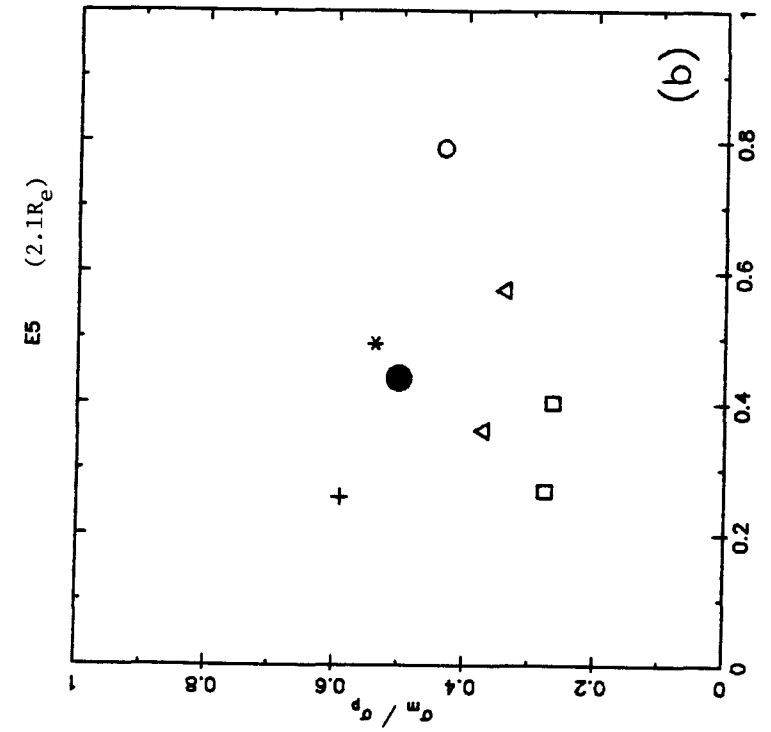

Fig. 18b

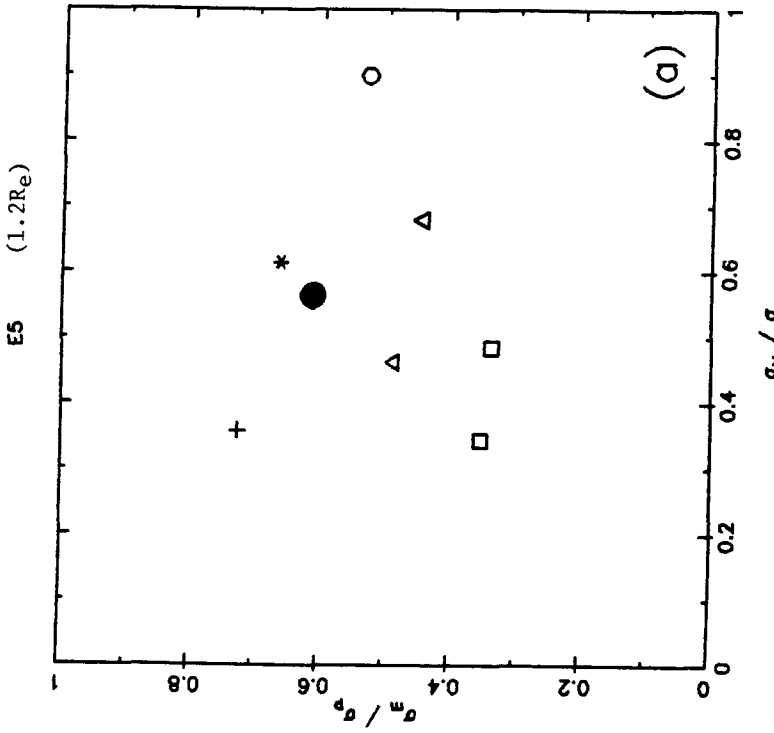

Fig. 18a

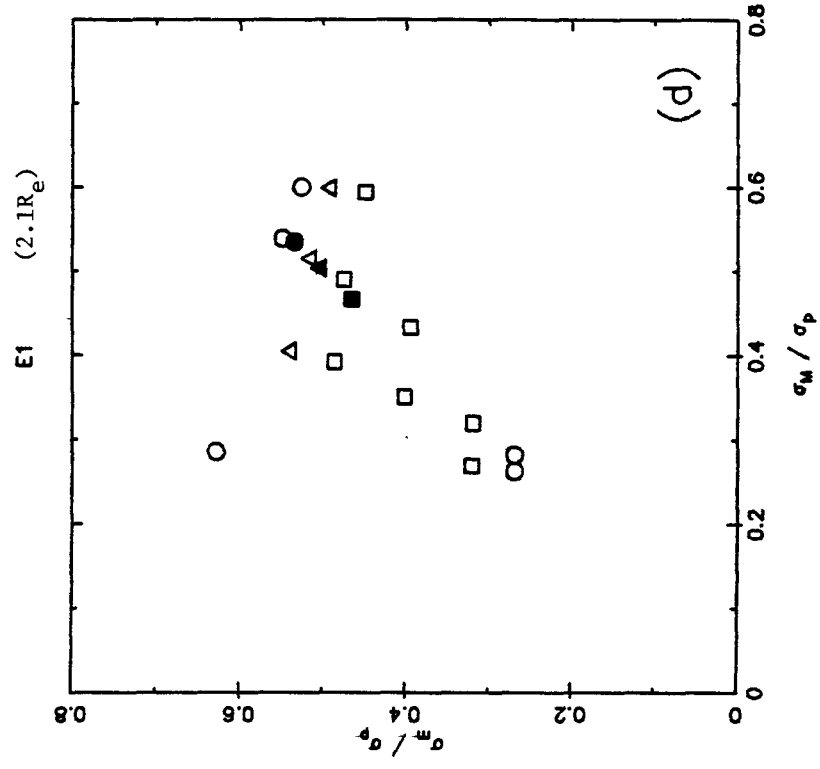

Fig. 18d

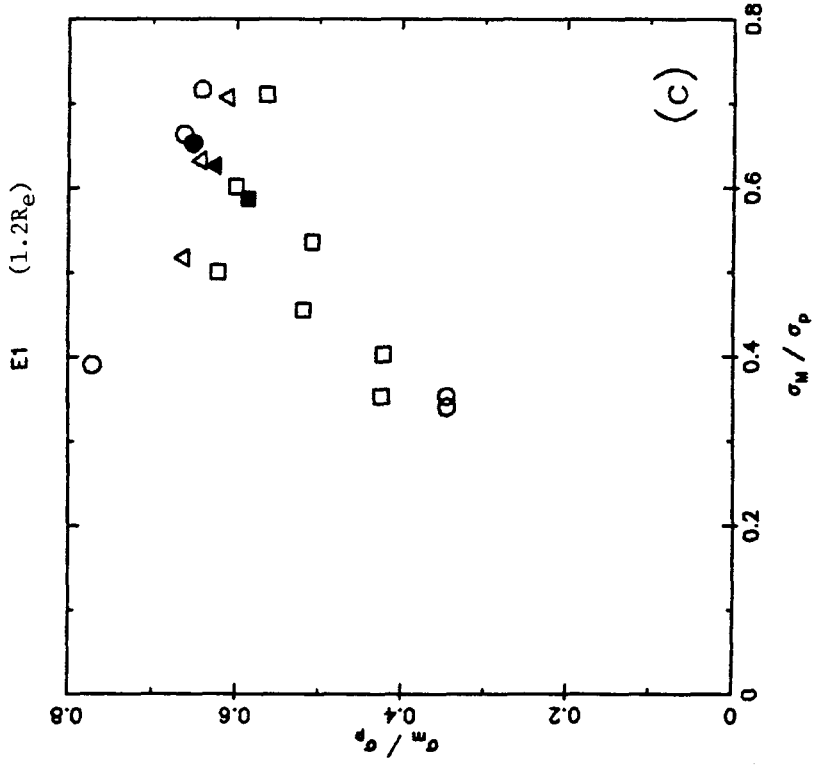

Fig. 18c

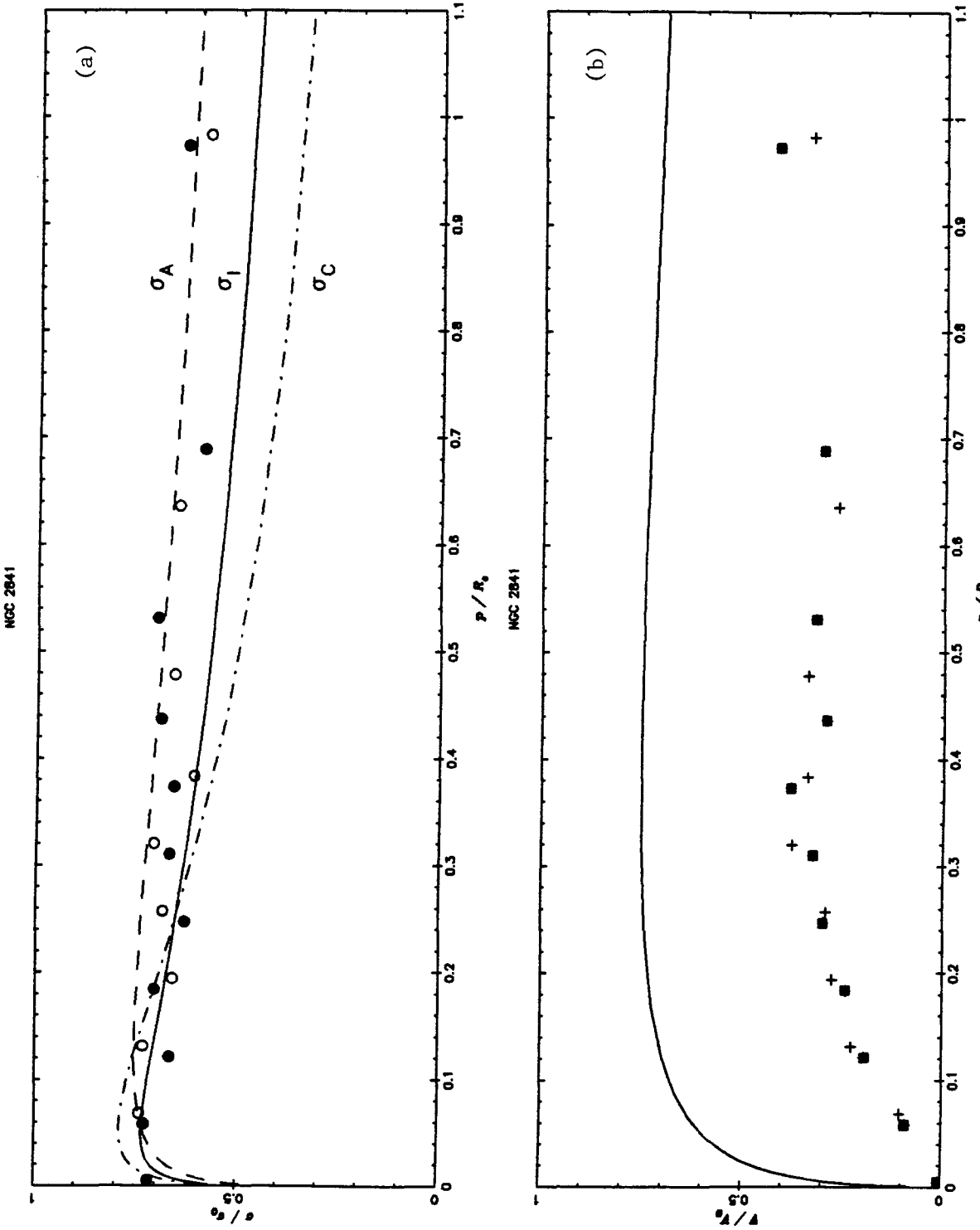
(a)
NGC 2841
σ_A
σ_l
σ_C
σ / σ_o
p / R_o
(b)
NGC 2841
V / V_o
p / R_o

Fig. 19

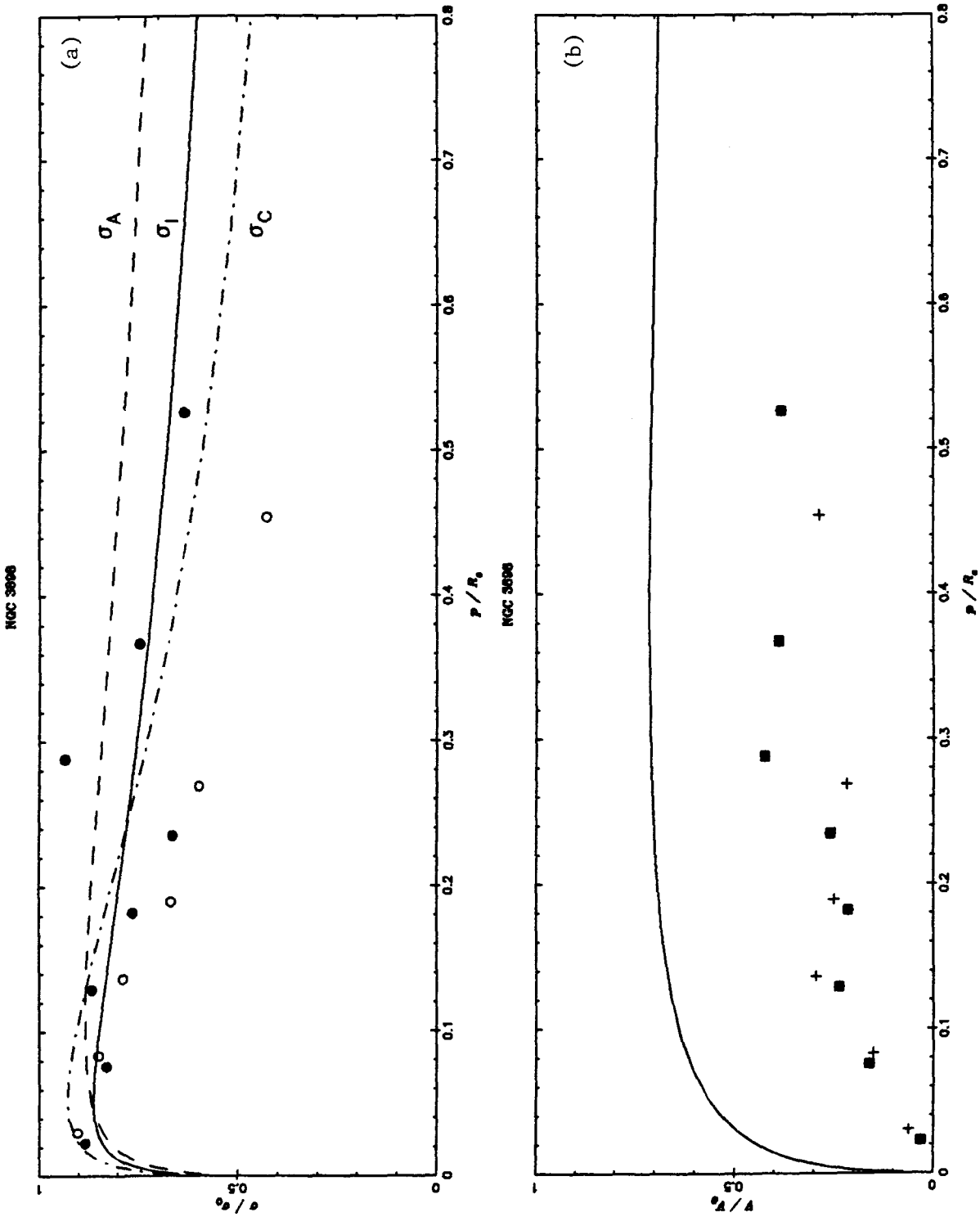
(a)
σ_A
σ_I
σ_C
NGC 3608
σ / σ_0
p / R_e
(b)
NGC 3608
V / V_0
p / R_e

Fig. 20

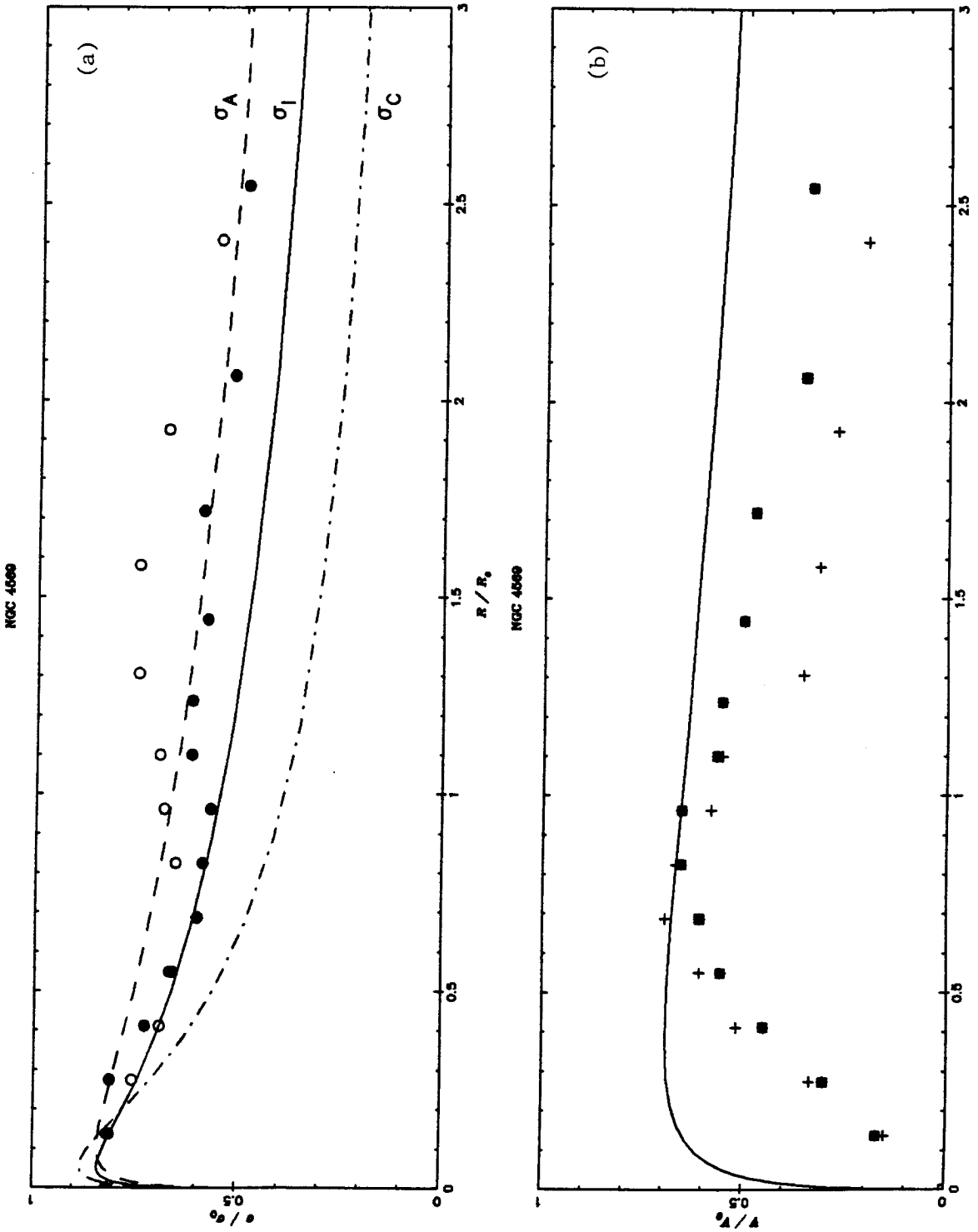
(a)
σ_A
σ_l
σ_C
NGC 4589
σ / σ_o
R / R_e
(b)
NGC 4589
V / V_o
R / R_e

Fig. 21

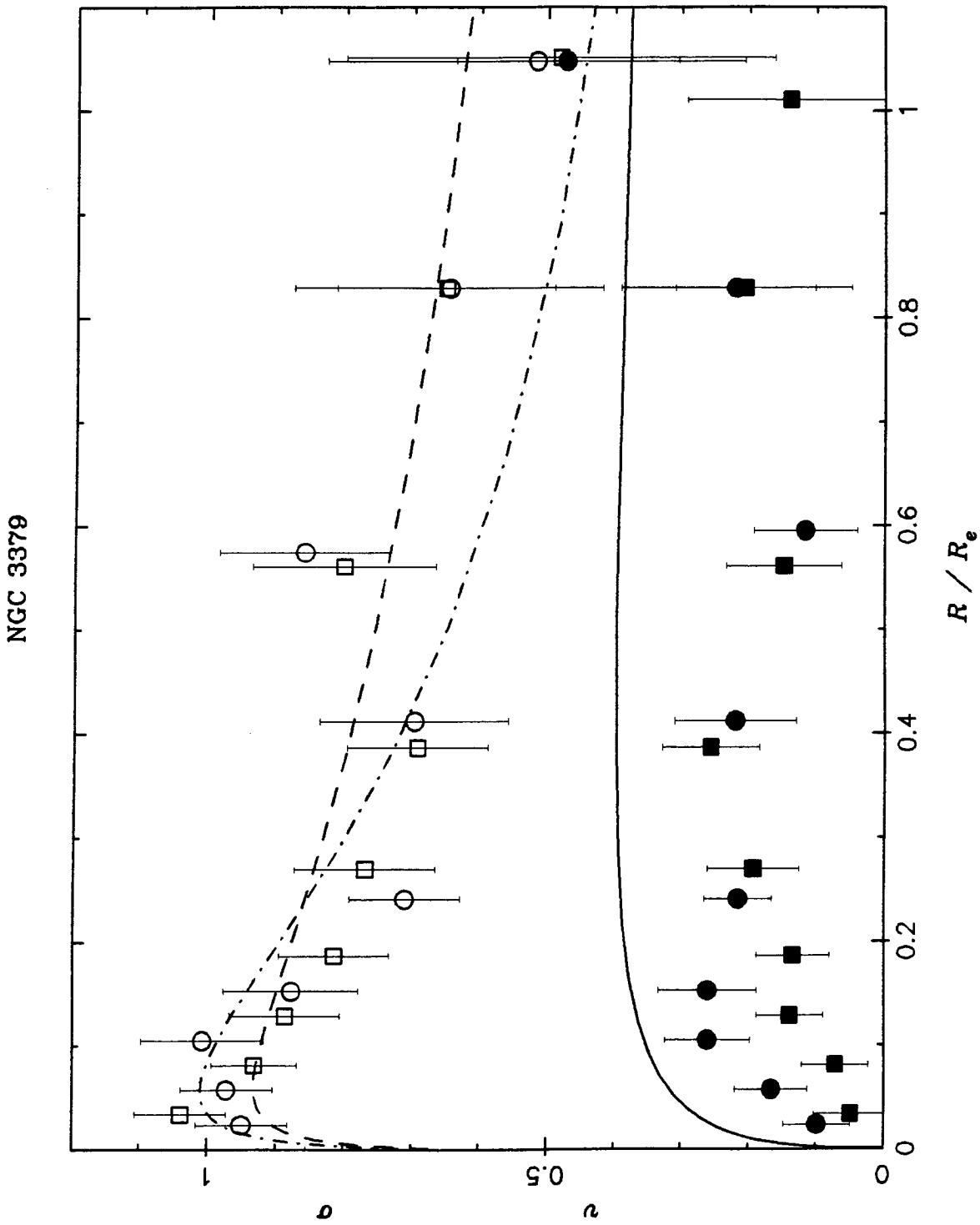

Fig. 22a

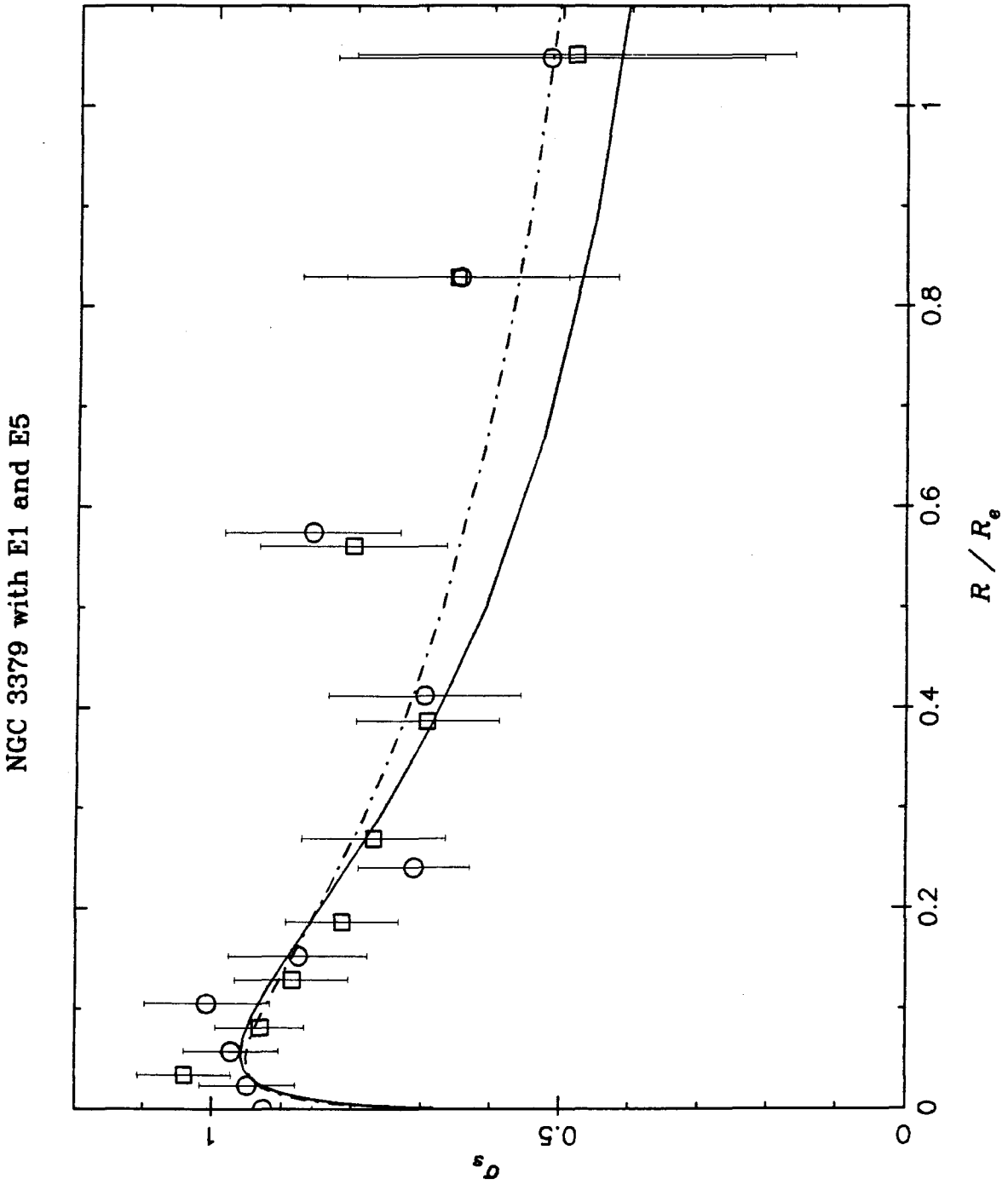

Fig. 22b

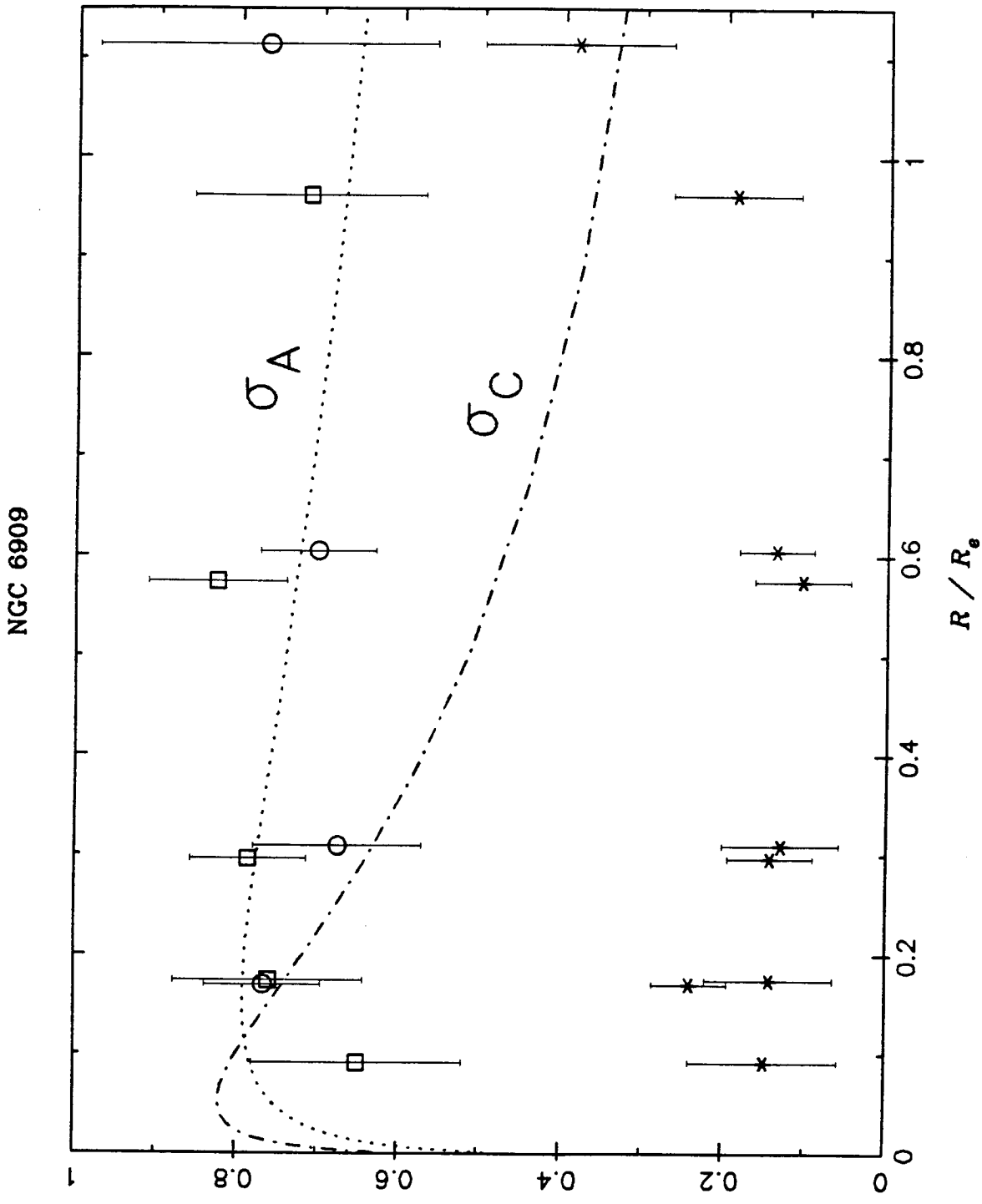

Fig. 22c

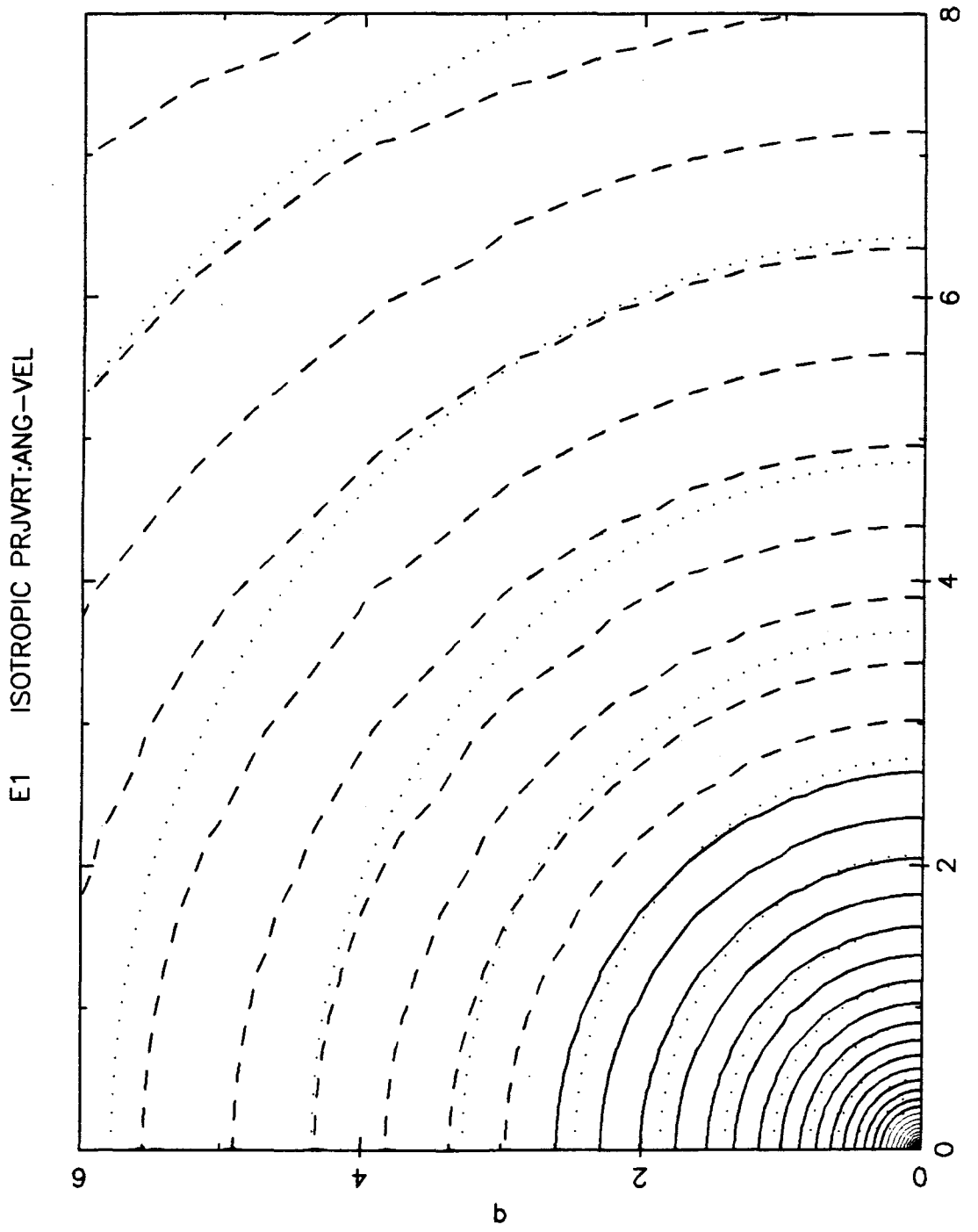

Fig. 23a

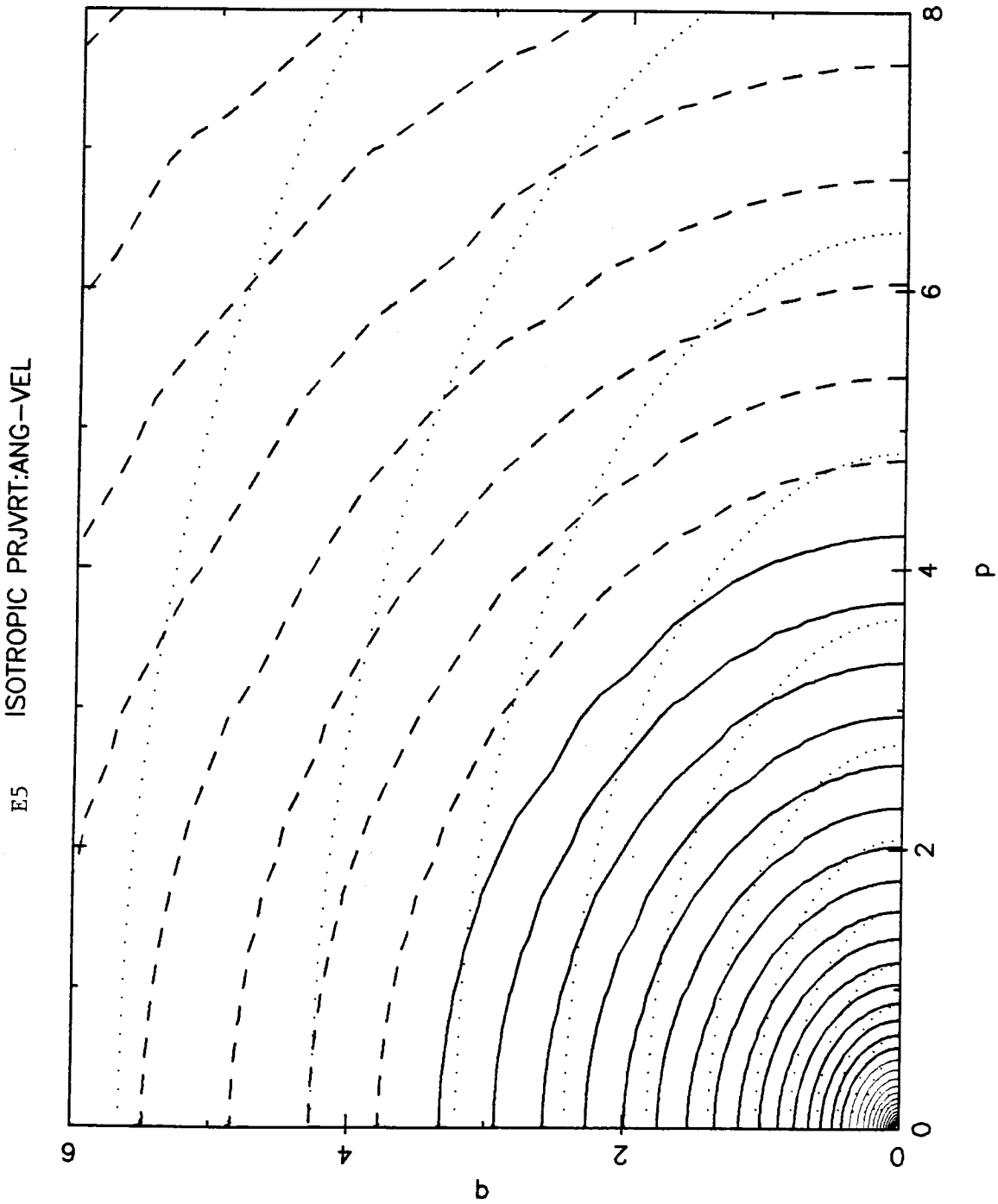

Fig. 23b

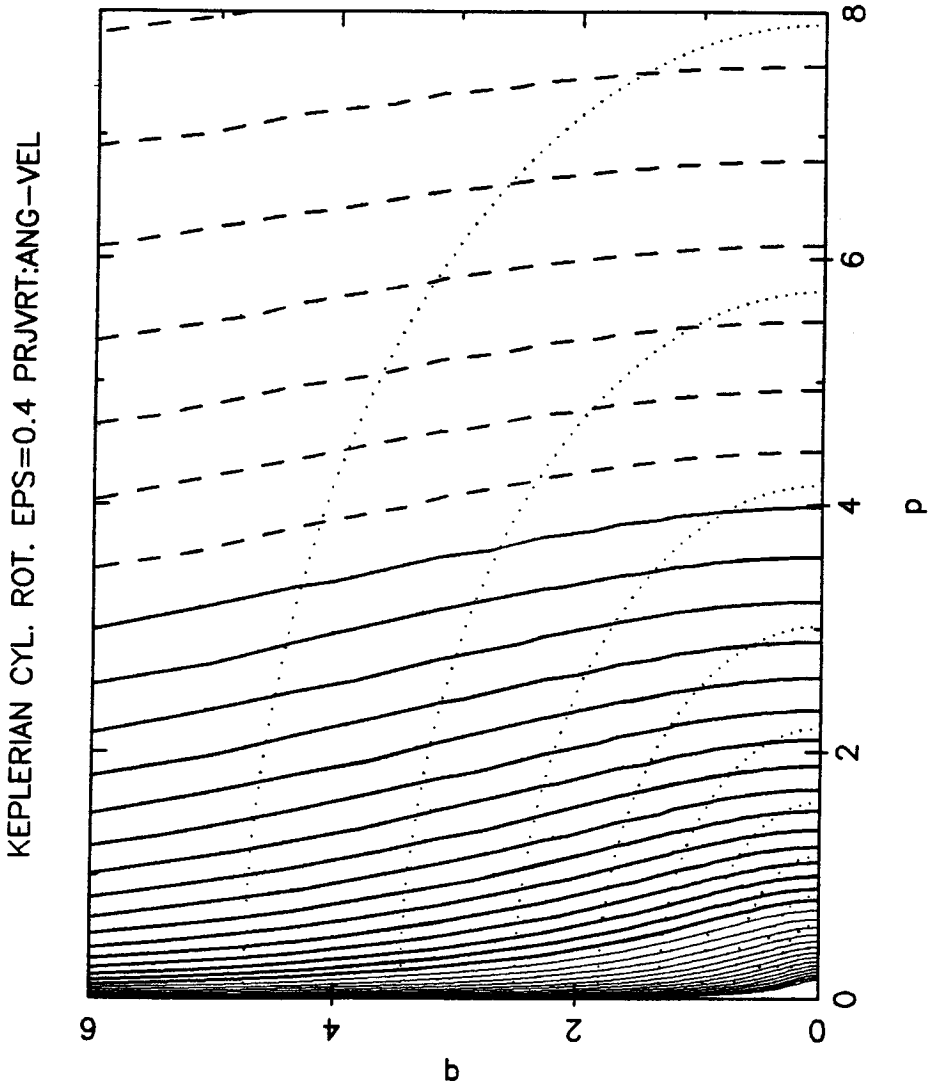

Fig. 23c

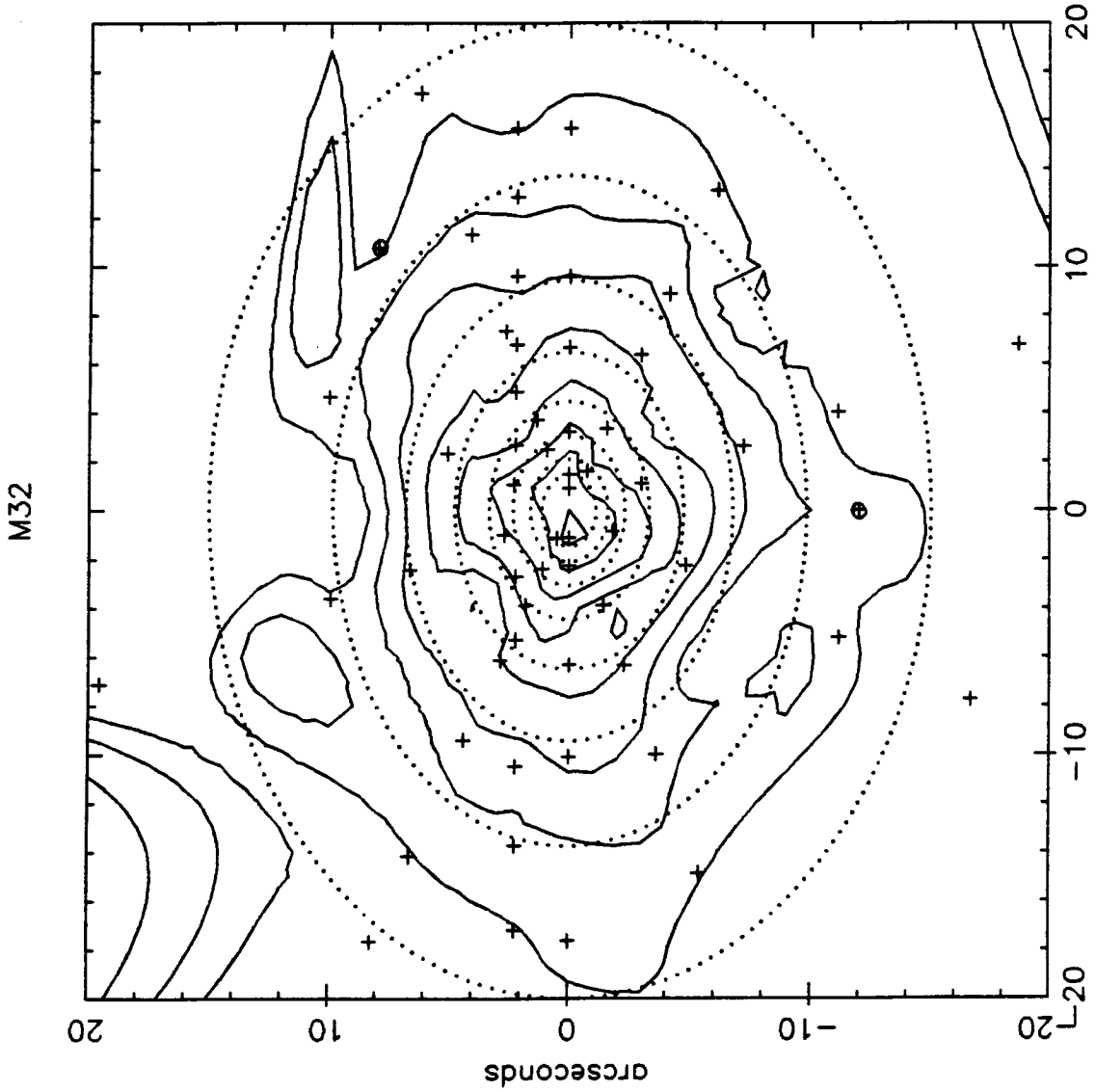

Fig. 24a

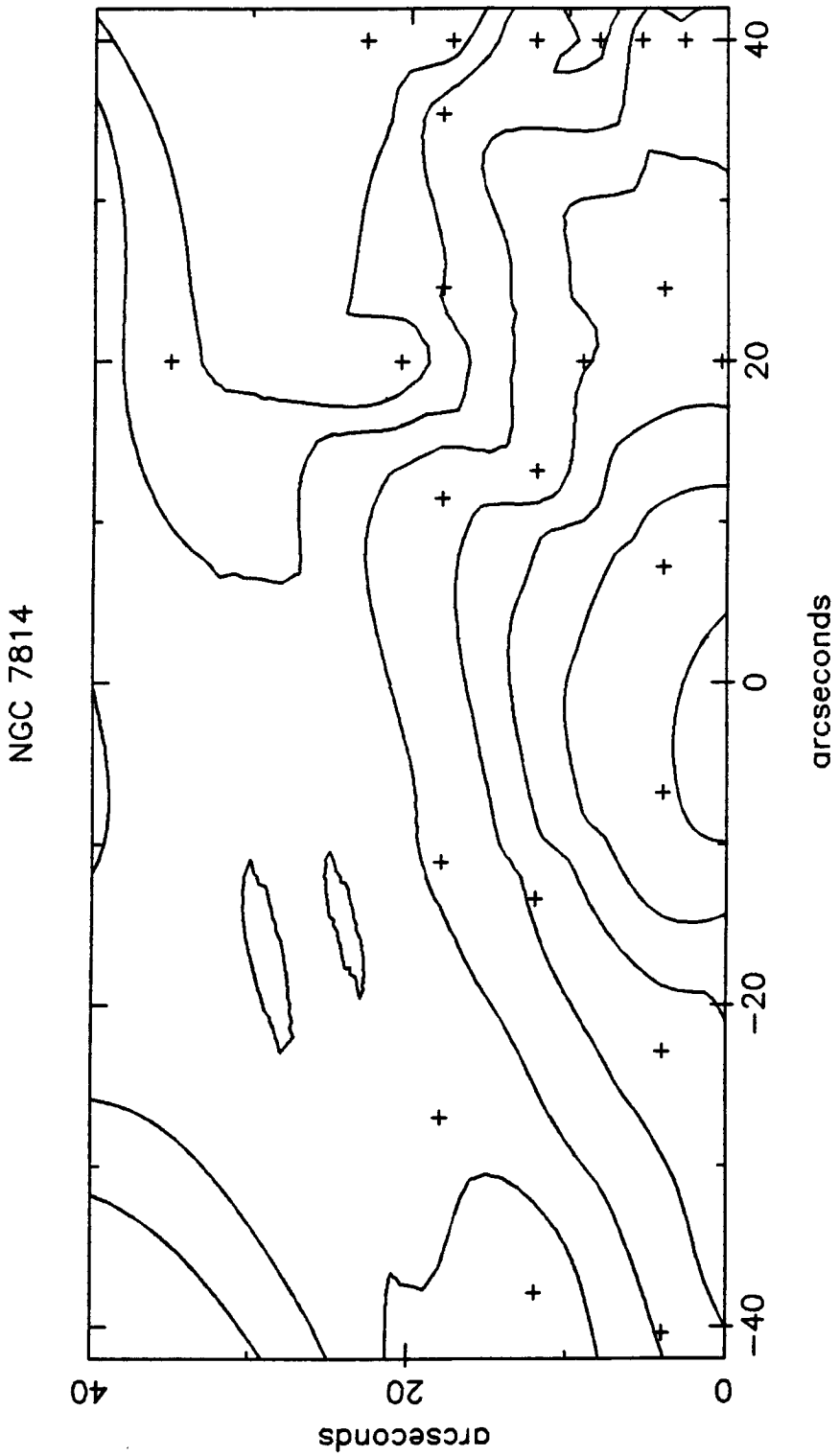

Fig. 24b

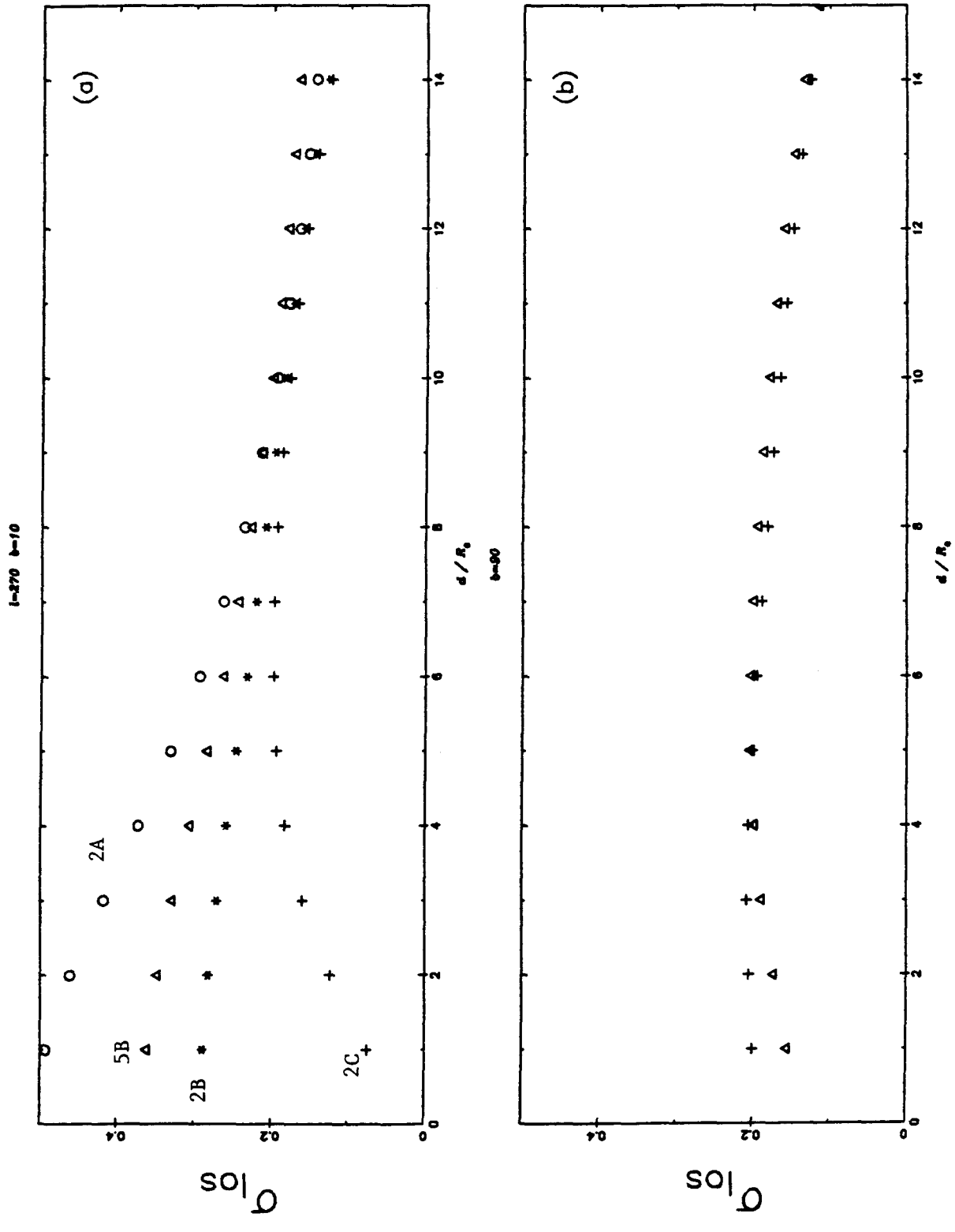

Fig. 25